Lipid Membranes: From Organizational Strategies in Cells to the Origins of Life

Caitlin E. Cornell

A dissertation
submitted in partial fulfillment of the
requirements for the degree of

Doctor of Philosophy

University of Washington

2020

Reading Committee:

Sarah L. Keller, Chair
Michael Schick
Joshua C. Vaughan

Program Authorized to Offer the Degree:

Department of Chemistry

University of Washington

Abstract

Lipid Membranes: From Organizational Strategies in Cells to the Origins of Life

Caitlin E. Cornell

Chair of the Supervisory Committee:

Sarah L. Keller

Department of Chemistry

Lipids, a fundamental building block of cells, can spontaneously self-assemble into vesicles, which are spherical shells consisting of a lipid bilayer. The structure of lipid bilayers determines their biological function: membranes are elastic, selectively permeable, and fluid barriers that separate the internal components of a cell from its external environment. Historically, the cell membrane has been viewed as a passive medium in which biologically active proteins reside. In the past several decades, investigation of the unique physical properties of multi-component lipid bilayers has uncovered the active organizational role of lipids in the cell membrane. Through changes in temperature or lipid composition, model ternary lipid bilayers can phase separate into coexisting liquid phases. Similarly, the membrane of living unperturbed yeast vacuoles exhibits coexisting liquid phases under stress conditions. Lipid membranes also have a role in the origins of cellular life: prebiotically-feasible bilayers concentrate the building blocks of protein and RNA, catalyzing the formation of biological polymers.

This text describes some physical properties of lipid membranes and their role in biological organization and the origins of cellular life. The chapters of this thesis start with (1) an introduction and then explore (2) the effect of general anesthetics on the phase behavior of synthetic and cell-derived membranes, (3) periodic small domains in synthetic and cell-derived membranes, (4) coexisting liquid phases on the submicron scale using cryo electron tomography, (5) miscibility transition temperatures of living, unperturbed yeast vacuole membranes, and (6) binding and stabilization of prebiotic fatty acid membranes by prebiotic amino acids. These examples demonstrate the importance of lipid membranes across many aspects of biology and the power of simple physical principles to explain complex phenomena.

To my aunt Mary Lou,
for teaching me to creatively
explore the world with
diligence and compassion.

Table of Contents

ACKNOWLEDGEMENTS 10
INTRODUCTION 12
1.1 (Over) One Hundred Years of Membranes: A Brief History of Biomembrane Research 12
1.2 General Structure and Properties of Lipids and a Lipid Bilayer 14
1.3 Liquid Immiscibility in Ternary Membrane Mixtures 16
1.4 Experimental Techniques to Probe Phase Behavior in Ternary Membrane Mixtures 18
1.5 Model Membrane Systems 19
1.5.1 Giant Unilamellar Vesicles (GUVs) 20
1.5.2 Giant Plasma Membrane Vesicles (GPMVs) 22
1.5.3 Yeast Vacuoles 25
1.5.4 Fatty Acid Vesicles and 'Protocells' 27
1.6 Overview of Dissertation 29
1.7 List of Publications 29
CHAPTER 2: *n*-alcohol Length Governs Shift in Lo-Ld Mixing Temperatures in Synthetic and Cell-Derived Membranes 31
2.1 INTRODUCTION 31
2.2 MATERIALS AND METHODS 32
Materials 32
Production of GUVs for T_{mix} Measurements 33
Measurement of T_{mix} 34
AC50 Values 35
Cell Culture and GPMV Isolation 35
Laurdan and C-laurdan Microscopy 36
Area Fractions 37
High-Pressure Microscopy 37
2.3 RESULTS AND DISCUSSION 37
N-alcohols Increase T_{mix} in Model Membranes 37
Increase in T_{mix} is Robust Across Lipid Ratios and Lipid Types 38
Butanol Increases L_o-L_d Contrast in GUVs, but Not in GPMVs 40
Nonmonotonic Shifts in T_{mix} for Long *N*-alcohols 43
Alcohol Anti-intoxicants Increase T_{mix} in GUVs 46

Minor Structural Changes in Alcohols Result in Large Shifts in Membrane T_{mix} 47
Hydrostatic Pressure Increases T_{mix} in GUVs 48
2.4 SPECULATIONS 49
2.5 CONCLUSION 50
2.6 ACKNOWLEDGEMENTS 51
2.7 SUPPLEMENTARY FIGURES AND TABLES 51
CHAPTER 3: Tuning Length Scales of Small Domains in Cell-Derived and Synthetic Model Membranes 57
3.1 INTRODUCTION 57
3.2 METHODS 59
GUV Electroformation 59
DPPC-loaded HPαCD 60
GUVs with Small Length Scales 60
GUV Temperature 61
GUV Osmotic Pressure 61
Cell Culture and GPMV Isolation 62
GPMV Temperature 62
GPMV Osmotic Pressure 63
Image Analysis 63
3.3 RESULTS 63
The Characteristic Length Scale is Inversely Related to Temperature 63
The Characteristic Length Scale Increases with Membrane Tension 67
Domain Morphology Varies with GUV Composition 68
3.4 MECHANISMS 70
Evaluation of Membrane Asymmetry 71
Evaluation of Membrane Tension 75
Evaluation of Phase Diagrams 75
Evaluation of Dipole Repulsion Contribution 76
3.5 CONCLUSION 77
3.6 ACKNOWLEDGEMENTS 78
3.7 SUPPLEMENTARY METHODS, FIGURES, AND CODE 79
CHAPTER 4: Direct Imaging of Liquid Domains in Membranes by Cryo Electron Tomography 84
4.1 INTRODUCTION 84
4.3 MATERIALS AND METHODS 86

Lipids 86
GUV Electroformation 87
Extrusion 87
Introduction of Trimeric mCherry 88
Fluorescence Imaging 88
Cryo Electron Tomography 89
Analysis of Thickness Mismatches 90
4.3 RESULTS 92
4.4 DISCUSSION AND CONCLUSION 99
4.5 ACKNOWLEDGEMENTS 101
4.6 SUPPLEMENTAL MATERIAL 102
CHAPTER 5: Yeast Alter Vacuole Membrane Phase Behavior in Response to Changes in their Growth Environment 111
5.1 INTRODUCTION 111
5.2 MATERIALS AND METHODS 112
Yeast Cell Culture 112
Temperature Experiments 112
Analysis of T_{mix} 113
Vacuole Isolation 114
Cyclodextrin:Ergosterol Complex 114
Microsome Preparation for Immuno-isolation of Vacuoles 115
Immuno-isolation 116
5.3 PRELIMINARY RESULTS AND DISCUSSION 116
Vacuoles of *S. cerevisiae* have a Characteristic T_{mix} 116
Vacuoles Grown at Low Temperature have a Similar T_{mix} to Those Grown at 30°C 118
Ergosterol is Important for Vacuole Membrane Phase Separation 119
5.4 FUTURE DIRECTIONS 120
Lipidomics of Yeast Vacuole Membranes at Different Growth Stages and Growth Temperatures 120
CHAPTER 6: Prebiotic Amino Acids Bind to and Stabilize Prebiotic Fatty Acid Membranes 123
6.1 INTRODUCTION 123
6.2 METHODS 124
Materials 124
Decanoic Acid Solution 124

Diffusion NMR 125
REDOR 125
Filtration Assay 126
NaCl and $MgCl_2$ Effects 126
Fluorescence Microscopy 126
Cryo Transmission Electron Microscopy 126
Turbidity 127
Critical Vesicle Concentration 127
Critical Aggregate Concentration 127
Rehydration 127
Size Exclusion Chromatography (SEC) 128
Dynamic Light Scattering 128
6.3 RESULTS 128
Amino Acids Bind to Decanoic Acid Vesicles 128
Amino Acids Increase Vesicle Stability Against Mg^{2+} and/or NaCl 132
Vesicle Stability Against Mg^{2+} Correlates with an Increase in Lamellarity 134
Serine, Glycine and the Other Relatively Hydrophilic Amino Acids Increase Turbidity 136
Amino Acids Plausibly Increase Vesicle Lamellarity in Pools Undergoing Wet-Dry Cycles 137
6.4 DISCUSSION AND CONCLUSIONS 138
6.5 ACKNOWLEDGEMENTS 140
6.6 SUPPLEMENTAL INFORMATION 141
COMPLETE BIBLIOGRAPHY 151
APPENDIX A: EXTENDED METHODS 168
A.A.1 Preparation of Giant Unilamellar Vesicles (GUVs) via Electroformation 168
A.A.2. Fluorescence Microscopy of GUVs to Determine T_{mix}. 171
A.A.3 Preparation of Large Unilamellar Vesicles (LUVs) via Extrusion 172
A.A.5 Cryogenic Freezing of LUVs via a Vitrobot 173
A.A.6 Preparation of In-Cell Yeast Vacuoles for Fluorescence Imaging 174
A.A.7 Preparation of Isolated Vacuoles for Fluorescence Imaging 175
A.A.8 Preparation of Fatty Acid Vesicles for Fluorescence Imaging 176
APPENDIX B: CODE 178
A.B.1 Code for “Tuning Length Scales of Small Domains in Cell-Derived and Synthetic Model Membranes 178

Name: 1DPairCorrelation_truncate.py 178
Name: 1DStructureFactor.py 181
A.B.2 Code for “Direct Imaging of Liquid Domains in Membranes by Cryo Electron Tomography” 183
Name: BilayerHeightMeasurements.py 183
Name: CombinedPlotter.py 188
Name: MixtureModel.py 189
Name: ColorMapMask_V2.py 193
A.B.3 Code for “Yeast Alter Vacuole Phase Behavior to Adapt to Their Growth Environment” 200
Name: MiscibilityTemp.py 200
Name: CombinedPlotter_V2.py 204

ACKNOWLEDGEMENTS

First and foremost, I want to thank my advisor, Sarah L. Keller. Sarah has tirelessly provided me intellectual, moral, and emotional support. There have been many times throughout these past six years that I have felt incompetent as a scientist and Sarah has always been there to assure me that I am capable. Sarah's thorough and diligent approach to science spills over into her approach to mentorship and advocacy. She has inspired me to pursue a scientific question until every angle has been explored, and she has taught me to remain receptive to other's experiences and the lessons that they give. Sarah has taught me more than science: the way she conducts research and how she interacts with scientists, regardless of their training or expertise, has shaped the scientist I am and inspired the mentor I hope to be.

I am also incredibly grateful for the talented and hilarious colleagues I have had the pleasure of working with for the past six years. Scott Rayermann, Matthew Blosser, Jonathan Litz, Joan Bleecker, Moshe Gordon, Ranee James, Christina Fowler, Catharine Chang, Glennis Rayermann, Brenda Kessenich, Chantelle Leveille, Zachary Cohen, and Heidi Spears – you have all kept me sane, entertained, and inspired. I count myself lucky because I consider every single coworker a friend. I look forward to laughing and drawing inspiration from all of you in the coming years.

Along with my official advisor, I have had many non-official mentors throughout graduate school. I would like to thank Roy Black for inspiring me right from the very beginning and treating me as an intellectual equal. I have learned so much from Roy and I look forward to continuing our discussions past my time at UW. I would also like to thank Michael Schick for consistently engaging with my research and providing endless support to my development as a scientist. I have also received ample mentorship and intellectual support from Sharona E. Gordon and Alexey J. Merz; both are brilliant scientists and excellent human beings.

I want to thank all of the brilliant collaborators I have had the privilege to work with on the projects outlined in this thesis. In particular, I am so grateful to have met and worked with Ilya and Kandace Levental. Over the course of our many collaborations, they have provided me with their support, their friendship, and their lab.

Thank you to my committee members Sharona E. Gordon, Michael Schick, Joshua C. Vaughan, and Kelly K. Lee (and my past committee member, Lutz Maibaum). They have all been encouraging and willing to engage in fruitful scientific conversations with me throughout these past six years.

Lastly, and arguably most importantly, I want to thank my friends and family. Without you, I would not have a PhD. Lisa Sofia Robinson is an amazing mother, a creative force, my ultimate inspiration, and the strongest person I know. Silas Cornell is an incredibly supportive father and his love and encouragement, especially while writing this thesis, has been immeasurable. My little brother, Ethan Cornell, has given me unconditional love and grace my entire life. He inspires me to be better every day. My older brother, Sam Cornell, has always encouraged me to pursue my passions. Wade Robinson is the most solid and self-confident person I know, and I am so grateful that he is in my mother's life, and in mine. Safi Karmy-Jones is my best friend, my confidant, my rock, and my family and her jokes will continue to sustain me in the coming years. Niket Thakkar's influence and creativity seeps out of every corner of this thesis. He has provided me endless emotional support and his ideas have inspired large portions of my work. He is my "pocket mathematician" and he constantly inspires my research and how I live my life. Finally, I want to thank Trupti Thakkar, Harshad Thakkar, Nehal Thakkar, Sachin Mehta, Nipa Eason, Jeremy Eason, and Aria Eason. They are my second family.

INTRODUCTION

Membranes are a hallmark of cellular life: they separate the cell from its external environment, compartmentalize functions within the cell, and facilitate cell-cell interactions. Each of the critical functions of a cell, such as growth, replication, and tissue assembly, depend on the cell membrane. To successfully perform these functions, the membrane must be 1) selectively permeable (*e.g.* permeable to water but impermeable to larger molecules like sugars and charged molecules like salts), 2) flexible (*e.g.* able to sustain large morphological changes during cell division), and 3) fluid (*e.g.* shown to undergo rapid lateral diffusion and reorganization of component molecules). Biological membranes exhibit these diverse material attributes because of the chemical properties of the lipids that comprise them. Lipid membranes play a prominent role in many fields: from biochemistry and biology, to soft matter physics and mathematics. Investigations of lipid systems have deepened our understanding of cellular biology, interfacial physics, and the origins of life, and it has ushered in developments in biomedicine and nanotechnology. It is difficult to overestimate the importance of lipid membranes to science, life, and everything in between.

This text will describe the physical properties of lipid membranes and their role in biological organization and the origins of life. This first chapter will provide a brief history of the study of biomembranes, followed by a discussion of the chemical and physical properties of lipids and the larger structures into which they self-assemble. The role of membranes in the origins of life will also be discussed, punctuated by an overview of the chapters within this text.

1.1 (Over) One Hundred Years of Membranes: A Brief History of Biomembrane Research

When Robert Hooke first peered through his microscope in 1665 at material scraped beneath the bark of a cork tree, he coined the term “cell” and jumpstarted the study of cell membranes (1). Hooke theorized that cells were made of a colloidal-gel material called ‘protoplasm’. The outline of cork cells, he postulated, was simply caused by a reaction between the colloidal protoplasm and the external liquid surrounding the cell which caused the contact layer to harden through aggregation (2). Until 1877, cells were thought to have stiff exteriors up until Wilhelm Pfeffer proposed that the cellular protoplasm was sheathed in a flexible skin, or plasma membrane (3).

A decade later while investigating plant inheritance, Charles E. Overton was struck by the peculiarity of the chemicals that could permeate the cell protoplasm barrier. With a major research

pivot, Overton began a fastidious osmometric study of chemicals that could cross the cell barrier (4). In 1899, he published a "suspicion" that the protoplasm barrier was impregnated with lipidic substances, such as cholesterol and lecithin (4). Now, Overton is recognized for his discovery, along with Hans Horst Meyer, that the propensity of general anesthetics to dissolve in oil is correlated with their clinical efficacy (5, 6).

Others were fascinated in the physical properties of oil thin films. In the late 1700s, Benjamin Franklin first described the behavior of an oil droplet spreading across the surface of water (1). Close to a century later in 1890, Lord Rayleigh repeated Franklin's experiment and estimated the thickness of the oil film to be ~10-20 angstroms (7). Lord Rayleigh's experiments sparked the curiosity of Agnes Pockels, an 18-year-old woman with scientific aspirations. In her kitchen, Pockels developed a device to measure the surface tension of a thin oil film on water (8). Around twenty years later, Irving Langmuir and Katharine Blodgett, refined Pockels' design and developed the Langmuir trough for high-resolution measurements of the surface tension of oil thin films, establishing the study of monolayers (9).

These separate lines of inquiry culminated in 1925 when Evert Gorter and Françoise Grendel extracted cell membranes from erythrocytes and determined that they were spherical thin films. Gorter and Grendel measured the surface area of the extracted material and discovered a value that was half of what they expected if the material assembled as a monolayer. They reported that cell membranes were likely bilayers, formed by two layers of oil-like molecules (10). The scientific community questioned this conclusion because the lipid extraction method and surface pressure dependencies changed the outcome of their experiment. It was not until scientists could *see* the bilayer that they began to believe it was the structural element of the cell membrane. In 1959, J. David Robertson was imaging myelin sheaths stained with potassium permanganate in an electron microscope when he discovered that every cell was surrounded by a tripartite structure: two dark lines separated by a lighter center. Robertson concluded that the dark lines were dense protein layers sandwiching a 'lipoid' core (11). In the early 1970s, researchers measured the ultrastructure of cell membranes using x-ray diffraction and confirmed Robertson's observations of a bilayer (12, 13).

Finally, in 1972 Singer and Nicolson published their 'fluid mosaic' model of the cell membrane. They postulated that the cell membrane is a "two-dimensional solution of globular proteins and lipids" (14). This model still features prominently in modern biology textbooks, but

it does not present a complete picture of the structure and organization of cell membranes. To understand why the Singer-Nicolson fluid mosaic model is an over-simplification, the next two sections will provide a general structure of lipids, the lipid bilayer, and the complex phenomena that a lipid bilayer can undergo.

1.2 General Structure and Properties of Lipids and a Lipid Bilayer

Lipids are surfactant molecules with a hydrophilic 'head' group and hydrophobic acyl 'tail'. In mammalian cells, phospholipids are the predominate lipid type (15, 16). Phospholipids consist of a phosphate group and a variable head group, linked to (typically) two fatty acid chains through a glycerol backbone. The phosphate group has a fixed negative charge at physiological pH, and the chemical structure of the head group alters the physical properties of the lipid. For example, some head groups have a neutral charge (*e.g.* phosphatidylserine; PS) which gives the lipid a net negative charge, and some head groups have a positive charge (*e.g.* phosphatidylcholine; PC, and phosphatidylethanolamine; PE) which balances the negative phosphate group, forming a zwitterionic lipid.

The hydrocarbon chains that comprise the lipid 'tail' group vary in length and degree of unsaturation (number of double bonds). Lipids are classified by their melting temperature (T_m), also known as the "main chain transition temperature". This temperature predominantly depends on the length and unsaturation of the acyl chains. For example, long-chain saturated lipids have higher T_m (*e.g.* butter) than short-chain unsaturated lipids (*e.g.* olive oil).

In the presence of water, lipids self-assemble into a variety of structures to protect the hydrophobic tails from water, and the structures they make depends on the molecular structure of the lipid constituents (Fig. 1.1). The area ratio of lipid head-to-tail determines the shape of the space occupied by the lipid. Lipids with small head groups (*e.g.* PE) take on a conical shape that is exaggerated if the lipid also has long, unsaturated acyl chains. These lipids tend to self-assemble into structures with a high degree of curvature, such as reverse micelles and inverted hexagonal phases (17). Lipids with a relatively equal head-to-tail ratio, such as PC lipids, take on a cylindrical shape and tend to form lamellar bilayers. In a mixture of lipid types, a bilayer may form under the appropriate thermodynamic conditions, but it may be less stable than a bilayer composed entirely of cylindrical lipids (18).

This thesis will treat all phases of lipid bilayers above T_m as belonging to a liquid-crystalline phase (L_α), and all phases below T_m as belonging to a solid-ordered, or gel, (S_o) phase (19). Lipid tails in the L_α phase are randomly oriented and fluid, while the S_o phase is characterized by lipid tails that are fully extended and closely packed. A lipid bilayer will transition from the S_o phase to the L_α phase when an intensive thermodynamic property is varied. For example, as the temperature of the system exceeds the characteristic T_m for the lipid species, it will transition from S_o to L_α.

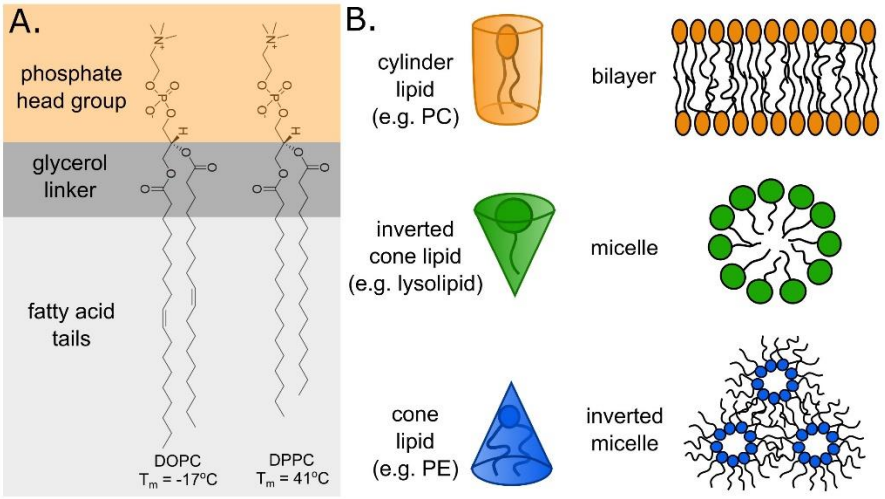

Figure 1.1. Lipids and self-assembled lipid structures. **A.** Glycerophospholipids have a basic anatomy: a phosphate headgroup, glycerol linker, and two acyl chains. Lipids can be categorized by their melting temperature (T_m). The degree of unsaturation and acyl chain length both contribute to this temperature. **B.** The structure of the lipids determines the spontaneous curvature of a self-assembled sheet of lipids. The shape of a lipid is characterized by the area of the headgroup relative to the area taken up by the acyl chains. PC lipids typically have an equal headgroup-to-tail ratio and are cylindrical in shape, forming bilayers when self-assembled in water. Lysolipids (*i.e.* lipids with one acyl chain) make inverted cones and form micelles. PE lipids, with their small headgroups, have a cone shape and form inverted micelles.

Sterols have a major effect on membrane lipids (20). Cholesterol, the most abundant lipid in mammalian plasma membranes (replaced by ergosterol in the membrane of yeast), is an amphiphilic molecule with a rigid, planar ring structure and a small hydroxyl 'head' group (21, 22). Below the phospholipid T_m the rigid planar ring of cholesterol disrupts the ordered packing of the acyl chains, and above the phospholipid T_m cholesterol further condenses the acyl chains (23).

The number of possible phases for a bilayer is found with the Gibbs phase rule, which state $F = C - P + 2$ where F is the number of intrinsic thermodynamic variables that can vary freely, C is the number of components, and P is the number of phases (24). In a two-component (binary)

system with a fixed composition, where both temperature and pressure can vary (F=2), the maximum number of phases that can coexist is 2. Researchers have demonstrated the coexistence of the L_α phase with the S_o phase in binary systems of a high-T_m lipid with cholesterol, a low-T_m lipid with cholesterol, and a high- and low-T_m lipid (20, 25).

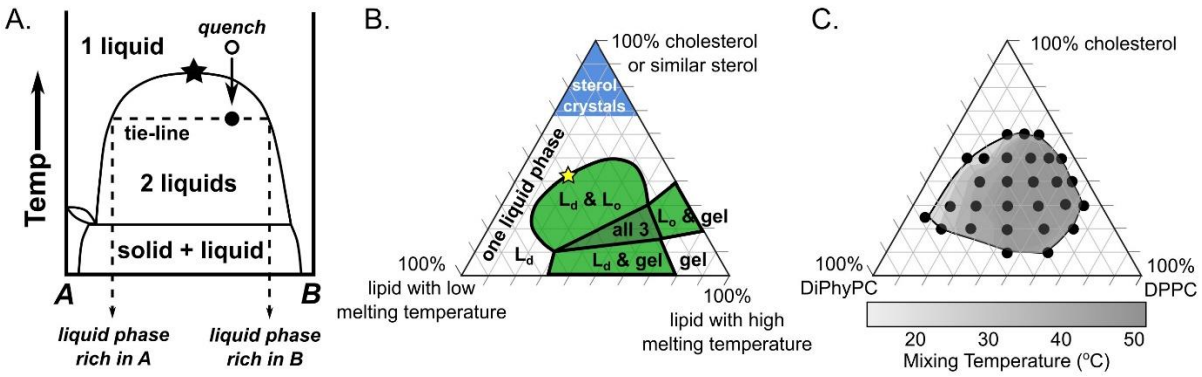

Figure 1.2. Phase diagrams of two-component and three-component lipid systems. **A.** Binary phase diagram of lipid "A" and lipid "B". When the temperature is dropped for a membrane with a composition represented by the open circle, it crosses the miscibility phase boundary and separates into two liquid phases, one rich in "A" and one rich in "B". The ratio of lipids in each of these phases is determined by the tie-line and can be computed using the Lever rule. The star represents the critical point. Adaptation of Fig. 3 from (25) **B.** Representative ternary phase diagram of a lipid with a low melting temperature, a lipid with a high melting temperature, and a sterol. Each vertex represents 100% of one of the components. At high ratios of sterol, the sterol is no longer soluble in a membrane and crystallizes. The green bounded areas represent ratios of the three components where phase coexistence is observed. The yellow star represents the empirically measured isothermal critical point for the system. Adaptation of Fig. 18.4 from (26) **C.** The experimentally measured phase diagram of DiPhyPC/DPPC/cholesterol, adapted from (27). The grayscale colorbar represents the measured miscibility transition temperatures (T_{mix}) of ratios (black circles) that fall in the L_d/L_o coexistence region.

1.3 Liquid Immiscibility in Ternary Membrane Mixtures

The discussion above brings us to the system at the center of this work: ternary membranes with a high-T_m lipid, a low-T_m lipid, and cholesterol. Ternary mixtures of these lipids can phase separate into two coexisting liquid phases (L_o and L_d) over a wide range of temperatures and compositions (25, 28). These simple systems have garnered significant interest in biology and biophysics as a model of a system that is thought to exhibit biological 'lipid rafts'(29). One possible definition of a lipid raft is as a liquid domain in a cell membrane (25). Many researchers

consider rafts to be important signaling platforms, enriched in particular lipids and membrane proteins (30). When micron-scale liquid domains were first observed in synthetic lipid membranes in 2001 (31), there was an explosion in experiments and controversial theories drawing a connection between these model membranes and lipid rafts. One major concern cropped up again and again: most evidence suggests that cellular lipid rafts are submicron in size, while ternary model membranes exhibit micron-scale domains.

Micron-scale domains have been observed at temperatures in ternary membranes close to freezing (~0°C) and up to the melting temperature of the highest T_m lipid in the membrane (27, 32–34). To understand the phase behavior of a ternary lipid system, it is helpful to have a phase diagram, or a map of the possible phase states observed at thermodynamic equilibrium. As the number of components in the system increases, so too does the complexity of the phase diagram. To begin, we will consider a phase diagram of a two-component lipid system, represented in Fig. 1.2A. On the x-axis the mol % of component A is varied from 100% to 0%, and on the y-axis an intensive thermodynamic variable (in this case, temperature), is varied. The curve represents the miscibility coexistence boundary, below which the system is phase separated into two coexisting phases and above which the system is mixed. Take for example a membrane of 30% lipid A and 70% lipid B at a temperature represented by the open circle in Fig. 1.2A. If the temperature is quenched below the phase boundary to the closed circle, the membrane will phase separate into two coexisting phases with proportions of each phase represented by ends of the tie-line. A tie-line follows the 'lever rule', which states that the distance from the quench point to the end of the tie-line rich in component A (or B) is inversely related to the amount of phase rich in A (or B) (26).

In a ternary membrane system, we can no longer represent the phase space of the system in two-dimensions. Instead, we use a Gibbs phase triangle, a two-dimensional graphic that represents all possible combinations of three lipid components (Fig. 1.2B). For example, a composition that is 100% cholesterol is represented by the top vertex. A binary system is represented by the points that fall along the edges of the triangle. Because this diagram is an equilateral triangle, the sum of all perpendicular lines to the axes from any point in the triangle is equal to a constant. Therefore, these perpendicular distances can be taken to be equal to the concentration of the components, whose sum is also a constant. Researchers have mapped the phase states for many possible ratios of a large variety of different ternary systems (28).

A system commonly used in this work is diphytanoylphosphatidylcholine (DiPhyPC; 16 4ME PC, T_m = <120°C), dipalmityolphosphatidylcholine (DPPC; 16:0 PC, T_m = 41°C), and cholesterol. Membranes composed of DiPhyPC, DPPC, and cholesterol are particularly convenient to study: due to the chemical structure of DiPhyPC (16-carbon chains with 4 sets of methyl groups that protrude perpendicular to the chain), its melting temperature is unusually low. This means that there is a large compositional space in which ternary membranes containing DiPhyPC can exhibit coexisting liquid phases. DiPhyPC is fully saturated and is less susceptible to photooxidation than its unsaturated counterparts (35, 36). The experimentally-mapped region of coexisting liquid phases for this system, adapted from (27), is shown in Fig. 1.2C. Here, the grayscale gradient corresponds to the measured miscibility transition temperature for each ratio of lipids (T_{mix}).

1.4 Experimental Techniques to Probe Phase Behavior in Ternary Membrane Mixtures

Researchers identify lipid phases and map phase diagrams for ternary membrane mixtures using a variety of experimental techniques. In this work, direct techniques for identifying coexisting domains are defined as methods that directly image phase separation. These include fluorescence microscopy, cryo electron microscopy (cryoEM) and tomography, and atomic force microscopy (AFM). Examples of indirect measurements are those that probe the molecular scale structure of phase-separated membranes, such as small-angle x-ray scattering (SAXS), small-angle neutron scattering (SANS), Förster resonance energy transfer microscopy (FRET), and nuclear magnetic resonance spectroscopy (NMR). Some researchers maintain a stricter definition of 'direct' and define a direct technique as one that measures the presence of lipid domains *without* a probe. In this case, fluorescence microscopy is considered indirect because it requires a fluorescent probe, which is typically a fluorophore conjugated to a lipid through the head group.

When a taut ternary lipid vesicle, poised at a composition that phase separates, is brought below its miscibility transition temperature, small domains nucleate, laterally diffuse, and collide. Over time, all of the domains will coalesce, and the equilibrated system will have one large domain of each phase. The phase enriched in high-T_m lipids is the L_o phase, and the phase enriched in low-T_m lipids is the liquid-disordered phase (L_d). Cholesterol partitions to both phases but is slightly enriched in the L_o phase.

Domain nucleation and growth is easily observed with a fluorescence microscope, but what happens if domains are nanoscale? If domains nucleate in a membrane, but stay small, they would be undetectable by an optical microscope. This conundrum was first introduced through indirect evidence for coexisting liquid phases in a binary system of DMPC and cholesterol. Using electron paramagnetic resonance (EPR) spectroscopy and spin-labeled lipids, researchers postulated the existence of two immiscible liquid phases at temperatures above DMPC T_m and >20% cholesterol (37). However, when these same compositions are viewed as vesicles under a fluorescence microscope, there is no evidence of micron-scale coexisting liquid phases (25).

Lipid rafts are hypothesized to be on the order of about 100 nm and some researchers have presented indirect evidence for the existence of *submicron* coexisting liquid phases in ternary (and quaternary) systems. Using FRET microscopy, researchers postulated that ternary systems that exhibit no discernable micron-scale phase separation (*e.g.* POPC/DPPC/cholesterol) have domains that are smaller than the optical resolution limit, but larger than the Förster radius of the FRET probe pair (approx. 8-10 nm) (38). In support of these results, researchers published small angle neutron scattering (SANS) data consistent with an interpretation that the existence of lipid domains in POPC/DPPC/cholesterol vesicles were 100nm (39). The idea that lipid rafts can arise from membrane phase separation is a compelling idea, however; the FRET results and SANS results are indirect and rely heavily on models to fit the data. In homage to the proverb "seeing is believing", all techniques in the work presented here are direct imaging methods.

1.5 Model Membrane Systems

Researchers have access to a rich complement of experimental and theoretical model systems to investigate liquid immiscibility in lipid membranes. The discussion below is focused on experimental model systems, and in particular, free-floating enclosed membrane vesicles. Free-floating enclosed lipid membranes have an aqueous interior separated from an aqueous exterior by a bilayer membrane. These systems have little-to-no contact with a surface and they are typically unilamellar, although true unilamellarity can be experimentally challenging to achieve (40). The free-floating vesicles outlined in this next section range from purely physicochemical (*e.g.* giant unilamellar vesicles) to completely biological (*e.g.* yeast vacuoles).

1.5.1 Giant Unilamellar Vesicles (GUVs)

Even before the Singer-Nicolson 'fluid mosaic' model of the lipid bilayer, researchers were using synthetic giant unilamellar vesicles (GUVs) to investigate biological membranes. In the early 1960s, researchers compared the physical properties and transverse dimensions of these synthetic GUVs to biological membranes and found that they were very similar (41). GUVs have remained the workhorse experimental model system of cell membranes and they are instrumental to the study of liquid immiscibility in lipid membranes.

GUVs can vary in composition and range in size from tens of microns to hundreds of microns. Vesicles smaller than GUVs are called large unilamellar vesicles (LUVs; ~100-1000nm) and small unilamellar vesicles (SUVs; ~10-100nm). Due to their size, GUVs are used in assays that require optical microscopy, while LUVs (and in some cases, SUVs) are used for direct imaging by cryoEM and for indirect spectroscopic methods like fluorescence spectroscopy (*e.g.* Laurdan generalized polarization measurements, FRET-pair fusion assays, leakage assays, etc.).

In this work, GUVs are used primarily to observe and measure miscibility transitions of ternary membrane mixtures. In Figure 1.3B(right) the GUV is at an elevated temperature at which all lipids in the membrane are liquid and uniformly mixed. At high temperatures, entropy drives the behavior of the system. As temperatures drop, lipid-lipid interactions start to dominate over entropy, and at temperatures below T_{mix}, the membrane demixes into coexisting liquid domains: the dark L_o domain and the bright L_d domain (Fig. 1.3A and 1.3B(left)). As illustrated in the membrane cross section, membrane phase separation is visualized by differential partitioning of a dye-labeled lipid. Lipid probes typically partition to the L_d phase, regardless of the lipid species attached to the dye (42–44). However, some dyes that label the L_d phase in GUVs will also label the L_o phase in giant plasma membrane vesicles (GPMVs) (45).

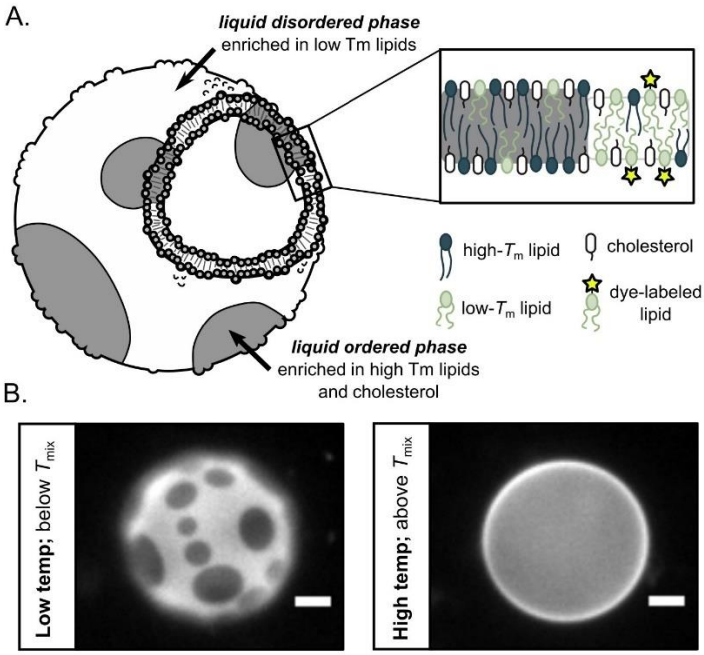

Figure 1.3. Giant Unilamellar Vesicles (GUVs). **A.** Schematic of a GUV in an aqueous solution below its T_{mix}. The gray spots are the "liquid ordered" (L_o) phase, and they are enriched in high T_m lipids and cholesterol. The bright area is the "liquid disordered" (L_d) phase, and it is enriched in low T_m lipids. The cutout shows the lipids that populate the two phases. A dye-labeled lipid selectively partitions to the L_d phase, which makes it the "bright" phase. Illustration adapted from Sarah L. Keller. **B.** Fluorescence micrographs of a 35/35/30 DOPC/DPPC/cholesterol membrane below its T_{mix} (left) and above its T_{mix} (right) (46). The membrane is labeled with 0.8 mol % TexasRed®-DHPE lipid. The scale bar is 20 μm.

Importantly, while each phase is enriched in particular lipid types, every lipid is in each phase. If a phase diagram has been mapped for the specific lipid composition in question, the endpoints of tie-lines can be used to identify the ratio of lipids in each phase and to calculate the partitioning of each lipid species into the phases. Phase-separated membranes along a tie-line have the same composition of the two coexisting liquid phases, regardless of the overall ratio of lipids in the entire membrane. This is significant for two reasons: 1) The bulk properties of the two phases (bending rigidity, line tension, thickness, etc.) do not change along the tie line and, 2) the mole fraction of the two phases changes monotonically along a tie-line, from 100% of the vesicle area in the L_d phase at one end to 100% of the vesicle area in the L_o phase at the other, and 50% of the area occupied by both phases at the midpoint (26).

GUVs can be produced by a variety of methods, including electroformation, which is discussed in Appendix A.1 (47). Each method has its advantages and disadvantages, but they all produce GUVs with compositional variation from vesicle to vesicle. Because of this, the T_{mix} values and

area fractions measured for each individual vesicle are centered around an average value for the population of vesicles. Researchers can measure T_{mix} for a lipid composition using fluorescence microscopy and varying the temperature of the sample. The percentage of vesicles that are phase-separated varies sigmoidally with temperature, and researchers define T_{mix} as the temperature at which 50% of vesicles are phase separated (for an example, see Fig. 2.1B) (26, 48). Uncertainty is quoted as 95% confidence intervals from bootstrap resampling of the sigmoid fit. The width of the sigmoid is an indication of the uniformity of lipid composition of the vesicles: the more compositional variation from vesicle to vesicle, the wider the sigmoid.

1.5.2 Giant Plasma Membrane Vesicles (GPMVs)

Synthetic membranes (*e.g.* GUVs) fail to recapitulate many of the core features of biological membranes. Neither the lipid composition nor the protein content of synthetic membranes comes close to matching the compositional diversity and complexity of biological membranes. In the early 1960s, researchers discovered that cultured cells can shed large vesicles from their plasma membrane upon treatment with chemical crosslinkers, like paraformaldehyde (49, 50). This process is an exaggeration of the natural cellular process of apoptosis, or cell death. In 2007, seminal observations of micron-scale phase separation in these cellular "blebs", or giant plasma membrane vesicles (GPMVs), reinvigorated the lipid raft hypothesis (51): could GPMVs be the missing link between phase separation in model membranes and lipid rafts in cells?

It has become abundantly clear, including through advances in cellular lipidomics, that the lipid composition of cell membranes is complex. Much of this complexity in mammalian lipidomes arises from combinatorial lipid synthesis. Tens of thousands of distinct lipid species can be created from several possible hydrophilic headgroups, backbones, and hydrophobic chains. In most mammalian cells, hundreds of these species are produced with less than 100 species making up greater than 90% of the cellular lipidome (22).

Membrane-associated proteins add more complexity, as 50%-75% w/w of a typical mammalian cellular membrane preparation is protein content (52). In fact, polypeptides are estimated to occupy ~20% of the area at the center of a membrane bilayer, and this has huge implications for membrane physical properties, such as fluidity, bending rigidity, and phase separation (52, 53).

Interestingly, different membranes within a *single* cell display a huge diversity in lipid composition. For example, the cholesterol content of the plasma membrane can be ~45 mol%, whereas the endoplasmic reticulum membrane has ~5 mol% cholesterol (22, 54). Cholesterol is not the only lipid to vary between organelles: glycosphingolipids are largely produced in the Golgi and therefore, are not present in the endoplasmic reticulum (16). Cardiolipin is a lipid found only in the inner membrane of mitochondria (16). Needless to say, this diversity likely has a significant impact on cellular function.

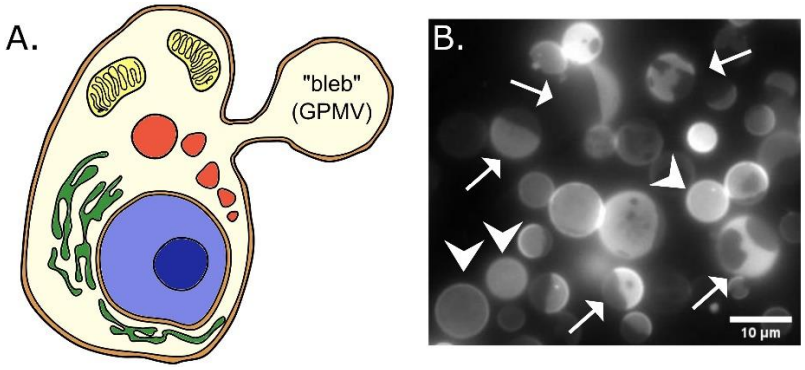

Figure 1.4. Giant Plasma Membrane Vesicles (GPMVs). **A.** Schematic of a blebbing cell that is producing a GPMV. This can occur after chemical vesiculation agents are added to a solution of adherent mammalian cells. The GPMV contains most of the native lipids and proteins of the plasma membrane but is missing all of the intracellular components of the native cell. **B.** A micrograph of a field of GPMVs derived from Madine Darby Canine Kidney (MDCK) cells. The arrows point to GPMVs that have phase separated and the arrowheads point to mixed GPMVs. The temperature of the system is 8°C. Image taken by Ilya Levental and Sarah L. Keller.

The discovery of micron-scale liquid-liquid phase separation in GPMVs has arguably bridged the gap between lipid rafts in cells and coexisting liquid phases in synthetic mimics. However, coexisting liquid phases have not been observed in GPMVs at physiological temperature (37°C). If membranes derived from cells exhibit micron-scale liquid domains when detached from the cellular environment, could the cytoskeleton and extracellular matrix (ECM) of the cell keep lipid rafts small? This question was first raised in conjunction with another conundrum: the diffusion rate of lipids in the plasma membrane is 5- to 100-fold reduced over their counterparts in synthetic membranes (55). Several possible solutions were proposed, including selective partitioning of particular lipid species into lipid rafts, coupling with the extracellular matrix, and membrane corrals formed by cytoskeletal pinning sites (56–60).

One of the most interesting of these theories involves coupling of plasma membrane phase behavior with cytoskeleton structural support. The theory, proposed by Machta et al., takes advantage of the phase behavior observed in GPMVs (61). When GPMVs are isolated from living cells, they appear homogeneous at physiological temperature (37°C). However, below a critical temperature of ~22°C, the membrane breaks out into coexisting micron-scale domains (62). Near this transition, GPMVs undergo fluctuations that are visible on the micron-scale, which are quantitatively similar with fluctuations in synthetic membranes that have been tuned to a critical point (62, 63). The correlation length for membrane fluctuations near a critical point diverges at the critical temperature (T_c). Specifically, above T_c, one ensemble average correlation length can describe the length scale of composition fluctuations, and as the temperature is decreased towards T_c, this length increases. At T_c, the correlation length diverges. Below T_c, the system phase separates into two coexisting liquid phases with a finite correlation length. One interesting prediction falls out of this description for plasma membrane phase behavior: at 37°C, the correlation length of the plasma membrane is estimated to be ~20 nm, which is in close agreement to the measured size of lipid rafts (30, 61). This temperature limitation on domain size, coupled with cytoskeleton corrals from membrane pinning sites, leads to a more complete picture of lipid rafts in the plasma membrane (61).

How do GPMVs compare to GUVs? GPMVs are typically smaller than GUVs (<10 μm), and they contain the full complement of plasma membrane lipids and membrane-associated proteins (64). The coexisting liquid phases in GPMVs are also termed L_o and L_d, but they differ significantly from GUVs in their physical properties such as membrane packing order and miscibility transition temperatures. For example, the difference in generalized polarization (GP) values (a proxy for lipid packing order), gathered from Laurdan polarization microscopy, between the L_d and L_o phase in GPMVs is much smaller than in GUVs (65). GPMVs and GUVs have significant compositional differences, especially in the makeup of the two liquid phases. For example, in GPMVs, the L_o phase is composed mostly of singly-unsaturated lipids and sterol, with very little saturated lipids, while the GUV L_o phase is typically rich in sterol and a fully saturated lipid (66).

GPMVs are a tractable system to investigate the biophysical properties of cell membranes, including phase partitioning of transmembrane proteins, diffusivity, and membrane packing order (65–68). Researchers must contend with several caveats such as the loss of some membrane asymmetry in GPMVs due to the increased activity of lipid scramblases during the vesiculation

process (51, 64). The type of chemical vesiculate also has a dramatic effect on the physical properties of GPMVs. For example, T_{mix} significantly decreases in GPMVs derived through NEM treatment compared with vesicles collected after treatment with DTT+PFA (45). Despite these significant caveats, GPMVs remain an excellent intermediate model system between fully synthetic membranes and the cell plasma membrane.

1.5.3 Yeast Vacuoles

In the last decade, a new model system for membrane phase separation has come to the fore: the yeast vacuole membrane. Vacuoles are lysosomal organelles in budding yeast such as *Saccharomyces cerevisiae* (*S. cerevisiae*). Evidence of membrane heterogeneities in yeast vacuoles has been recorded since the early 1960s. Using freeze fraction electron microscopy, researchers found that the membrane of intact and unfixed yeast vacuoles exhibits domains depleted of large proteins (69). These domains are physiologically regulated: proteins are homogeneously distributed on vacuole membranes during the logarithmic stage of yeast growth, and large, protein-depleted domains appear during the stationary phase of growth (69). In many cases, these domains are about 200 nm, or larger, in diameter which makes them resolvable with optical microscopy.

Yeast vacuoles are a fungal equivalent to mammalian lysosomes, and they also regulate intracellular pH and osmotic pressure. When yeast become deprived of nutrients, the vacuole assists in degrading lipid droplets (an energy rich organelle replete with triacyl glycerides and sterol esters) and proteins in a process called autophagy. During active growth in the logarithmic stage, yeast cells contain many small multi-lobed vacuoles. Late in the growth cycle when cells are glucose-starved, vacuoles fuse into one large spherical vacuole (1-5 μm in diameter) that occupies a large portion of the cell volume (Fig. 1.5C) (70).

Shape is not the only change that vacuoles endure during the yeast growth cycle: the stat-phase vacuole membrane demixes into domains depleted in many integral membrane proteins and lipid species (Fig. 1.5 B and Fig. 1.5C)(69–73). A striking example of this heterogeneous membrane organization is seen in the partitioning of the vacuole-specific proton pump, Vph1. Vacuoles in the stationary phase, imaged with endogenously labeled Vph1-GFP and a lipid-sensitive dye FM4-64, clearly show that Vph1 selectively partitions to the putative L_d phase on a vacuole membrane

(70, 74). Many other vacuolar proteins have shown similar domain preferences, including many proteins involved in the TORC signaling pathway essential in yeast metabolism (75, 76).

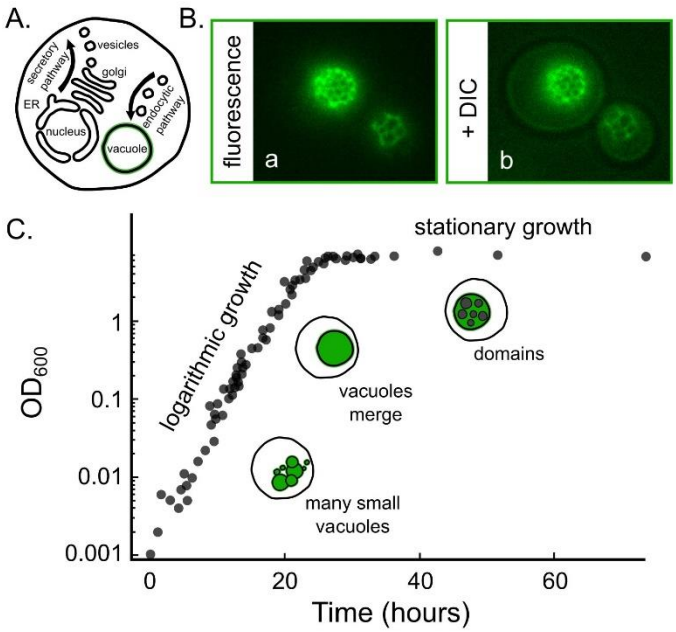

Figure 1.5. Yeast vacuoles. **A.** Schematic of a yeast cell. The vacuole is highlighted in green. **B.** Fluorescence micrographs of phase-separated yeast vacuoles. The vacuoles are labeled with endogenously labeled Vph1-GFP imaged via fluorescence microscopy (left; a) and fluorescence and differential interference contrast (DIC) microscopy (right; b) to show the outline of the cell that contains the vacuole. **C.** Growth curve for *S. cerevisiae* adapted from (74). Data points are measurements of the yeast culture optical density at 600 nm taken from 0 hr to 80 hrs. In the early logarithmic stage of growth, yeast cells have many small vacuoles. In the late logarithmic stage, the vacuoles fuse into one large vacuole that spans a large volume of the cell. In the stationary stage of growth, vacuole membranes break out into domains. A and B are adapted from (74).

Vacuolar domains exhibit a striking zoo of shapes and sizes: from hexagonally packed circles and stripes, to fully separated ‘half-moons’. As such, vacuole membranes display the whole gamut of domain morphologies observed in GUVs (70, 74). Other researchers have postulated that these domain morphologies may be associated with compositional changes during different stages in the growth cycle (70, 71); however, it is likely that the observed shifts in morphology are a result of changes in osmotic pressure that increase the membrane tension, allowing domains to coalesce. In fact, the geometric patterns on some vacuoles closely resemble a modulated phase, hinting at the role membrane curvature may play in domain morphology and homeostasis (see Chapter 3 Section 3.1 for a detailed discussion of modulated phases).

Domains readily appear on vacuoles in the glucose-starved stationary phase of growth, but other cellular stresses can also induce domains. For instance, researchers have shown that acidifying the media in which yeast are grown can cause vacuole membranes to break out in domains (70). Similarly, nitrogen-starvation, osmotic stress, and translation inhibition can all lead to domain formation (70). Domains are also dependent on several signaling pathways that control lipid and sterol transport and synthesis, including the TORC signaling pathway and lipid droplet microautophagy (70, 71, 76, 77).

The observation that vacuoles phase separate has been exciting for biologists and biophysicists alike. Phase separation in yeast vacuoles appears to be an ATP-independent process that effectively organizes cell membrane components, allowing valuable cellular energy currency to be used elsewhere in the cell. The observation of phase separation in such a complex biological environment highlights the broad applicability of elegant thermodynamic principles.

1.5.4 Fatty Acid Vesicles and 'Protocells'

Fatty acid vesicles are lipid bilayers composed of fatty acids and their ionized species (*e.g.* decanoic acid and decanoate soap) (78). Fatty acids are chemically and structurally distinct from glycerophospholipid vesicles in that they have only one aliphatic chain, with no glycerol backbone and no large headgroup. In this thesis, fatty acid vesicles are primarily used to investigate protocells and the origins of cellular life. This membrane system differs from phospholipid membranes: fatty acid membranes are dynamic while phospholipid membranes are quite stable. For example, the concentration of free monomers in equilibrium with self-assembled vesicles is considerably higher for single-chain fatty acids than for double-chain glycerophospholipids, and as a result, the interchange of molecules between the two leaflets is expected to occur much more rapidly than in phospholipid bilayers (78).

Fatty acid vesicles are so dynamic, in part, because they are composed of single- rather than double-tailed lipids, and because the pH-range and concentration range in which they exist is limited (Fig.1.6 D). Fatty acids self-assemble into vesicles in a very narrow range of pH values and fatty acid concentrations (79–83). Below the critical vesicle concentration (CVC) or at low pH, fatty acids exist as an oil; at high pH, fatty acids form micelles (78). This is because, in order for fatty acids to form a bilayer, there must be a roughly equal ratio of neutral non-ionized

molecules and their negatively charged soap counterparts (78). The chain length of the fatty acid determines the concentration and pH range suitable for vesicles, with long-chain fatty acids forming vesicles at higher pH values and lower CVCs (Fig. 1.6)(78).

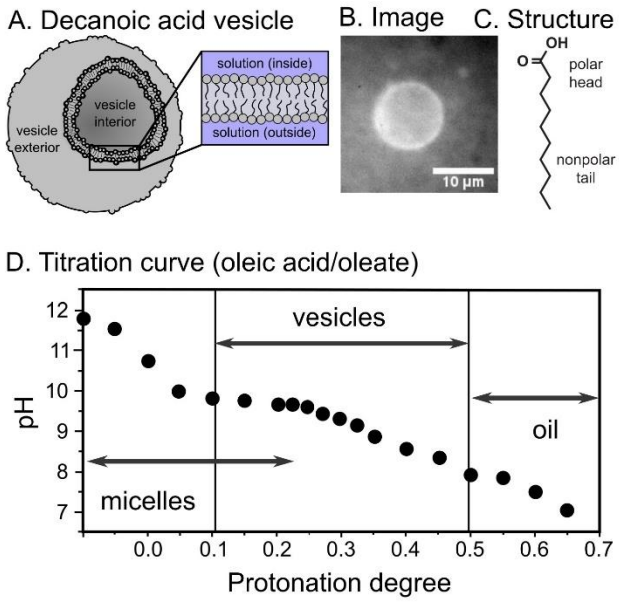

Figure 1.6. Fatty acid vesicles. **A.** Schematic of a fatty acid (*e.g.* decanoic acid) vesicle in an aqueous solution. **B.** Fluorescence micrograph of a decanoic acid vesicle labeled with Rhodamine 6G and floating in a D_2O solution. **C.** Chemical structure of decanoic acid. **D.** Titration curve for a system of oleic acid/oleate. As the degree of protonation changes, the predominant self-assembled structure shifts from micelles, to vesicles, and finally to oil. A, B, and C are adapted from (84) and D is adapted from (78).

It is this chemical simplicity that has stimulated great interest in fatty acid vesicles as potential protocellular membranes. Protocells are the simplest conception of a modern cell that could have existed before biology. The essential components of a protocell are: 1) compartments and separation of the inner components from the exterior environment, 2) heredity, and 3) entities that drive catalysis (85). Fatty acid vesicles fulfill the compartmentalization requirement, *and* their dynamism has proven useful for other biological requirements like self-reproduction and persistent motion. Researchers have shown that oleic acid (18 carbons) undergoes autocatalytic formation of vesicles, and generates a pH gradient across, and within, the vesicle that leads to persistent motion (86, 87). Even more exciting is that fatty acids have been isolated from meteors and are easily synthesized from prebiotic compounds (88, 89).

Some observations bring into question the feasibility of the formation of fatty acid vesicles on the early Earth. For example, fatty acid vesicles clump in the presence of high concentrations of NaCl (such as is present in the Earth's oceans), and they completely collapse when in solution with divalent cations, like Mg^{2+} (a cation essential for RNA catalysis) (82, 83, 90, 91). These facts alone bring into question the feasibility of the formation of fatty acid vesicles on the early Earth. However, as I will describe in Chapter 6, many of the molecular constituents of biological polymers (*e.g.* amino acids, RNA bases, and sugars) can protect decanoic acid membranes from salt-induced destabilization (92, 93).

1.6 Overview of Dissertation

This dissertation follows two themes: 1) membrane physical properties and phase separation in synthetic, cell-derived, and living cell membranes, and 2) the role of amphiphiles in the origins of life. The discussion will begin with simple membrane systems and evolve in complexity over the course of the manuscript, describing the effect of alcohols on phase behavior in GUVs and cell-derived membranes, investigating a modulated phase in GUVs and cell-derived membranes, probing phase separation on the nanometer length-scale with GUVs using cryo electron microscopy, and finally, investigating the relationship between growth temperature and mixing temperature in yeast vacuoles. The text will finish with a discussion on the role of decanoic acid membranes in the origins of life. Detailed methods and code to compute figures presented in the manuscript can be found in the Appendix.

1.7 List of Publications

I have produced the following publications:

1. Cornell, C.E., Mileant, A., Thakkar, N., Lee, K.K., and Keller, S.L. Direct Imaging of Lipid Domains in Nanoscale Vesicles by CryoEM. PNAS (2020) *117* (33), 19713-19719.

2. Xue, M., Black, R.A., **Cornell, C.E.,** Drobny, G.P., and Keller, S.L. A step toward molecular evolution of RNA: Ribose Binds to Prebiotic Fatty Acid Membranes, and Nucleosides Bind Better than Individual Bases Do. ChemBioChem (2020) *21*, 1-5.

3. Cornell, C.E., Black, R.A., Xue, M., Litz, H.E., Ramsay, A., Gordon, M., Mileant, A., Cohen, Z.R., Williams, J.A., Lee, K.K., Drobny, G.P., Keller, S.L., Prebiotic Amino Acids Bind to and Stabilize Prebiotic Fatty Acid Membranes. PNAS (2019) *116* (35), 17239-17244.

4. Blosser, M.C., **Cornell, C.E.**, Rayermann, S.P., and Keller, S.L. Phase Diagrams and Tie Lines in GUVs. In *The Giant Vesicle Book;* Dimova, R. and Marques, C. Taylor & Francis (2019).

5. Cornell, C.E., Skinkle, A.D., He, S., Levental, I., Levental, K.R., and Keller, S.L. Tuning Length-scales of Small Domains in Cell-derived Membranes and Synthetic Model Membranes. Biophysical Journal (2018) *115* (4), 690-701.

6. Cornell, C.E., McCarthy, N.L.C., Levental, K.R., Levental, I., Brooks, N.J., and Keller, S.L. *n*-alcohol Length Governs Shift in L_o-L_d Mixing Temperatures in Synthetic and Cell-Derived Membranes. Biophysical Journal (2017) *113*, 1200-1211.

7. Rayermann, S.P., Rayermann, G.E., **Cornell, C.E.,** Merz, A.J., and Keller, S.L. Hallmarks of Reversible Separation of Living, Unperturbed Cell Membranes into Two Liquid Phases. Biophysical Journal (2017) *113*, 2425-2432.

8. Bergeron-Sandoval, L.-P., Hossein, K.H., Chang, C., **Cornell, C.E.,** Keller, S.L, Francois, P., Hendricks, A.G., Ehrlicher, A.J., Pappu, R.V., Michnick, S.W. Endocytosis caused by liquid-liquid phase separation of proteins. BioRxiv (2017). DOI: https://doi.org/10.1101/145664

CHAPTER 2: *n*-alcohol Length Governs Shift in Lo-Ld Mixing Temperatures in Synthetic and Cell-Derived Membranes

*This chapter was first published in the *Biophysical Journal* in 2017. It was written in collaboration with N.L.C McCarthy, K.R. Levental, I. Levental, N.J. Brooks, and S.L. Keller. The full citation can be found at the end of Chapter 1 on pg. 29.

2.1 INTRODUCTION

Scientists have invested decades of research in understanding how *n*-alcohols affect model lipid membranes, largely with the goal of clarifying mechanisms by which ethanol consumption perturbs mammalian cell membranes. The results tell a compelling story: *n*-alcohols partition into membranes near lipid headgroups where they disorder carbon chains of neighboring lipids or probes (94–96). Concomitantly, *n*-alcohols alter physical properties of liquid-phase membranes: lipid lateral mobilities increase (97–99), ion channel cation permeabilities increase (100), membrane areas increase (101), thicknesses decrease (102), bending moduli decrease (101), area compressibilities decrease (101), interfacial tensions decrease (101), gel-liquid transition temperatures decrease (103), $L_\alpha - H_{II}$ transition temperatures shift (104), and lateral pressure profiles shift (99, 105). However, the magnitudes of most of these effects are modest. For example, relatively high concentrations of ethanol (120 mM) decrease membrane gel-liquid melting temperatures by only 0.3˚C (103).

One striking exception to the rule that *n*-alcohols tend to have a minimal effect on physical properties of membranes was recently reported by Veatch and colleagues (48). Using cell-derived giant plasma membrane vesicles (GPMVs), they found that short-chain *n*-alcohols dramatically decreased miscibility transition temperatures (T_{mix}). The shift in T_{mix} (~4 ˚C for 120 mM ethanol) is more than an order of magnitude larger than ethanol's effect on membrane melting temperatures (48, 103). Both studies used 120 mM ethanol because this concentration is reported by Pringle et al. as the anesthetic concentration (AC50) at which 50% of tadpoles lose their righting reflex (106). The ethanol concentration at which proteins begin to denature is at least an order of magnitude higher (107). Strikingly, the result that short-chain *n*-alcohols decrease T_{mix} by ~4˚C holds equally well for ethanol, propanol, octanol, and decanol at the AC50 concentration (48).

Cell-derived GPMVs have several advantages as experimental systems. They are large enough (~10 μm) to image by conventional microscopy, they contain significant amounts of functioning,

native proteins, they retain extraordinary complexity in their lipid and protein compositions (similar to cell plasma membranes), and the spatial distribution of the lipids and proteins in their membranes can by probed by fluorophores (45, 51, 62, 108–110). At high temperatures, GPMV membranes appear uniform by epifluorescence microscopy. Below T_{mix}, GPMV lipids and proteins demix into coexisting liquid-ordered (L_o) and liquid disordered (L_d) phases (45, 51, 62, 110).

The result that *n*-alcohols dramatically shift miscibility transition temperatures in GPMVs leads to the clear question of whether *n*-alcohols also shift T_{mix} in simpler membranes of giant unilamellar vesicles (GUVs) composed of ternary lipid mixtures. We are motivated to ask this question because the phenomenon of membranes demixing into L_o and L_d phases has been largely understood in the context of GUVs composed of ternary mixtures of a lipid with a high melting temperature, a lipid with a low melting temperature, and cholesterol. The relative amounts of each lipid type can be quantitatively tuned in GUVs (111), making them an ideal system for mapping phase diagrams. General features within phase diagrams of ternary membranes are relatively well understood. For example, researchers know how to tune lipid ratios to achieve membranes that are likely to exhibit gel phases, or coexisting L_o and L_d phases, or critical phenomena, and they have used this information to provide a broader context to interpret results from specific cell-derived membranes (62, 112, 113). However, an enduring challenge has been to quantitatively predict the effect of substituting or adding new membrane components (45, 114), including *n*-alcohols.

Here, we find that the addition of short-chain *n*-alcohols to ternary GUVs significantly shifts miscibility transition temperatures, and that the magnitude of the shift is large, as in cell-derived GPMVs. However, to our surprise, we find that the direction of the shift is *opposite* in the two systems. We describe experiments that explore this phenomenon, and we offer a plausible speculation to explain why short-chain *n*-alcohols *decrease* miscibility transition temperatures in GPMVs and *increase* them in GUVs.

2.2 MATERIALS AND METHODS

Materials

Phosphocholine (PC) lipids including DOPC (dioleoyl-PC, or di-18:1-PC), DPPC (dipalmitoyl-PC, or di-16:0-PC), POPC (palmitoyl-oleoyl-PC, or 16:0-18:1-PC), di16:1-Δ9cis-PC, di18:1-Δ6cis-PC, di14:1-Δ9cis-PC, lyso(18:0)-PC, and palmitoyl sphingomyelin (PSM or 18:1-16:0 SM) were from Avanti Polar Lipids (Alabaster, AL). Texas Red dihexadecanoyl-PE was

from Life Technologies (DHPE; Grand Island, NY), and cholesterol was from Sigma Aldrich (chol; St. Louis, MO). Lipid structures appear in Fig. 2S1. Stock solutions of laurdan (Invitrogen, Carlsbad, CA) and C-laurdan (a gift from Dr. B. R. Cho, Seoul, Korea) were prepared in ethanol and DMSO. Alcohols (ethanol, propanol, butanol, pentanol, hexanol, octanol, decanol, tetradecanol, hexadecanol, propofol, and 2,6-di-*tert*-butylphenol), dimethyl sulfoxide (DMSO), and all additional reagents were from Sigma Aldrich unless specified. All alcohols were purchased at their highest available purity. All materials were used as from the manufacturer without further purification.

Production of GUVs for T_{mix} Measurements

GUVs with diameters on the order of $10^1 – 10^2$ μm were electroformed (115) in either pure (18 MΩ-cm) water or in alcohol solutions (0.0025 – 480 mM alcohol in 18 MΩ-cm water). At ethanol concentrations above 1.2 M, PC-membranes are partially solubilized; above 7 M, mixed micelles form (116). Alcohols with low water solubilities (tetradecanol, hexadecanol, and 2,6-di-*tert*-butylphenol) were first dissolved in DMSO before being dissolved in water. For these alcohols, the maximum final concentration of DMSO in aqueous solution was 210 mM, too small to measurably affect miscibility transition temperatures. Control experiments were conducted to verify that shifts in T_{mix} values due to producing GUVs of 35:35:30 DOPC/DPPC/cholesterol in 18 MΩ-cm water (T_{mix} = 30.4 ± 0.29 ˚C) vs. in DMSO solutions approximately 7-fold more concentrated (1.4M) than those used in *n*-alcohol experiments (T_{mix} = 31.1 ± 0.04 ˚C) were smaller than shifts in T_{mix} due to the type of *n*-alcohol used.

GUVs used in measurements of T_{mix} were electroformed as follows. An aliquot of 0.25 mg of lipids in chloroform was spread evenly on an ITO-coated glass slide (Delta Technologies, Loveland, CO). The lipid mixture contained 0.8 mol% Texas Red DHPE, a dye-labeled lipid that selectively partitions to the L_d phase (117). The slide was placed under vacuum for >30 min to evaporate the chloroform. A capacitor was created by separating two ITO-coated slides with two rectangular Teflon bars (0.3 mm thick). The gap between the bars was filled with water or alcohol solution, and all edges were sealed with vacuum grease. An AC voltage of 10 Hz and 1.5 V was applied to the capacitor for 1 hr at 60 ˚C. Vesicles were then extracted from the capacitor and diluted 5-10-fold in water or alcohol solution at 60 ˚C to make a stock solution.

Measurement of T_{mix}

Electroformation produces populations of vesicles with distributions of miscibility transition temperatures, reflecting slight differences in lipid ratios from vesicle to vesicle. Uncertainties in ratios of PC-lipids in electroformed vesicles have been estimated at <2 mol% (34). Techniques for minimizing uncertainties in T_{mix} (25, 26) were followed.

To image vesicles, several drops of vesicle stock solution were deposited between glass coverslips, and the edges were sealed with vacuum grease. This assembly was thermally coupled to a home-built temperature stage for a Y-FL epifluorescence microscope (Nikon, Melville, NY) via a layer of thermal grease (Omega Engineering, Stamford, CT). An Alpha-Omega (Lincoln, RI) controller adjusted temperature via a thermoelectric heater/cooler using feedback from a thermistor (0.2 ˚C accuracy, Sensor Scientific, Fairfield, NJ). Images were captured through an air objective using a CoolSnapFX camera (Photometrics, Tucson, AZ) and processed using ImageJ (public domain http://rsbweb.nih.giv/ij). The percent of vesicles that exhibited coexisting L_o and L_d phases was recorded over temperature steps between 10 ˚C and 50 ˚C. Typically, ~100 vesicles were imaged at each step, over three fields of view. A nonlinear least squares fit to a sigmoidal curve of % phase separated = 100 x $(1 - (1 / (1 + e^{-(T - T_{mix}) / B})))$ yields T_{mix}, at which 50% of vesicles are phase separated, and B, which relates to the width of the transition (48). The shift in miscibility transition temperature, ΔT_{mix}, is defined as T_{mix} (with alcohol) – T_{mix} (without alcohol). Uncertainties for each measurement correspond to 95% confidence intervals of the fit, as shown in Fig. 2.1. For the data in Fig. 2.1, the dimensionless term $\Delta T_{mix}/T_{mix} = 0.00626 \pm 0.00115$ (for temperatures expressed in Kelvin). Uncertainties for a set of measurements due to day-to-day variation is typically <0.5 ˚C. For example, four experiments on different days using dilute concentrations of (0.05 – 1 mM) butanol yielded ΔT_{mix} of 0.43 ± 0.14 ˚C.

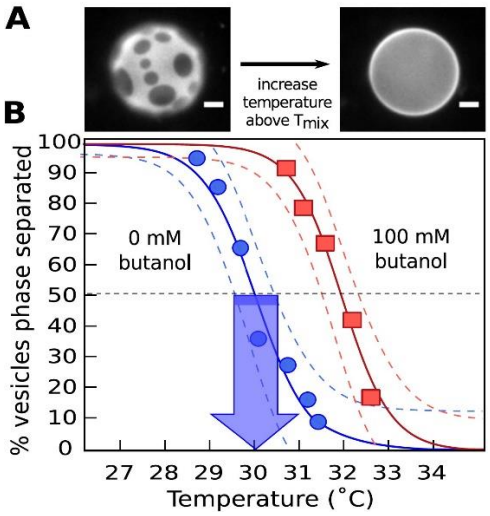

Figure 2.1. A. Left: Below T_{mix}, 35/35/30 DOPC/DPPC/chol vesicles exhibit domains of L_o (dark) and L_d (bright) phases. In taut vesicles, domains merge until only one domain of each phase remains (118). **Right:** Above T_{mix}, all lipids mix uniformly. Scale bar is 20 µm. **B**. T_{mix} is higher for 35/35/30 DOPC/DPPC/chol vesicles in 100 mM butanol (squares, T_{mix} = 32.3 ± 0.19 ˚C) than in pure water (circles, T_{mix} = 30.4 ± 0.29 ˚C). Each point records the percent of vesicles with coexisting L_o and L_d phases at a given temperature. Dashed lines are 95% confidence intervals (48). The arrow points to T_{mix} for the left curve; the width of the arrow's base is the uncertainty.

AC50 Values

To compare results with Gray et al. (48), we used AC50 values from Pringle et al. (106): 120 ± 10 mM for ethanol, 54 ± 6 mM for propanol, 12 ± 1 mM for butanol, 0.7 ± 0.1 mM for hexanol, 0.06 ± 0.9 mM for octanol, and 0.013 ± 0.2 mM for decanol. An exponential regression of these values gives 2.96 mM for pentanol. More recent AC50 values by Alifimoff et al. are similar: 190 ± 16 mM for ethanol, 73 ± 2.4 mM for propanol, 10.8 ± 0.77 mM for butanol, 2.9 ± 0.11 mM for pentanol, 0.57 ± 0.37 mM for hexanol, 0.059 ± 0.0031 mM for octanol, and 0.0126 ± 0.00048 mM for decanol (119). At the AC50, *n*-alcohols are several mol% of membranes (106).

Cell Culture and GPMV Isolation

Rat basophilic leukemia (RBL) cells were maintained at 37˚C in humidified 5% CO_2 in growth medium containing 60% modified Eagle's medium, 30% RPMI medium, 10% fetal calf serum, 2 mM glutamine, 100 units/mL penicillin, and 100 µg/mL streptomycin. GPMVs were isolated and imaged as previously described (66). Briefly, cells were washed in GPMV-buffer (10 mM HEPES, 150 mM NaCl, 2 mM $CaCl_2$, pH 7.4) and incubated for 1 hr at 37˚C in GPMV-buffer supplemented with 25 mM paraformaldehyde and 2 mM dithiothreitol. Differences between results in GUVs and

GPMVs are not due to paraformaldehyde and dithiothreitol; miscibility temperatures of GUVs in 18 MΩ-cm water (T_{mix} = 31.8 ± 0.15 ˚C, for GUVs of 35:35:30 DOPC/DPPC/cholesterol) are indistinguishable from temperatures of GUVs in 25 mM paraformaldehyde and 2 mM dithiothreitol (T_{mix} = 31.9 ± 0.09 ˚C), where uncertainties are determined as in Fig. 2.1 for single experiments. We verified that our conditions sufficiently replicated the conditions of Gray et al. (48): we found that a short chain *n*-alcohol (butanol) decreases T_{mix} in GPMVs, whereas a long-chain *n*-alcohol (butanol) increases T_{mix} (Fig. 2S6).

Laurdan and C-laurdan Microscopy

GUVs used for laurdan microscopy were electroformed by a method described previously (66) that is functionally equivalent to the method used to produce GUVs for measurements of T_{mix}. Specifically, 1 µL of a chloroform/methanol (2:1 v/v) solution containing 5 mg/mL of lipids was spread on two platinum electrodes within a Teflon chamber. The lipid mixture contained 0.5 mol% laurdan. The chamber was placed under vacuum for 1 h to dry the solvent and form a lipid film. Next, 350 µL of an aqueous solution (0.2 M sucrose with or without alcohol) was added to the chamber. GUVs were grown by applying an AC voltage of 10 Hz and 2.5 V across the electrodes for 1 h at 52˚C. GUVs were then collected and diluted in 1 mL of 0.2 M glucose with or without alcohol.

GUVs and GPMVs were imaged at 20˚C and 5˚C, respectively, by confocal microscopy on a Nikon A1R with spectral imaging at 60x and an excitation of 405 nm. The emission was collected in two bands: 433-463 nm and 473-503 nm. MATLAB (The MathWorks, Natick, MA) was used to calculate two-dimensional general polarization (2D GP) maps, where GP for each pixel was calculated from a ratio of the two fluorescence channels as previously described (120). Briefly, each image was background subtracted and thresholded to retain only pixels with intensities 3-5 standard deviations greater than the background in both channels (66). The difference in generalized polarization (ΔGP) between L_o and L_d phases was determined for each vesicle, where GP for each phase was derived from average pixel intensities (I) from large, representative areas via: $GP = [\sum_{420}^{460} I - \sum_{470}^{510} I]/[\sum_{420}^{460} I - \sum_{470}^{510} I]$

Area Fractions

Micrographs of vesicle equatorial sections yielded vesicle diameters, which were ~80 – 250 μM. Videos of the same vesicles were collected such that the top, spherical cap of the vesicle lay within the <5 μm depth of field of the microscope objective; the remainder of the vesicle appeared as a bright ring. Centers of vesicles whose bright ring remained in the field of view were identified by custom MATLAB code available by public license in the "Track_Vesicle" program (118, 121). Drift of free-floating vesicles in the *x*-*y* plane was corrected by stacking video frames on vesicle centers. Areas out of focus were excluded, yielding squares with edges ~15 – 60 μm. Pixel intensities were thresholded so the L_d phase was white and the L_o phase was black. Images within the 2D squares were projected onto 3D spherical surfaces using MATLAB code by Sarah Veatch (122). The area fraction of the L_d phase was the 3D projected area of all white pixels divided by the projected area of all pixels in the image.

High-Pressure Microscopy

GUVs were electroformed as in the production of GUVs for T_{mix} measurements, except that a 0.5 mm PDMS O-ring was used instead of Teflon bars. After electroformation, GUVs were transferred into a custom-built high pressure cell mounted on a Nikon Eclipse TE2000-E inverted microscope equipped with a Zyla sCMOS-based camera (Andor Technology, Belfast, UK) (123). The body of the cell was constructed from high tensile strength stainless steel with openings for 0.5 mm thick, 5 mm^2 diamond optical windows, which can withstand ≤ 2500 bar. 1 bar = 10^5 Pa = 0.987 atm. Hydrostatic pressure was applied via a water-filled pressure generator (4000 bar, SITEC-Sieber Engineering, Maur, Switzerland) and a hydraulic network similar to that described previously (124). Temperature was set at 40 ˚C using a water bath, and images were collected over 3 fields of view. The pressure was increased from ambient pressure to a maximum of 450 bar, in steps of 50 bar. After each step, the sample equilibrated for 30 seconds and images were collected over 3 fields of view.

2.3 RESULTS AND DISCUSSION

N-alcohols Increase T_{mix} in Model Membranes

When ternary GUVs are formed in aqueous solutions of short-chain *n*-alcohols, the temperatures at which the vesicles demix into coexisting L_o and L_d phases *increase* relative to GUVs in water. For example, in Fig. 2.1, T_{mix} increases by 1.9˚C for vesicles of 35/35/30 DOPC/DPPC/chol in 100 mM butanol. This shift is in the opposite direction to that observed in

cell-derived GPMVs (48). The difference between the GUV and GPMV results is not due to proteins denaturing, which occurs at butanol concentrations that are roughly an order of magnitude higher (107).

The increase in T_{mix} that we observe in model GUVs is robust across a range of short-chain *n*-alcohols and is proportional to the concentration of alcohol in solution (Fig. 2.2a). When the concentration of each *n*-alcohol is scaled by its AC50 value (106), the data within the shaded area of Fig. 2.2a collapse (Fig. 2.2b). The same result holds when AC50 values from (119) are used (Fig. 2S2). A similar scaling occurs in cell-derived GPMVs (48). Because the AC50 value of an *n*-alcohol is proportional to its partition coefficient from water into PC bilayers (125), the observation of scaling implies that the magnitude of ΔT_{mix} is colligative for short-chain *n*-alcohols: the value of ΔT_{mix} depends only on the mole fraction of alcohol in the membrane.

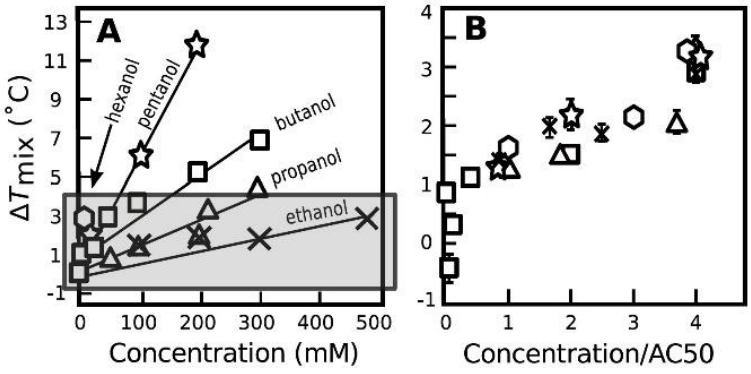

Figure 2.2. A. Increases in miscibility transition temperatures of 35/35/30 DOPC/DPPC/chol vesicles scale with the concentration of *n*-alcohol in the aqueous solution. Lines are least square fits. **B**. Data from the shaded region in Panel A are rescaled by AC50 values from (106). Because AC50 values are reported to be proportional to partition coefficients of *n*-alcohols from water into PC bilayers (125), concentration/AC50 should be proportional to the concentration of *n*-alcohol in the membrane. Each point represents a single experiment for which symbols are typically larger than uncertainties, determined as in Fig. 2.1. Standard deviations for repeated experiments are typically ±0.5 ˚C.

Increase in T_{mix} is Robust Across Lipid Ratios and Lipid Types

The result that short-chain *n*-alcohols increase T_{mix} by several degrees in model GUV membranes is robust. Fig. 2.3 shows that this result holds for membranes composed of different ratios of DOPC, DPPC, and cholesterol. The Gibbs triangle in Fig. 2.3 plots T_{mix} values for control GUVs (without butanol) with five different lipid ratios. When GUVs of these same ratios are produced in butanol solutions, T_{mix} increases independent of whether the ratios are varied along a vertical (Fig. 2.3a) or horizontal (Fig. 2.3b) path in the triangle. A corollary is that short-chain

n-alcohols increase T_{mix} independent of whether the majority of the GUV area is covered by the L_o phase or by the L_d phase. Similarly, T_{mix} increases independent of whether the GUV membrane is close to or far from a miscibility critical point.

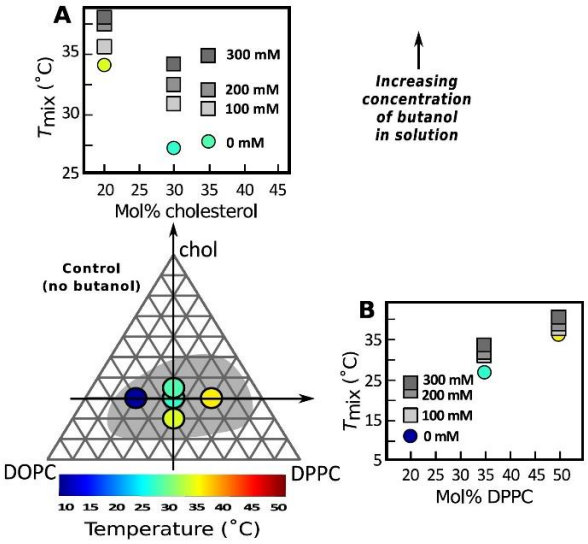

Figure 2.3. Miscibility transition temperatures of GUVs of five different ratios of DOPC/DPPC/chol increase with the concentration of butanol in solution. Colors within circles on the Gibbs triangle record T_{mix} in the absence of butanol. The grey region denotes compositions over which a transition from one uniform phase to coexisting L_o and L_d phases is observed at a temperature between 15˚C and 40˚C, from (34). GUVs in Panel **A** contain increasing cholesterol fractions (following the vertical arrow on the triangle). GUVs in Panel **B** maintain a constant fraction of cholesterol (following the horizontal arrow). Each point represents a single experiment for which uncertainties are smaller than symbols.

The result that short-chain *n*-alcohols increase T_{mix} is also robust for membranes composed of lipids with different shapes. Lysolipids are cone-shaped lipids with a single acyl tail, which means that lysolipid head groups have larger cross-sectional areas than lysolipid tails. One consequence of this shape is that lysolipids are thought to shield membrane cholesterol, whereas alkanols displace it (126). In Fig. 2.4, we replace half of the unsaturated DOPC lipids with lyso(18:0)-PC lipids, and we find that butanol still increases T_{mix}; the change in lipid shape did not change the sign of ΔT_{mix}.

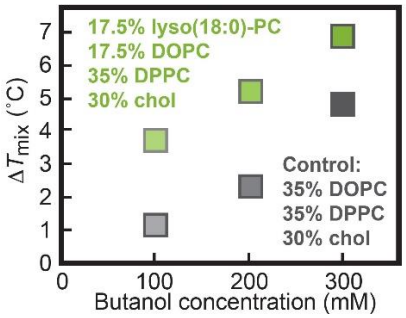

Figure 2.4. Miscibility transition temperatures of GUVs composed of 17.5/17.5/35/30 lyso(18:0)-PC/DOPC/DPPC/chol (green, top) and composed of 35/35/30 DOPC/DPPC/chol (grey, bottom) increase with the concentration of butanol in solution (increasing darkness of the points). Each point represents a single experiment for which uncertainties are smaller than symbols. ΔT_{mix} is with respect to vesicles with no butanol.

The robustness of the result extends to membranes containing lipids with high biological relevance. In Fig. 2.5, we alter two of the three GUV components. Specifically, we replace DOPC with POPC, and we replace DPPC with PSM. POPC is a common substitute for DOPC because it is ~18 mol% of PC-lipids in human red blood cells (127). Similarly, pSM constitutes ~25 mol% of sphingomyelin lipids in red blood cells (127). T_{mix} values for control GUVs (without butanol) agree with the previously mapped miscibility phase diagram of POPC/pSM/cholesterol (32, 128). In Fig. 2.5a-b, the ratios of POPC, pSM, and cholesterol are varied in analogy to Fig. 2.3. For all lipid ratios, T_{mix} of GUVs increases with the concentration of butanol in solution.

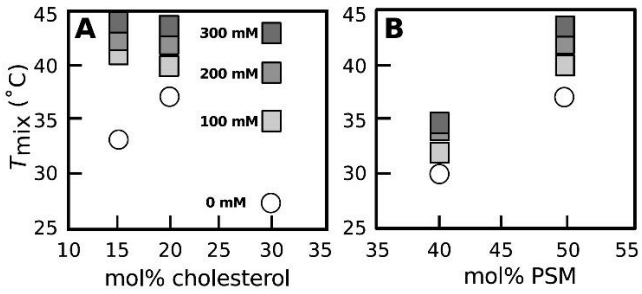

Figure 2.5. Miscibility transition temperatures for GUVs composed of POPC/pSM/chol increase with the concentration of butanol in solution. **A.** The molar ratio of POPC to pSM is held constant at 1:1 while the fraction of cholesterol is increased. **B**. The fraction of cholesterol is held constant at 30 mol% while the ratio of PSM to POPC is increased. Each point represents a single experiment for which uncertainties are smaller than symbols.

Butanol Increases L_o-L_d Contrast in GUVs, but Not in GPMVs

Why does the addition of short chain *n*-alcohols increase T_{mix} in model GUV membranes (Figs. 1-5) and decrease T_{mix} in cell-derived GPMVs (48)? The simplest explanation is that short-chain

n-alcohols in GUV partition much more strongly into one of the membrane phases than the other (129–131). Given that short-chain alcohols lie directly below lipid headgroups in membranes (94), we expect these alcohols to strongly partition to the L_d phase of GUVs instead of the L_o phase. GPMVs are more complex; it is difficult to predict how short-chain alcohols would partition between the L_d and L_o phases of a GPMV. If an alcohol were to instead partition roughly equally between the two membrane phases as an "inert diluent", T_{mix} would decrease over all lipid ratios (131–133). At the very least, we can state that our results in Figs. 2.3 and 2.5 are not consistent with the phase boundary merely translating within the plane of the Gibbs phase triangle, such that T_{mix} would increase at some lipid ratios and decrease at others. To illustrate these concepts, Fig. 2.6a shows T_{mix} increasing over all lipid ratios, and Fig. 2.6b shows the phase boundary translating.

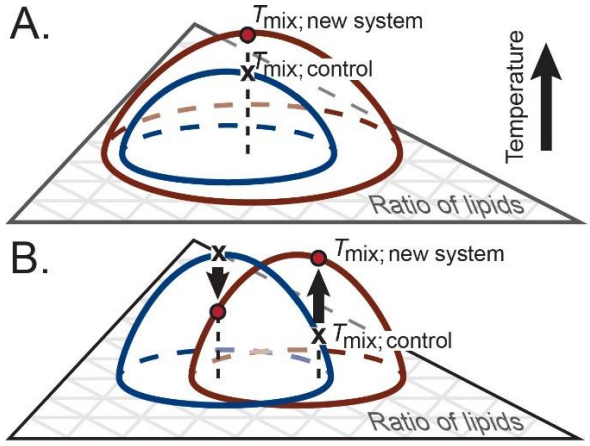

Figure 2.6. Two scenarios of how miscibility transition temperatures (the curved surfaces) may shift in response to changes in the composition of a membrane. The Gibbs phase triangle in the *x*-*y* plane contains all possible ratios of the three components of the ternary membrane. Panel A shows an increase in T_{mix} over all lipid ratios, moving from the control to the new system. Panel B shows an increase in T_{mix} for some lipid ratios (upward arrow) and a decrease for others (downward arrow).

Leung and Thewalt (134) found that a particular probe (napthopyrene) partitions strongly to L_d phases in GUVs, increases the difference in lipid chain order between the two phases, and increases T_{mix}. They found that an alternate probe (laurdan) partitions weakly between the two membrane phases and does not have these effects (134). If short chain *n*-alcohols partition strongly to L_d phases in GUVs and weakly between the two membrane phases in GPMVs, then we would expect short chain *n*-alcohols to increase the difference in lipid chain order between L_o and L_d phases in GUVs and to not increase it substantially in GPMVs. To test this idea, we used the generalized polarization (GP) of laurdan as a qualitative measure of the difference between L_o and L_d phases in GUVs and in GPMVs. Laurdan's emission spectrum reflects its exposure to aqueous solvent, which in turn reflects the packing of the lipid headgroups, determined in part

by the conformational order of lipids in the membrane. Lipid order is a function of membrane composition, and changes in GPMV lipid composition that increase the difference in GP between the L_o and L_d phases tend to increase T_{mix} of GPMV membranes (65, 66, 134–136).

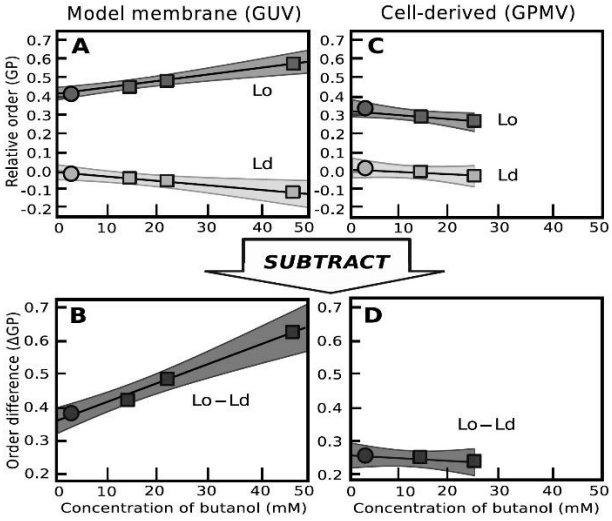

Figure 2.7. Differences between laurdan GP values in L_o and L_d phases in GUVs increase with butanol concentration in solution (panels **A**-**B**) and remain roughly constant in GPMVs (panels **C**-**D**). GUVs were composed of 35/35/30 DOPC/ DPPC/chol, and GPMVs were derived from RBL cells. Points represent average GP values for batches of 20-30 vesicles on different days. The slope of each line arises from a linear regression with fixed intercepts to offset untreated batch differences from day to day. Shaded areas are 95% confidence intervals of the fit. Slopes of the lines in Panels B and D are $4.80 \times 10^{-3} \pm 1.37 \times 10^{-3}$ and $-6.81 \times 10^{-4} \pm 1.58 \times 10^{-3}$, in normalized units of ΔGP/[(butanol concentration)(butanol's membrane-water partition coefficient from (106))]. Table S1 and Fig. 2S5 contain corresponding data for GUVs and GPMVs with tetradecanol and hexadecanol.

Figs. 2.7a-b show that the addition of butanol, a short-chain *n*-alcohol, does indeed increase the difference in laurdan GP between L_o and L_d phases in GUVs, consistent with our expectation that these alcohols strongly partition to the L_d phase in GUVs. Because short-chain *n*-alcohols generally decrease lipid acyl chain order in model membranes (95, 137–141), it may seem surprising that incorporation of butanol into the membrane increases the laurdan GP of the L_o phase in Fig. 2.7a. However, given that short-chain *n*-alcohols have an antagonistic relationship with cholesterol in membranes (126), *n*-alcohols that partition primarily to the L_d phase might be expected to drive more cholesterol into the L_o phase (137, 142, 143), where cholesterol would increase the order of saturated lipids (20, 25). Our results in Figs. 2.7a-b are less consistent with butanol strongly partitioning to the L_o phase. If most of the butanol partitioned to the L_o phase, we would expect its laurdan GP to decrease for two reasons: (a) short chain alcohols decrease lipid

chain order (137) and (b) butanol would be expected to displace cholesterol to the L_d phase, where it would increase the chain order of the lipids in the L_d phase (144). Instead, the opposite trends in GP values are observed in Figs. 2.7a-b.

Figs. 2.7c-d tell a very different story for cell-derived GPMVs: butanol does not significantly increase the difference in laurdan GP for GPMVs. This result implies that any differential partitioning of butanol between the L_o and L_d phases in GPMVs is modest. The contrast between the GUV results in Figs. 2.7a-b and the GPMV results in Figs. 2.7c-d is reminiscent of the contrast between probe partitioning results in GUVs vs. GPMVs: in several cases, the same probe partitions strongly between L_o and L_d phases in GUVs and weakly between the phases in GPMVs (45, 65, 67, 110).

Theoretically, differential partitioning of butanol between L_o and L_d phases in GUVs is measureable from area fractions of the two phases (48). Experimentally, this idea is challenging to test. In control GUVs of 35/35/30 DOPC/ DPPC/chol in water, the L_d phase covers 35.5% of the area (± a standard deviation of 3.4% for n = 18 vesicles). For GUVs of the same lipid composition in 50 mM butanol, the L_d phase covers 37.2 ± 4.0% for n = 20 vesicles. Within uncertainty, these two values are equivalent. The following estimate shows that even a scenario in which all butanol partitions to one phase would be difficult to resolve within these uncertainties. If we approximate the area per DOPC lipid in a bilayer with 30 mol% cholesterol to be 52.8 $Å^2$ (145) and the thickness of a bilayer to be ~5 nm (146), then every bilayer unit with 100 lipids in each monolayer has a volume of ~2.6 x 10^{-22} L. If 50 mM butanol in solution partitions into the bilayer with a coefficient of 1.52 as in erythrocytes (106), then each 200-lipid bilayer should harbor ~12 molecules of butanol, or 6 mol%. Butanol molecules are smaller than lipids. Therefore, with an uncertainty of 4%, we cannot expect to optically resolve area fraction increases due to differential partitioning of butanol.

Nonmonotonic Shifts in T_{mix} for Long *N*-alcohols

To review, short chain *n*-alcohols increase membrane T_{mix} in GUVs. One of these alcohols, butanol, increases the difference in laurdan GP between the L_o and L_d phases of GUVs, presumably as a result of strong preferential partitioning of the butanol to the L_d phase. As the length of *n*-alcohols increases, we expect a crossover in behavior. Specifically, we expect *n*-alcohols of medium lengths to partition more equally between the L_d and L_o phases, resulting in a decrease in

T_{mix} and no significant increase in ΔGP. Once the number of carbons in *n*-alcohols exceeds a second threshold, we expect the alcohols to again strongly partition to only one of the membrane phases, this time to the L_o phase. This expectation is reasonable given that a recent calculation predicts that short, saturated alkyl chains partition preferentially to an L_d phase, that medium chains partition equally, and that long chains partition preferentially to an L_o phase (147).

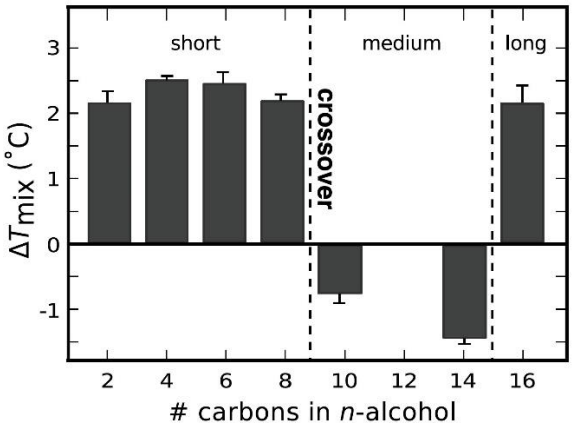

Figure 2.8. Increasing the number of carbons in *n*-alcohol solutions results in nonmonotonic shifts in T_{mix} for GUVs composed of 35/35/30 DOPC/DPPC/chol. ΔT_{mix} is with respect to GUVs in water. Concentrations of *n*-alcohol solutions correspond to three times the AC50 in (106). AC50 values for tetradecanol and hexadecanol were estimated at 5 μM. Each point represents a single experiment with uncertainties as in Fig. 2.1. Fig. 2S3 contains corresponding data at lower *n*-alcohol concentrations.

Fig. 2.8 supports the notion that a crossover does indeed occur. Fig. 2.8 shows that T_{mix} increases when GUVs of 35/35/30 DOPC/DPPC/chol are produced in solutions containing *n*-alcohols with short alkyl chains (≤ 8 carbons). In contrast, for medium chains (10-14 carbons), T_{mix} decreases. For long chains (≥ 16 carbons), T_{mix} increases again. The data in Fig. 2S5c are consistent with this view: as a medium chain *n*-alcohol (tetradecanol) is introduced to a GUV solution there is no significant increase in the difference in laurdan GP between the L_o and L_d phases. Recent theory suggests that the greatest decrease in T_{mix} should occur when the *n*-alcohol slightly prefers the L_d phase (133).

The designation of *n*-alcohols as "short", "medium", and "long" invokes relative terms that depend upon characteristics of the membrane in which the alcohol is embedded. Upon switching from GUVs to GPMVs, *n*-alcohols with 2-10 carbons behave as alcohols in our "medium" category: they decrease T_{mix} in GPMVs (11). A length of 16 carbons qualifies as "long" in both types of membranes: in GPMVs, hexadecanol increases T_{mix} (130). A switch from "medium" to

"long" behavior in GPMVs, where $\Delta T_{mix} \approx 0$, occurs at an alkanol length of 14 carbons (48), as seen in Fig. 2S4. Addition of tetradecanol to GPMVs results in no significant increase in the difference in laurdan GP values (Fig. 2S5D). Gray et al. discuss this switch in behavior as an analogy of the "cutoff effect" (48), the decrease in efficacy of alcohols as general anesthetics when *n*-alcohols exceed a cutoff length (125, 148).

Three natural length scales arise in Fig. 2.8: the length of the alcohol's alkyl chain, the length of the lipid's acyl chain, and the length from the lipid's glycerol backbone to its double bond. These lengths are shown in Fig. 2S1. In Fig. 2.9, we decrease the length of *n*-alcohols that qualify as "short" by replacing DOPC with two types of analogous lipids. The first type of replacement uses a lipid with the same length of carbon chain as DOPC and a double bond at a new position (the Δ6 position rather than the Δ9 position). With this substitution, the crossover in behavior occurs at 6 carbons (i.e. only *n*-alcohols with 2, 4, or 6 carbons result in a significant increase T_{mix} whereas *n*-alcohols with 8 or 10 carbons do not). The second type of replacement uses lipids with shorter acyl chains, retaining the double bond at the Δ9 position. These new substitutions push the crossover length of the *n*-alcohol down to 4 carbons (for 16:1Δ9PC lipids) and down to 2 carbons (for 14:1Δ9PC lipids).

These results imply that the length of the lipids and the position of each lipid's double bond determine how an *n*-alcohol partitions into L_d versus L_o phases. One of the primary differences between GUV and GPMV membranes is in the length and unsaturation of the lipids. Given the high occurrence of polyunsaturated lipids in GPMVs (66), and that *n*-alcohol partition coefficients are highly sensitive to lipid polyunsaturation (149), it is plausible that different *n*-alcohols qualify as "short", "medium", and "long" in GPMV membranes than in GUV membranes. It is also plausible that the significant protein content of GPMVs contributes to differences in partitioning of *n*-alcohols between L_d and L_o phases of GUVs vs. GPMVs. Generalizing from *n*-alcohols to other types of amphiphiles, a long list of molecules are known to partition differently into L_d vs. L_o phases in GUVs than in GPMVs (e.g. 18). To highlight the magnitude of this differential partitioning, at least one probe's preference for the L_d versus the L_o phase is reversed in the two types of membranes (45). In summary, differences in how *n*-alcohols partition between the two phases in GUVs and GPMVs may explain why short-chain alcohols increase T_{mix} in GUVs and decrease T_{mix} in GPMVs.

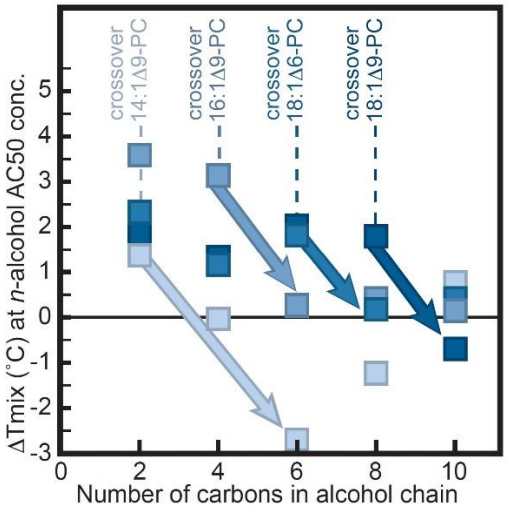

Figure 2.9. Shift in miscibility transition temperatures for GUVs composed of 35/35/30 mol% mixtures of an unsaturated lipid, DPPC, and cholesterol. Four types of unsaturated lipids were used. For all four, incorporation of an *n*-alcohol with 2 carbons into the membrane produces a positive ΔT_{mix}. A significant decrease in T_{mix} (> 1˚C, shown by arrows) occurs at a crossover alkanol length characteristic of each unsaturated lipid. Labeled right to left in the figure, with symbols from darkest to lightest, the unsaturated lipid is either DOPC (18:1 *cis*Δ9 PC), a DOPC analog with the double bond in a different position (18:1 *cis*Δ6 PC), or DOPC analogs with shorter acyl chains (16:1 *cis*Δ9 PC or 14:1 *cis*Δ9 PC). All GUVs were in *n*-alcohol solutions at three times the AC50 concentrations in (106). ΔT_{mix} is with respect to vesicles in water. Each point represents a single experiment. Symbols are larger than uncertainties determined as in Fig. 2.1.

Alcohol Anti-intoxicants Increase T_{mix} in GUVs

If we consider shifts in T_{mix} as a consequence of how impurities partition into L_o and L_d phases of membranes, we gain a method of predicting whether small molecules will increase or decrease T_{mix}. Here we focus on dihydromyricetin (DHM) and Ro15-4513. Both are expected to partition to membranes: Ro15-4513 is roughly twice as hydrophobic as butanol. DHM and Ro15-4513 are termed "anti-intoxicants" because they reverse the effects of ethanol in cultured neurons as well as whole organisms, at least at concentrations of 3 μm and 100 nM, respectively (150, 151). These two compounds are also anti-intoxicants in terms of reversing the effect of ethanol on T_{mix} in cell-derived GPMVs (130). Namely, ethanol decreases T_{mix} in GPMVs, whereas DHM and Ro15-4513 increase it (130). The increase in T_{mix} implies that DHM and Ro15-4513 partition strongly to only one of the membrane phases in GPMVs. Given that DHM and Ro15-4513 both feature polar groups and bulky ring structures, they are expected to strongly partition near lipid headgroups in the L_d phase of GUVs and to thereby increase T_{mix} in GUVs. Fig. 2.10 shows that T_{mix} of GUVs incubated in 3 μM DHM is indeed higher (by ~0.5˚C) than for GUVs in water. Likewise, Fig. 2.10

shows that T_{mix} for GUVs incubated in 100 nM Ro15-4513 is ~1.3 ˚C higher than for GUVs in water.

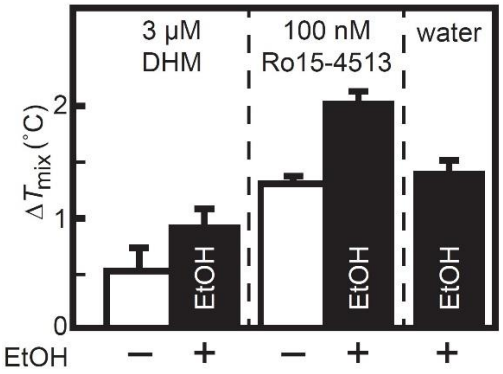

Figure 2.10. 35/35/30 DOPC/DPPC/chol GUVs produced in 3 μM DHM or 100 nM Ro15-4513 alone (white bars) have elevated miscibility transition temperatures with respect to control GUVs in water (ΔT_{mix}). Similarly, GUVs produced in 120 mM ethanol (EtOH, black bars) have higher miscibility temperatures under all conditions in the figure. Each bar represents a single experiment for which uncertainties are calculated as in Fig. 2.1.

Minor Structural Changes in Alcohols Result in Large Shifts in Membrane T_{mix}

In Fig. 2.10, a cursory description of the bulky, amphiphilic structures of DHM and Ro15-4513 led to a prediction that the compounds would partition strongly into the L_d phase and increase T_{mix}. However, partition coefficients are not always straightforward to predict, as for propofol and its membrane-soluble structural analog 2,6-di-*tert*-butylphenol (Fig. 2.11). This pair is particularly interesting because propofol is a general anesthetic, whereas 2,6-di-*tert*-butylphenol is not (152). Gray et al. previously found that propofol decreases T_{mix} in cell-derived GPMVs, whereas 2,6-di-*tert*-butylphenol does not shift T_{mix} (48). In other words, propofol behaves as a short-chain alcohol does in GPMVs.

In Fig. 2.11, we find that propofol also behaves as a short-chain alcohol in GUVs: ternary vesicles in propofol have higher values of T_{mix} than vesicles in water. No significant shift in T_{mix} occurs for the non-anesthetic analog at identical concentrations. We are unaware of any current models that would predict the partitioning of propofol and 2,6-di-*tert*-butylphenol into L_d vs. L_o phases. Future models to predict partitioning might incorporate area-to-volume ratios of molecules, as in (68).

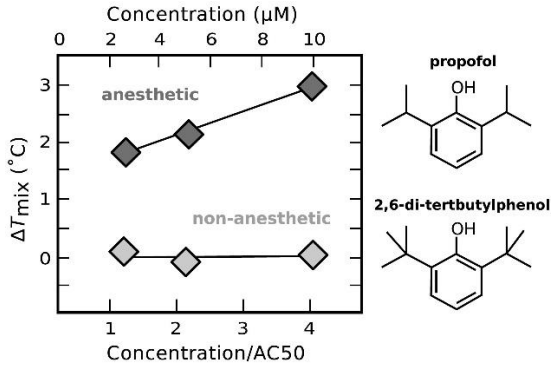

Figure 2.11. Propofol, a general anesthetic, increases T_{mix} in 35/35/30 DOPC/DPPC/chol GUVs. In contrast, 2,6-di-*tert*-butylphenol, which is structurally similar but anesthetically inactive, does not increase T_{mix}. Each point represents a single experiment. In all cases, symbols are larger than uncertainties determined as in Fig. 2.1.

Hydrostatic Pressure Increases T_{mix} in GUVs

Because T_{mix} of a GUV membrane is an equilibrium property, it can be tuned by adjusting thermodynamic parameters. For example, T_{mix} increases as model vesicles are subjected to increasing hydrostatic pressure (153), indicating that a demixed membrane fills less volume than a uniformly mixed membrane. This result, that T_{mix} increases with pressure, holds whether the membrane originates from a model GUV or from a cell-derived GPMV (130).

Although GUVs and GPMVs are alike in that T_{mix} increases with pressure, we have seen in Figs. 2.1-2.5 that the two systems are dissimilar in their response to short-chain *n*-alcohols. Fig. 2.12 provides an equivalent illustration of this point. Increasing concentrations of butanol *decrease* the miscibility transition pressure, P_{mix}, in model GUVs at constant temperature. These GUV data are consistent with the hypothesis that butanol strongly partitions into only one membrane phase in GUV membranes, such that membranes spontaneously demix over a wider range of conditions. In contrast, in GPMVs, increasing concentrations of butanol *increase* P_{mix} in cell-derived GPMVs (130). Specifically, 12 mM butanol increases P_{mix} by 240 ± 30 bar (130). These GPMV data are consistent with the hypothesis that butanol partitions roughly equally into both membrane phases in GPMV membranes, such that membranes spontaneously demix over a narrower range of conditions.

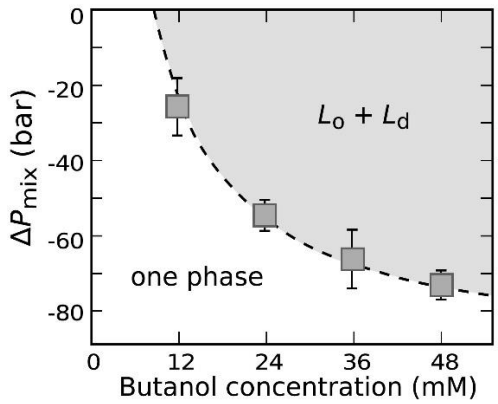

Figure 2.12. Miscibility transition pressures for GUVs of 35/35/30 DOPC/DPPC/chol decrease with increasing concentration of butanol in solution. Values of ΔP_{mix} are relative to control vesicles in water. Each point represents a single experiment for which uncertainties derive from fits to sigmoidal curves of % vesicles separated vs. hydrostatic pressure, in analogy to Fig. 2.1.

2.4 SPECULATIONS

In Figs. 2.1-2.9, we observe shifts in T_{mix} and ΔGP that are consistent with (1) short-chain *n*-alcohols partitioning strongly to L_d phases in ternary GUVs, (2) medium-chain alcohols partitioning roughly equally between L_d and L_o phases, and (3) long-chain alcohols partitioning strongly to L_o phases. In this model, the magnitude of the shift in T_{mix} depends on the concentration of *n*-alcohol in a membrane. The experimental question of whether *n*-alcohol concentrations are roughly equivalent in model and cell membranes is not well resolved (125, 154). Our focus on differential partitioning of *n*-alcohols between L_o and L_d phases does not exclude other possible modes of action that may differ between GUV and GPMV systems, e.g. *n*-alcohols behaving as lineactants, interacting with proteins, distributing at different distances from the membrane midplane, or competing with cholesterol for phospholipid association.

We speculate that the tendency of an *n*-alcohol to partition differentially between L_o and L_d phases depends on characteristic length scales of membrane lipids, set by the location of double bonds and by the length of lipid chains. If this speculation is valid, then GPMVs with different lipid compositions (perhaps due to cell cycle, state, or growth conditions (67, 155)) would be have different crossover lengths of *n*-alcohols (c.f. Fig. 2.9). Similarly, we speculate that any compound that partitions strongly to only the L_o or L_d phase will prove to raise T_{mix} in membranes. Predicting how subtle structural differences between compounds (e.g. between propofol and 2,6-di-*tert*-butylphenol) are manifested in their partitioning between L_o and L_d phases within an all-atom

simulation would be expensive given current capabilities. However, the tendency of a compound to strongly preferentially partition to one membrane phase over another may prove to map onto other membrane physical parameters, such as changes in lateral pressure profiles (149) that may be easier to calculate or simulate.

Models that invoke differential partitioning of molecules between L_o and L_d phases predict a variety of results. Dilute concentrations of an impurity cause critical temperatures (and hence T_{mix}) to increase in models that consider differential solubilities (131)(133). or differential partitioning within an Ising model (129). Experiments in which dilute impurities were added to two-component bulk mixtures found that critical temperatures increased when the impurity had a low solubility in one of the components and decreased when the impurity was likely to be soluble in both components (156). In another model, Schick (157) used the well-known result (158) that for a one-component membrane undergoing a phase transition, an impurity that preferentially partitions into the membrane phase with higher entropy decreases the transition temperature. He showed that a term that relates partitioning of the impurity to the change in transition temperature would also appear in equations describing multi-component membranes. This term, combined with a predicted differential partitioning of alkyl chains (147) could explain why short-chain alcohols decrease T_{mix} in GPMVs, but not why they increase T_{mix} in GUVs.

2.5 CONCLUSION

Here we show that *n*-alcohols with ≤8 carbons increase T_{mix} for membranes of ternary GUV membranes over a range of *n*-alcohol concentrations. This increase is robust for membranes of several lipid types and ratios. As chain lengths of alcohols increase, their effect on membranes is non-monotonic: *n*-alcohols with 10-14 carbons decrease T_{mix} in the GUVs in this study; for n=16, T_{mix} increases. Previous experiments using cell-derived GPMVs also found that as chain lengths of alcohols increase, their effect on membranes evolves: *n*-alcohols with ≤10 carbons decrease T_{mix} in GPMVs; for n=16, T_{mix} increases (48, 130). A full summary of how the GUV data in Figs. 2.1-2.12 compare with previous GPMV data appears in Table S1 of the Supporting Material.

Results from GUVs and GPMVs are equally consistent with a scenario in which the partitioning of *n*-alcohols into L_d vs. L_o phases changes as the length of the alcohol increases. In this scenario, alcohols that are shorter than a characteristic length scale set by the membrane would strongly preferentially partition to the L_d phase, increasing T_{mix}. One piece of evidence in support

of this scenario is that for GUVs in butanol solutions, laurdan ΔGP values increase with the butanol concentration, as shown in Figure 7. In contrast, *n*-alcohols of medium length (e.g. tetradecanol, *n* = 14) decrease T_{mix} with no significant effect on laurdan ΔGP (Fig. 2S5).

2.6 ACKNOWLEDGEMENTS

We thank Sarah Veatch for experimental advice, and for her MATLAB program to project 2D images onto 3D spheres; Joseph Lorent for his program to create laurdan 2D GP images; Michael Schick and Sharona Gordon for insightful discussions; Barbara Diaz-Rohrer for hospitality; Scott Rayermann and Niket Thakkar for assistance with MATLAB and python; and the UW Statistical Consulting Service for the correct linear regression to apply in Fig. 2.7. C.E.C was funded by the National Institute of General Medical Sciences of the National Institutes of Health (NIH) under award T32GM008268. Research in the Keller Lab was supported by National Science Foundation grant MCB-1402059. The Levental Lab was supported by the Cancer Prevention and Research Institute of Texas (R1215) and the NIH (1R01GM114282). The Brooks Lab was supported by Engineering and Physical Sciences Research Council Programme Grant (EP/J017566/1) and an EPSRC Centre for Doctoral Training Studentship (EP/F500076/1) awarded by the Institute of Chemical Biology to N.L.C.M. All high-pressure data are openly available from Imperial College London; please see contact details at www.imperial.ac.uk/membranebiophysics.

2.7 SUPPLEMENTARY FIGURES AND TABLES

Table S1. Comparison of GUV and GPMV results.

GUVs from ternary lipid mixtures (This work)	**GPMVs derived from RBL cells (References (1) and (2))**	**Figure in main text**
Similarities		
1. Short-chain *n*-alcohols cause large shifts in T_{mix} at the AC50 concentration.		Fig. 2
2. Shifts in T_{mix} scale with anesthetic dose of short-chain *n*-alcohols.		Fig. 2
3. Shifts in T_{mix} diminish when the length of *n*-alcohols reaches a cutoff.		Fig. 8-9
4. Long-chain *n*-alcohols (*n* = 16) increase T_{mix}.		Fig. 8
5. Anti-intoxicant compounds (DHM and Ro15-4513) increase T_{mix}.		Fig. 10
6. Propofol, a general anesthetic, shifts T_{mix}; its nonanesthetic analog does not.		Fig. 11
Differences		
1a. Short *n*-alcohols **increase** T_{mix}.	**1a.** Short *n*-alcohols **decrease** T_{mix}.	Fig. 2
2a. Short *n*-alcohols **increase** order differences between L_o and L_d phases (by laurdan generalized polarization)	**2a.** Short *n*-alcohols **do not affect** order differences between L_o and L_d phases (by laurdan generalized polarization)	Fig. 7
3a. With increasing concentrations of butanol, P_{mix} **decreases**.	**3a.** With increasing concentrations of butanol, P_{mix} **increases**.	Fig. 12

Figure S1. Names and structures of lipids used in this study. Structures are from (159).

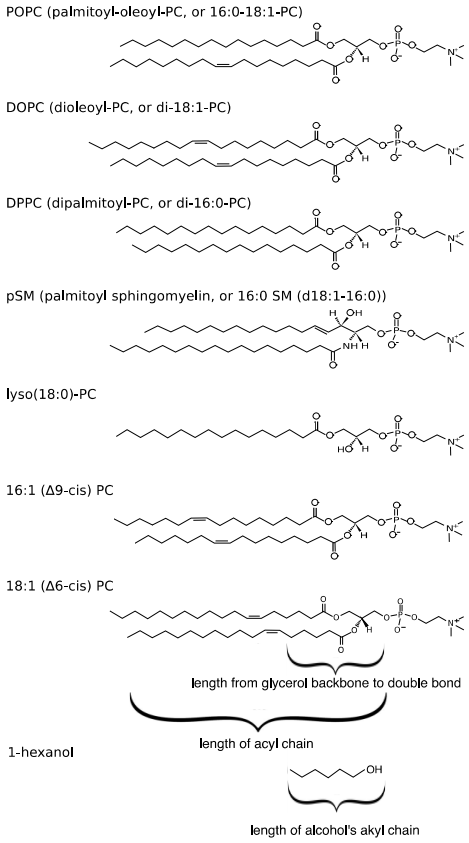

Figure S2. Increases in miscibility transition temperatures of 35/35/30 DOPC/DPPC/chol vesicles scale with *n*-alcohol concentrations up to several times each *n*-alcohol's AC50 value. In Panels **A** and **B**, data from Fig. 2a in the main text are rescaled by each *n*-alcohol's AC50 value from reference (106) (Panel **A**) and from (119) (Panel **B**). Data diverge at *n*-alcohol concentrations greater than 5 x AC50 (which far exceed physiologically relevant values). Panel **C** shows data from panel **B** below 5 x AC50. Symbols are identified in Fig. 2a.

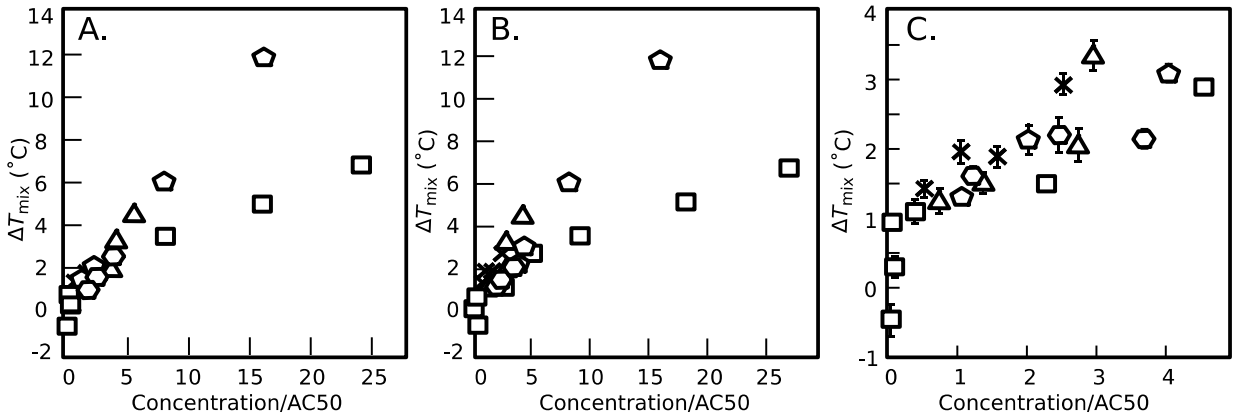

Figure S3. The data in this figure reproduce the data in Figure 8 at two additional AC50 values. In this figure, concentrations of *n*-alcohol solutions are a factor of one (Panel **A**) and two (Panel **B**) times the AC50, whereas in Figure 8, concentrations are three times the AC50. For *n*-alcohols of lengths 2-10 carbons, AC50 values were from (106). AC50 values for tetradecanol and hexadecanol were estimated at 5 μM. Increasing the number of carbons in *n*-alcohol solutions results in nonmonotonic shifts in T_{mix} for GUVs composed of 35/35/30 DOPC/DPPC/chol. ΔT_{mix} is calculated with respect to control GUVs in water. Each bar represents a single experiment with uncertainties as in Fig. 1.

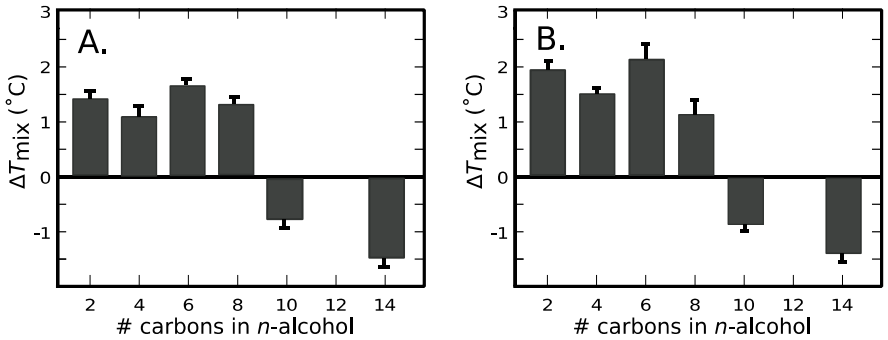

Figure S4. Data from Gray et al. (48) and Machta et al. (130). Increasing the number of carbons in *n*-alcohol solutions results in a crossover in the sign of ΔT_{mix} for GPMVs derived from RBL cells. ΔT_{mix} is calculated with respect to control GPMVs in water. Concentrations of *n*-alcohol solutions are a factor of two times the AC50 for ethanol, octanol, decanol, and hexadecanol and a factor of one times the AC50 for tetradecanol. The value of ΔT_{mix} for hexadecanol was found by assuming additive effects of ethanol and hexadecanol in a GPMV solution containing two times the AC50 of each *n*-alcohol. Data points for ethanol, octanol, decanol, and tetradecanol are extracted from (48) and the data point for hexadecanol is extracted from (130). Each bar represents a single experiment with uncertainties as in Fig. 1.

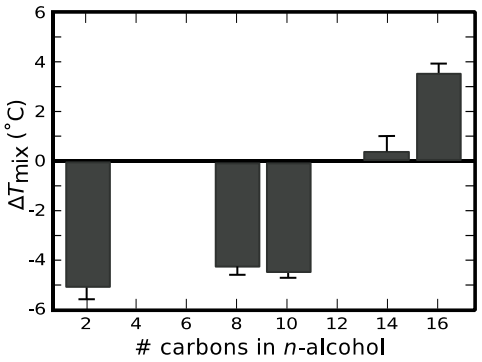

Figure S5. Differences between laurdan GP values in L_o and L_d phases in GUVs and GPMVs remain roughly constant with 1-tetradecanol concentration in solution (panels **A**-**D**). Differences between laurdan GP values in L_o and L_d phases in GUVs and GPMVs slightly increase with

1-hexadecanol concentration in solution (panels **E**-**H**). GUVs were composed of 35/35/30 DOPC/ DPPC/chol, and GPMVs were derived from RBL cells. Points in the GUV plots represent average GP values for batches of 20-30 vesicles. The slope of each line arises from a linear regression. Points in the GPMV plots represent average GP values for batches of 20-30 vesicles on different days. The slope of each line arises from a linear regression with fixed intercepts to offset untreated batch differences from day to day. Shaded areas are 95% confidence intervals of the fit. Slopes of the lines in Panels **C**, **D**, **G**, and **H** are $8.94 \times 10^{-7} \pm 2.29 \times 10^{-6}$, $-1.77 \times 10^{-6} \pm 2.80 \times 10^{-6}$, $4.46 \times 10^{-7} \pm 5.82 \times 10^{-7}$, and $4.06 \times 10^{-7} \pm 5.76 \times 10^{-7}$ in units of ΔGP/(butanol concentration x partition coefficient from (106)).

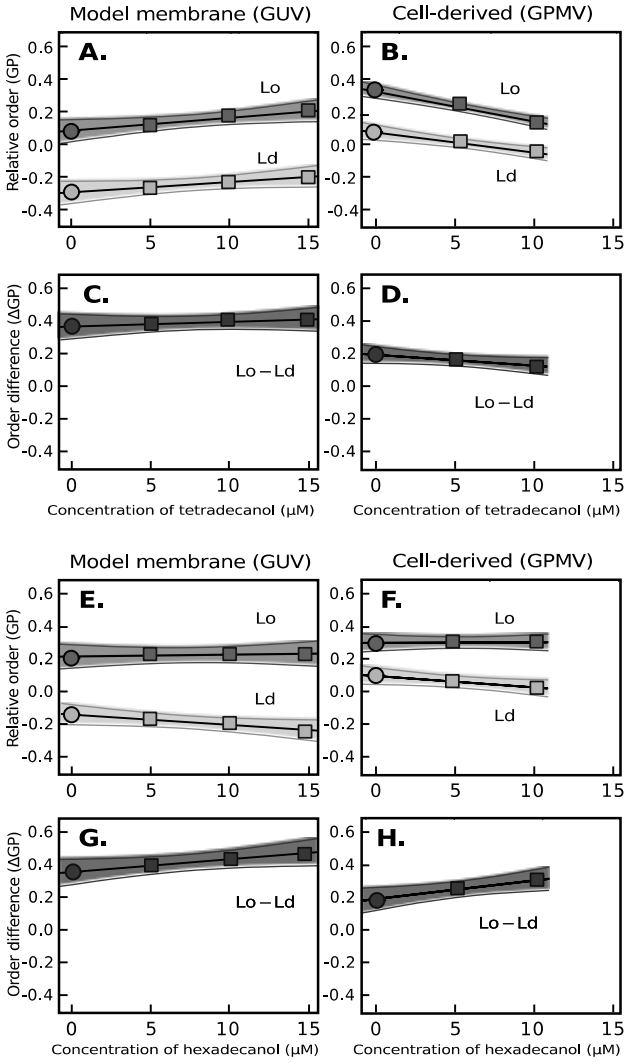

Figure S6. Changes in miscibility transition temperature of GPMVs isolated from RBL cells. **A.** GPMVs incubated in a solution of butanol have a decreased miscibility transition temperature compared to GPMVs incubated in buffer. **B.** GPMVs incubated in a solution of hexadecanol have an increased miscibility transition temperature compared to GPMVs incubated in buffer. Points represent average ΔT_{mix} values over three trials and error bars represent the standard deviation.

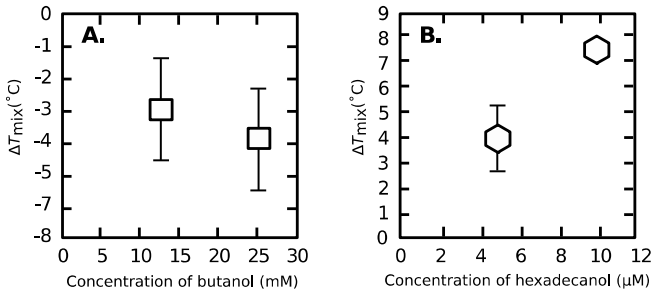

CHAPTER 3: Tuning Length Scales of Small Domains in Cell-Derived and Synthetic Model Membranes

*This chapter was first published in the *Biophysical Journal* in 2018. It was written in collaboration with A.D. Skinkle, S. He, I. Levental, K.R. Levental, and S.L. Keller. The full citation can be found at the end of Chapter 1 on pg. 29.

3.1 INTRODUCTION

Coexisting liquid phases are found within membrane systems that are as simple as three-component lipid vesicles and as complex as protein-rich vacuole membranes within living yeast cells (31, 33, 34, 74). These phases, named liquid ordered (L_o) and liquid disordered (L_d (23)), are enriched in lipids with high and low melting temperatures, respectively (34, 122, 128). When phase separation occurs in a vesicle, liquid domains nucleate, diffuse, collide, and coalesce until only one domain of each phase persists (Fig. 3.1A-C, (34, 118, 160)). In this case, the size of the domain is limited only by the size of the vesicle.

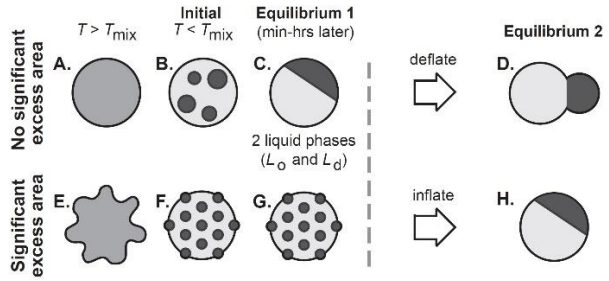

Figure 3.1. Schematic of ternary GUVs. Above T_{mix}, all lipids mix uniformly within the membrane (panels **A** and **E). (B)** In a membrane with no significant excess area, a decrease in temperature below T_{mix} causes domains of L_o and L_d phases to nucleate on the surface of the GUV. **(C)** Domains diffuse and coarsen until only one domain of each type remains, **(D)** even after subsequent deflation. **(F-G)** In a membrane with significant excess area, small domains can appear either due to hindered coarsening or due to a transition to a single phase of a microemulsion or modulated phase. **(H)** When excess area of the flaccid membrane is removed, domains of L_o and L_d phases may coarsen (160).

However, under some conditions, domains are much smaller than the size of the vesicle. Here, we explore how membrane physical parameters can be tuned to adjust the characteristic length scales of micron-scale domains in lipid membranes. The length scales that define rafts, which are described as sub-micrometer clusters of distinct lipids and proteins within cell membranes (29), may be determined by some of these same parameters.

Micron-scale domains are typically classified in three ways, depending on their spatial autocorrelation, $G(\vec{r})$. An excellent recent review of the topic is by Schmid (161). Membranes near a miscibility critical point are characterized by a $G(\vec{r})$ that behaves as $(x/r)^{1/2} e^{-r/x}$ where ξ is the correlation length, as in Fig. 3.2B. Mechanisms of adjusting length scales in model and cell-derived membranes near a critical point (e.g. adjusting temperature and pinning sites) are extensively discussed elsewhere (61, 162, 163). Here, our focus is on mechanisms leading to modulated phases and microemulsions.

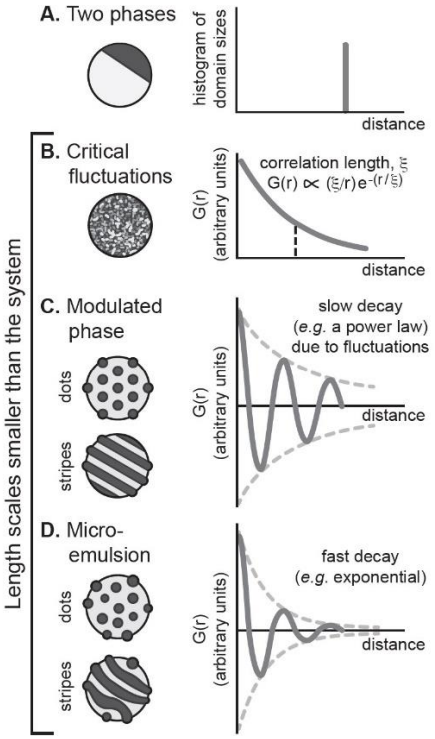

Figure 3.2. Schematic of four types of membrane behavior. **A.** Domains in a GUV exhibiting two liquid phases eventually merge into one large domain. **B.** GUVs exhibiting critical fluctuations produce a $G(\vec{r})$ that behaves as $(x/r)^{1/2} e^{-r/x}$. **C.** A modulated phase yields an oscillating $G(\vec{r})$ bounded by a slow decay, e.g. a power law. **D.** A microemulsion yields an oscillating $G(\vec{r})$ bounded by a fast decay, e.g. an exponential.

A modulated phase is characterized by an oscillating $G(\vec{r})$ bounded by a slow decay, for example a power law decay due to fluctuations (164), as in Fig. 3.2C. A microemulsion's $G(\vec{r})$ also oscillates, but is bounded by a fast (e.g. exponential) decay as in Fig. 3.2D (165–167). Both a modulated phase and a microemulsion yield a peak at non-zero wavevector in the structure factor,

obtained by Fourier transform of $G(\vec{r})$. The designation of modulated phase versus microemulsion does not determine the mechanism by which the phase forms. Similarly, the designation does not determine if domains are rounded (which we will call dots) or elongated (which we will call stripes). In the experimental literature, the term "modulated phase" has sometimes been used to describe all micron-scale domains in vesicles, even if those domains may arise from a microemulsion.

Here, we observe small domains in membranes of GUVs and GPMVs. The GUVs are made from synthetic mixtures of lipids, and we establish a slight excess area and asymmetry in the vesicle membrane by delivering lipids to the outer leaflet of GUVs via cyclodextrin. GPMVs are derived directly from the plasma membranes of live cells and are composed of a rich complement of cellular lipids and proteins. We then evaluate characteristic length scales and fluorescence levels in both systems to test proposed mechanisms of modulated phases and microemulsions. Two characteristic length scales can be assessed: the width of domains and the distance from the center of one domain to the center of the nearest neighbor.

3.2 METHODS

GUV Electroformation

Phosphocholine (PC) lipids (Avanti Polar Lipids, Alabaster, AL), cholesterol (chol; Sigma Aldrich, St. Louis, MO), and Texas Red dihexadecanoyl-PE (DHPE; Life Technologies, Grand Island, NY) were used as purchased without further purification. GUVs 10-100 μm in diameter were electroformed in 200-300 mM sucrose (168). Specifically, 0.25 mg of lipids in stock solutions were spread evenly on ITO-coated slides. Lipid stock solutions in chloroform typically contained diphytanoylphosphatidylcholine (DiPhyPC; 4 ME 16:0 PC), dipalmitoylphosphatidylcholine (DPPC; 16:0 PC), cholesterol, and 0.8 mol% Texas Red DHPE, a dye that selectively partitions to the L_d phase. One set of experiments used PC lipids in which the typical ester-linkages were replaced by ether linkages (4 ME 16:0 Diether PC and 16:0 Diether PC). In all cases, lipid-coated slides were placed under vacuum for >30 min to evaporate the chloroform. A capacitor was created by sandwiching 0.3 mm Teflon spacers between two lipid-coated slides, filling the gap with sucrose solution, and sealing the edges with vacuum grease. An AC voltage of 10 Hz and 1.5 V was applied across the capacitor for 1 hr at 60˚C. The resulting GUVs were diluted 10-fold in 200-300 mM glucose solution and stored at 60˚C for ≤ 2 hrs before use. Immediately before imaging

using a TE-2000-s inverted epifluorescence microscope (Nikon, Melville, NY), GUV solutions were further diluted 2-fold in glucose solution in a glass-bottomed chamber on the microscope stage. Images were captured through an air objective using a Photometrics CoolSnapFX camera (Photometrics, Tucson, AZ) at a resolution of 0.17 μm/pixel and manipulated using ImageJ (https://imagej.nih.gov/ij/). To preserve the fidelity of the data, manipulation of images was limited to adjusting overall brightness or implementing linear (gamma = 1) contrast enhancements.

DPPC-loaded HPαCD

Vesicles of DPPC lipids were produced by hydration in 200-300 mM glucose. Specifically, a mass of 10.3 mg of DPPC in chloroform was dried evenly on the walls of glass test tubes. The tubes were placed under vacuum for >30 min to evaporate the chloroform. A solution of 1 mL of 200-300 mM glucose was introduced to the tubes at 60˚C and allowed to sit for ~20 min so that DPPC vesicles formed. Solid hydroxypropyl-α-cyclodextrin (HPαCD; Sigma Aldrich) was added to the resulting vesicle solution to a concentration of 70 mM. The solution was stirred at 60˚C for 2 hrs before use.

GUVs with Small Length Scales

Control images were collected of GUVs that had settled to the bottom of the imaging chamber. The L_d phase is enriched in the dye, and appears bright; the L_o phase appears dark. Next, 30 μl of DPPC-loaded HPαCD solution was added to the GUV solution and equilibrated for ~5 min. The HPαCD presumably inserts its cargo of DPPC into the outer leaflet of the GUVs, establishing a difference in area between the outer and inner leaflets. The resulting change in lipid composition appears to be minimal. We tracked the fraction of membrane area that appears dark in three GUVs of 35/35/30 DiPhyPC/DPPC/cholesterol; this fraction increased by only 4.3 ± 0.9% after treatment with DPPC-loaded HPαCD. To estimate the corresponding maximum change in mole fraction of any one of the lipids, we scaled the percent change in area fraction by the length of the longest possible tie-line for membranes of DiPhyPC/DPPC/cholesterol at 22˚C (169), propagating the largest standard deviations in all cases. This process yields an upper bound of 3.9 mole %. Propagation of the smallest standard deviations yields 2.0 mole %. Area fractions were determined as described in the Supplemental Methods.

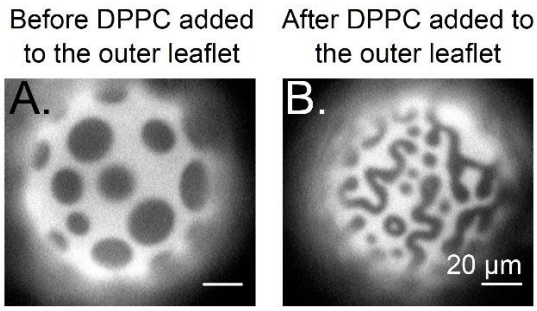

Figure 3.3. Insertion of DPPC into the outer leaflet of a GUV with large domains of coexisting L_o and L_d phases induces the formation of dots and meandering stripes with smaller widths. Micrographs are vesicles of 35/35/30 DiPhyPC/DPPC/cholesterol at room temperature before and after addition of 70 mM DPPC-loaded HPαCD. The miscibility transition temperature of this lipid composition is ~46˚C. Scale bars are 20 µm.

Within 5 min of introduction of the DPPC-loaded HPαCD, vesicle membranes that had previously exhibited L_o-L_d phase separation acquired features with smaller length scales. These features persisted throughout the duration of experiments (≤1 hr). For example, Fig. 3.3 illustrates that round domains in a GUV of 35/35/30 DiPhyPC/DPPC/cholesterol evolve into dots and meandering stripes with widths <10 µm. A similar technique was employed previously by researchers who introduced glycolipid micelles to vesicle solutions and observed stripes nucleating from L_o and L_d domains, followed by scission of the stripes into dots (170).

GUV Temperature

For experiments in which temperature was adjusted, GUV solutions were placed between coverslips, and coverslip edges were sealed with vacuum grease. Heat sink grease (Omega, Stamford, CT) thermally coupled the coverslip assembly to a home-built temperature stage on an upright Y-FL Nikon microscope. An Alpha-Omega (Cumberland, RI) temperature controller drove a thermoelectric heater/cooler. Temperature was sensed by a thermistor probe (0.2˚C accuracy, Sensor Scientific, Fairfield, NJ). Unless otherwise noted, temperature was adjusted stepwise, and thermal equilibrium was reached after each step.

GUV Osmotic Pressure

For experiments in which osmotic pressure was adjusted, GUVs were formed in 300 mM sucrose solutions and diluted in 300 mM glucose solutions. To increase membrane tension (and decrease excess area), water was added to dilute the outside solution to 250 mM glucose. To

decrease membrane tension (and increase excess area), a solution of 1 M glucose was added to increase the concentration of the outside solution to 350 mM glucose. To minimize movement of vesicles, solutions were not stirred. Hence, solution concentrations likely vary through space and time.

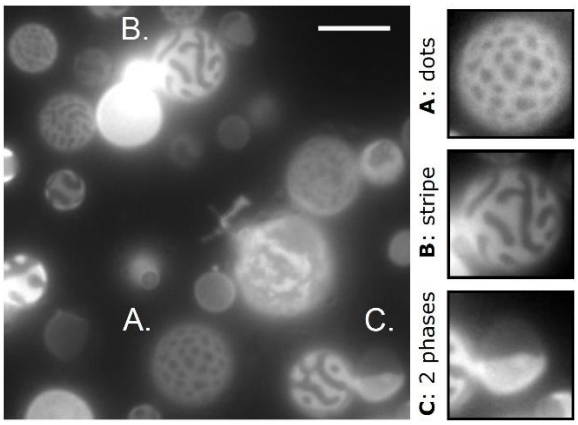

Figure 3.4. A field of GPMVs derived from MDCK cells in an isotonic buffer solution. This micrograph contains examples of dots (panel A), stripes (panel B), and coexisting L_o and L_d phases (panel C). Scale bar is 10 μm.

Cell Culture and GPMV Isolation

Madin Darby canine kidney (MDCK) cells were maintained in Dulbecco's modified Eagle's medium (DMEM) supplemented with 10% fetal calf serum, 2 mM glutamine, 100 units/mL penicillin, and 100 μg/mL streptomycin at 37˚C in humidified CO_2. Before isolation, cell membranes were labeled with 5 μg/mL of the fluorescent disordered phase marker FAST DiO (Life Technologies, Carlsbad, CA) for 10 min on ice. GPMVs were isolated and imaged as previously described (66). Briefly, cells were washed in GPMV buffer (10 mM HEPES, 150 mM NaCl, 2 mM $CaCl_2$, pH 7.4) and then incubated with GPMV buffer supplemented with 25 mM paraformaldehyde and 2 mM dithiothreitol for 1 h at 37˚C. A fraction of GPMVs derived from MDCK cells exhibit stripes and dots without any addition of lipids to the outer leaflet, as shown in Fig. 3.4. A similar diversity of morphologies has been reported in GPMVs derived from zebrafish cells (171).

GPMV Temperature

For experiments in which temperature was adjusted, GPMVs were imaged as previously described in detail (110). Briefly, a small chamber was created using silicon grease between two coverslips. The bottom coverslip was BSA-coated, and 5 μL of GPMV solution were placed into

this chamber and allowed to deposit onto the BSA-coated coverslip. This chamber was then attached to the stage of a Warner (Hamden, CT) temperature regulator and cooled to 8˚C for ~510 min until most vesicles had undergone phase separation. Temperature was then raised in increments and images were collected ~1 min after the desired temperature was reached (unless otherwise noted), in order to allow the sample to reach thermal equilibrium.

GPMV Osmotic Pressure

For experiments in which osmotic pressure was adjusted, a chamber was created by attaching a small, hollow plastic cylinder (specifically, a cloning ring) to a coverslip-bottom cell culture dish (MatTek, Ashland, MA) leaving the top open. 100 µL of GPMV solution was placed into this chamber and GPMVs were allowed to settle to the surface of the coverslip for 20 min at 8˚C, with the temperature controlled as in the previous section. To lower the osmolarity of the exterior solution, cold water was added to the chamber in 5 µL increments. To increase the osmolarity, a solution of 1 M NaCl was added to achieve a final concentration of 300 mM NaCl. GPMVs were imaged after each addition. In order to minimize movement of GPMVs, solutions were not stirred. Hence, solution concentrations likely vary with space and time.

Image Analysis

The method of measuring area fractions, the analysis of 1-dimensional autocorrelation functions (1D $G(\vec{r})$), and the fast Fourier transform of $G(\vec{r})$ to yield the structure function, $S(\vec{k})$ (including Python scripts used to calculate $G(\vec{r})$ and $S(\vec{k})$) appear in the Supplementary Information.

3.3 RESULTS

The Characteristic Length Scale is Inversely Related to Temperature

To put our results in context, we will review a few aspects of phase-separated membranes. As temperature increases in a GUV in which L_o and L_d phases coexist, the ratios of the lipids in the two phases become more similar (169). Consequently, the line tension between the L_o and L_d phases decreases. In other words, the energetic cost of forming an interface between the two phases decreases as temperature approaches the miscibility transition.

Now we consider a vesicle with significant excess area, which means that the vesicle has more membrane than is needed to cover a sphere with the same volume. As shown in Figs. 3.3 and 3.4,

dots and stripes appear in both GUVs exposed to DPPC-loaded cyclodextrin (which inserts DPPC lipids into the outer leaflet) and GPMVs derived from MDCK cells. Figs. 3.5 and 3.6 illustrate that as temperature increases in GUV and GPMV membranes with excess area, large domains transform into smaller domains. When these small domains are stripes, their wavelengths decrease with increasing temperature. In other words, the total length of the interface increases. In Fig. 3.5, the apparent hysteresis of the GUV at 21˚C and 24˚C is a result of rapid temperature cycling. When temperature is held for several minutes, no hysteresis is observed (Fig. 3S1). For a closed vesicle, an increase in temperature is accompanied by an increase in the surface to volume ratio, decreasing membrane tension (172).

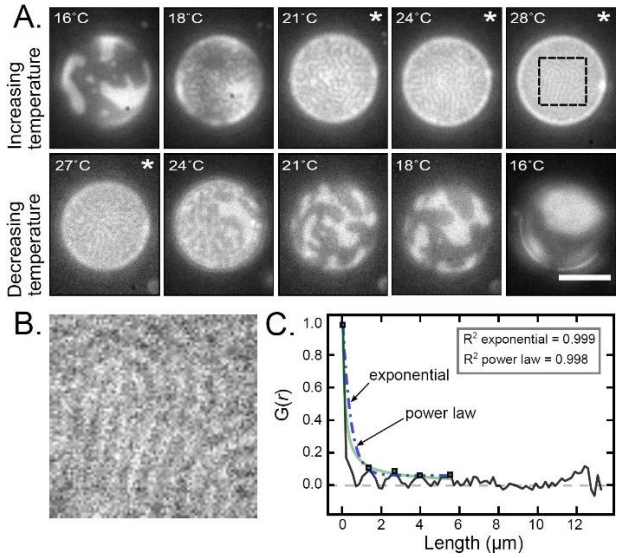

Figure 3.5. The characteristic wavelength of stripes decreases as a function of temperature in GUVs composed of 35/35/30 DiPhyPC/DPPC/cholesterol treated with DPPC-loaded HPαCD. **A.** The same GUV is shown in all panels. The scale bar is 20 μm. **B.** Enlargement of the dashed box at 28˚C in A. **C.** 1D $G(\vec{r})$ of the image in B, performed in the x-direction, perpendicular to the stripes. Five maxima (squares) are fit to an exponential curve (dot-dashed line) and a power law (light line), yielding R^2 coefficients of 0.999 and 0.998, respectively. The camera resolution is 0.17 μm/pixel. Images with asterisks were analyzed by 1D Fourier transforms as in Fig. 3.6 and used in Fig. 3.7.

We quantify the characteristic wavelength of stripes by computing $G(\vec{r})$ and $S(\vec{k})$ of images. The characteristic wavevector (k) of the image appears as a peak in $S(\vec{k})$. For example, the image at 16˚C in Fig. 3.6A yields the $S(\vec{k})$ in Fig. 3.6C, which has a peak corresponding to a characteristic

wavelength of 0.89 ± 0.08 μm. Fig. 3.7A-B show that wavelengths decrease with temperature for both GUVs and GPMVs. Each wavelength corresponds to the summed widths of one dark stripe and one white stripe, where the width of a dark stripe corresponds to wavelength minus the width of the bright stripe. The width of the bright stripe corresponds to the half-width of the first peak in the $G(\vec{r})$. The widths of both the dark and bright stripes decrease with temperature for both GUVs and GPMVs (Fig. 3.7C-D).

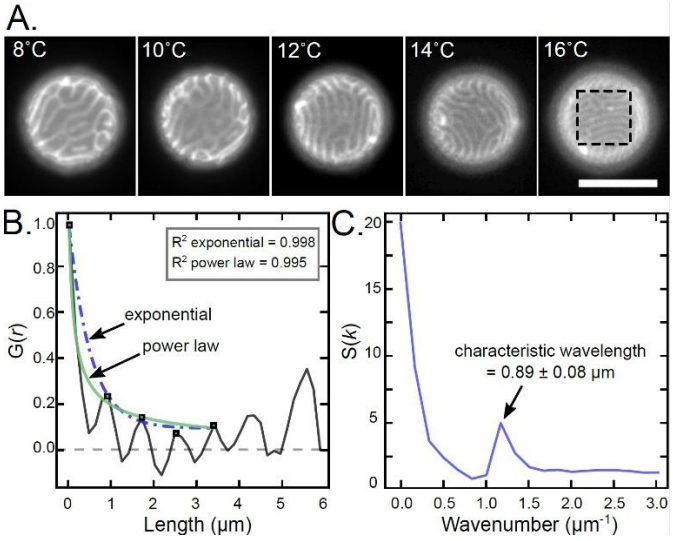

Figure 3.6. The characteristic wavelength of stripes decreases as a function of temperature for GPMVs derived from MDCK cells. **A.** Micrographs of a single GPMV from 8˚C to 16˚C. Scale bar is 10 μm. **B.** 1D $G(\vec{r})$ of the area in the dashed box at 16˚C, performed in the y-direction, perpendicular to the stripes. Five maxima (squares) are fit to an exponential curve and a power law, both yielding R^2 coefficients of 0.998. **C.** $S(\vec{k})$ of the $G(\vec{r})$ in B. The peak in $S(\vec{k})$ corresponds to the characteristic wavelength, which is 0.89 ± 0.08 μm at 16˚C, where the uncertainty is half the length of a pixel. The camera resolution is 0.16 μm/pixel.

Fig. 3.5C and Fig. 3.6B illustrate that when micron-scale domains are wrapped on a sphere with diameter ~10 μm, the distinction between a modulated phase and microemulsion is difficult to assess from a single image. Visually, the small-scale stripes in Fig. 3.5A and 3.6A are more reminiscent of stripes produced by simulations of a modulated phase than of a microemulsion (see Fig. 3.3 of (167)). However, within uncertainty, the autocorrelation functions in Fig. 3.5C and 3.6B are equally well bounded by a function that decays with a power law, as a modulated phase would, and with an exponential, as a microemulsion would. Although it is beyond the scope of this

paper, researchers could plausibly differentiate between modulated phases and microemulsions by collecting a series of images over time of a stationary vesicle exhibiting small domains and then computing the average of the Fourier-transformed images for each wave vector. If the domains were due to a microemulsion, then the averaged Fourier coefficients would approach zero even for those wave vectors at which the structure factor exhibits a peak. If the average of those Fourier coefficients were non-zero, then the domains would be due to a modulated phase (167, 173). Alternatively, researchers who specialize in tethering membranes to flat surfaces may be able to observe small-scale domains if the tethers allow undulations in the membrane. By imaging large areas approaching infinite sheets, stripes could be narrowly defined as uniform lines with a common director, and deviations from this ideal morphology could be characterized by the density of branching points or the persistence length of the director. Independent of whether the vesicles that we investigate exhibit a modulated phase or a microemulsion, we test how the length scales in the system vary with physical parameters to evaluate theoretical predictions associated with mechanisms of the formation of small domains.

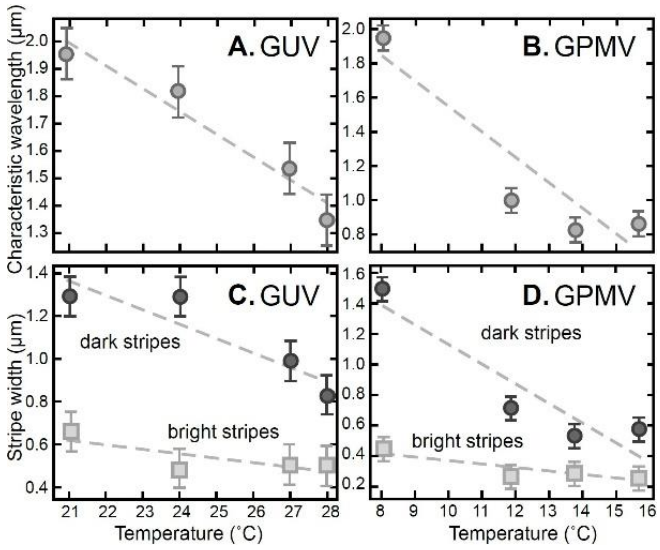

Figure 3.7. Characteristic wavelengths and stripe widths decrease with increasing temperature. Panels A and C correspond to the single GUV in Fig. 3.5 (using only images marked with asterisks). Panels B and D correspond to the single GPMV in Fig. 3.6 (excluding the out-of-focus image at 10˚C). Wavelengths and uncertainties were found as described in Fig. 3.6 and an uncertainty corresponding to half a pixel is shown. The decrease in stripe width is not necessarily expected to be linear with temperature, but if it were then slopes of -0.08 ± 0.01 μm/˚C in Panel A and -0.14 ± 0.18 μm/˚C in Panel B

would emerge. $G(\vec{r})$ and $S\left(\vec{k}\right)$ for each point in A and B are shown in Figs. 3S2 and 3S3, respectively.

The Characteristic Length Scale Increases with Membrane Tension

Small-scale domains appear in vesicle membranes with excess area. Fig. 3S1 shows that increasing membrane excess area in a population of GPMVs through changes in osmotic pressure increases the fraction of GPMVs displaying features with small domains. Here we test how changes in membrane tension affect the characteristic length scale of domains. We increase the osmotic pressure of the solution on the exterior of GUVs and GPMVs (which should decrease membrane tension (174)), and we observe a decrease in the size of domains in both GUVs (Fig. 3.8A) and GPMVs (Fig. 3.9A). Reversing the osmotic pressure difference reverses the effect (Fig. 3.8B and 3.9B). The same trend has been observed via micropipette aspiration of GUVs (personal communication, P. Cicuta and L. Parolini, Univ. of Cambridge, 8 March 2018).

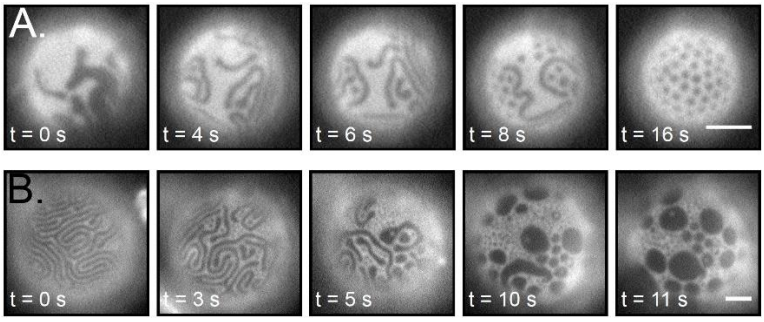

Figure 3.8. Widths of domains increase with membrane tension for GUVs of 35/35/30 DiPhyPC/DPPC/cholesterol treated with DPPC-loaded HPαCD. **A.** Over time, the osmotic pressure of the exterior glucose solution is increased by 50 mM such that the membrane tension presumably decreases. **B.** Over time, the osmotic pressure of the exterior solution is decreased by 50 mM such that the membrane tension presumably increases. Scale bars are 20 μm.

Figs. 3.8A and 3.9A show the evolution of vesicles from L_o and L_d phases to elongated stripes, and then from stripes to dots. The same sequence occurs in vesicles in contact with surfaces (175). Separately, the first image in Fig. 3.8B shows that stripes can appear on surfaces of vesicles that are ≥ 100 μm in diameter; other researchers have suggested that modulated phases appear only in vesicles with a diameter smaller than ~50 μm, albeit in a simulation (176).

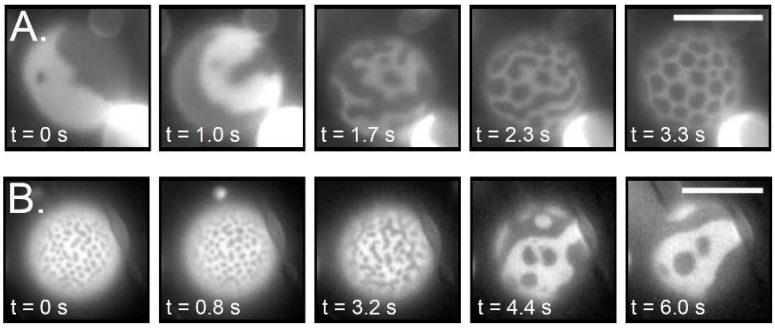

Figure 3.9. Widths of domains increase with membrane tension for GPMVs derived from MDCK cells. **A.** Over time, the osmotic pressure of the exterior solution is increased by raising the concentration of NaCl by 150 mM such that the membrane tension should decrease. **B.** Over time, the osmotic pressure of the exterior solution is decreased by adding water. Scale bars are 10 μm.

Domain Morphology Varies with GUV Composition

The morphology of a modulated phase or microemulsion (*e.g.* the arrangement of dark and bright areas into stripes or dots) is dependent on the membrane's curvature and lipid composition (170, 177, 178). Here, we investigate a series of GUVs that initially exhibit coexisting L_o and L_d phases. Their overall lipid compositions lie at the numbered points on the arrow in Fig. 3.10. To induce the formation of stripes and dots, we introduce additional DPPC molecules to the GUV outer leaflet via cyclodextrin. As described in the methods, treatment of vesicles with DPPC-loaded HPαCD results in a change of area fraction of only 4.3 ± 0.9%, so we expect perturbations in overall lipid composition to be minor.

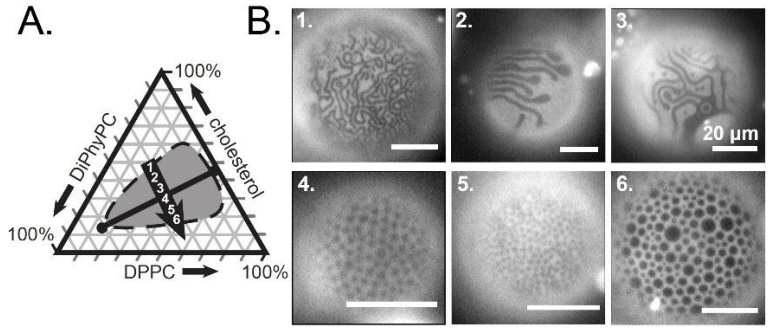

Figure 3.10. The ratio of lipids in DiPhyPC/DPPC/cholesterol vesicles influences the morphology of small-scale membrane domains. **A.** Gibbs phase triangle for DiPhyPC/DPPC/cholesterol vesicles with no excess area. The shaded area corresponds to compositions that exhibit L_o-L_d coexistence at 22˚C, reproduced from (169). The black line connecting the circles denotes a tie-line at 22˚C. **B.** Micrographs of GUVs with initial lipid compositions corresponding to the numbers along the arrow in A. The GUVs were treated with DPPC-loaded HPαCD. The resulting morphologies include stripes (at compositions 1, 2, and 3) and dots (4, 5, and 6). Scale bars are 20 μm.

The arrow in Fig. 3.10 is roughly perpendicular to the tie-line that passes through 40% DiPhyPC, 40% DPPC, and 30% cholesterol at 22˚C (169). The length of a tie-line reflects the difference in compositions of the L_o and L_d phases within a membrane. When a vesicle's overall lipid composition falls on a short tie-line, differences in the physical properties of the L_d and L_o phases (*e.g.* the bending rigidities and the thicknesses) are minor, and the line tension between the L_o and L_d phases is small (51, 63, 114). For example, in Fig. 3.10A, point 1 lies near a miscibility critical point. Vesicles made from the lipid composition at point 1 demix along a short tie-line into L_o and L_d phases of similar compositions. When DPPC is inserted into the outer leaflet of these vesicles, stripes appear (Fig. 3.10B). On the other hand, when a vesicle's overall lipid composition falls on a long tie-line, differences in the lipid compositions and physical properties of the L_o and L_d phases become significant and the line tension is large. Examples appear at points 4, 5, and 6 in Fig. 3.10A. When DPPC is inserted into the outer leaflet of these vesicles, dots appear (Fig. 3.10B). In our experiments, we achieve low line tension between L_o and L_d phases by adjusting the ratio of the three membrane components; other researchers have achieved this effect by gradually replacing one of the three components with a fourth component (177, 179–181).

If we instead produce a series of initial GUVs with lipid compositions that lie along a single tie-line (rather than perpendicular to it), then we expect the compositions of the L_d and L_o phases to remain constant and the area fraction of the phases to vary, assuming that area fractions are approximately linearly related to mole fractions. For example, as the overall lipid composition changes from points 1 through 4 in Fig. 3.11A, the membrane's area fraction of the dark, L_o phase should linearly increase. When DPPC is inserted into the outer leaflet of this series of vesicles, small dots and stripes appear. In this new morphology, the fraction of the membrane area that appears dark still increases monotonically across the series of GUVs (Fig. 3.11B, C).

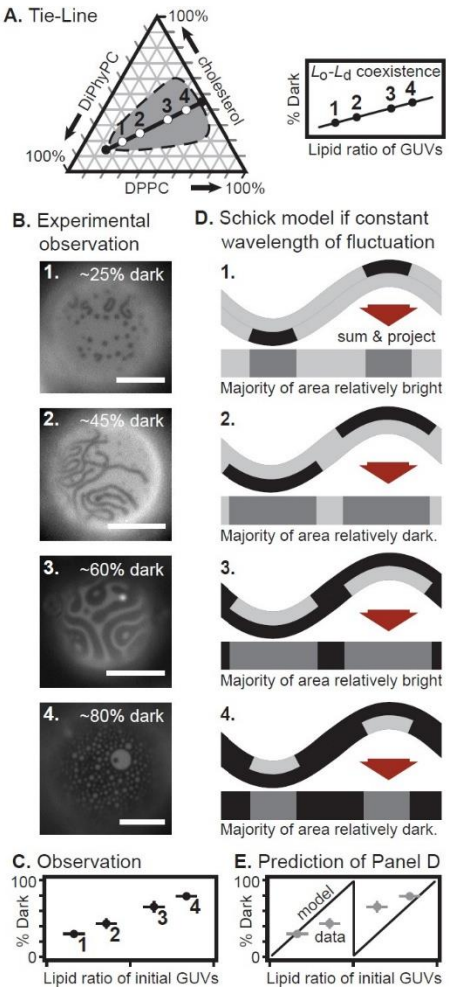

Figure 3.11. A. Gibbs phase triangle for DiPhyPC/DPPC/cholesterol vesicles without excess area. The shaded area highlights lipid ratios that exhibit L_o-L_d coexistence at 22˚C (169). The black line connecting the circles denotes a tie-line at 22˚C (169). **B**. GUVs with L_o and L_d phases were made from the four lipid ratios along the tie-line in Panel A. After the GUVs were treated with DPPC-loaded HPαCD to have excess area, the GUVs exhibited small dots and stripes, as shown in the micrographs. Scale bars are 20 μm. The area fraction of dark membrane increases monotonically for the four vesicles in the micrographs. **C.** Likewise, the area fraction of dark membrane increases monotonically for a population of vesicles (data from Fig. 3S4). The lipid ratio on the *x*-axis is the fractional length along a tie-line. The tie-line and its uncertainty are described in (24). **D.** If a constant wavelength of membrane fluctuation is assumed within the Schick model (165), then the area fraction of membrane that appears dark would be expected to vary with the sawtooth pattern in Panel E.

3.4 MECHANISMS

Our results create an opportunity to evaluate proposed mechanisms of how stable, small (albeit micrometer-scale) domains arise in vesicle membranes. These mechanisms were recently reviewed by Schmid (161). Several mechanisms do not apply to our experiments. For example, our GUV system is not consistently close to a miscibility critical point (63, 162, 169). Similarly, our GUVs

lack hybrid lipids that might act as lineactants (182, 183), and small length scales arise equally in vesicles with and without hybrid lipids (180). Because GUVs are synthetic vesicles rather than plasma membranes of living cells, our systems are not subject to membrane recycling (184, 185), cytoskeletal coupling (61, 163, 186, 187), or mismatch between monolayer curvature and the curvature imposed by a rigid cell wall (188). Moreover, because our vesicles initially exhibit large-scale coexisting L_o and L_d phases before we introduce DPPC to the outer leaflet, the small-scale features we observe are not due to trapped coarsening (160, 172, 189–191), which is depicted in Fig. 3.1E-G. They are also not due to the kinetic effect of viscous fingering (34).

Remaining proposed mechanisms include coupling of local lipid composition to either monolayer or bilayer spontaneous curvature (165–167, 170, 178, 191–200), and balancing the energetic cost of forming an interface with a repulsion term arising from lipid dipoles (180, 198, 199). These mechanisms are not mutually exclusive, and some predict similar behavior. To our knowledge, all of these mechanisms predict that an increase in temperature results in a decrease in the characteristic size of domains, as we observe in Figs. 3.5A and 3.6A. A similar qualitative result has been reported for vesicles near their mixing temperature (172). In order to evaluate the mechanisms, we discuss membrane asymmetry, tension, and lipid dipoles in the three sections below.

Evaluation of Membrane Asymmetry

One class of theories and simulations posits that small-scale features arise in membranes when the local lipid composition couples to the local monolayer or bilayer curvature (165–167, 170, 178, 191–200). An experimental basis for these theories lies in the observation that monolayer spontaneous curvatures of different lipids vary widely (201, 202). Recent theory by Schick and coworkers (165–167, 192) proposes that lipid composition couples to membrane height fluctuations. This theory predicts that over a range of temperatures and tensions, lipid compositions spatially vary as in a microemulsion. Characteristic sizes of domains are predicted to be $\geq$ 100 nm (166), and the largest features are expected when the differences in spontaneous curvatures of all the lipids is small (165), as in our system in which all phospholipids are PC lipids. Schick notes that in membranes that contain a mixture of lipids with a wide range of spontaneous curvatures, such as "membranes with ternary mixtures of cholesterol, PC, and PE … one would expect … the characteristic wavelengths to be appreciably smaller" (165). Membranes of GPMVs satisfy this

criterion because they contain a significant fraction of lipids that produce high monolayer curvatures (e.g. lipids with phosphatidylethanolamine headgroups and/or polyunsaturated tails, (66)). However, micron-scale domains are readily observable in both types of membranes that we use: GUVs with PC lipids and GPMVs with a wide complement of lipids.

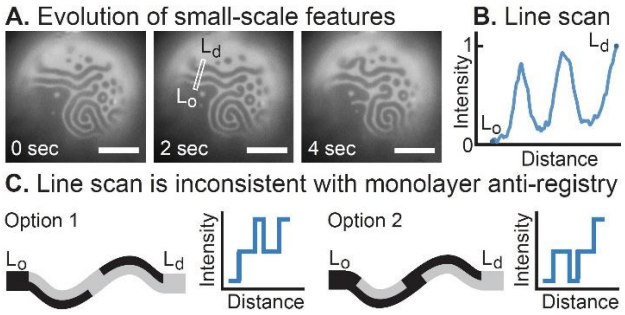

Figure 3.12. Fluorescence levels in GUVs with excess area imply that stripe and dot domains are registered across both monolayer leaflets of the bilayer. As DPPC is delivered to the surface of a vesicle composed of 35:35:30 DiPhyPC/DPPC/cholesterol, stripes and dots appear at the boundary of the L_o and L_d phases and evolve through time. Scale bars are 20 μm. **B.** A line scan (10 pixels wide) across the boundary yields only two fluorescence levels. To preserve image fidelity, no correction was made for the slight brightness gradient across the image, which likely arises from objects out of the plane of focus. **C.** In contrast, anti-registration of domains as in the Schick theory (165) predicts three fluorescence levels, either as in Option 1 or Option 2.

The Schick theory posits that monolayer regions with different spontaneous curvatures will be enriched (or depleted) in lipids with non-cylindrical shapes, (e.g. PE-lipids or lysolipids) such that monolayer domains are anti-registered across the bilayer. For example, a lipid for which the cross-sectional area of the head group is smaller than that of the tails will be enriched within the bright monolayer regions in Fig. 3.12. As a comparison, in flat bilayers containing domains of L_o and L_d phases, the penalty incurred for domains in one leaflet misaligning with domains in the opposite leaflet is large (0.016 k_BT/nm^2) (203).

Two lines of evidence are inconsistent with anti-registration of domains in vesicles of DiphyPC/DPPC/cholesterol with excess area. The first is found in Fig. 3.12A, which shows a time series shortly after HPαCD has inserted DPPC into the outer leaflet of a membrane that had previously demixed into L_o and L_d phases. In the time series, small-scale structure arises from fingering and scission events at the boundary of the L_o and L_d phases, as previously observed (170, 204). Anti-registration of domains would result in the observation of three fluorescence levels

across the boundary (Fig. 3.12C): instead, only two fluorescence levels are experimentally observed (Fig. 12B).

The second line of evidence is in Fig. 3.11. GUVs electroformed with initial compositions at the four numbered points along the tie-line in Fig. 3.11A exhibit L_o and L_d phases. In these 2-phase vesicles, domains in one monolayer of the membrane are in registration with domains of the same phase in the opposing monolayer. Excess area was introduced to these membranes through the addition of DPPC to the outer leaflet by cyclodextrin and fluorescence micrographs were collected. Contrast between domains arises from a dye-labeled lipid that preferentially partitions with one domain type. Standard fluorescence microscopy techniques record fluorescence levels of bilayers (the sum of the monolayers) and excel at distinguishing fractions of areas that appear relatively bright and dark rather than absolute fluorescence levels. Because the Schick model posits that domains are anti-registered, we can test a prediction. If a constant wavelength of membrane fluctuation is assumed within the Schick model, then the area fraction of the bilayer that appears dark (relative to the rest of the membrane) should vary in a sawtooth pattern for vesicles of the four compositions (Fig. 3.11D, E). The experimental data in Fig. 3.11B, C contradict this scenario. Specifically, the area fraction that appears dark increases monotonically rather than in a sawtooth pattern. A related monotonic increase in area fraction of synthetic GUVs is reported by Goh et al. (177).

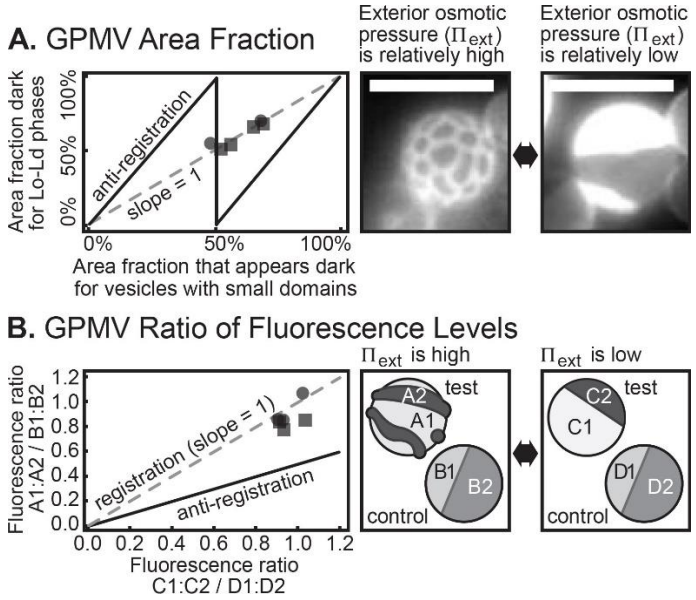

Figure 3.13. To distinguish whether small domains in cell derived GPMV membranes result from registration or antiregistration of monolayer domains, GPMVs were followed through shifts in the osmotic pressure of the exterior solution, which increased (squares) or decreased (circles) membrane

tension. Throughout the transition, **A.** the fractional area that appeared dark was roughly constant (such that the data lie along a line with slope = 1 as in Fig. 3.11E), and **B.** the ratio of fluorescence intensities of bright and dark domains was roughly constant (normalized by a ratiometric measurement to account for photobleaching). Both results are consistent with registration of domains (and inconsistent with anti-registration of domains). Data points in panel A report single measurements for single vesicles. Data points in panel B result intensities averaged over three different 2x2 pixel areas for each bright and dark region. Scale bars are 10 μm.

Two related lines of evidence show that domains are in registration with cell-derived GPMVs with excess area. The first appears in Fig. 3.13A. The osmotic pressure of the exterior solution was shifted to vary membrane tension such that GPMV membranes transitioned from coexisting L_o and L_d phases to small-scale domains (or the reverse). The area fractions of dark membrane regions of six GPMVs were evaluated before and after the transition. All pairs of area fractions lie close to a line with a slope of 1. Because monolayer domains are assumed to be in registration across the membranes of GUVs exhibiting L_o and L_d phases, this result implies that the monolayer domains are also in registration in GPMVs exhibiting small-scale domains. As in Fig. 3.11E, if a constant wavelength of membrane fluctuation is assumed within the Schick model (165), which posits that dark regions in one monolayer leaflet are in anti-registration with dark regions in the opposite leaflet, then the area fraction of membrane that appears dark would be expected to vary with a sawtooth pattern.

The second line of evidence for registration of domains in GPMVs appears in Fig. 3.13B. Within a single field of view, some GPMVs (which have excess area) exhibit stripes or dots, whereas others (which lack significant excess area) contain coexisting Lo and Ld phases. In Fig. 3.13B, these two types of vesicles are named "test" and "control". After application of osmotic pressure to remove excess area, the test vesicles contain coexisting Lo and Ld phases, in which domains in each lipid monolayer are presumed to always be in registration across the membrane. This system can be used to assess whether stripe or dot domains in the test vesicle are in registration. If the ratio of fluorescence levels in the test vesicle to the control vesicle is unchanged by the application of osmotic pressure, then the stripe or dot domains represent regions in which dark domains are in registration across both monolayer leaflets of the membrane. If the ratio differs by a factor of 2, then stripe or dot domains are in antiregistration. A ratiometric measurement eliminates any artifacts due to photobleaching; the measurement leverages the fact that bleaching occurs at the same rate in all vesicles. In total, the data in Fig. 3.13 are consistent with registration and inconsistent with anti-registration.

Evaluation of Membrane Tension

Figs. 3.8 and 3.9 show how the characteristic length scale of domains can be tuned via membrane tension: as membrane tension increases, stripe widths increase (Fig. 3.8B and Fig.3. 9B). The Schick theory considers membrane tension in two regimes. Only one of these regimes is considered in (165) in which "the theory predicts that… if one increases the surface tension of the membrane, making it more taut, then … characteristic length decreases." This is the opposite of what we observe. Equation 6 in (166) gives a fuller story. When membrane tension is initially low, increases in tension decrease the characteristic length, as in the Schick statement above. However, it is reasonable to expect that the membrane tension in our GUVs is initially high because the vesicles appear taut and exhibit coexisting L_o and L_d phases before the addition of DPPC to the outer monolayer. When membrane tension is initially high, the Schick theory predicts that increases in tension increase the characteristic length.

An earlier theory, which should be equivalent to the Schick theory in the limit of a flat membrane, yields similar re-entrant behavior (205)(206). Although Equations 2.8b and 2.12 in (205) predict that an increase in surface tension should result in a decrease in domain size, Fig. 3.6a in (206) shows two trends. For a vesicle with two domains, a configuration with three domains can be reached either by increasing the exterior pressure or by decreasing it, depending on the initial conditions.

A separate theory by Harden et al. considers domains in a modulated phase that arises due to a spontaneous bilayer curvature of the membrane within the domain (196). This scenario is relevant to our system in the plausible case that the DPPC added to the outer monolayer preferentially partitions to one phase, likely the L_o phase. The theory predicts that the characteristic length of dots and stripes increases with membrane tension, assuming that energetic cost of forming an interface is held constant (196). Our results in Figs. 3.8 and 3.9 are consistent with this prediction.

Evaluation of Phase Diagrams

In Fig. 3.12, As DPPC is delivered to the outer membrane of a GUV, small domains appear at the boundary of the L_o and L_d phases. This observation is consistent with the Schick theory for modulated phases and microemulsions (167) and the theory of Harden et al. for modulated phases (196). Specifically, the Schick theory allows for a first-order transition from a 2-phase region of L_o and L_d coexistence to a region of a modulated phase over a wide range of parameters and, when

evaluated in a way that accounts for fluctuations in the system, a first-order transition from a 2-phase region to a microemulsion over a narrower range of parameters, as shown in Fig. 3.2 of (167). Similarly, in the theory of Harden et al., a direct transition is allowed from a 2-phase "flat" region to a modulated phase of stripes or dots if membrane tension is decreased, as occurs when we introduce DPPC molecules to GUV membranes. Knowledge that the transition is first-order does not distinguish between a modulated phase and a microemulsion (207).

Next, we evaluate whether stripes or dots are favored as we vary membrane tension or line tension in the initial GUVs. A decrease in membrane tension in Figs. 3.8A and 3.9A result in a sequence from 2-phases to stripes, and then to dots, as predicted by Harden et al. (196). The topic of line tension is tackled in Fig. 3.10. When DPPC is delivered to a GUV with a lipid composition that lies near the L_o-L_d miscibility critical point, where line tension is low, stripes tend to be observed. When the GUV is initially far from the critical point, where line tension is high, dots are observed. This observation contradicts the prediction of Harden et al., which asserts that as line tension increases, stripes should be favored over dots (196). The prediction holds for a set of GUVs with constant membrane tension and constant area fraction of each phase. Because we apply the same protocol to all GUVs, we assume that membrane tensions are, on average, constant. Similarly, because the path of the arrow in Fig. 3.10 bisects a series of tie-lines, the area fraction of dark and white regions in all GUVs should be, on average, 50:50, although there is a distribution of values within each population of GUVs.

Evaluation of Dipole Repulsion Contribution

The simplest models that produce a discrete length scale in 2-dimensional systems like membranes consider only two energy terms: a local attractive term and a long-range repulsion term (208). The attractive term arises from a cost per unit length of an interface, which favors coalescence of domains and domain budding (209). In monolayers at an air-water interface, the repulsion arises from a difference in dipole density between two lipid phases (197, 210–213). The magnitude of the dipolar term in lipid bilayers is contentious for two reasons. First, electrostatic interactions are diminished by the aqueous solution surrounding a bilayer; nevertheless, small-scale membrane structures are observed in solutions of high ionic strength (204). Second, the dipoles may largely cancel, depending on their location within the bilayer.

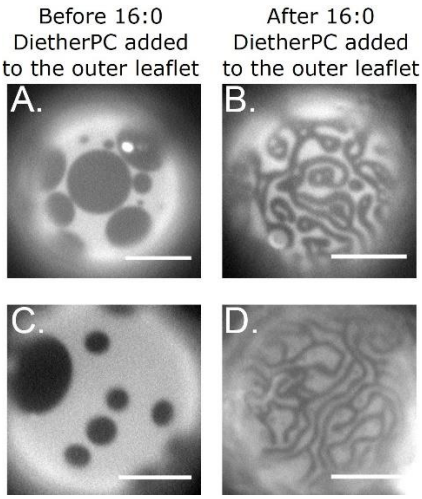

Figure 3.14. Insertion of 16:0 Diether PC into the outer leaflet of a GUV with coexisting L_o and L_d phases induces the formation of meandering stripes with smaller widths. Micrographs are representative images of four vesicles of 35/35/30 4ME 16:0 DietherPC/16:0 DietherPC/cholesterol, two at room temperature before the addition of 70 mM 16:0 DietherPC-loaded HPαCD, and two after the addition. Scale bars are 20 μm.

Several models that describe small-scale features in membranes incorporate a dipolar repulsion term in the free energy (176, 180, 199, 214). The predicted length scales depend on the magnitude of the dipolar term, which in turn depends on the location of dipoles within the bilayer. Here, we directly test an assumption by Usery et al. (180) that the dipolar repulsion term arises from carbonyl groups at the ester-linkage between lipid headgroups and chains. If this assumption were true, then replacing all ester-linked lipids with ether-linked lipids (which lack carbonyl groups) should result in a lack of small-scale patterns on vesicle surfaces. The data in Fig. 3.14 contradict the assumption. In this experiment, DPPC and DiPhyPC were replaced with their ether-linked counterparts to produce vesicles analogous to Fig. 3.3.

3.5 CONCLUSION

Here, we have evaluated how characteristic lengths of small-scale features in membranes of GUVs and GPMVs vary with temperature, tension, and lipid composition. We find that length scales increase as temperature decreases and as tension increases, that area fractions and fluorescence levels imply that domains are registered across both monolayer leaflets, and that stripes are favored for lipid compositions that are expected to have a low energetic cost of forming an interface.

Our results are consistent with most predictions of an early theory on vesicle shape deformations (205)(206) and with the Schick theory of microemulsions (165–167, 192), with the caveat that the initial membrane tension cannot be low. However, the Schick theory posits that monolayer domains are anti-registered across the bilayer, whereas we find evidence that domains are registered, both in model GUVs and in cell-derived GPMVs. Ways in which the Schick theory could become more complete would be to include the effect of fluctuations and the energetic cost of thickness variations that would accompany domain registration (personal communication, M. Schick, University of Washington, 2 May 2018). Similarly, our results are consistent with some predictions of the theory of Harden et al. for modulated phases (196) but do not agree with the prediction that dots should be favored over stripes when the energetic cost of forming an interface is low; we observe the opposite. Our results are consistent with general theories that balance a local attractive term and a long-range repulsion term, with the caveat that the source of the repulsion does not appear to originate with carbonyl group dipoles of ester-linked lipids, as proposed by Usery et al. (180). This leaves the question of how domain repulsion arises, which is challenging to address in lipid bilayers (as opposed to monolayers).

In several theories, the mean bilayer spontaneous curvature is integral to the description of a modulated phase (170, 198, 199, 215). In our GUV experiments, we established a mean bilayer spontaneous curvature by introducing excess lipid to the outer leaflet of vesicles that had previously phase separated into L_o and L_d phases. The addition of outer leaflet lipids is not strictly necessary: other researchers have noted that a bilayer spontaneous curvature could arise from slowly decreasing the temperature of GUVs (personal communication, P. Cicuta and L. Parolini, Univ. of Cambridge, 8 March 2018). Small-scale features have been previously reported in a wide range of membranes, including vacuoles in living yeast cells (74), zebrafish GPMVs (171), and synthetic GUVs, both with (170) and without (177, 179, 180) the explicit addition of lipids to the outer leaflet, illustrating the robustness of the result and its applicability to a broad class of membranes.

3.6 ACKNOWLEDGEMENTS

We thank Lutz Maibaum, Peter Olmsted, Michael Schick, and Tristan Ursell for theoretical insights. Research in the Keller lab is supported by National Science Foundation grant MCB-1402059 to S.L.K. The Levental lab is supported by the Cancer Prevention and Research Institute

of Texas (R1215) and NIH/NIGMS (grants RO1GM114282, RO1GM100078, R01GM124072) and the Volkswagen Foundation (grant 93091). C.E.C. was funded by the National Institutes of General Medical Sciences of the NIH under award T32GM008268.

3.7 SUPPLEMENTARY METHODS, FIGURES, AND CODE

Figure 3S1. Small domains in a GUV do not exhibit hysteresis when temperature is cycled. The same 35/35/30 DiPhyPC/DPPC/cholesterol vesicle treated with DPPC-loaded HPαCD is shown in all panels. The scale bar is 20 μm.

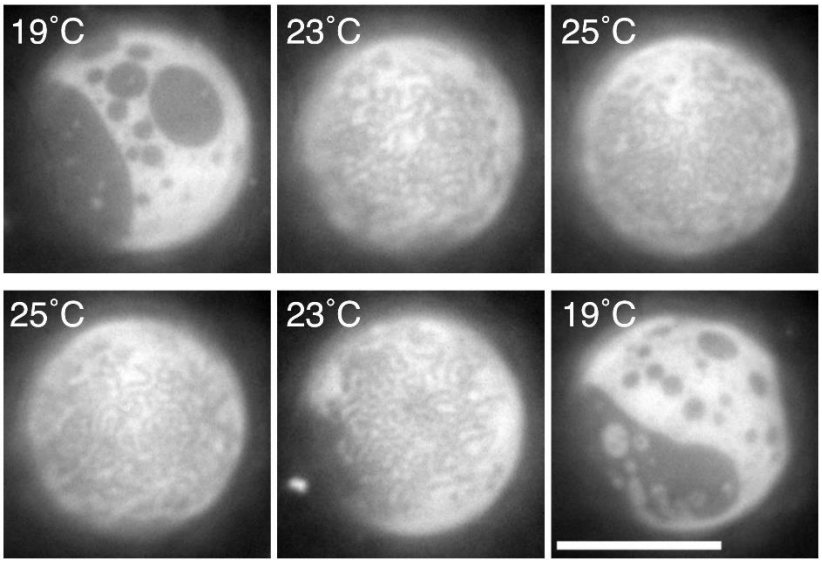

Figure 3S2. The fraction of GPMVs exhibiting small domains increases in hypertonic solution. **A.** A field of GPMVs derived from MDCK cells in an isotonic solution. **B.** The same field of GPMVs after addition of 250 mM NaCl to the outer solution. Images were collected ~1 min after the addition of NaCl solution. Scale bars are 20 μm.

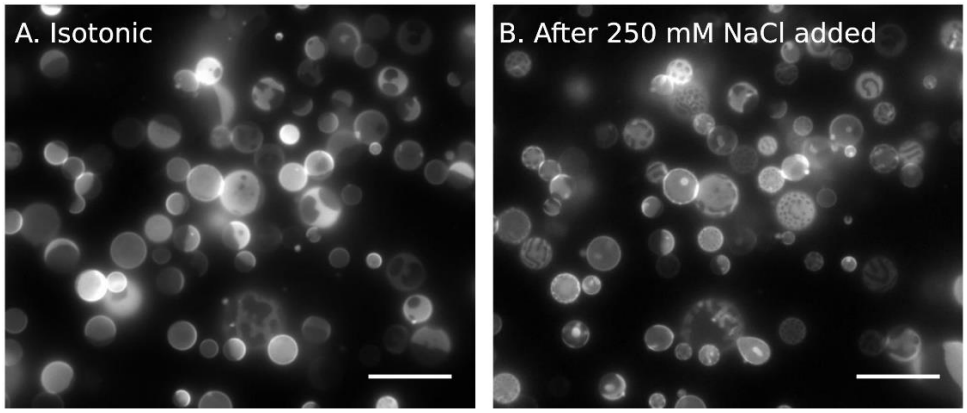

Table 3S1. Lipid compositions of the ratios in Fig. 3.11A-C and Fig. 3S4.

Ratio	DiPhyPC/DPPC/cholesterol
1	60/20/20
2	49/26/25
3	28/40/32
4	15/47/38

Figure 3S3. G(*r*) and S(*k*) for the points in Fig. 3.7A. In panels A-D, the grey curves are fits to a power law and the dot-dashed curves are fits to an exponential.

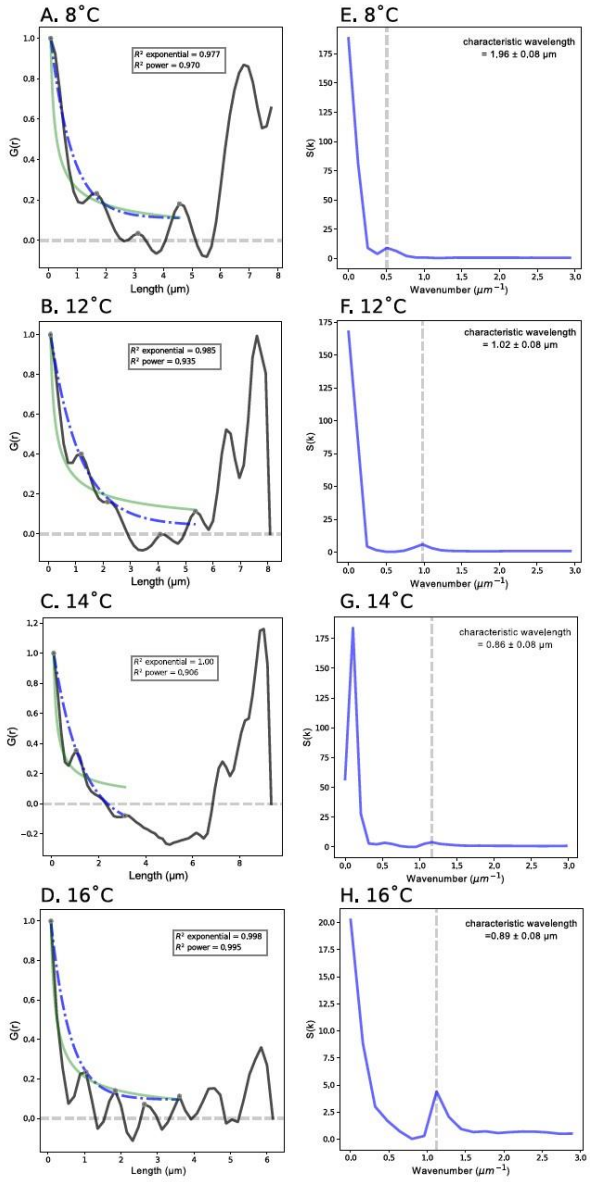

Figure 3S4. G(*r*) and S(*k*) for the points in Fig. 3.7B. In panels A-D, the gray curves are fits to a power law and the dot-dashed curves are fits to an exponential.

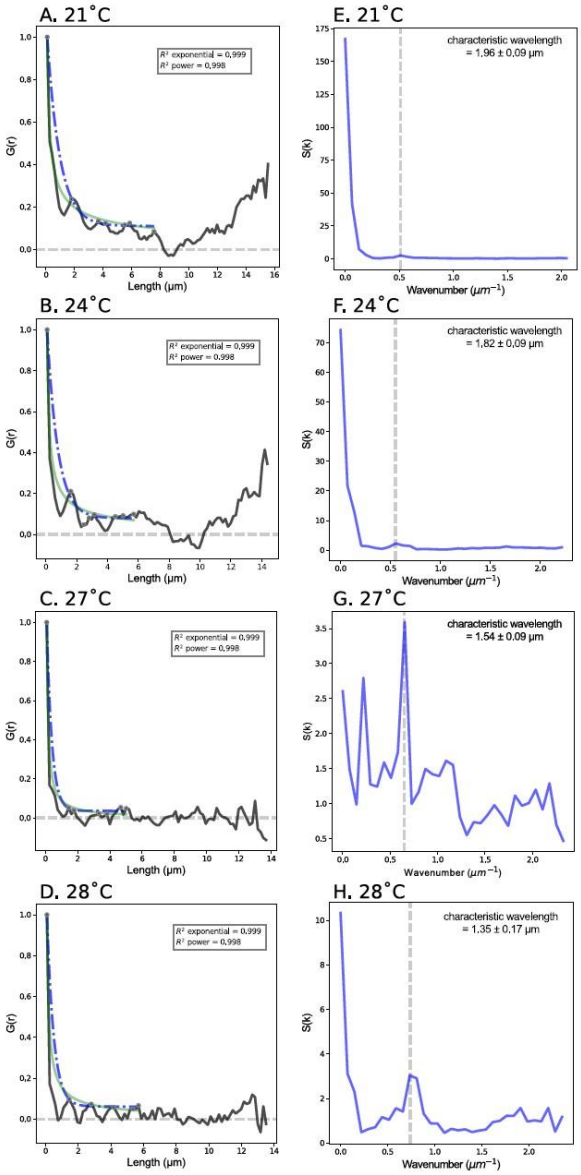

Figure 3S5. The fraction of area that appears dark increases monotonically from lipid ratio 1 to 4 (Fig. 3.11A) for a population of vesicles. The bars represent the average area fraction for each lipid ratio. The numbers of vesicles analyzed for lipid ratios 1-4 were 6, 10, 9, and 6, respectively. The error bars represent the standard deviation.

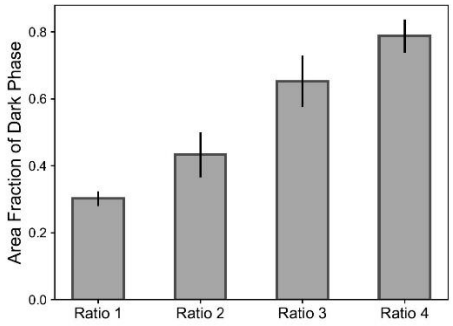

Supplemental Methods

For membranes exhibiting small-scale domains, images of vesicles were collected such that the top, spherical cap of the vesicle lay within the < 5μm depth of field of the microscope objective; the remainder of the vesicle appeared as a bright ring. Square areas were drawn (edge length 15-60 μm) that included only areas in focus. Pixel intensities were thresholded to yield only white and black areas. Images within the 2D squares were projected onto 3D spherical surfaces using MATLAB code by Sarah Veatch (122). The area fraction of the dark regions was the 3D projected area of all black pixels divided by the projected area of all pixels in the image.

For vesicles exhibiting large-scale coexisting L_o-L_d coexistence, images were collected when domains aligned roughly perpendicular to the field of view. Area fractions were then assessed geometrically by evaluating the surface area of spherical caps relative to the surface area of an entire sphere.

Radial Distribution Function and Structure Factor

We define the two-dimensional radial distribution function (RDF) for the image as:

$$g(\boldsymbol{r}) = \frac{\langle \delta\rho(\boldsymbol{r}' + \boldsymbol{r})\delta\rho(\boldsymbol{r}')\rangle}{\langle \delta\rho(\boldsymbol{r})\rangle^2}$$

where $\delta\rho(\boldsymbol{r})$ is the contrast between the two-dimensional image grey value vector and the image average grey value:

$$\delta\rho(\boldsymbol{r}) = \rho(\boldsymbol{r}) - \bar{\rho}$$

and

$$\bar{\rho} = \frac{\int d\boldsymbol{r}\rho(\boldsymbol{r})}{\int d\boldsymbol{r}}$$

To implement the above definition for our pixelated image, we put the grey value vector into matrix representation:

$$\bar{\rho}(\boldsymbol{r}) = \rho_{i,j}$$

where $\boldsymbol{r}$ is the position vector represented by a matrix element as a pixel at the *i*-th row and *j*-th column. The average density can be calculated as:

$$\bar{\rho} = \sum_{i=1}^{m}\sum_{j=1}^{n}\frac{\rho_{i,j}}{mn}$$

and the contrast:

$$\delta\rho(\boldsymbol{r}) = \delta\rho_{i,j} = \rho_{i,j} - \bar{\rho}$$

Thus, the 2-D $g(\boldsymbol{r})$ becomes:

$$g(r) = g(r_{i,j}) = \frac{\left(\sum_{k,l=1}^{m.n}\delta\rho_{k,l}\cdot\delta\rho_{k+i,l+j}\right)}{\sum_{k,l=1}^{m.n}\delta\rho_{k,l}}$$

for all $i \in (1, m)$ and $j \in (1, n)$. The one-dimensional RDF, $g(r)$, is the two-dimensional function that reports modulation in the direction perpendicular to the stripes and is averaged over the direction parallel to the stripes in the image, assuming translational invariance:

$$g(r) = g(r_i) = \sum_{j=1}^{n}\frac{g(r_{i,j})}{n}$$

Due to the finite size of the image, the calculation yields fewer data points as the separation between two correlated pixels increases and approaches the image size, thus the quality of $g(r)$ degrades as r increases.

We can also calculate the one-dimensional structure factor as a Fourier transform of the 1-D $g(r)$ of the image using the generic definition (216):

$$S(k) = 1 + \bar{\rho}\int g_{\alpha,\beta}(r)\, e^{-i\boldsymbol{k}\cdot\boldsymbol{r}} d\boldsymbol{r}$$

The actual Fourier transform is carried out using the fast Fourier transform function provided in the NumPy v 1.14 Python software package (217, 218).

CHAPTER 4: Direct Imaging of Liquid Domains in Membranes by Cryo Electron Tomography

*This chapter was first published in the *PNAS* in 2020. It was written in collaboration with A. Mileant, N. Thakkar, K.K. Lee and S.L. Keller. The full citation can be found at the end of Chapter 1 on pg. 29.

4.1 INTRODUCTION

Seeing is believing, which makes images powerful. Current advances in microscopy have revolutionized our understanding of cellular components, macromolecular assemblies, protein structure, and membrane organization. For example, images of micron-scale synapses in stimulated immune cells have successfully led to the development of quantitative models of membrane protein interactions (219). Similarly, direct imaging has demonstrated that vacuole membranes in living yeast cells phase separate (69, 74) and that model and cell-derived membranes exhibit critical phenomena (63, 162). However, in all of these examples, the membrane features span micrometer length scales. Challenges persist in observing membrane features that are far smaller than the diffraction limit of light, especially in model lipid vesicles under native solution conditions (a phrase that describes vitrified vesicles captured in a fully hydrated state). As a result, a wide range of quantitative questions has remained impossible to answer. For example, if a vesicle membrane contains nanodomains, what are the sizes and distributions of those domains across the vesicle surfaces? Similarly, do submicron domains fit quantitative predictions of modulated phases or of microemulsions (165, 220)?

New approaches are needed in order to overcome current limitations and to complement current methods. Transmission electron microscopy (TEM) can achieve near-atomic resolution, and freeze-fracture TEM has successfully been used to identify coexisting solid and liquid phases in simple, lipid membranes (221–224). However, freeze-fracture is an unwieldy technique that images a metal-shadowed surface of a membrane. To date, freeze-fracture has achieved contrast between liquid domains and the rest of the membrane only when membranes contain large protein complexes (69). A more common way of identifying submicron liquid domains by TEM is gold-labeling of proteins and lipids (e.g. (225, 226)). This method results in over-counting (which can be misinterpreted as self-clustering proteins) if labeling uses both primary and secondary

antibodies or if multiple labels are conjugated to a single antibody (227). Other methods of imaging submicron liquid domains have their own limitations. Atomic force microscopy (AFM) requires deposition of membranes on solid substrates (114, 228–234). Near-field scanning optical microscopy (NSOM) places cantilevers in contact with membranes, which may alter membrane structures (235). Standard super-resolution optical techniques cannot image small enough features, and expansion microscopy relies on cross-linked proteins (236).

Here, we introduce and test two new methods for identifying submicron domains in membranes from direct cryo-electron tomography (cryo-ET) images. To our knowledge, we (and the jointly submitted manuscript by Heberle et al.) are the first to collect cryo-ET images of ternary model membranes under native solution conditions. Of the two new methods, the first is entirely label-free and leverages differences in thicknesses of the domains versus the rest of the membrane (Fig. 4.1). We benchmark this label-free approach against known phase diagrams to demonstrate that it accurately quantifies the area fractions of coexisting liquid-ordered (L_o) and liquid-disordered (L_d) phases in membranes. The second method employs a probe that is fluorescent, electron-dense, and labels the membrane through a single binding site. Our goal is for the probe to enable direct, model-free comparisons for a single vesicle sample analyzed by both fluorescence microscopy and electron microscopy. We test a panel of probes and find that a trimeric mCherry label performs best in this role.

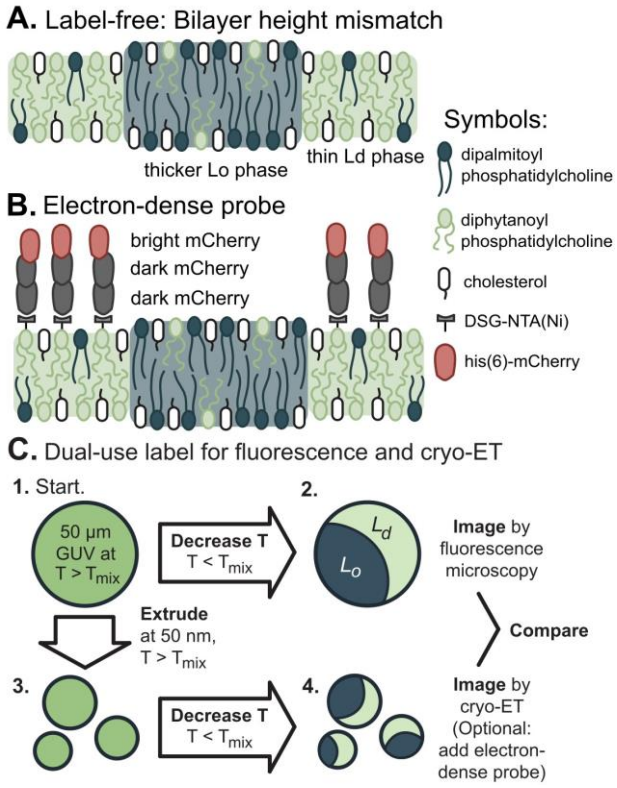

Figure 4.1. Two methods for direct identification of lipid domains in vesicles using cryo-ET. **A.** The label-free method identifies the difference in thickness between the L_o phase and L_d phase. **B.** The labeling method deploys a linear trimer of mCherry that is both fluorescent and electron-dense. A his6-tag on the terminal mCherry protein binds to a nickel-chelated lipid that preferentially partitions to the L_d phase. **C.** The mCherry label enables imaging a single starting solution of giant unilamellar vesicles (GUVs) by both fluorescence microscopy and cryo-ET.

4.3 MATERIALS AND METHODS

Lipids

Phosphocholine (PC) lipids (Avanti Polar Lipids, Alabaster, AL), cholesterol (chol; Sigma Aldrich, St. Louis, MO), and Texas Red dihexadecanoyl-PE (DHPE; Life Technologies, Grand Island, NY) were used as purchased without further purification. Lipid stock solutions in chloroform contained, at minimum, a ternary mixture of diphytanoyl-PC (DiPhyPC; 4 ME 16:0 PC), dipalmitoyl-PC (DPPC; 16:0 PC), and cholesterol. DiPhyPC and DPPC are zwitterionic; cholesterol is uncharged. Features of this ternary mixture is that its miscibility phase diagram has been mapped in detail (27), and the saturated carbon chains of DiPhyPC resist oxidation (63). Stock solutions for cryo-ET experiments with mCherry labels, which were limited to lipid Ratios 2 and 5, also contained 2 mol% of a nickel-chelating lipid of dioleoylglycerosuccinylimino-

diacetic acid (18:1 DGS-NTA(Ni), which replaced 2 mol% DiPhyPC), whereas stocks for fluorescence microscopy controls of GUVs contained 0.8 mol% Texas Red DHPE.

GUV Electroformation

Solutions containing 2 x 10^{-6} moles (~0.76 mg) of lipids were spread evenly on slides coated with indium tin oxide. The slides were placed under vacuum for >30 min to evaporate the chloroform. A capacitor was created by sandwiching 0.3 mm Teflon spaces between two lipid-coated slides. The gap was filled with 335 mM sucrose, and the edges were sealed with vacuum grease. Sucrose has been previously shown to not shift the miscibility transition temperature of electroformed vesicles of DiPhyPC/DPPC/cholesterol (111). GUVs 10-100 μm in diameter were electroformed (47) by application of an AC voltage of 1.5V at 10 Hz across the capacitor for 1 hr at 60°C.

Extrusion

Two solutions were produced: a "thickness mismatch buffer" of 150 mM NaCl and 25 mM HEPES and an "mCherry buffer" of 150 mM NaCl, 25 mM HEPES, and 1 mM tris(2-carboxyethyl)phosphine (TCEP). GUVs were diluted 5-fold in one of the buffers and then concentrated by centrifugation at approximately 10,000 rcf for 10 min. Supernatant was removed. Approximately 10-20 μl of centrifuged and concentrated GUVs were re-diluted in 100 μl of buffer and stored at 60°C for <15 minutes before extrusion in order to ensure that vesicles were well above their mixing temperatures, which ranged from 25˚C to 48˚C. A mini-extruder (Avanti Polar Lipids) with a heat block and two 1 ml gas-tight syringes were maintained in an oven at 75°C before use. Most GUVs were extruded 29 times at 75°C in polycarbonate membranes with 50 nm pores (to be maximize consistency with the jointly-submitted manuscript by Heberle et al., which used 50 nm pores). The only exception was that GUVs of lipid Ratios 4, 5, and 6 for thickness mismatch experiments were extruded through membranes with 100 nm pores. The resulting small vesicles were stored at room temperature for < 1 hr before vitrification.

Despite initial electroformation, extruded vesicles were often not unilamellar. This is surprising because electroformation typically yields unilamellar vesicles. We found that vesicles electroformed and extruded in pure water were always multilamellar, with at least two lamellae

per vesicle. When we increased the ionic strength of the buffer with NaCl, we produced more unilamellar vesicles. Interestingly this result is the opposite to that reported in (40).

Introduction of Trimeric mCherry

Extruded vesicles containing 2 mol% DGS-NTA(Ni) lipids were diluted in "mCherry buffer", lightly vortexed with 2 mM trimeric mCherry (237) and allowed to incubate for >25 min at room temperature. The DSG-NTA(Ni) concentration that we used is an order of magnitude lower than the concentration of DPIDA determined by Scheve et al. to shift a membrane's miscibility transition temperature. Specifically, to induce steric crowding, Scheve et al. used 25 mol% DPIDA, a similar lipid that is similar to DSG-NTA(Ni) and that binds a histidine-tagged protein roughly the same size as mCherry, his-GFP (238). To ensure that the mCherry trimer was not aggregated in solution, we performed dynamic light scattering and found an average particle radius of 3.04 ± 0.3 nm, which is close to the measured radius for GFP (~2 nm; PDB:1GFL), a protein almost identical to mCherry (Fig. 4S9 & Text 4S4). The mCherry trimer presents a larger volume of electron-dense material than a single mCherry molecule. The first mCherry in the trimer is fluorescent, and the last mCherry binds monovalently through a his6-tag to the nickel atom on a DGS-NTA(Ni) lipid (Fig. 4.1). At pH 7.4 (the pH of our “mCherry buffer”), the free carboxyl group on DGS-NTA(Ni) is negatively charged. By cryoET, we did not observe a difference in shape or lamellarity of vesicles with or without DGS-NTA(Ni).

Fluorescence Imaging

Immediately before imaging, GUV solutions were further diluted 10-fold in one of the buffers and sandwiched between two coverslips. The edges of the coverslips were sealed with vacuum grease. Both DGS-NTA(Ni) and Texas Red DHPE preferentially partition to the L_d phase, which appears bright by fluorescence microscopy; the L_o phase appears dark. GUV images were viewed through an air objective on a Nikon Y-FL upright epifluorescence microscope (Nikon, Melville, NY), captured on a Photometrics CoolSnapFX camera (Photometrics, Tucson, AZ), and manipulated using ImageJ (http://imagej.nih.gov/ij/). To preserve the fidelity of the data, image manipulation was limited to adjusting overall brightness or implementing linear (γ=1) contrast enhancements.

Solutions of extruded vesicles were mixed with 6 nm colloidal gold fiducial markers (Aurion, Wageningen, Netherlands) and applied to glow-discharged C-flat holey carbon grids (Electron Microscopy Science, Hatfield, PA) or QUANTIFOIL R 2/2 holey carbon grids (Quantifoil Micro Tools GmbH, Großlöbichau, Germany) and plunge-frozen into liquid ethane using a Vitrobot Mark IV (FEI, Hillsboro, OR) at 100% humidity and temperatures of either 25°C (for height mismatch) or 4°C (for trimeric mCherry).

The thinness of the water film on the grid can perturb larger vesicles by flattening them and by introducing interactions with the air-water interface. We estimated the thickness of the water film as follows. The average thickness of each tomogram is 126.7 nm (499 unbinned pixels). The thinnest region of vitreous ice containing a vesicle is 244 pixels in the reconstructed tomogram. Due to resolution anisotropy of tomographic reconstructions from limited angular sampling, the z-dimension is stretched relative to the x- and y-dimensions. To account for this, the gold fiducial markers were measured perpendicular to the tilt axis and were found to be an average diameter of 28.2 pixels (7.1 nm). Measurement of the gold markers in the z-dimension indicates that the data is elongated by factors ranging from 1.2 – 1.7. Incorporating the most extreme elongation factor, the minimum observed ice thickness is ~36 nm. Given that membrane domains were observed in vesicles over the entire range of sizes, with expected area fractions, this perturbation is minor at the 0° plane where vesicles were evaluated.

Data were collected on a TF20 TEM (FEI, Hillsboro, OR) or a Glacios cryo-TEM (ThermoFisher Scientific, Waltham, MA) operated at 200 kV with a K2 Summit direct electron detector (Gatan, Pleasanton, CA) collecting 200 ms frames in counting mode. Frames were aligned using UCSF MotionCor2 (239) through the Appion web interface (240). Tilt-series were collected on the TF20 TEM with a bidirectional tilt-scheme of -48° to 48° in 3-degree steps at a nominal magnification of 14,500x (pixel size 2.54 Å/pixel) with a total dose of ~100 $e^-/Å^2$. Tilt-series on the Glacios TEM were collected in a dose-symmetric tilt-scheme (241) between -63° and 66° in 3-degree steps at 22,000x (pixel size 1.91 Å/pixel) with a total dose of 74 $e^-/Å^2$.

The IMOD software suite (242, 243) was used to align each tilt series and to generate tomograms with contrast transfer function correction by ctfphaseflip in Etomo with defocus estimates from CTFFIND4 (244). Resulting tomograms were binned by two to a pixel size of 5.04 Å or 3.82 Å and then median filtered. Measurements were confined to central slices of the resulting stack due to resolution anisotropy and missing-wedge effects from limited angular sampling. These slices were projected in the z-direction in groups of 10 (analysis with groups of 20 can be found in Fig. 4S4), for a composite stack 5.04 nm or 3.82 nm thick, and Gaussian filtered ($\sigma = 0.75$) for display in ImageJ (245). To preserve fidelity of image stacks, the only contrast enhancement was linear ($\gamma = 1$). Projection images of vesicles were also collected (SI Appendix, Fig. 4S5), but it was challenging to achieve sufficient contrast between the leaflets of the bilayer and the background to perform thickness measurements.

Analysis of Thickness Mismatches

Cryo-electron tomograms were analyzed to yield the fraction of bilayer corresponding to the L_o and L_d phases. A detailed schematic of the analysis process can be found in Fig. 4S1. We cropped fields of tomograms to retain only the areas in which the membrane was resolvable in the central tomographic slice as two bands of lipid headgroups with high electron density (Fig. 4.2C). In some cases, different lipids may give rise to different apparent electron densities due to the mass and charge of their headgroups. In Fig. 4.2C and Fig. 4.4, there is no clear evidence of two distinguishable electron densities within the bilayer regions that can be resolved as two distinct leaflets. In theory, all vesicles are spherical (or cylindrical), and the central slices of tomograms always cut perpendicularly through the equator of each vesicle, leading to sharp, distinct electron densities for each leaflet of the membrane. However, if vesicles are not spherical, then a tomogram slice can cut obliquely through part of the membrane, such that the leaflets are not resolvable at that location. An extreme example would be a vesicle in the shape of a right triangle; a thick tomographic slice that cut horizontally through the triangle could potentially resolve some features in the vertical wall of the triangle and not in the hypotenuse.

Images were Canny filtered (246) to detect the inner and outer edges of the bilayer using the original Python program “BilayerHeightMeasurements.py” that the authors have made available by public license at https://github.com/caitlin-cornell23/cryoEMliposomes. The apparent bilayer

thickness was defined to be the minimum distance between each pixel on the inner leaflet and all possible pixels on the outer leaflet; this distance is not necessarily the same as the absolute bilayer thickness. It is not necessary to know the absolute thickness – the analysis identifies a difference in thicknesses between two membrane phases. A rolling average over two distance values was applied to smooth the pixel-to-pixel variation. As our study demonstrates, this method consistently resolves differences in membrane thickness on the order of ~1 nm.

Observed minimum distances, d, in a given sample were assigned to L_o or L_d phases using Bayesian inference. First, 20-30 images per control sample at or near the ends of tie-lines (i.e. Ratios 1, 3, 4, and 6) were used to construct Gaussian kernel density estimates (218) of the probability of observing a particular value of the distance in each membrane phase, $p(d|L_o)$ and $p(d|L_d)$, respectively. Then, for intermediate ratios of lipids (Ratios 2 and 5), the likelihood of observing a particular distance is $p(d) = p(d, L_o) + p(d, L_d)$. Incorporating the fact that the phases are mutually exclusive and defining $p(L_o)$ as a mixing coefficient parameter yields $p(d) = p(L_o)\, p(d|L_o) + [1 - p(L_o)]\, p(d|L_d)$. The fraction of the membrane that corresponds to the L_o phase, $p(L_o)$, was constrained from 0 to 1 with the otherwise uninformative prior of $p(L_o) \sim \mathit{Uniform}(0,1)$. This prior, in combination with the likelihood above, gives the mixing coefficient's posterior distribution, up to a normalization constant that we determined by numerical integration. This Bayesian inference procedure is in the original Python 3.6 program "MixtureModel.py" that the authors have made available through public license at https://github.com/caitlin-cornell23/cryoEMliposomes. The mixture coefficient's posterior distribution is described throughout the text using the mean and two standard deviations.

In Fig. 4.4, domains were mapped onto individual tomograms of Ratio 2 and Ratio 5 vesicles by calculating the probability that each observed distance corresponds to the L_o phase. More specifically, we used Bayes' theorem to calculate

$$p(L_o|d) = \frac{p(d|L_o)\, p(L_o)}{p(L_o)p(d|L_o) + [1 - p(L_o)]p(d|L_d)}$$

where probabilities on the right-hand side come from the calculation described above and $p(L_o)$ is approximated by its posterior mean. This procedure is implemented in the original Python 3.6

program “ColorMapMask_V2.py” that the authors have made available through public license at https://github.com/caitlin-cornell23/cryoEMliposomes.

4.3 RESULTS

Figure 4.1 summarizes the two methods we developed for identifying coexisting liquid disordered (L_d) and liquid ordered (L_o) phases in vesicles by cryo-ET (Fig. 4.1). The first method exploits the difference in bilayer thicknesses of the phases. The second method employs a label that preferentially partitions to the L_d phase. We tested these methods on systems that represent the broad class of membranes known to separate into macroscopic L_d and L_o phases in GUVs. Specifically, we imaged uncharged membranes composed of ternary mixtures, consisting of a lipid with a low melting temperature (diphytanoyl-phosphocholine, DiPhyPC)), a lipid with a high melting temperature (dipalmitoyl-phosphocholine, DPPC), and a sterol (cholesterol) (27). Cryo-ET resolves submicron features of intact vesicles in aqueous environments. Therefore, to our knowledge, we (and the jointly submitted manuscript by Heberle et al.) are the first to image submicron domains in membranes with coexisting liquid phases under native solvent conditions.

To maximize differences between the L_d and L_o phases so they are distinguishable, we mixed the lipids in ratios that fall along an unusually long tie-line (Fig. 4.2A and Table 4.1) (27). The endpoints of tie-lines represent the lipid compositions of the two phases. As a result, when we use cryo-ET to image submicron vesicles, we expect to observe L_o domains that are significantly (~1 nm) thicker than membranes of the surrounding L_d phase (233). The same concept applies when we use fluorescence microscopy to image GUVs labeled with Texas Red DHPE; L_o domains are significantly darker than the surrounding L_d phase (Fig. 4.2B and (27)).

	mole % DiPhyPC	mole % DPPC	mole % Chol	mole % L_o phase
Ratio 1	68	17	15	0%
Ratio 2	35	35	30	50%
Ratio 3	6	52	42	100%
Ratio 4	66	21	13	10%
Ratio 5	48	32	20	20%
Ratio 6	5	58	37	90%

Table 4.1: Vesicles were produced from six lipid ratios. Ratios 1, 2, and 3 fall on a tie-line measured at 22°C from (27). Ratios 4, 5, and 6 fall on a parallel line. DGS-NTA(Ni) lipids were included in each mixture only when trimeric mCherry probes were used and only in Ratios 2 and 5, replacing,

2 mol% of DiPhyPC. Values of the mole % of all lipids that are expected to be in the L_o phase are derived from two methods: fluorescence microscopy of GUVs and nuclear magnetic resonance (NMR) of multilamellar vesicles (27). Uncertainties in the mole % of L_o phase are ± 6%, propagated from uncertainties ≤ 3% for each tie-line endpoint, as measured by NMR (27).

One of our central goals was to quantitatively benchmark cryo-ET results for 10-100 nm vesicles against fluorescence microscopy results for vesicles roughly a thousand times larger. To ensure that the lipid composition of vesicles did not vary with their size, we made careful choices about how we produced vesicles. Because different techniques incorporate different ratios of lipids into vesicles (247–249), we produced all vesicles by the same technique: electroformation (Fig. 4.1C). We maintained some of these vesicles as giant unilamellar vesicles (GUVs) to image by fluorescence microscopy, and we extruded others through 50- or 100-nm pores to image by cryo-ET (Fig. 4.2 and SI Appendix, Fig. 4S1, 4S2, 4S5). All vesicle solutions (whether GUVs or extruded vesicles) were diluted into buffer solutions. The dark areas in the representative images of Fig. 4.2B are consistent with the fraction of L_o phase in Table 1, within measurement uncertainty, which strongly suggests that the buffer does not shift the tie-line in Fig. 4.2A.

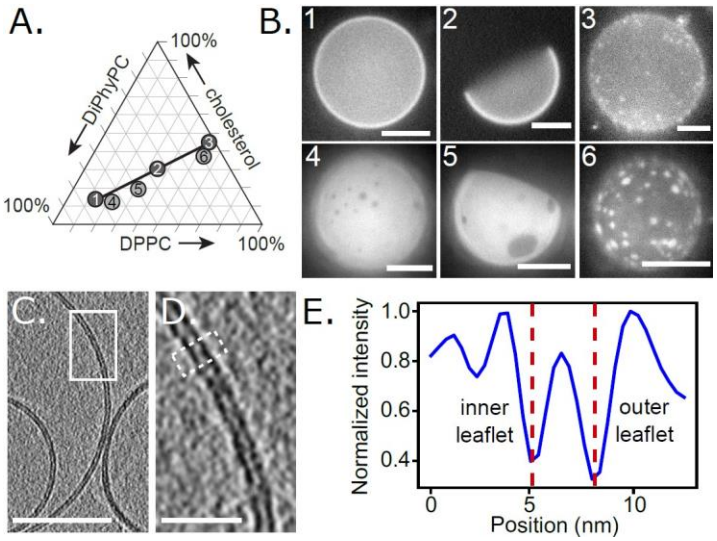

Figure 4.2. The fraction of membrane area in the L_o phase increases monotonically along tie-lines. **A.** All possible ternary mixtures of DiPhyPC, DPPC, and cholesterol fall within the triangle. Ratios 1, 2, and 3 lie on a tie-line at 22°C (27). Ratios 4, 5, and 6 lie on an extrapolated line parallel to the known tie-line. **B.** Representative fluorescence micrographs of GUVs made from Ratios 1-6. The GUVs contain 0.8 mol% of the dye Texas Red DHPE, which preferentially partitions to the L_d phase. To facilitate visualization of area fractions, images were captured shortly after domains nucleated, before all domains completely coalesced. Scale bar is 20 µm. **C.** Slice at 0˚ through a cryoET

tomogram of a field of vesicles made from Ratio 4. Bilayer regions are resolvable as two distinct monolayer leaflets. Scale bar is 50 nm. The field of vesicles containing Panel C is reproduced in Fig. 4S2. **D.** Enlarged image of the area in the white box in Panel C. Scale bar is 10 nm. **E.** A linescan reveals two troughs, which correspond to the clearly resolved dark bands of the inner and outer leaflets of the membrane in Panel D. The linescan was 10 pixels wide and taken across the area in Panel D outlined in the white dashed line.

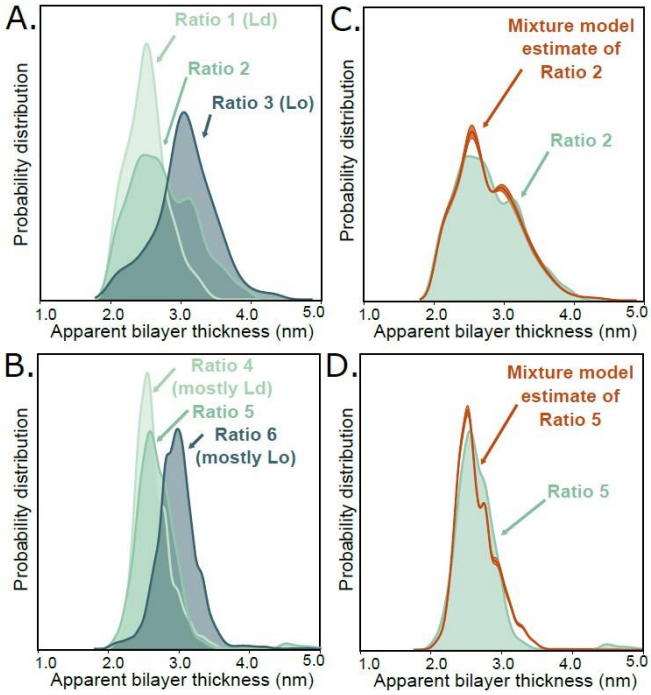

Figure 4.3. Quantitative agreement between ratios of L_o and L_d phases measured by cryo-ET and ratios expected from GUV phase diagrams. **A, B.** Approximately 5000 apparent bilayer thickness values are plotted for each lipid ratio (derived from measurements of the central slice of 20-30 vesicles, representing 10 tomograms of vesicle fields per lipid ratio, from one preparation session and one imaging session for Ratios 1, 2, and 3, and another for Ratios 4, 5, and 6.). For all six ratios, Gaussian kernel density estimates (which plot the probability of measuring each distance, similar to a histogram) were calculated for all three ratios. **C, D.** The ratio of the membrane area in the L_o phase vs. the L_d phase can be estimated directly from images using a mixture of kernel density estimates, calculated using Ratios 1 and 3 for panel C and Ratios 4 and 6 for panel D. For Ratio 2 and Ratio 5, this procedure yields area ratios of 43:57 ± 3 L_d:L_o and 83:17 ± 2 L_d:L_o, respectively.

To identify L_d and L_o domains by the first cryo-ET method, we took a probabilistic approach, separating distributions of bilayer thicknesses into component parts associated with each phase. Critically, this approach sets no thickness cutoff and makes no assumptions about the size, spatial arrangement, or absolute thicknesses of domains. First, we collected cryo-electron tomograms for two types of control vesicles, which we made from lipid ratios that lay at the two ends of a tie-line

(Ratios 1 and 3). To identify the two leaflets of vesicle membranes, we performed a Canny edge filter to the central slice of each tomogram. We established an objective procedure to determine apparent bilayer thicknesses; specifically, we evaluated the minimum distance from every pixel on the inner leaflet of vesicles to all possible pixels on the outer leaflet (Fig. 4.3A and Fig. 4.4). Because this procedure identifies differences in thicknesses rather than absolute thicknesses, it is robust to subtle changes in how different research groups might defocus tomograms, apply contrast transfer functions, or create edge filter algorithms.

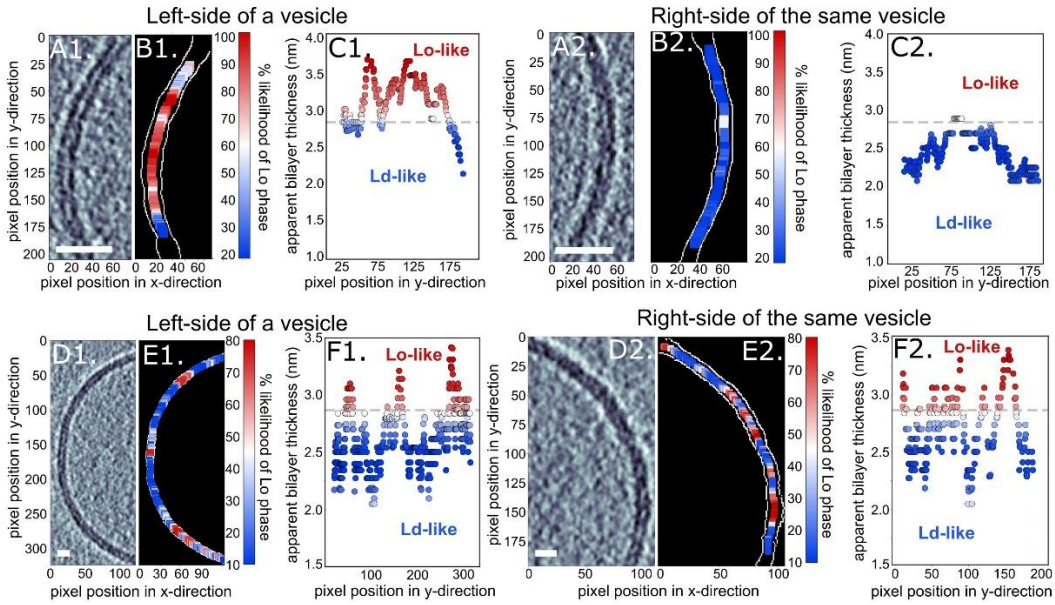

Figure 4.4. Apparent membrane thicknesses identify regions consistent with L_o vs L_d phases. Panels A, B, and C are from a single vesicle made from the lipids in Ratio 2. Similarly, Panels D, E, and F are from a single vesicle of Ratio 4. **A1, A2, D1 & D2.** Label-free tomogram slices showing bilayer regions resolved as two distinct monolayer leaflets. Scale bars are 10 nm. **B1, B2, E1 & E2.** Each slice after detection of the two edges of the bilayer (white pixels). **C1, C2, F1 & F2.** The location of each pixel on the inner edge of the bilayer vs. the minimum distance from that pixel to the outer edge. Colors represent the likelihood (from 0% to 100%) that each distance corresponds to the thicker, L_o phase instead of the thinner, L_d phase. A horizontal dashed line shows the apparent bilayer thickness for which there is a 50% likelihood of being in the L_o phase. More examples of colormap images are found in Fig. 4S3.

For the two control samples, distributions of thicknesses formed two distinguishable peaks corresponding to a thinner L_d membrane (Ratio 1) and a thicker L_o membrane (Ratio 3). We repeated this procedure for vesicles made from Ratio 2, which lies between Ratios 1 and 3. This

intermediate composition falls in a region of the phase diagram in which membranes exhibit coexisting L_d and L_o membrane phases. Because this composition is far from a miscibility critical point, domains of L_d and L_o always coarsen into micron-scale regions in taut GUVs (118). Therefore, the area fraction of L_d and L_o phases that has been previously measured in taut GUVs (27) should be equivalent to the area fraction in submicron domains imaged by cryo-ET.

In Fig. 4.3A, it is clear that cryo-ET of submicron vesicles of Ratio 2 indeed yields a distribution of bilayer thicknesses that corresponds to a mixture of thin and thick membranes. In Fig. 4.4, it is clear that this probe-free method can resolve submicron domains. Domains in Fig. 4.4 are constrained to submicron sizes for the obvious reason that the vesicle themselves are submicron, and perhaps also for the more subtle reason that excess area in nonspherical membranes allows submicron domain configurations (220). Next, we quantitatively evaluated the probability that each thickness corresponds to the L_d versus the L_o phase, using the mixture model described in the methods. This analysis led to the conclusion that vesicles made from Ratio 2 contain domains and that 43 ± 3% of the membrane area is in the L_d phase.

This area fraction of 43 ± 3% L_d phase, measured by cryo-ET in submicron vesicles, is in statistical agreement with values measured in vesicles that are hundreds to thousands of times larger. Quantitative tie-lines have been previously measured by NMR of multilamellar vesicles of the same lipid composition (35/35/30 DiPhyPC/DPPC/cholesterol), and edges of liquid-liquid coexistence regions have been previously measured by fluorescence microscopy of GUVs (27). These previous experiments have firmly established that micron-scale GUVs made from lipids mixed in Ratio 2 contain 50% ± 6 mole % L_d phase, which agrees with our cryo-ET values within the experimental uncertainty of the two methods.

Next, we tuned the lipid composition (and area fraction) of vesicles to show that thickness mismatches quantitatively identify domains in membranes that do not lie exactly on tie-lines, with controls that do not lie exactly at endpoints. For example, Ratios 4, 5, and 6 lie on a line that is parallel and near the tie-line of Ratios 1, 2, and 3. The two new controls (Ratios 4 and 6) are near endpoints, but are not purely L_d or L_o phases. Applying the cryo-ET imaging and analysis above leads to the conclusion that for vesicles made from Ratio 5, 83 ± 2% of the area is L_d phase

(Fig. 4.3D). This value is in excellent agreement with two independent measurements for micron-scale vesicles. A value of 80 ± 6 mole % of L_d phase is expected for intact vesicles (27), and 76 ± 6 area % of L_d phase was determined by atomic force microscopy of GUVs ruptured on mica surfaces (233). In summary, a label-free approach of identifying domains by membrane thicknesses accurately quantifies the amount of L_d and L_o phases.

Switching our focus to identify L_d or L_o domains by the second method, namely by partitioning of a probe, we surveyed labels that are both fluorescent and electron-dense. Our goal was to find a single probe to serve two purposes: to image micron-scale GUVs by fluorescence microscopy and to image submicron domains in ~100 nm vesicles by cryo-ET. This requirement of a dual use imposed several challenging criteria. The probe: **1**: must be highly electron dense so that it is visible by cryo-ET, **2**: must be fluorescent, and **3**: must partition strongly with membrane domains. Moreover, for the probe to be non-perturbing, it must meet additional criteria. **4**: Any fluorescent or electron-dense moiety must be attached to the probe through a single binding site in order to avoid over-counting (227) or crosslinking (250). **5**: The probe must partition strongly to the membrane so that it can be used at low concentrations (136). **6**: The probe must not severely perturb the membrane's shape (as, for example, a BAR domain protein would (251)). **7**: The probe must not aggregate or induce membranes to stick to each other.

We tested a panel of 7 probes (SI Appendix, Table 4S1 and Fig. 4S6) and found that our criteria were best met by an mCherry trimer that binds through a single site to DGS-NTA(Ni) lipids incorporated into electroformed vesicles. Other probes fell short by aggregating (A206K GFP), causing vesicles to aggregate (A206K GFP), and/or producing no discernable contrast between membrane phases (14:0 PE-DTPA(Gd), GM1 lipids with Cholera Toxin B, monomeric mCherry, and 18:1 DGS-NTA(Ni) without mCherry).

In Fig. 4.5, we establish proof of principle that membranes labeled by a single probe can be imaged by both fluorescence microscopy and cryo-ET. To image micron-scale GUVs with our dual-use mCherry trimer, we added the probe directly to GUV solutions. Fluorescence micrographs in Fig. 4.5A-B show that the probe strongly preferentially partitions to the L_d phase. To image smaller vesicles with our dual-use probe, we extruded unlabeled GUVs and then added

mCherry trimer to the resulting solution (Fig. 4.1C). In many cryo-ET tomograms, clusters of mCherry trimers appear in a single layer on membrane surfaces (Fig. 4.5C-F), consistent with the bright labeling of domains we observed in GUVs. Trimers in the clusters are evenly spaced ~3 nm apart (SI Appendix, Fig. 4S7), consistent with monovalent binding to DGS-NTA(Ni) lipids in L_d domains.

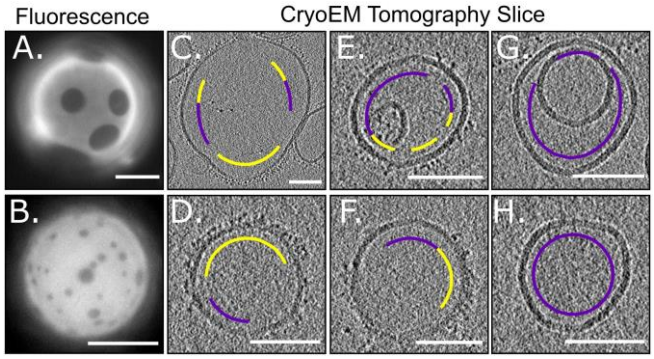

Figure 4.5. Trimeric his6-mCherry as a dual-use probe to image GUVs by fluorescence microscopy and to image submicron vesicles by cryo-ET. Lipids were mixed in Ratios 2 (top row) and 4 (bottom row). **A-B.** Fluorescence micrographs in which trimeric his6-mCherry labels the L_d phase of GUVs. Scale bars are 20 μm. **C-H.** Cryo-ET tomographic central slices of extruded vesicles. On the exterior of vesicles, regions that are densely covered by a brush of trimeric his6-mCherry (yellow arc) are clearly distinguishable from areas that are devoid of his6-mCherry (magenta arc). Scale bars are 100 nm. A larger version of this figure appears in SI Appendix, Fig. 4S7-4S8.

The utility of any probe, including the mCherry trimer, to image domains by cryo-ET or to determine areas of L_o vs. L_d phases is mitigated by four observations, all of which are illustrated in Fig. 4.5. **1**: When vesicles touch, it is unclear if an absence of probe denotes an L_o domain or simply inaccessibility of the probe to the membrane surface. For applications in which the addition of charged lipids is acceptable, their presence can help maintain separation between membranes. **2**: When membrane regions are sparsely labeled, it is unclear whether they should be assigned to the L_o phase or to the L_d phase. **3**: Uniform mixing of the probe is challenging to achieve – some vesicles appear unlabeled (Fig. 4.5G-H). **4**: Two regions of the sample are unusable: the interior vesicles of multilamellar structures, which are inaccessible to the probe, and the air-water interfaces, which trap unbound probes (SI Appendix, Movie 4S1). An advantage of tomography is that the air-water interface can be computationally sliced away.

4.4 DISCUSSION AND CONCLUSION

Here, we leveraged cryo-ET imaging to develop two methods of identifying liquid domains in membranes. Both methods present strengths and limitations.

The main advantage of using membrane thickness to identify liquid domains in unstained vesicles is that the technique is probe-free. The method is non-specific to the type of lipids, as long as there is a measureable thickness mismatch between phases. For example, membranes containing sphingomyelins (and which more closely mimic eukaryotic plasma membranes) have significant thickness mismatches between L_o and L_d phases (229).

In addition, using membrane thickness to identify liquid domains avoids all concern that labels may shift transition temperatures (136) or lead to oxidation (252). Because the analysis is statistical, it works well when distributions are built from a large number of thickness measurements. For example, the distributions of Ratios 1 and 3 in Fig. 4.3A reflect ~5000 points. Conversely, the method will fail if images are not representative. For example, in isolation, the micrograph in Fig. 4.4A2 could be misinterpreted as signifying that all membranes in Ratio 2 are nearly entirely in the L_d phase. Another feature of the technique is that it does not require vesicles to be unilamellar or spherical, so it can be applied to uncharged vesicles extruded through 100 nm pores, which are typically neither unilamellar (40) nor spherical (Fig. 4.2 and Fig. 4.5). Membrane thickness differences can also be used to qualitatively identify domains in membranes derived from cells, as in the companion article by Heberle et al.

However, a quantitative version of this approach is limited to membranes in which the difference in thicknesses between the L_d and L_o phases is resolvable. Luckily, many membranes fulfill this criterion (114, 229–233). Thickness differences can be maximized through savvy choices for the types of lipids in the system and the ratios at which they are mixed. For example, mixing long, saturated lipids with short, unsaturated or methylated lipids typically results in thick L_d phases and thin L_o phases (229–233). Existing phase diagrams and tie-lines, which are reviewed in (20, 26) and discussed further in the Supplementary Information, can be leveraged to quantitatively and accurately measure the relative amounts of L_d and L_o phases.

The main advantage of using an mCherry probe to identify liquid domains is that the label is both fluorescent and electron-dense, enabling similarly prepared vesicles (made from the same batch of lipids, on the same day, using the same methods up to the final extrusion step) to be directly imaged by both fluorescence microscopy and cryo-ET. A potential biological application of dual-use probes is in identifying lipid domains in yeast vacuole membranes. Briefly, vacuole membranes of *S. cerevisiae* demix into coexisting liquid phases after the cells experience nutrient depletion (74). A probe could be used to facilitate correlation of fluorescence images with cryo-EM micrographs in order to identify when liquid domains first appear in the membranes.

Dual-use probes of this type are also necessary for some types of controls. For example, domain sizes in membranes of 13.65/25.35/39/22 DOPC/POPC/DSPC/cholesterol are reported to be different in GUVs and in ~60 nm vesicles (39); a dual-purpose probe could be used to distinguish if the discrepancy is due to different vesicle sizes or merely due to sample-to-sample variations in lipid composition. This point is powerful because lipid ratios in electroformed giant unilamellar vesicles can differ from ratios in hydrated, multilamellar vesicles (the basis of most protocols for imaging submicron domains) (47). An additional advantage of the mCherry probe is that it attached to a lipid through a single binding site, which avoids over-counting.

With all probes, it can be difficult to achieve uniform labeling, especially when vesicles are near an air-water interface or are in contact with each other, as is common when vesicles are composed of only zwitterionic lipids. Likewise, for all probes, it is difficult to determine whether clusters of probes originally nucleated on the membrane or in solution. An advantage of the mCherry probe is that it has been shown to aggregate only at relatively high concentrations (>25 μM (253)). A remaining challenge is that the mCherry probe appears to strongly partition to the air-water interface of cryo-ET grids, and any protein at this location has the potential to denature. Looking to the future, productive approaches could include synthesis of quantum dots that label membranes via a single linker.

In conclusion, we have developed two new methods to identify submicron domains in membranes. One method employs thickness differences, and the other employs dual-use probes. We generate the first direct cryo-ET images of <100 nm liquid domains in protein-free, model

membranes under native solvent conditions. We use these images to quantitatively correlate the area fractions of L_d (and L_o) phase in small vesicles on length scales smaller than 100 nm and in giant vesicles on length scales greater than micrometers.

Our approach complements existing methods for imaging <100 nm liquid domains in membranes, including freeze-fracture TEM (221–224), TEM of gold-labeled membranes (225, 226), AFM (114, 228–233), and NSOM (235). All of these methods suffer from low throughput. Nevertheless, they are valuable because they circumvent limitations of spectroscopic methods (e.g. NMR, electron paramagnetic resonance, and fluorescence resonance energy transfer) and scattering methods (e.g. X-ray and neutron scattering) (39, 128, 254–256). These indirect methods typically measure only average properties of domains and typically generate data that must be analyzed in the context of models. Direct imaging of 10-100 nm liquid domains is valuable because it can potentially allay concerns that submicron domains are artifacts (257). Direct imaging is vital for testing domain nucleation theories (258), evaluating microemulsion mechanisms (165), assessing simulations (259), and probing discrepancies between results in GUV and in ~60 nm vesicles (39).

4.5 ACKNOWLEDGEMENTS

We thank Eva Schmid and Dan Fletcher for their kind gift of trimeric mCherry. We thank Jeanne Stachowiak for her kind gift of monomeric mCherry and A206K GFP, as well as for expert advice on the development of EM-compatible probes. We thank Avanti Polar Lipids for the gift of Aurora-DSG nanoparticles. We thank Ilya Levental and Fred Heberle for outstanding collegiality: they saw us present the results in this manuscript at the 2019 Biophysical Society Meeting, informed us of their complementary project, and simultaneously submitted with us. We hope our feedback influenced their manuscript as positively as their feedback influenced ours. Seed funding for this project was provided by UW Royalty Research Grant A122781 to S.L.K. Lipid research in the Keller lab is supported by National Science Foundation grants MCB-1402059 and MCB-1925731. K.K.L. was supported by NIH grant R01-GM099989. C.E.C. and A.M. were funded by the National Institutes of General Medical Sciences of the National Institutes of Health under award T32GM008268 (to C.E.C.) and T32-GM007750 (to A.M.).

4.6 SUPPLEMENTAL MATERIAL

Text 4S1. Details of using tie-lines to quantify relative amounts of L_d and L_o phases.

When quantifying relative amounts of L_d and L_o phases, microscopists tend to report the area fraction of each phase, whereas spectroscopists tend to report mole fractions. For precise conversions of area fractions into mole fractions, cholesterol's "area condensation" of the surrounding lipids must be considered (26). Unfortunately, area condensation values have been measured for only a small number of binary mixtures of cholesterol and PC-lipids (145, 260–265) , and the area per lipid has been measured in an even smaller number of ternary mixtures (256).

Text 4S2. Details of dynamic light scattering measurement (DLS) of trimeric mCherry in buffer.

Stocks of trimeric mCherry (100 µM) were thawed and diluted into ‘mCherry buffer’ to 10 µM (a protein concentration of approximately 1 mg/ml). 10 µL of this diluted solution was added to a quartz cuvette and placed in a Dynapro dynamic light scattering instrument (Wyatt Technologies, Santa Barbara CA). Measurements were recorded at room temperature and were made in three technical trials of 25 runs each.

TABLE 4S1:
Probes unsuitable for distinguishing Lo and Ld phases by cryo ET

Probe: 18:1 DSG-NTA(Ni) lipid
Composition of vesicle: 30/30/40 mol% diphytanoyl-PC/dipalmitoyl-PC/cholesterol
Method of vesicle formation: Hydration and extrusion
How probe was incorporated: 1 or 5 mole % in stock lipid mixture
Problem(s): There is no significant contrast between the Lo and Ld phases.
Image location: Fig.4 S1, Panel A

Probe: his-tagged A206K GFP bound to DSG-NTA(Ni) lipid
Composition of vesicle: 1/19/40/40 DSG-NTA(Ni)/DiPhyPC/DPPC/cholesterol
Method of vesicle formation: Electroformation and extrusion through 100-nm pores
How probe was incorporated: A206K GFP was added to vesicles after extrusion
Problem(s): Vesicles stick to each other, not all vesicles are labeled, and contrast is poor.
Image location: Fig. 4S1, Panel B

Probe: his-tagged monomeric mCherry
Composition of vesicle: 3/17/40/40 DSG-NTA(Ni)/DiPhyPC/DPPC/cholesterol
Method of vesicle formation: Electroformation and extrusion through 100-nm pores
How probe was incorporated: mCherry was added to vesicles after extrusion
Problem(s): Vesicles are successfully labeled, but contrast is poor.
Image location: Fig. 4S1, Panel C

Probe: Aurora™Gold-DSG Nanoparticles
Composition of vesicle: 5/25/30/40 Aurora™Gold-DSG/DiPhyPC/DPPC/cholesterol
Method of vesicle formation: Electroformation and extrusion or hydration and extrusion
How probe was incorporated: In vesicle formation
Problem(s): The nanoprobes do not remain associated with the membrane after extrusion.
Image location: Fig. 4S1, Panel D

Probe: Nanogold® labeled his-tag mCherry
Composition of vesicle: 1/19/40/40 DSG-NTA(Ni)/DiPhyPC/DPPC/cholesterol
Method of vesicle formation: Electroformation and extrusion
How probe was incorporated: Labeled mCherry with Nanogold, added labeled protein to extruded vesicles
Problem(s): Gold labeling was unsuccessful.

Probe: Gadolinium salt of DSPE (14:0 PE-DTPA(Gd))
Composition of vesicle: 1/29/30/40 14:0 PE-DTPA(Gd)/DiPhyPC/DPPC/cholesterol
Method of vesicle formation: Electroformation and extrusion or hydration and extrusion
How probe was incorporated: During vesicle formation
Problem(s): The salt dissociates in solution
Image location: Fig. 4S1, Panel E

Probe: GM1 and Cholera Toxin B-FITC
Composition of vesicle: 2/28/30/40 GM1/DiPhyPC/DPPC/cholesterol
Method of vesicle formation: Electroformation and extrusion
How probe was incorporated: Cholera Toxin B was added to extruded vesicles
Problem(s): The molar mass of 12 kDa is too small, and contrast was poor.
Image location: Fig. 4S1, Panel F

Figure 4S1. Schematic of post-tomographic reconstruction image processing protocol

Schematic of protocol for image processing of reconstructed tomograms. **A.** (1) Tomograms are collected. (2) A slice of the tomogram at 0° is cropped to exclude bilayer regions that are not in focus. (3) A Canny edge detection algorithm is run to identify edges of the bilayer. (4) A pixel on the inner edge is chosen and the distance from that pixel to every pixel on the outer edge is computed. The minimum distance is recorded as the "apparent bilayer thickness". This process is repeated for every pixel on the inner edge. Apparent bilayer thicknesses are acquired as in Steps 1-4 for ~10-20 cropped images of vesicle membranes composed of each ratio of lipids. (5) A distribution of apparent thicknesses is built for each lipid ratio. The distributions are computed as kernel density estimates, which determine the probability that a certain apparent thickness will be measured for vesicle membranes composed of each ratio. (6) The distributions of Ratio 2 (and Ratio 5) are modeled as linear combinations of the distributions of Ratios 1 and 3 (and of Ratios 4 and 6), respectively. The percent of Ratio 2 and Ratio 5 that correspond to the L_o phase is determined from this linear model. **B.** Each measurement of apparent thickness from an image has a likelihood (from 0% to 100%) that it comes from the L_o distribution (instead of the L_d distribution). Colors are used to map this likelihood directly onto images. The ratio of the membrane area in the L_o phase vs. the L_d phase can be estimated directly from images using a mixture of kernel density estimates, calculated using Ratios 1 and 3 for Ratio 2 and Ratios 4 and 6 for Ratio 5. We measure 57 ± 3% for the L_o phase in Ratio 2, which agrees, in measurement uncertainty, with values measured by ^{2}H-NMR (50 ± 6%) (27) and from AFM (40 ± 15%) (114). For Ratio 5, we measure 17 ± 2% for the L_o phase, which agrees, in measurement uncertainty, with 20 ± 6% from ^{2}H-NMR (27) and 24 ± 6% from AFM (114).

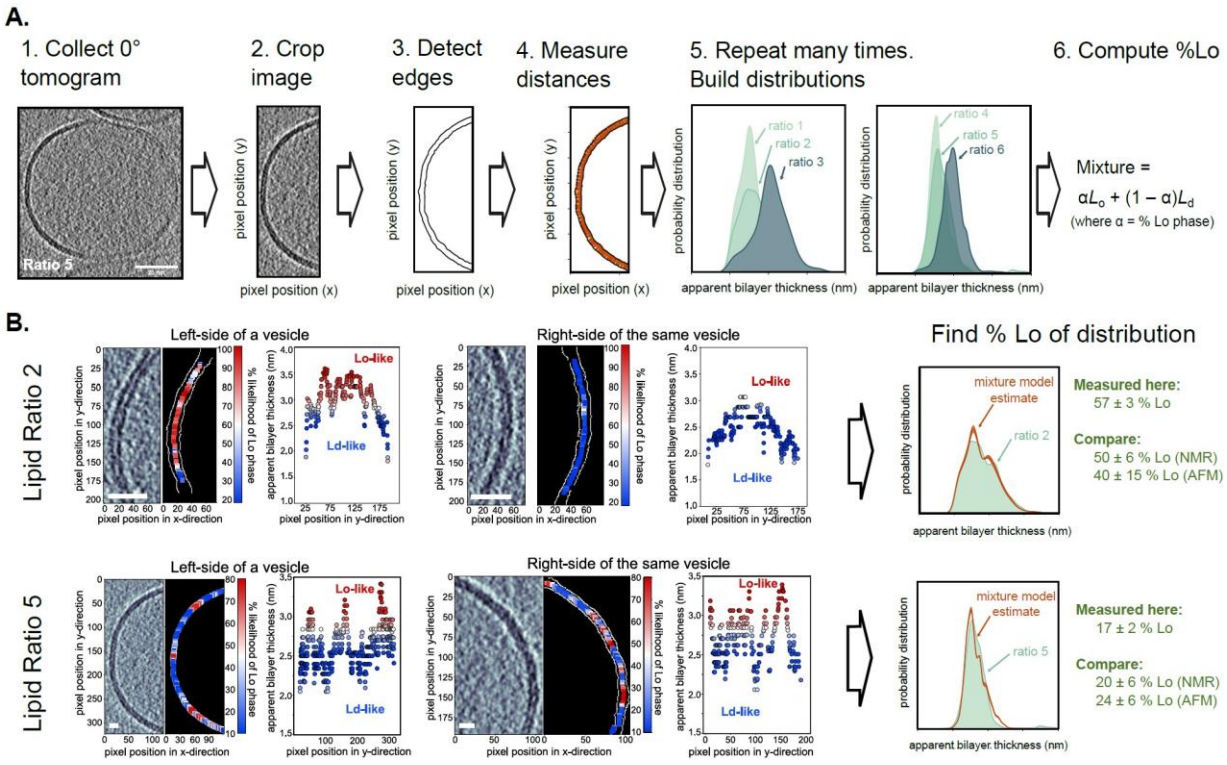

Figure 4S2. Cryo-electron tomograms of vesicles from lipid ratios 1, 2, 3, and 4.
Slices at 0˚ through cryoET tomograms, showing fields of vesicles. As is typical throughout our study, most of the vesicle slices in this figure (including all examples in Panel D) are not circular. **A.** Vesicles composed of lipid Ratio 1. **B.** Vesicles of Ratio 2. **C.** Vesicles of Ratio 3. **D.** Vesicles of Ratio 4. The angular range of the tilt series in panels A-C is ~122˚. Decreased bilayer resolution at positions corresponding to 12 o'clock and 6 o'clock on each vesicle are due to missing-wedge effects (266) from limited angular sampling. Decreasing these angular ranges results in larger areas of low resolution. For example, the tomogram in panel D was collected under conditions of very limited angular range (-24˚ to 40˚) and shows large areas of low resolution (asterisks). For comparison, arrows point to several areas in which the two leaflets of bilayers are well resolved. The dark spot at the bottom of panel D is a gold bead used to align the tomogram. Figure 2C of the main text is a cropped version of panel D in this figure. Scale bars are 50 nm.

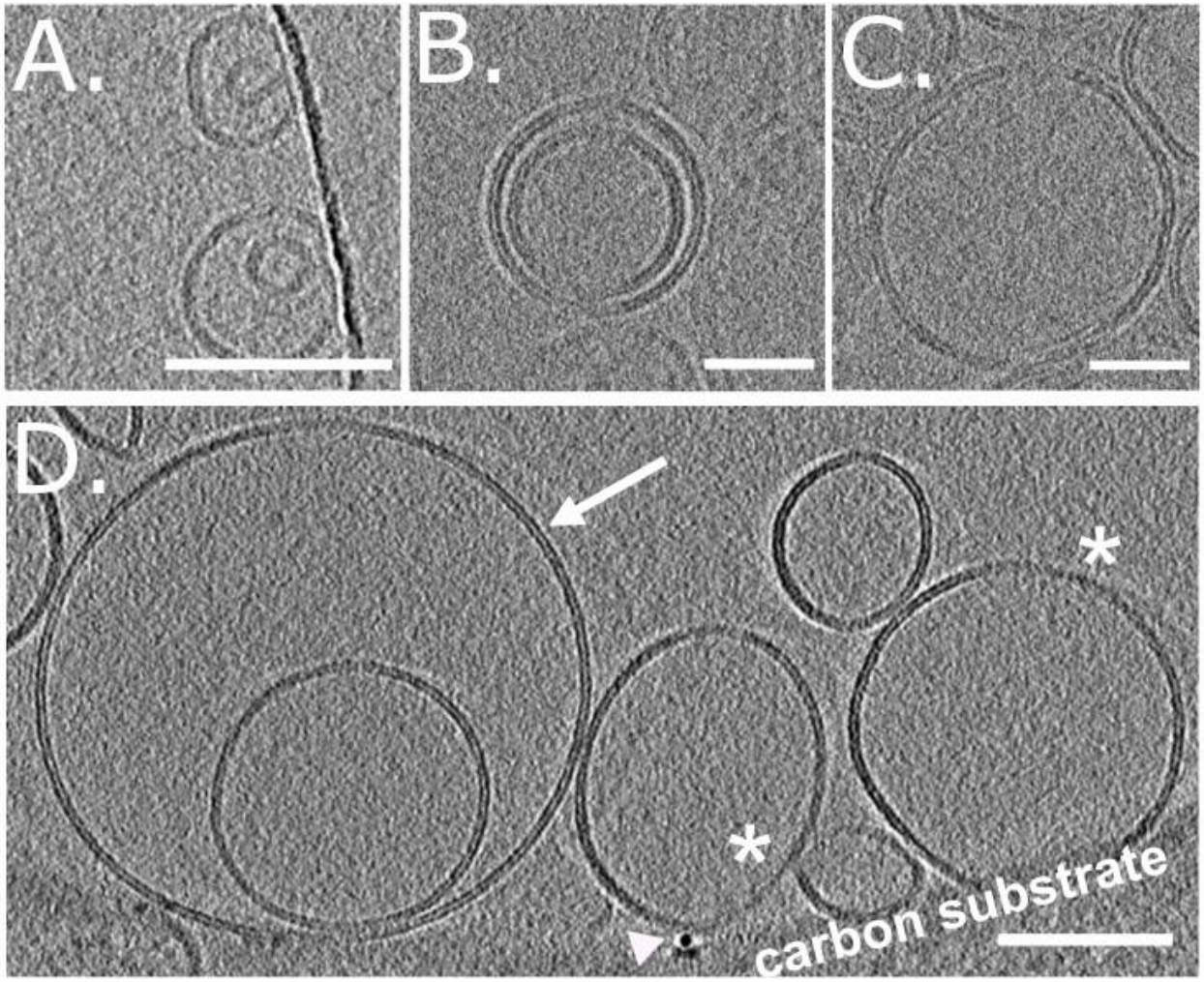

Figure 4S3. Colormaps of probability that each membrane pixel corresponds to the L_o phase Apparent membrane thicknesses identify regions of membranes that are consistent with L_o vs L_d phases, as described in Fig. S1. Panels A, B, and C correspond to four different vesicles composed of lipids in Ratio 2. Panels D, E, and F correspond to four additional vesicles of Ratio 5. **A1-4 and D1-4.** Slices of label-free tomograms at 0° showing bilayer regions resolved as two distinct monolayer leaflets. **B1-4 and E1-4.** Each slice after detection of the two edges of the bilayer (small, white pixels). **C1-4 and F1-4.** For each pixel on the inner edge of the bilayer, its location on the y-axis is plotted against the minimum distance from that pixel to the outer edge (the apparent membrane thickness). Colors represent the likelihood (from 0% to 100%) that each distance corresponds to the thicker, L_o phase instead of the thinner, L_d phase.

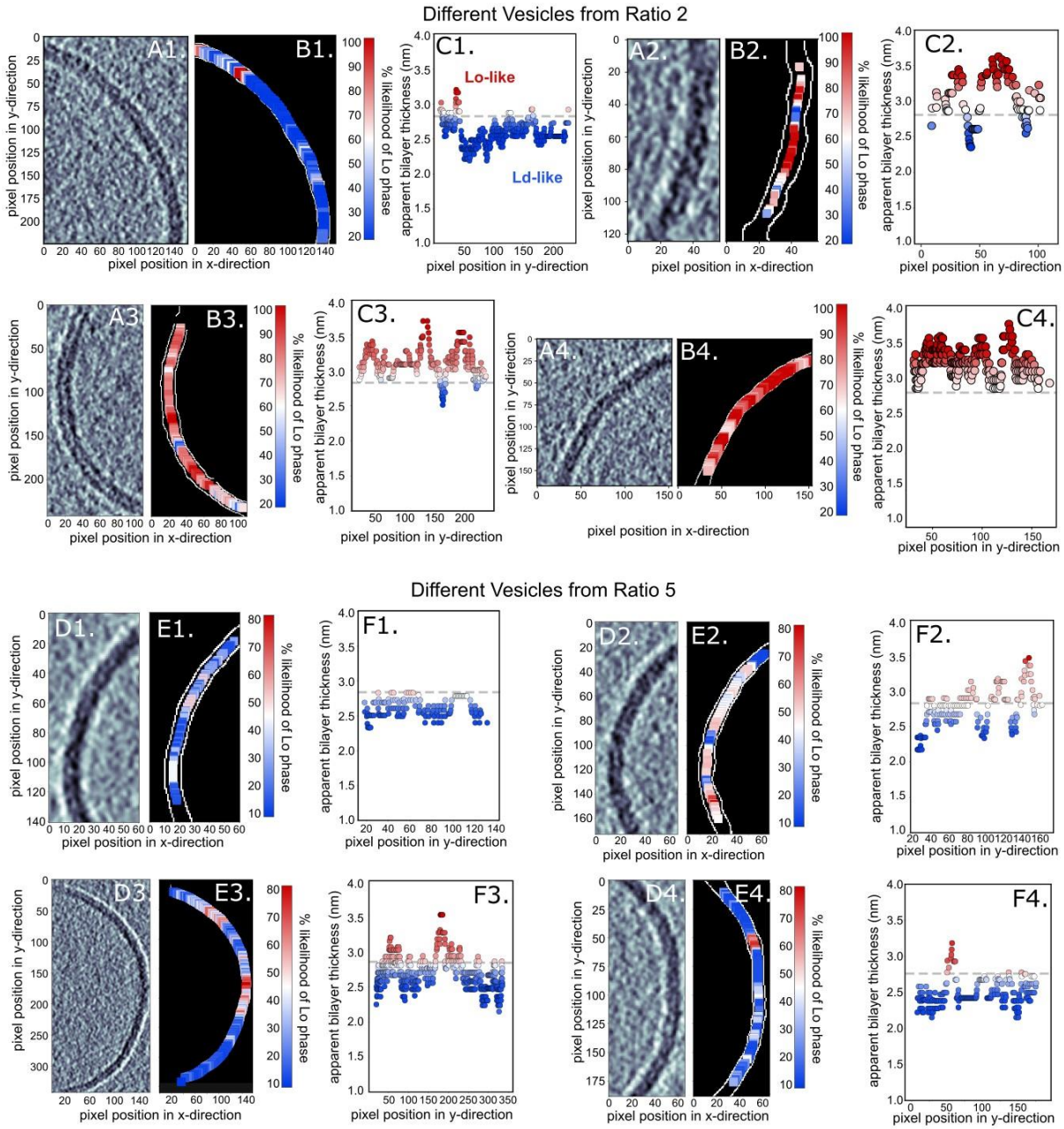

Figure 4S4. Cryo-ET quantitatively identifies L_o membrane, even when thicker slices used.
When thicker tomogram slices are analyzed, good quantitative agreement persists between results from cryo-ET and results from ^{2}H-NMR and AFM. For this figure, tomograms were projected in the z-direction in groups of 20 (rather than in groups of 10 as in all other figures), resulting in thicker tomogram slices. **A.** Approximately 5000 apparent bilayer thickness values are plotted for each lipid ratio (derived from measurements of the central slice of 20-30 vesicles, representing 10 tomograms of vesicle fields per lipid ratio). Gaussian kernel density estimates (which plot the probability of measuring each distance, similar to a histogram) were calculated for all three ratios. **B.** The ratio of the membrane area in the L_o phase vs. the L_d phase can be estimated directly from images using a mixture of kernel density estimates, calculated using Ratios 4 and 6. For Ratio 5 this procedure yields an area ratio of 73:27 ± 8 L_d:L_o. These data agree, within measurement uncertainty, with results from ^{2}H-NMR that vesicles composed of lipid Ratio 5 contain 20 ± 6% L_o phase (27) and with results from AFM of 24 ± 6% L_o phase (114).

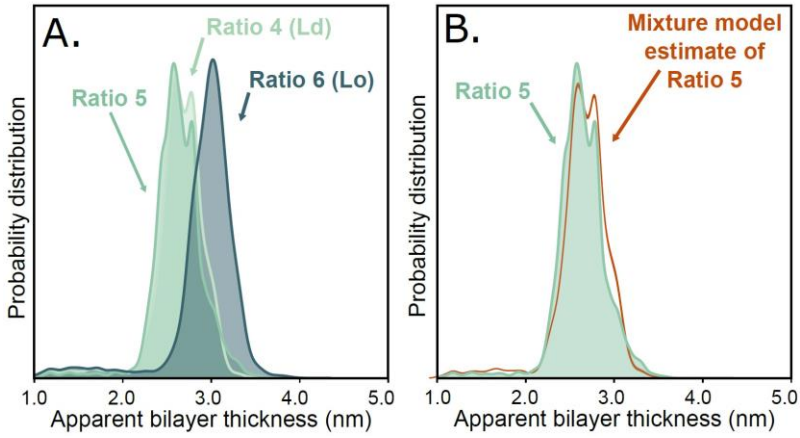

Figure 4S5. CryoEM projection images of Ratios 1, 2, and 3 from Table 1.
Typically, cryoEM projection images did not produce sufficient contrast between the leaflets of the bilayer and the background. The three projection images below show unusual exceptions in which both leaflets of bilayer membranes are resolvable. Dark spots in panels A and C are gold beads. Mottled, dark grey regions at the upper-left corner of panel A and the lower-right corner of panel B are the carbon substrate. Scale bars are 100 nm.

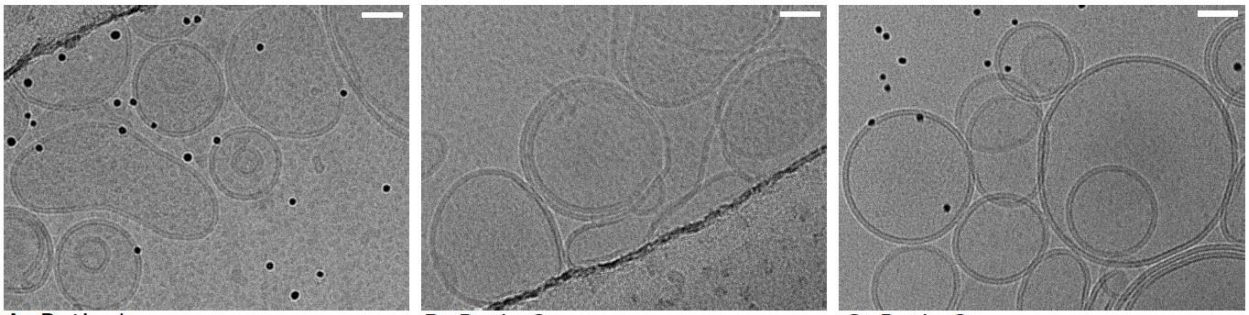

Figure 4S6. CryoEM tomograms and projection images of probes in Table S1.
Images in A, B, and D-F are typical representative examples, and the image in C is a "best case" example. Dark spots in panel D are gold beads that are used to align tomograms. Dark grey regions in the upper-left corners of panels D-F are the carbon substrate. Scale bars are 100 nm.

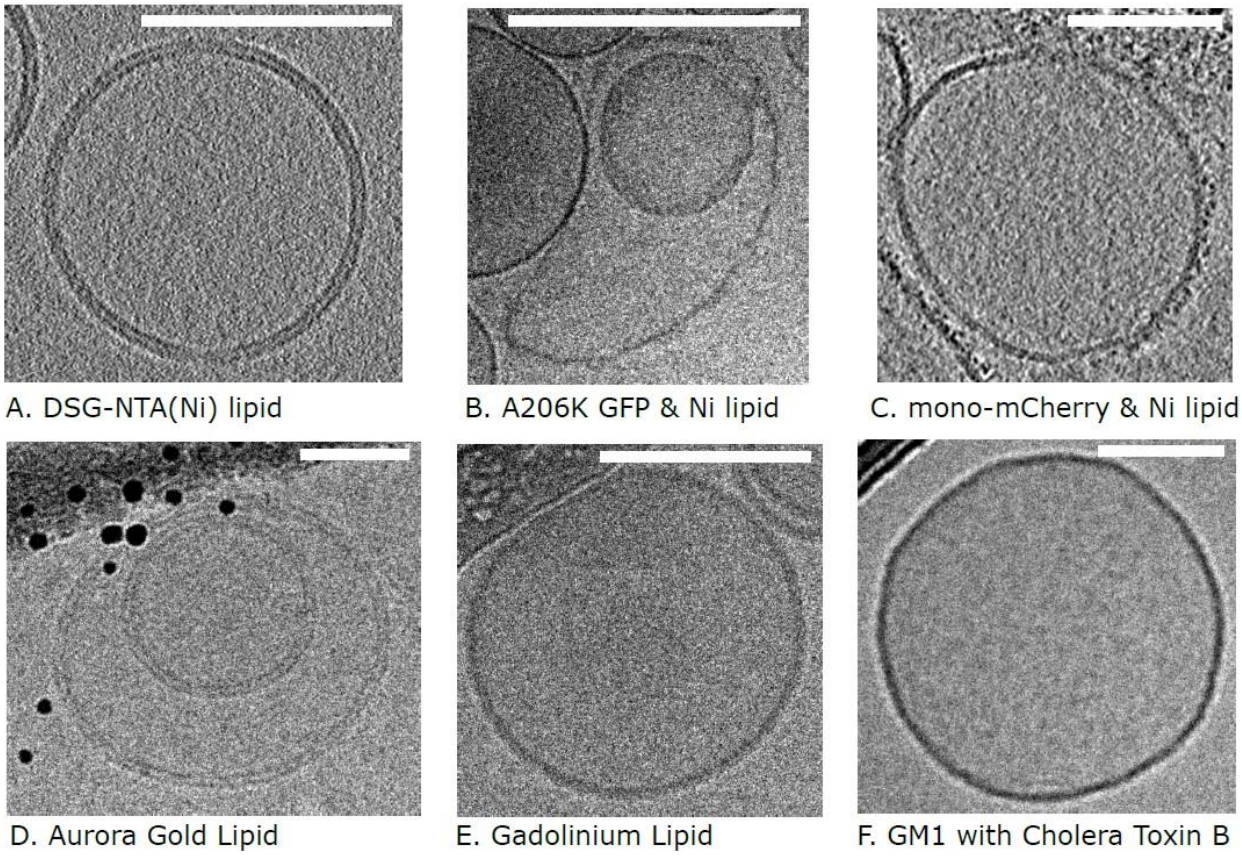

Figure S7. Intensity line scan of trimeric mCherry from Figure 5D.
The arrow points to a region encompassing two proteins (bounded by red lines). A line scan with a width of 5 pixels was conducted over this region, yielding the intensity profile on the right. The distance between the centers of the proteins is ~3.5 nm, the distance between the centers of the two peaks. Scale bar is 100 nm.

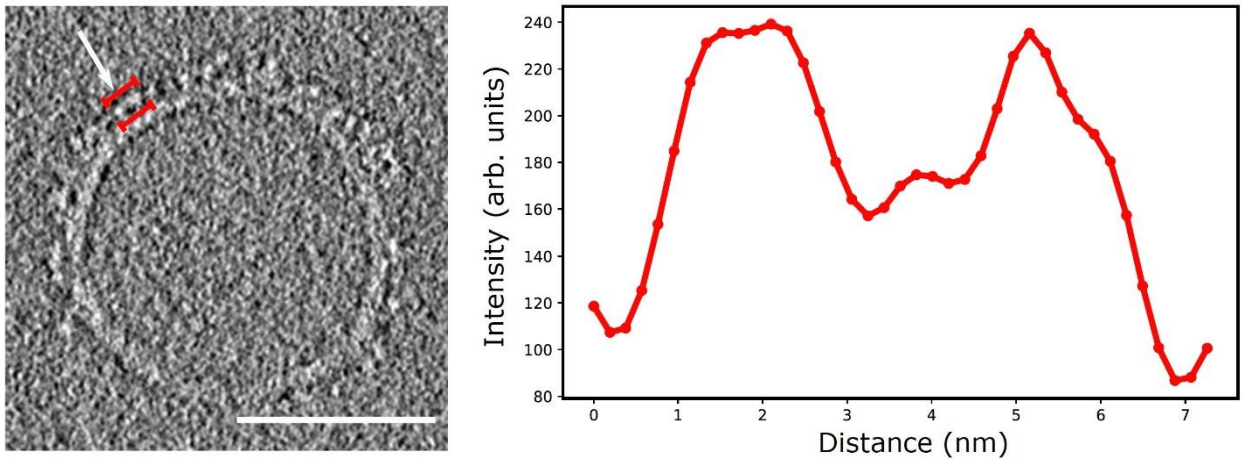

Figure 4S8. Larger version of Fig. 5 from the main text.

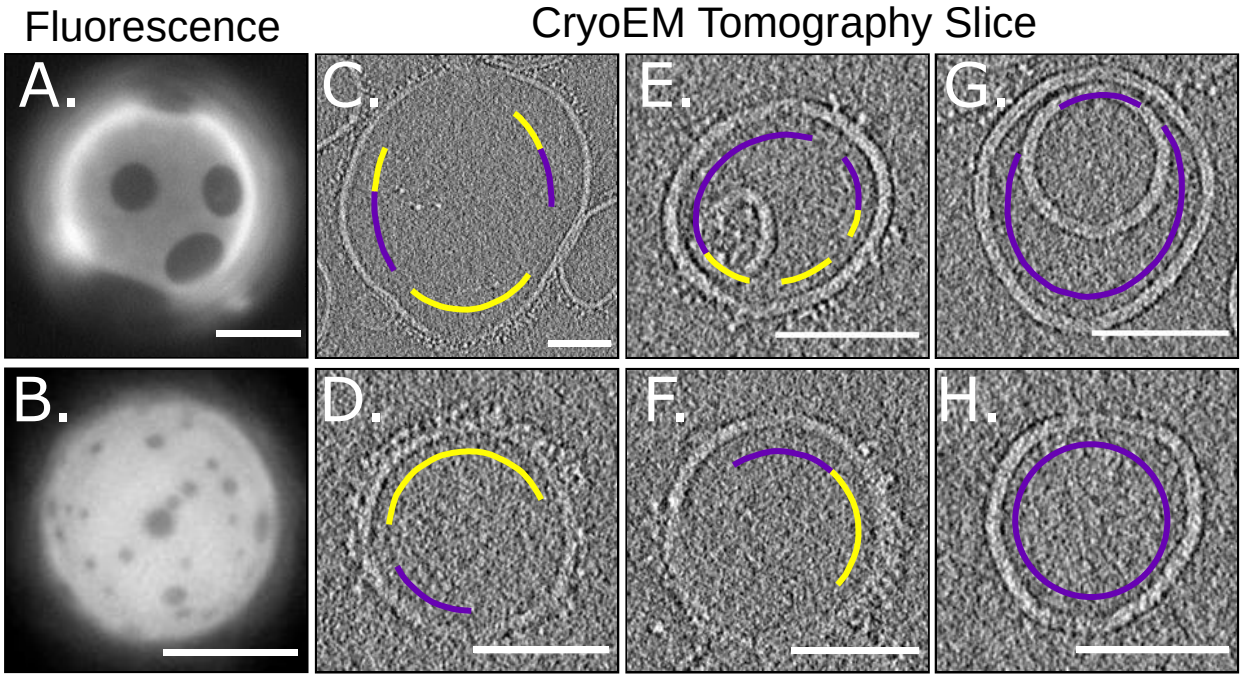

Figure S9. Dynamic light scattering of trimeric mCherry in buffer.
Trimeric mCherry is not significantly aggregated in 'mCherry buffer'. The highest average percent intensity measured by dynamic light scattering corresponds to small particles. Specifically, at intensities greater than 90%, the average particle radius is 3.04 ± 0.3 nm, is close to the measured radius for GFP (~2 nm; PDB:1GFL), a protein that is almost identical in structure to mCherry. The average polydispersity index is ~15-20%, which is reasonable for a small protein composed of three domains connected by flexible linkers. All data were collected from 3 technical replicates of 25 readings each.

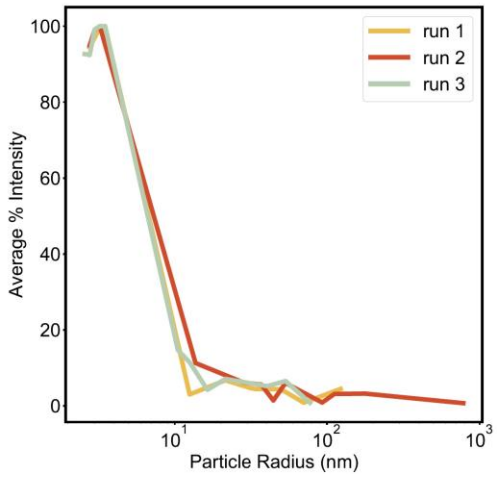

CHAPTER 5: Yeast Alter Vacuole Membrane Phase Behavior in Response to Changes in their Growth Environment

*This chapter contains unpublished preliminary results collected in collaboration with C.L. Leveille, J. Reinhardt, R. Ernst, A. Merz, and S.L. Keller. The text was written in collaboration with C.L. Leveille.

5.1 INTRODUCTION

Compartmentalization and spatial organization are key factors in biological emergent behavior. The distinct functions of each cellular organelle arise from the highly regulated spatial arrangement of molecules. For most cellular structures, this organization requires an immense energetic input; cells must consume ATP at a rate of ~10^9 ATP/s/mammalian cell 3000μm^3 volume (267). A growing body of research has implicated thermodynamic phase separation as an organizational mechanism in cells. For example, membrane-less organelles, like stress granules and nucleoli, form through liquid-liquid phase separation and require little-to-no ATP to form and dissolve (268–270). Another striking example of phase separation in biology comes from the membrane of yeast vacuoles: in nutrient-depleted growth conditions, vacuole membranes break out into compositionally distinct domains (69, 70, 271).

Membranes of *S. cerevisiae* vacuoles exhibit the hallmarks of liquid-liquid phase separation: 1) domains disappear above a characteristic temperature (T_{mix}) and reappear below that temperature and, 2) domains diffuse in the plane of the membrane and merge on the time scales of liquids (74). Domains are also tightly regulated by the cell, appearing only when cells have entered the stationary (or nutrient-depleted) stage of growth. Specifically, the lipids in yeast vacuole membranes are uniformly mixed during the logarithmic stage of growth. In the stationary stage, the membrane demixes into compositionally distinct domains (Fig. 6.1B) (70, 271).

A growing body of evidence implies that vacuole membrane domains are important in yeast homeostasis and environmental adaptation. For example, proteins responsible for the regulation of the cellular stress response and sterol homeostasis (*e.g.* ltc1 and IVY1 in the TORC signaling pathway) selectively partition to vacuole domains under stress conditions (75–77), and energy-rich lipid droplets tend to co-localize with domains before they are engulfed by the vacuole (72). If domains are functionally important, *how* does the cell regulate membrane phase separation?

Researchers have shown that the lipid composition of membranes from a related cellular system depends on their growth temperature. Specifically, the T_{mix} of giant plasma membrane vesicles (GPMVs) derived from ZF4 zebrafish cells scales with the growth temperature of the cells (171). The lipid composition also changes: cholesterol increases by about 4 mol% for cells grown at 28°C vs 20°C, and cells grown at 20°C have 4.5 ± 2 % more lipids with one highly unsaturated chain (> 4 double bonds) than cells grown at 28°C (171). This relationship between lipid composition and T_{mix} has been well established in model systems. For example, cholesterol is essential for the formation of coexisting liquid phases in model giant unilamellar vesicles (GUV), and its depletion destroys liquid-liquid domain coexistence (33).

Here, we investigate the phase behavior and lipid compositional adaptation in the vacuole membranes of *S. cerevisiae*. Specifically, we quantify the characteristic T_{mix} for yeast at their optimal growth temperature (30°C) and for yeast grown below this temperature (25°C). We demonstrate that the predominant sterol in yeast, ergosterol, is important in the regulation of vacuolar membrane phase separation. We also present preliminary results showing that the lipid composition of the vacuole changes from the logarithmic to the stationary growth stage. We hypothesize that vacuoles exhibit domains in the stationary growth stage due to dramatic changes in the lipid composition. In the future, we will perform quantitative lipidomics on pure isolates of logarithmic and stationary stage vacuoles, grown at both 25°C and 30°C.

5.2 MATERIALS AND METHODS

Yeast Cell Culture

The yeast strain, *Saccharomyces cerevisiae* contained the following genetic mutations: *MATa, his3D1, lys2D0, ura3D0, leu2D0, VPH1-GFP::HIS3M.* Cultures were grown in synthetic complete media containing 0.4% glucose. For log stage experiments, cultures (1 L) were grown in a shaking incubator at 225 rpm to an optical density of 1.0 using 600 nm wavelength light (OD_{600}), for ~17 hrs at 30°C. For stationary stage experiments, cultures (200 mL) were incubated at 25°C and 30°C at 225 rpm. Yeast were harvested after ~3 days of growth and the optical density was between OD_{600} ~6-8 (for yeast grown under these conditions, the growth curve plateaus at this optical density).

Temperature Experiments

To dilute cells for imaging, an isosmotic solution of conditioned media was made from the grown culture. Specifically, 1 mL of culture was centrifuged at 1100 rpm and the supernatant was

collected and spun again at 1100 rpm to remove remaining cells. To enhance contrast for imaging, a 20% OptiPrep solution in conditioned media was prepared. Briefly, 200 µL of OptiPrep (60% OptiPrep Density Gradient Medium Sigma Cat#D1556) was added to 800 µL media and vortexed. Coverslips were coated with 3 µL of 1 mg/mL Concavilin-A (ConA; EPC Elastin Products Co. no. C2131) in coat buffer (50 nM HEPES, 20 mM calcium acetate, 1 mM $MnSO_4$ pH 7.5). Immediately prior to use, salt was rinsed off of coverslips using MilliQ water and dried with N_2 gas. Samples of 5 µL of cells were diluted into 5 µL of conditioned media containing 20% OptiPrep and placed onto a ConA-coated cover slip. Cells were sandwiched between two coverslips and allowed to settle and adhere to the coated surface for 10 minutes.

Images were acquired on a Nikon upright microscope (Nikon; Melville, NY) using a Blackfly 2.3 MP Mono USB3 Vision camera (FLIR; Wilsonville, OR). Samples were illuminated with an X-Cite 110 LED light source (Excelitas; Waltham, MA) and filtered through an IR cut filter (Chroma Technology; Bellows Falls, VT) to prevent aberrant heating of the sample from the optics. A temperature cuff (Harvard Biosciences Inc.; Holliston, MA) on a 100x oil immersion objective was used to maintain the temperature of the objective in contact with the sample. Thermal grease (Omega Bio-tek; Norcross, GA) kept the sample in thermal contact with a home-built, temperature-controlled stage (Omega Engineering; Norwalk CT). Temperature was sensed by a thermistor probe (0.2°C accuracy, Advanced Thermoelectric; Nashua, NH). Temperature was adjusted stepwise in increments of 2°C, starting at 5°C below the growth temperature, and increasing until domains were no longer observed. Temperature sweeps were completed within 3-5 minutes to prevent genome transcription alteration of the cells in response to a temperature change. Micrographs were acquired at 2°C interval. Images were analyzed later to determine the fraction of vacuole membranes that contained two coexisting liquid phases at each temperature.

Images were post-processed using ImageJ (http://imagej.nih.gov/ij). To preserve the fidelity of the data, image manipulation was limited to adjusting overall brightness or implementing linear (γ=1) contrast enhancements.

Analysis of T_{mix}

To compute miscibility transition temperatures, images were analyzed using the original python programs MiscibilityTemp.py, MiscibilityAnalysis.py, and CombinedPlotter_V2.py which can be found in Appendix B. Briefly, images at each temperature are loaded and the user selects

vacuoles that are phase separated and vacuoles that are mixed. The percent of phase separated vacuoles is computed for each temperature and fit with the following equation from (48):

$$\%\ Phase\ Separated = 100 * 1 - \frac{1}{1 + e^{-\frac{(x-c)}{d}}}$$

Where x is the temperature of the system for each image and c is T_{mix}, which represent the temperature where 50% of the vacuoles are phase separated. D is a constant that describes the slope of the curve at the transition temperature.

Vacuole Isolation

A 1 L culture was grown to an OD_{600} 1.0. Cells were harvested in a swinging-bucket rotor (3200 x g) for 10 min at room temperature, resuspended in 0.1 M Tris (pH 9.4) and 10 mM dithiothreitol, and incubated for 10 min at 30°C. The cells were again sedimented in a swinging-bucket rotor (3200 x g) for 5 min at room temperature and then resuspended in spheroplasting buffer (600 mM sorbitol, 50 mM potassium phosphate pH 7.5, and 8 % growth media). Lytic enzyme (Zymolase 20T, Seikigakui; further purified by ion exchange chromatography) was added, and the cells were incubated for 25 min. The spheroplasted cells were sedimented in a swinging-bucket rotor (3200 x g) for 5 min at 4°C. For hypoosmotic lysis, spheroplasts were resuspended in 15% Ficoll buffer (10 mM PIPES-KOH pH 6.8, 200 mM sorbitol, and 15% w/v Ficoll), and diethylaminoethyl-dextran was added to a final concentration of 0.005-0.01% w/v. Spheroplasts were incubated for 2 min on ice, then 3 min at 30°C. The resulting spheroplast lysates were added to a SW-41 ultracentrifuge tube and overlaid with a step gradient of 8%, 4%, and 0% Ficoll and 10 mM PIPES-KOH pH 6.8. Ultracentrifugation at 30,000 x g for 90 min at 4°C resulted in pure vacuoles at the 4%-0% Ficoll interface.

To image cell-free vacuoles, 5 µL of the isolated vacuole prep was diluted in 45 µL 0.8% agarose and mounted between a microscope slide and coverslip. Images were collected on an Olympus IX71 fluorescence microscope (Olympus Corporation; Waltham, MA) with an electron-multiplying charge-coupled device camera using a 63x oil immersion objective.

Cyclodextrin:Ergosterol Complex

To make a methyl-β-cyclodextrin (MβCD; Sigma-Aldrich; St. Louis, MO) and ergosterol (Sigma-Aldrich, St. Louis, MO) complex at 10:1 MβCD:ergosterol, ergosterol was dissolved for a 0.2 mM final solution in a glass test tube. The solute chloroform was evaporated using a gentle

stream of N_2 to create a thin film. The film was rehydrated in 2.5 mM MβCD in 10 mM PIPES-KOH pH 6.8. The tube was vortexed and then sonicated in a bath sonicator for 1-3 min. To encourage complexes to form, the solution was incubated in a 37°C water bath overnight.

Microsome Preparation for Immuno-isolation of Vacuoles

For log stage experiments, one 1 L growth (4000 OD_{600} units) was inoculated and diluted to 0.1 OD_{600} from a starter culture and grown for 8 hrs, shaking continuously at 220 rpm and 30°C. For stationary stage experiments, 4 1 L growths were inoculated and diluted to 0.1 OD_{600} from a starter culture and grown for 48 hrs at 220 rpm and 30°C and harvested at an OD_{600} of 7.5-8, yielding 7500-8000 OD_{600} units total. Samples were sedimented in a swinging-bucket rotor (3000 x g) for 5 min at room temperature and resuspended in 25 mL of pre-cooled PBS buffer. Pellets were kept on ice for the duration of the isolation procedure to prevent chemical changes to the lipids. Samples were sedimented again in a swinging-bucket rotor (3000 x g) for 5 min at 4°C. The supernatant was discarded, and the pellet was snap frozen in liquid N_2 and stored at 80°C until needed.

To start the prep, pellets were thawed on ice and then resuspended in 10 mL lysis buffer (prepared fresh before the procedure; 25 mM HEPES pH 7.0, 1 mM EDTA, 0.6 M mannitol, Protease Inhibitor Cocktail [PIC; (CLAP w/o L) 25 mg chymostatin (C7268-25MG Sigma Aldrich), 25 mg antipain (A6191-25MG Sigma Aldrich), 25 mg pepstatin (P5318-25MG Sigma Aldrich)], and 1:40,000 benzonase). 1000 OD_{600} units of cells were placed onto pre-cooled zirconia glass beads (13 g of 0.5 mm diameter beads) in a 15 mL falcon tube and filled to the top with lysis buffer. Tubes were sealed with parafilm and medical tape, and then placed on ice. To break apart cells, tubes of cells and beads were placed in a FastPrep-24™ 5G bead beating grinder and lysis system (MP Biomedicals; Burlingame, CA). Samples were shaken at 5 m/s for 15 s intervals 10x with 45 s rest intervals. Lysate was transferred (without the beads) to fresh 15 mL tubes. Beads were washed with 6 mL of lysis buffer to extract all of the lysate and combined with the rest of the lysate. Cellular material was sedimented in a swinging-bucket rotor (3,234 x g) for 5 min at 4°C twice. Supernatant was transferred to fresh 15 mL tubes and centrifuged again (3,234 x g) for 5 min at 4°C. Samples were transferred and pooled (2 samples per tube) and sedimented in a swinging-bucket rotor (10,800 rpm) at 4°C for 20 min. Samples were then ultracentrifuged at 31,200 rpm at 4°C for 1 hr.

After ultracentrifugation, the supernatant was removed (carefully, as the supernatant contains contaminates like lipid droplets). The pellet was washed with 15 mL of lysis buffer and then resuspended in 1 mL of lysis buffer. The sample was then snap frozen in liquid N_2 and stored at 80°C prior to the immuno-isolation protocol.

Immuno-isolation

Previously prepared microsomes were thawed on ice and DynaBeads® (Sigma-Aldrich, St. Louis, MO) were washed and then suspended in 1 mL IP buffer (1 M HEPES pH 7.0, 4 M NaCl, 0.5 M EDTA) and placed in a magnetic tube holder. Microsome samples were then sonicated using a tip sonicator equipped with a MS72 tip for 10 s and a duty cyle of 0.7 at 50% amplitude. Sample was sedimented by swinging-bucket rotor (3000 x g) at 4°C for 3 min. 800 µL of sonicated supernatant was added to 800 µL of IP buffer on DynaBeads® for a total volume of 1600 µL. The sample was allowed to bind to the beads by rotating overhead for 2 hrs at 4°C and 2 rpm. Samples were then placed on the magnetic bead holder and supernatant was removed. The bound sample was collected after washing 2x with wash buffer (1 M HEPES pH 7.0, 4 M NaCl, 0.5 M EDTA, 8 M urea) and then 2x with IP buffer. Supernatant was then replaced with elution buffer (3 mL of buffer; 2,634 µL water, 0.3 mL 10x PBS pH 7.4, 3 µL EDTA, 3 µL DTT and 60 µL 2 mg/mL GST-3C) and rotated overhead at 2 rpm for 2 hrs at 4°C. The supernatant was collected and then re-sedimented to get rid of residual DTT and protease at 70,000 rpm for 2 hrs at 4°C. The supernatant was discarded, and pellets were resuspended in residual supernatant and snap frozen in liquid N_2 before lipidomics analysis.

5.3 PRELIMINARY RESULTS AND DISCUSSION

Vacuoles of *S. cerevisiae* have a Characteristic T_{mix}

Vacuoles of the yeast *Saccharomyces cerevisiae* are similar to mammalian lysosomes in that they regulate the pH and osmolarity of the cell. There are many proteins that are exclusive to the vacuolar membrane, including the highly abundant proton-pump, Vph1 (272). Vacuoles can be visualized through an endogenous GFP label on Vph1 (70). During the early logarithmic stage of growth, there are many small, multilobed vesicles in each cell. As the cells grow, the vacuoles fuse until one large vacuole fills most of the volume of the cell, and Vph1 is uniformly distributed on the membrane. A remarkable change occurs when yeast reach the stationary stage of growth: Vph1 becomes heterogeneously distributed on the vacuole membrane into distinct domains (Fig. 5.1 B).

Previously, Rayermann et al. demonstrated that these domains exhibit two hallmarks of liquid-liquid phase separation: 1) domains diffuse and coalesce in the plane of the membrane, and 2) domains disappear and reappear at a characteristic T_{mix} when temperature is cycled (74).

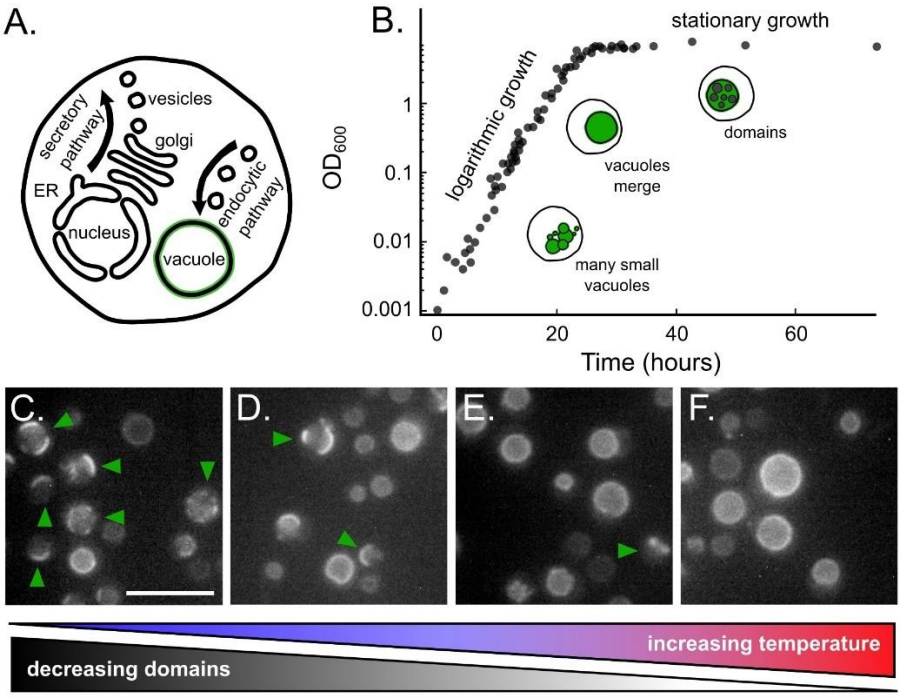

Figure 5.1 Vacuoles of *Saccharomyces cerevisiae* exhibit coexisting liquid phases in the stationary stage of growth. **A.** Schematic of a yeast cell from Fig. 1C in (74). **B.** Growth curve of yeast used in this study and adapted from (74), where OD_{600} is the optical density at 600 nm. **C-F.** Micrographs of vacuoles labeled with GFP-Vph1 taken at 24°C, 28°C, 32°C, and 36°C, respectively. Green arrows point to vacuoles with coexisting liquid phases. Scale bar is 10 μm.

Quantitative knowledge of T_{mix} is powerful; a membrane's T_{mix} is acutely sensitive to its composition and highly correlated with physical properties of the membrane such as lipid packing order and membrane thickness (46, 65, 229, 233). To quantify the characteristic T_{mix} of yeast vacuoles, we used a strain of yeast with endogenously labeled GFP-Vph1 and cycled the temperature of the sample on a home-built microscopy stage. For yeast grown at their optimal growth temperature of 30°C, most vacuoles are phase separated at low temperatures (24°C; Fig 5.1 C), and the fraction of vesicles with domains decreases as the temperature increases (Fig. 5.1 D-F). We imaged vacuoles at increasing temperatures in 2°C increments and computed the percent of phase separated vacuoles for each temperature using a custom counting program (Appendix B. XX). T_{mix} is defined as the temperature at which 50% of vesicles (or vacuoles) are phase separated.

We performed temperature sweeps from 5°C below the growth temperature to a temperature in which >90% of vacuoles were mixed for 8 separate samples (Fig. 5.2 A). The preliminary results in the inset in Fig. 5.2B shows that T_{mix} is dependent on the optical density of the yeast culture (the stage of growth of the yeast).

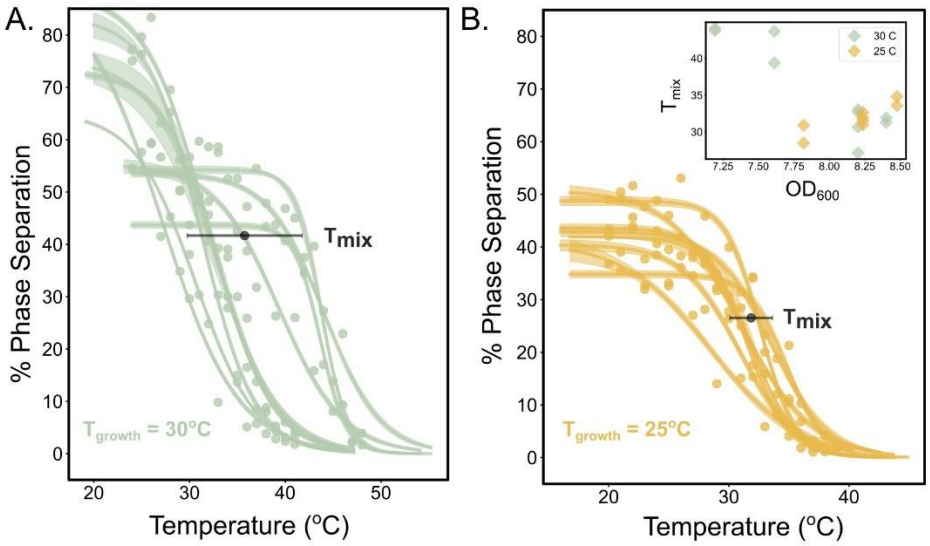

Figure 5.2 Preliminary results for T_{mix} of membranes of yeast vacuoles inside living yeast cells grown to stationary stage. **A.** Plot of the percent of phase separated vacuoles at each temperature for vacuoles grown at their optimal growth temperature (30°C). Each line is a sigmoid (described in the Methods) fit to points from individual temperature sweeps. Lines are bounded by 95% confidence intervals from bootstrap resampling of the sigmoid fit. The black point is the average T_{mix} for all sweeps, and horizontal, black error bars represent the standard deviation in T_{mix}. **B.** Plot of the percent of phase separated vacuoles at each temperature for vacuoles grown at a suboptimal growth temperature (25°C). Data are fit and represented as described in Panel A. The inset is a plot of the OD_{600} when vacuoles were harvested for imaging versus the measured T_{mix} for the population of vacuoles. Data form two clusters, with higher T_{mix} values corresponding to lower OD_{600}.

Vacuoles Grown at Low Temperature have a Similar T_{mix} to Those Grown at 30°C

The lipidome of yeast vacuoles is highly regulated throughout the growth cycle and the composition of each organelle is tuned to optimize the physical properties of its membrane (*e.g.* the endoplasmic reticulum, which has regions of high curvature, has a higher fraction of cone-shaped PE lipids than the plasma membrane) (273–276). This is not unique to yeast: in zebrafish, the growth temperature has a striking effect on the composition of the plasma membrane (171).

GPMVs derived from zebrafish cells exhibit T_{mix} values that scale with the growth temperature of the original cells, which hints at the possibility that a similar phenomenon may occur in yeast cells.

In Fig. 5.2 B, the average T_{mix} for yeast grown at the sub-optimal temperature 25°C is 31.8 ± 1.8°C. At first glance, this is significantly lower than the average T_{mix} for yeast grown at 30°C; however, within uncertainty, the T_{mix} for both growth temperatures is the same. There are many possible explanations for this surprising result, the most compelling of which is made evident when we examine the relationship between the OD_{600} of the yeast at harvest and their T_{mix}. From the inset of Fig. 5.2 B, it is clear that there are two populations of T_{mix} values: one population, harvested at lower OD_{600}, exhibits higher T_{mix} and the other population has both a lower T_{mix} and higher OD_{600}. The optical density of a yeast culture is correlated with the stage of growth of the cells, which indicates that the T_{mix} may be more closely tuned to growth stage than initial growth temperature.

Ergosterol is Important for Vacuole Membrane Phase Separation

The composition of the vacuole membrane, specifically the sterol composition, presumably changes in response to growth and environmental stress. In model lipid membranes, the presence of a sterol is essential for liquid-liquid phase coexistence. Similarly, there are many tantalizing hints that ergosterol is important in the formation of domains in yeast. For example, genetic knockout experiments demonstrated that a sterol transporter located at vacuole-ER contact sites is essential for domain formation (77). In their seminal paper, Toulmay & Prinz demonstrated that when the sterol-exchanger, methyl-β-cyclodextrin (MβCD), was added to solutions of vacuoles in cell lysate, membrane domains disappeared (70). This showed, they argued, that the removal of ergosterol from stationary stage vacuoles shifts their composition away from a 2-phase region and into a 1-phase region. However, experiments with MβCD come with several caveats, namely that the molecule is an exchanger; if there were sterol in the cell lysate, MβCD could easily deliver from the lysate to vacuole membranes. A similar uncertainty surrounds the genetic knockdown experiments because the *direction* of sterol transport is unknown (77).

We directly investigated the importance of ergosterol in domain formation by treating fully isolated log stage vacuoles (which do not exhibit domains) with MβCD. To add ergosterol, we complexed ergosterol and MβCD in a 1:10 ratio and added this solution to isolated log stage vacuoles. Surprisingly, we found that the addition of ergosterol had no effect; vacuole membranes

were completely mixed. When we treated isolated log stage vacuoles with empty MβCD, domains appeared on ~70-80% of vacuole membranes (Fig. 5.3 B).

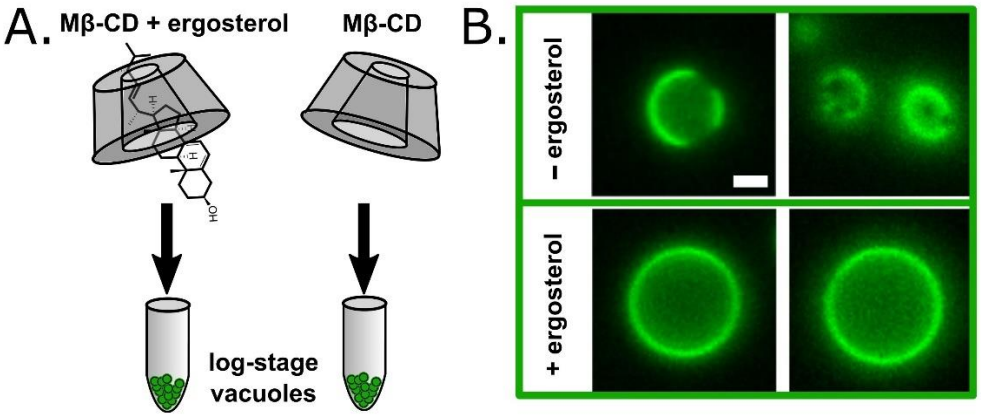

Figure 5.3 Removing ergosterol from log stage vacuoles induces phase separation. **A.** Schematic of experimental procedure to add ergosterol to isolated vacuoles and to remove it. Ergosterol is added to vacuoles using complexed MβCD:ergosterol in a ratio of 10:1. Ergosterol is removed from vacuoles with empty MβCD. **B.** Micrographs of isolated log stage yeast vacuoles labeled with GFP-Vph1. Under wild-type conditions, log stage vacuoles do not exhibit domains. When ergosterol is removed, vacuole membranes demix into coexisting liquid phases. When ergosterol is added, the vacuole membranes stay mixed. Scale bar is 2 μm.

The composition of the vacuole membrane is complex, harboring hundreds of lipid species, proteins, and organellar contact sites. The clear role for ergosterol in vacuole membrane phase separation implies that yeast actively control the sterol composition of vacuole membranes in order to achieve domain formation.

5.4 FUTURE DIRECTIONS

Lipidomics of Yeast Vacuole Membranes at Different Growth Stages and Growth Temperatures

Lipidomics is a powerful tool to uncover the molecular players responsible for cell membrane structure and behavior. In collaboration with R. Ernst and J. Reinhardt in Saarland, Germany, we are investigating the total lipid composition of ultra-pure preps of yeast vacuoles in the log stage and stationary stages of growth, as well as vacuoles grown at 30°C and 25°C.

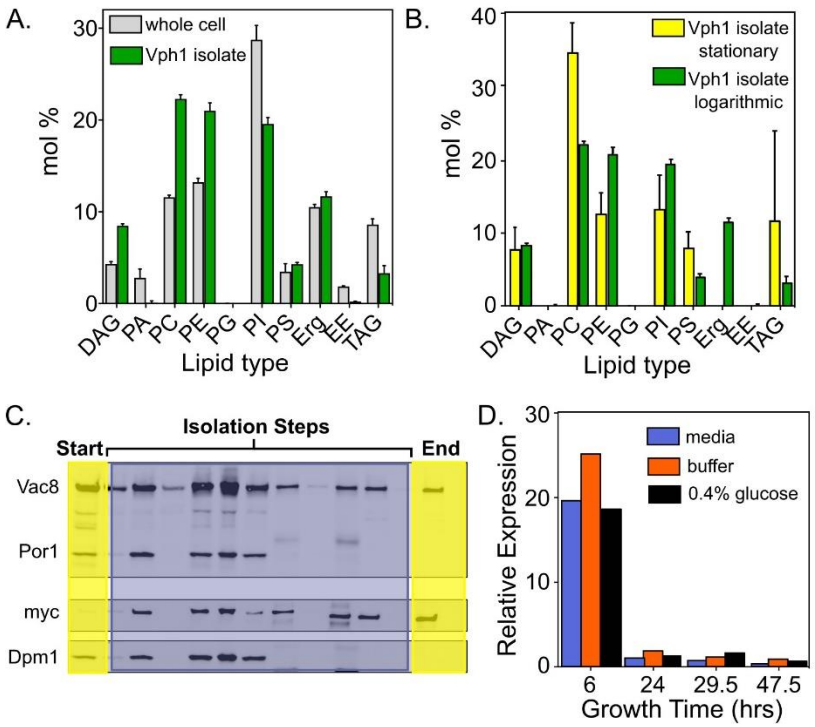

Figure 5.4 Preliminary lipidomics of isolated yeast vacuoles reveal changes in the lipidome from log stage to stationary stage. **A.** Mole percent of each lipid headgroup type for whole yeast cell isolates and vacuole isolates in the log stage of growth. Vacuoles are isolated using Vph1 as a tag as specified in the Methods. **B.** Mole percent of each lipid headgroup type for vacuoles isolated in the log stage and stationary stage of growth. Strikingly, ergosterol is depleted in stationary stage vacuoles. These results have significant caveats as the isolation protocol has not yet been optimized for stationary stage yeast. **C.** Western blot of products from the isolation protocol described in the Methods. The **start** column shows the presence of the vacuole (vac8), the bait tag (myc), the ER (Dpm1), and mitochondria (Por1). The **end** column shows that only the vacuole is isolated. **D.** One challenge to optimizing the isolation protocol for stationary stage yeast is that Vph1 is significantly downregulated in the stationary stage, even under different buffer conditions.

Figure 5.4 shows our preliminary lipidomics data. In Fig. 5.4 A, it is clear that the lipid composition of the vacuole is significantly different than the lipid composition of the whole cell, and in Fig. 5.4 B, we see that the lipid composition changes drastically from log stage to stationary stage. In particular, ergosterol is substantially decreased in log stage vacuoles. However, there is a significant caveat with these preliminary results: the immuno-isolation protocol has not been optimized for stationary stage vacuoles.

The immuno-isolation protocol, developed by R. Ernst and J. Reinhard, utilizes a tag-and-bait system where an organelle-specific protein is engineered with a specific tag. This protein is then

immuno-precipitated from the cell lysate, which yields a pure prep of the organellar membrane. In log stage vacuoles, tagged Vph1 is abundant and results in an excellent yield of vacuolar membrane (Fig. 5.4 C). As shown in Fig. 5.4 D, the relative expression of Vph1 drastically decreases with growth time and as a result, the yield from stationary stage isolation is poor. This makes comparison of log stage preps and stationary stage preps difficult. Currently, we are exploring other bait proteins with much higher abundance in stationary stage vacuole membranes.

CHAPTER 6: Prebiotic Amino Acids Bind to and Stabilize Prebiotic Fatty Acid Membranes

*This chapter was first published in *PNAS* in 2019. It was written in collaboration with R.A. Black, M. Xue, H.E. Litz, A. Ramsay, M. Gordon, A. Mileant, Z.R. Cohen, J.A. Williams, K.K. Lee, G.P Drobny, and S.L. Keller. The full citation can be found at the end of Chapter 1 on pg. 29.

6.1 INTRODUCTION

In a minimal cell, a membrane sequesters proteins and RNA components from the surrounding aqueous solution. Prebiotic membranes would have spontaneously self-assembled from fatty acids (78, 277), which are known to be generated by abiotic reactions and delivered to Earth by meteorites (88, 89). However, fatty acid membranes are unstable in solutions containing salt at concentrations > 200 mM or divalent cations at low millimolar concentrations (80). This presents a significant challenge in establishing the plausibility that the first protocell membranes were comprised of fatty acids because salt would have been prevalent in early oceans (278) and pools and because Mg^{2+} (or Fe^{2+}) is essential for RNA catalysis (279, 280). Although glycerol monoester (281, 282), long-chain alcohols (81, 283), decylamine (284, 285), and citrate (91) increase the stability of fatty acid vesicles (cell-like structures that separate an interior volume from the bulk solution), the prebiotic availability of these agents in sufficient quantities is uncertain (286). These observations lead to the question: what molecules that were likely found in prebiotic pools and oceans might interact with and stabilize fatty acid membranes? Amino acids are the building blocks of proteins, and ten amino acids are deemed prebiotic (287–290). These molecules are excellent candidates for stabilizing agents of fatty acid membranes.

An additional challenge in explaining the origin of protocells is accounting for the co-localization of proteins, RNA, and membranes as a single unit. A prevalent view is that these three structures were formed through separate and independent processes, followed by a random event that led to their co-localization. We have proposed an alternate, auto-amplification scenario in which fatty acid vesicles bound and concentrated the building blocks of proteins and RNA, which in turn stabilized fatty acid vesicles, leading to further binding of the building blocks (83, 92). If the resulting conformational constraints and increased local concentration of the building blocks facilitated formation of proteins and RNA, then the co-localization of these macromolecules with

fatty acid membranes would be explained. We previously reported results with RNA bases and ribose that support part of this scenario (92). Here we seek to complete the picture by investigating interactions between amino acids and fatty acid membranes to show that all of the major components of protocells could have self-assembled into a single unit.

Our focus is on molecules that are prebiotically plausible. Previous studies have shown evidence for interactions between fatty acid vesicles and non-prebiotic amino acids and peptides (291–295). Here, we use decanoic acid as our fatty acid rather than longer-tailed versions that produce more stable membranes but are less prebiotically plausible. We choose unmodified prebiotic amino acids rather than versions altered to optimize specific reactions. We interrogate interactions between the decanoic acid membranes and the amino acids with multiple techniques: cryo electron microscopy (cryo TEM), fluorescence microscopy, nuclear magnetic resonance spectroscopy, centrifuge filtration assays, and turbidity measurements.

We find that several amino acids bind to fatty acid membranes and that a subset stabilize fatty acid membranes in the presence of salt and Mg^{2+}. Moreover, we find that an amino acid's stabilization of the membrane persists after mixing and dilution to lower overall concentrations, alleviating the need for consistently high concentrations. Together, these results explain how protocells could have endured in the presence of salt and Mg^{2+} and provide a plausible mechanism by which the building blocks of proteins could have co-localized with early membranes.

6.2 METHODS

Materials

Sodium chloride was purchased from Thermo Fisher Scientific (Waltham, MA), centrifugal filters from MilliporeSigma (Burlington, MA), and decanoic acid from Nu-Chek Prep (Elysian, MN). L-leucine ($^{13}C_6$), decanoic-10,10,10-$^{2}H_3$ acid and D_2O were from Cambridge Isotope Laboratories (Andover, MA). Decanoic-2,2-$^{2}H_2$ acid was from C/D/N Isotopes (Quebec, CA). All other chemicals were from Sigma. Except for NMR experiments, all solutions were prepared in 18 MΩ-cm water.

Decanoic Acid Solution

Decanoic acid was dissolved, with heating, in 190 mM NaOH to yield a 180 mM stock solution. This stock, 0.5 M monosodium phosphate, and 4 M NaCl were diluted into water to yield a solution of 50 mM decanoic acid, 30 mM sodium phosphate, and 100 mM NaCl. The pH was

then adjusted to 6.83 by adding a small volume of 1 M HCl. This resulting solution is referred to as “the decanoic acid solution” and was used in all experiments except where indicated otherwise. Generally, "decanoic acid" in the text refers to mixtures of the protonated and unprotonated forms.

Diffusion NMR

Pulsed field gradient nuclear magnetic resonance (PFG-NMR) experiments were performed on a Bruker Avance III 700 MHz NMR instrument with a 5 mm Broadband Observe (BBO) probe at 25 °C. The “stebpgp1s” pulse sequence was applied to probe each amino acid's translational diffusivity (D), which was found via $\ln(I/I_0) = -\gamma^2G^2\delta^2D(\Delta-\delta/3)$. In this equation, G is the gradient strength, which varied from 10% to 95% of the maximum strength (53.5 Gauss/cm) for samples in which amino acids were in the presence of decanoic acid, and from 10% to 75% of the maximum strength for samples in the absence of decanoic acid. The variable I is the observed ^{1}H NMR peak intensity corresponding to each G, where I_0 is the intensity at the initial G value. γ is the gyromagnetic ratio of ^{1}H (4257.64 Hz/G), δ is the length of the gradient pulse (set to 0.002 s), and Δ is the diffusion time (set to 0.3 s). PFG-NMR experiments detected a series of 1D ^{1}H spectra and the diffusion coefficients were extracted by fitting the signal intensity decay at increasing gradient strengths to the equation above. Data were analyzed by extracting NMR peak intensities using the TopSpin 3.5 software package (Bruker) and exporting peak intensities to OriginPro (OriginLab, Northampton, MA), which fit the equation above and generated uncertainties of the fit. For PFG-NMR experiments, samples contained 50 mM of the amino acids leucine, glycine and serine or 10 mM lysine in the presence or absence of 50 mM deuterated decanoic acid, and were prepared in a solution of 50 mM sodium phosphate and 50 mM NaCl in D_2O at pH7 and room temperature.

REDOR

10 mM leucine uniformly labeled with ^{13}C was mixed with 72 mM decanoic acid labeled with ^{2}H at either the 2- or 10-carbon, and ^{2}H-free water, at pH 7.6. Samples were then lyophilized and analyzed in a 11.74 T Bruker Avance III 500 MHz, narrow-bore spectrometer using a Bruker TriGamma probe tuned for ^{1}H-^{13}C-^{2}H triple resonance. The REDOR (xy-8) pulse sequence was used (296). Samples were spun at 10 kHz magic-angle spinning frequency. S0 and S1 were collected for dephasing times of 0.8, 3.2, 5.6, 8.0 and 10.4 ms and required 1024, 2048, 2048, 2048 and 4096 scans, respectively. The CP time was 1.5 ms. During this time, the ^{1}H power was ramped from 70% to 100%. Field strengths were: 83 kHz ^{1}H $\pi/2$ pulse, 56 kHz ^{13}C π pulses, and 66 kHz

^{2}H π pulses. During dephasing and acquisition, 100 kHz SPINAL-64 decoupling was applied on the ^{1}H channel. Data were processed with 20 Hz Gaussian line broadening and baseline correction. Chemical shift referencing was achieved externally using adamantane. The methylene ^{13}C shift was set to 38.5 ppm.

Filtration Assay

The decanoic acid solution was added to solid base or amino acid such that the final concentration of the compound was 10 mM. The compound was ground with the end of a stirring rod to facilitate dissolution and vortexed for ~6 sec. After 30 min, 1.5 ml of solution was transferred to an Amicon Ultra-4 3K filter and centrifuged in a Beckman Allegra X-30R swinging bucket centrifuge at 3,000 *g* for 10 min at 21 °C. To assay bases (adenine and thiouracil) in the starting material and filtrate, absorbance at 260 nm was measured using an Agilent 8453 spectrophotometer, with uncertainties reported as standard error of the mean of 3 trials. To assay amino acids, (a) samples were diluted 225-fold in 0.2 M bicine at pH 9.1, (b) 750 µL of 1.5 mg/ml fluorescamine dissolved in dimethylsulfoxide was added to 315 µL of each diluted sample, and (c) after ≥ 20 min, fluorescence was measured with excitation at 400 nm and emission at 460 nm using a Perkin Elmer LS-50B fluorimeter. The assay had a standard error of ~1%.

NaCl and $MgCl_2$ Effects

Methods for evaluating the flocculation of decanoic acid by NaCl are described in (92). $MgCl_2$ was added to the decanoic acid solution from a 50 mM stock solution, prior to adjusting the pH to 6.83. The resulting solution was then added to a test tube containing a solid amino acid (or to an empty test tube for the control) and vortexed briefly.

Fluorescence Microscopy

This procedure was conducted as in (92); decanoic acid vesicles were labeled with the dye rhodamine 6G.

Cryo Transmission Electron Microscopy

The decanoic acid solution was added to enough solid amino acid (or nothing for a control) to yield a 10 mM solution. After 1 min, samples were vortexed for ~6 sec. Samples were then applied to glow-discharged c-flat Holey Carbon grids (Electron Microscopy Science, Hatfield, PA) and plunge-frozen into liquid ethane using a Vitrobot Mark IV (FEI, Hillsboro, OR) at 4 °C and 100% humidity. The images were collected on a FEI T12 Spirit TEM (FEI, Hillsboro, OR) under-focused by 1.9 µm at a nominal magnification of 52,000x. Linear contrast enhancement was

applied in ImageJ, a public domain program available for free download at https://imagej.nih.gov/ij/.

Turbidity

For most experiments, the decanoic acid solution was added to a test tube containing solid amino acid (or to an empty tube as control); for Fig. 6S7 and parts of Fig. 6.4B, 10 µL of a 1 M solution of amino acid in 50 mM sodium phosphate, pH 6.83 (or the buffer alone) was layered on 990 µL of the decanoic acid solution. Samples were mixed with a vortexer about one min after the addition of the solution to solid amino acid for the experiment reported in Fig. 6.3C. The timing of mixing in the other turbidity experiments is described in the figure legends. Turbidity values for individual samples were found as follows: each sample was plated in triplicate, and absorbance at 490 nm was measured three times with a Multiskan Spectrum microplate reader. The turbidity of that sample was taken to be the average of the nine readings, less the value of a water blank. The figures report the average of the sample values from multiple independent experiments, or, for Fig. 6.4B, from multiple replicate samples in one experiment. The reported standard deviations are based on these sets of values.

Critical Vesicle Concentration

This method is described in the legend of Fig. 6S10.

Critical Aggregate Concentration

Solutions of various decanoic acid concentrations, containing 30 mM sodium phosphate and 100 mM NaCl at pH 6.83, were added to solid amino acid such that the final amino acid concentration was 10 mM. Controls contained no amino acid. After ~30 sec, the solution was vortexed for ~6 sec. 30 min later, 8 µL of a 1 mg/mL solution of merocyanine 540 in 1:1 ethanol:water was added to 2.5 mL of the sample. Absorbance was measured with an Agilent 8453 Diode Array UV-Vis spectrophotometer from 400 nm to 700 nm, and the background at 650 nm was subtracted. The normalized intensity is reported as the intensity at 564 nm divided by the intensity at 530 nm, as detailed in (82).

Rehydration

Samples were dried in a 60 °C oven. Water was added to restore the original volume. After 30 min, samples were agitated gently by hand. After another 30 min, samples were heated for ~3 sec in an 80 °C water bath and then vortexed for ~2 sec. Absorbance at 490 nm was measured one day later with a Multiskan Spectrum microplate reader.

Size Exclusion Chromatography (SEC)

Vesicles were prepared as described in the "Decanoic acid solutions" section above, with or without amino acids, except that 5 mM calcein was added prior to decanoic acid. Free calcein was separated from vesicles by size exclusion chromatography over a column of Sepharose 4B equilibrated with a solution of 20 mM decanoic acid, 30 mM sodium phosphate, and 100 mM NaCl, at pH 6.83. Specifically, 0.5 ml of each sample was applied to a column containing 5 ml of Sepharose 4B, and 0.5 ml fractions were collected. Vesicles elute from the columns in the first few fractions. In each experiment, one of the first four fractions was imaged by fluorescence microscopy.

Dynamic Light Scattering

Decanoic acid solutions were prepared with 25 mM decanoic acid (rather than 50 mM) in order to avoid multiple scattering effects. Solutions were analyzed at 25 °C on a Zetasizer Nano ZS (Malvern, Worcestershire, United Kingdom) with a 633 nm helium-neon laser using back-scattering detection (at an angle of 173° to the incident light). The average diameter and polydispersity index from the cumulant method were determined using Zetasizer software (Dispersion Technology Software version 5.00). The reported data are the averages of three runs with a single sample for each condition; variation among runs was negligible. A strong indication that the comparison is valid is that both samples had a polydispersity index of 0.3, which meets Malvern's criteria for acceptable data (43). Dynamic light scattering has been previously used as an indicator of fatty acid vesicle size (44, 45); here we used it to compare two samples rather than to determine absolute values.

6.3 RESULTS

Amino Acids Bind to Decanoic Acid Vesicles

Evidence that amino acids bind to decanoic acid vesicles emerges from two types of experiments: diffusion NMR spectroscopy and filtration assays. Diffusion NMR exploits the fact that when molecules in solution bind to surfaces, even transiently, the apparent rate at which they diffuse decreases. Of the ten amino acids that are widely regarded as prebiotically plausible (287–290), we chose three characteristic structures to investigate with this technique: glycine has no side chain, leucine has a hydrophobic side chain, and serine has a hydrophilic side chain. The structures of the fatty acid and amino acids we used appear in SI Appendix, Fig. 6S1, and the experiments are summarized in Table S1. As a positive control, we chose a positively charged amino acid,

lysine, which is not considered prebiotic (287–290). Lysine should bind to negatively charged decanoic acid headgroups. We attempted to include aspartic acid (to represent amino acids with acidic side chains), but it was insoluble under our experimental conditions.

On their own in solution, amino acids move freely with single, fast diffusion coefficients, as shown in Fig. 6.1A and Table 1. When the amino acids are in the presence of decanoic acid vesicles, separate fast and slow sets of coefficients appear, which arise from the bi-exponential curves in Fig. 6.1B. The reason the fast coefficients in Fig. 6.1B (with decanoic acid) are slightly lower than in Fig. 6.1A (without decanoic acid) is likely that decanoic acid solutions have a higher bulk viscosity than water (297). The slow set of coefficients is due to binding of amino acids to decanoic acid surfaces, in accordance with other NMR diffusion results (298). This binding could be due to amino acids associating with the outer surface of vesicles and micelles (whose structures appear in SI Appendix, Fig. 6S1), traversing the vesicle membrane, or associating with the inner surface of vesicles. Within Fig. 6.1B, stronger binding is reflected in a higher y-intercept (the intensity) for the second slope; hence, leucine (which is hydrophobic) and lysine (which is positively charged) bind more strongly to decanoic acid vesicles than serine and glycine do.

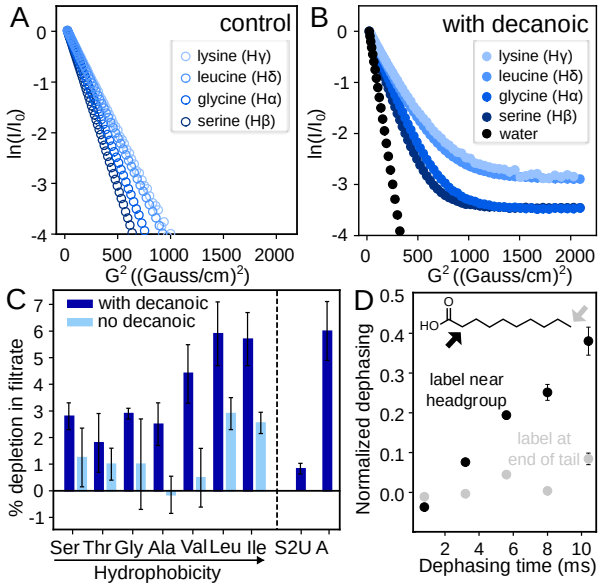

Figure 6.1. Amino acids bind to fatty acid vesicles. **A.** Lysine, leucine, glycine, and serine diffuse freely in solution with one characteristic diffusion coefficient indicated by a straight line on a plot of the square of the NMR magnetic field gradient strength (G^2, where G is dB/dz in units of Gauss/cm and B is the magnetic field) vs. normalized peak intensity (ln I/I_0). The slope of the line yields the first coefficient in Table 1. **B.** When the amino acids are in decanoic acid solutions containing micelles and vesicles, two slopes (and two diffusion coefficients) are distinguishable. Water, which is a negative control because it is not expected to bind to vesicles, shows only one

slope. **C.** Amino acids are retained with decanoic acid vesicles in a centrifugal filtration assay (dark bars). Controls (light bars) were performed in the absence of decanoic acid; given that decanoic acid is a surfactant, controls may represent an overestimate of the binding to the filtration unit that occurs in the presence of decanoic acid. Error bars represent standard errors of the mean for independent experiments conducted 7 (Ser), 10 (Thr), 5 (Gly), 17 (Ala), 5 (Val), 7 (Leu), 5 (Ile), 3 (thiouracil), 3 (adenine), and 4 (controls) times. The P values for the differences between Ser, Thr, Gly, Ala, Val, Leu, and Ile and their respective controls without decanoic acid are 0.15, 0.65, 0.25, 0.15, 0.04, 0.10, and 0.04 (Student's two-tailed *t* test). The P values for Ser, Thr, Gly and Ala compared to leucine are 0.01, 0.02, 0.06 and 0.03. Thiouracil (S2U) and adenine (A) were insufficiently soluble in the absence of decanoic acid to run controls. The hydrophobicity ranking is from (299). **D.** Leucine and the headgroups of decanoic acid molecules interact within a distance < 5 Å in lyophilized samples. $^{13}C\{^{2}H\}$ REDOR dephasing occurs when decanoic acid is labeled near its carboxyl group (filled symbols) and not when labeled at the terminal methyl group (open symbols).

	Diffusion Coefficient (m^2/s)		
	No vesicles (fast)	With vesicles (fast)	With vesicles (slow)
Water	1.692×10^{-10}	1.563×10^{-10}	Not applicable.
Serine	6.373×10^{-10}	6.132×10^{-10}	1.8×10^{-12}
Glycine	7.645×10^{-10}	7.397×10^{-10}	1.0×10^{-12}
Leucine	5.210×10^{-10}	4.951×10^{-10}	3.0×10^{-12}
Lysine	4.888×10^{-10}	4.580×10^{-10}	1.0×10^{-11}

Table 6.1. Translational diffusion coefficients for water and for amino acids in solutions with and without decanoic acid vesicles. Maximum uncertainties are ± 0.63% for water, ± 2.4% for fast coefficients of amino acids, and ± 61% for slow coefficients. The corresponding Table 6S2 lists values for each experiment and describes how experimental uncertainties were calculated. If uncertainties are neglected, the percent of each amino acid that binds to vesicles is calculated to be 3% for Gly, 3% for Ser, 5% for Leu, and 6% for Lys, in agreement with values in Fig. 6.1C.

The diffusion coefficients in Table 1 tell us that the new set of (slow) coefficients is not merely due to encapsulation of amino acids within vesicles. In samples without vesicles, leucine's diffusion coefficient corresponds to a length scale of 18 µm within the NMR time scale of 0.3 seconds (via the 1-dimensional diffusion equation $r^2 = 2Dt$, where r is the length, D is the diffusion coefficient, and t is the time). Limiting the length to 10 µm, the approximate size of a decanoic acid vesicle, would yield a diffusion coefficient of 1.7×10^{-10} m^2/s, which is two orders of

magnitude greater than for leucine in the presence of vesicles. Additional support that the slow diffusion coefficient is due to binding is that diffusion coefficients for highly mobile (*e.g.* unsaturated) phospholipids across the surface of bilayers have comparable values within uncertainty, on the order of 10^{-12} to 10^{-11} m^2/s (299).

Using an independent test of binding based on centrifugal filtration, we find that the three most hydrophobic amino acids (valine, leucine, and isoleucine) are retained to a greater extent when they are in the presence of decanoic acid vesicles and micelles (Fig. 6.1C). Retention of the four least hydrophobic amino acids (serine, threonine, glycine, and alanine) is insignificant relative to controls and is significantly less than the retention of leucine. These results support our conclusion that association of amino acids with vesicles is indeed due to binding rather than a nonspecific effect such as encapsulation within vesicles, because encapsulation would yield the same retention in all cases. To quantify the maximum signal that we would expect from nonbinding effects, we repeated the experiment with thiouracil (which differs from the nucleobase uracil by the substitution of a sulfur for an oxygen atom). We chose thiouracil because it is negligibly retained with decanoate micelles, which suggests that its binding to vesicles should be low as well (92). The result, depletion in the filtrate of 0.8 ± 0.2%, indicates that no more than ~1% of the thiouracil is depleted from the filtrate due to encapsulation in vesicles. If some or all of the ~1% is due to binding, the amount encapsulated and unbound is even lower (Fig. 6.1C). Our positive control, using the same assay for detection, was the nucleobase adenine, which interacts strongly with micelles and vesicles (92). As expected, adenine is strongly retained (Fig. 6.1C).

Our results in Fig. 6.1B-C, namely that hydrophobic and positively charged amino acids bind most strongly to fatty acid vesicles, imply that the amino acids' side chains contribute to the binding. We interrogated leucine's mode of interaction with decanoic acid by testing if it interacts with hydrogen atoms close to the headgroup of decanoic acid, with hydrogens at the end of decanoic acid's carbon chain, or both. To conduct this test, we employed rotational-echo double-resonance (REDOR) NMR spectroscopy, which measures the dipolar coupling between ^{13}C and ^{2}H nuclei. $^{13}C\{^{2}H\}$ REDOR is commonly used to probe protein-membrane interactions (300–303). We found that leucine interacts with a hydrogen near the headgroup of decanoic acid, but not at the end of the tail (Fig. 6.1D, SI Appendix, Fig. 6S2). Specifically, we lyophilized solutions containing labeled leucine and decanoic acid vesicles. We measured the dephasing of ^{13}C-labeled

leucine by two versions of decanoic acid: one ^{2}H-labeled at the 2-carbon that adjoins the carboxyl group and one ^{2}H-labeled at the 10-carbon at the end of the carbon chain. We find significant dephasing in the former case (indicating that the moieties interact over distances <5 Å) and not in the latter.

Amino Acids Increase Vesicle Stability Against Mg^{2+} and/or NaCl

What significance does the binding of amino acids to fatty acid membranes hold for the origins of life on Earth? As described in the introduction, a challenge in constructing a plausible scenario in which the first protocells incorporated fatty acid membranes is that individual, ~10 µm vesicles are unstable in the presence of divalent and monovalent ions (80) that would have been present in early oceans (278) and pools and, in the case of Mg^{2+} or Fe^{+2}, would have been required for RNA catalysis (279, 280). Here we show cases in which amino acids stabilize individual, large fatty acid vesicles against such cations.

Fig. 6.2E shows that 10 mM Mg^{2+} converts individual, ~10 µm vesicles into punctate structures (compare with Fig. 6.2A). The addition of serine or glycine, amino acids that lack hydrophobic side chains, to decanoic acid solutions with Mg^{2+} has an enormous positive effect: these amino acids convert the punctate structures back to intensely bright ~10 µm vesicles (compare Fig. 6.2B-C with 6.2F-G). In contrast, the addition of leucine, which has a hydrophobic side chain, provides no protection against the Mg^{2+} (Fig. 6.2H).

We conducted three tests to verify that the ~10 µm vesicles observed in solutions with serine are indeed vesicles rather than oil droplets. First, we showed that with or without Mg^{2+}, the vesicles can encapsulate calcein and retain it through the process of size exclusion chromatography (SI Appendix, Fig. 6S3 C-D and 6S4 C-D). In contrast, oil droplets of decanoic acid exclude calcein, so are visually distinct from vesicles (SI Appendix, Fig. 6S3 G-H). Second, we showed that the size of individual, free-floating vesicles in the presence of serine and Mg^{2+} does not visibly increase over 24 hours (SI Appendix, Fig. 6S5 K-L), whereas oil droplets coalesce unless they are on glass surfaces (304). Third, we showed that bulk solutions containing Mg^{2+} (with or without serine) do not separate with a clear layer on the bottom and an oil layer on top, as a solution of oil droplets does (SI Appendix, Fig. 6S5).

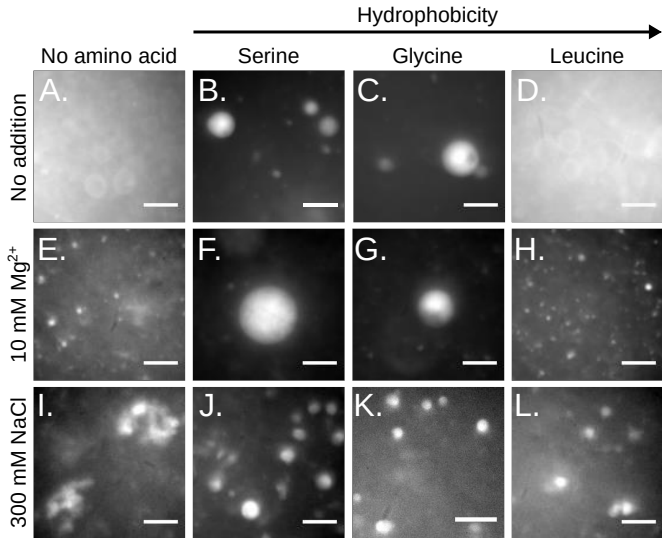

Figure 6.2. Amino acids can stabilize decanoic acid vesicles against Mg^{2+} and NaCl. **A.** Micron-scale vesicles self-assemble in the decanoic acid solution described in the Methods. **B-C.** In the presence of 10 mM serine or glycine, vesicles appear brighter, consistent with multilamellar structures. Vesicle lumens are aqueous; they can be labeled with calcein, a soluble dye (Fig. S4). **D.** In contrast, in the presence of 10 mM leucine, vesicles are indistinguishable from those in panel A. **E-H.** When the decanoic acid solutions include 10 mM Mg^{2+}, bright vesicles are retained if the solutions also contain serine or glycine. In contrast, in solutions without amino acid or in the presence of leucine, micron-scale vesicles are replaced by punctate aggregates. **I-L.** When 300 mM NaCl is added at room temperature to 80 mM decanoic acid at pH 7.65, vesicles flocculate. After heating the solution to 60 °C to disaggregate the flocs and then cooling to 30˚C, individual vesicles re-form in solutions containing 30 mM serine, glycine, or leucine. In contrast, in solutions without amino acid, flocs re-form. All panels are fluorescence micrographs; scale bars are 10 μm.

The mechanism by which Mg^{2+} eliminates individual, ~10 μm vesicles presumably involves binding of this cation to the carboxylate headgroups of the membrane. This mechanism forms the basis of three speculations: serine may block the binding of Mg^{2+} through interaction of its side chain hydroxyl group and decanoic acid headgroups; glycine may block it through interaction of its amine with the headgroups (because its amine can rotate relatively freely around the □-carbon); and leucine may fail to block the binding of Mg^{2+} because its side chain orients in the bilayer such that leucine's amine and/or carboxyl group is less accessible to fatty acid headgroups. Although our micrographs clearly show that Mg^{2+} eliminates ~10 μm decanoic acid vesicles, it is difficult to characterize the structures that replace them. At least some of the puncta are consistent with vesicles, but a few approach 1 μm in size, and poor correspondence between puncta labeled with rhodamine 6G and calcein implies that the membranes allow leakage of vesicle contents.

Individual, ~10 μm decanoic acid vesicles are also unstable in the presence of high NaCl concentrations (80). Vesicles flocculate immediately when 300 mM NaCl is added to decanoic acid solutions at room temperature, whether or not the solutions contain amino acids. However, when these solutions contain serine, glycine, or leucine (amino acids that span a wide range of hydrophobicities) and are temperature cycled, a striking, beneficial change occurs. Heating the flocs to 60 ˚C causes them to disaggregate, and as the solutions cool to 30-32 ˚C, flocs re-form in solutions without amino acids (Fig. 6.2 I), whereas serine, glycine, and leucine reduce flocculation (SI Appendix, Fig. 6S5 G-J), retaining many discrete, bright vesicles (Fig. 6.2 J-L). To confirm that these structures are vesicles rather than oil droplets, we verified that they do not behave as oil droplets: they do not float to the top of a solution in a separate layer, and they do not visibly grow over 24 hours (SI Appendix, Fig. 6S5). Our results are important because they imply that amino acids could have enabled large, individual decanoic acid vesicles to form in early oceans or drying pools, in which salt levels may have been high (278).

Vesicle Stability Against Mg^{2+} Correlates with an Increase in Lamellarity

Two lines of direct evidence imply that an amino acid's success in stabilizing individual, ~10 μm vesicles in the presence of Mg^{2+} correlates with an increase in the number of lamellae in each vesicle. The first evidence follows from the fluorescence micrographs in Fig. 6.2A-C and 6.3A-B, which show that individual vesicles are brighter in the presence of serine and glycine, suggesting that more decanoic acid membranes are present in each vesicle. As noted above, we know that the bright structures are not oil droplets because they have lumens that encapsulate calcein, whereas oil droplets exclude calcein (SI Appendix, Fig. 6S3).

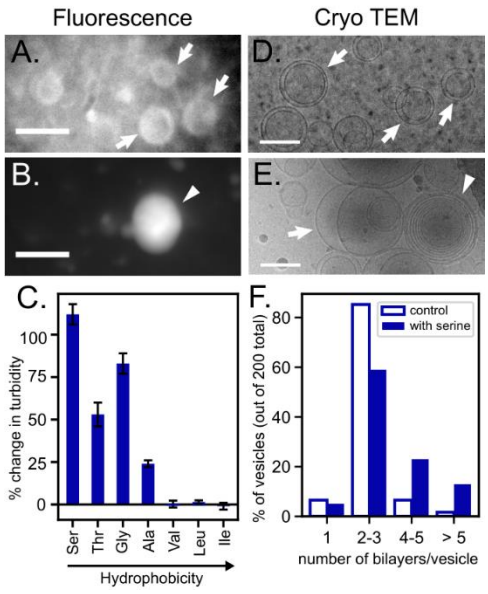

Figure 6.3. Serine increases vesicle lamellarity. **A-B**. Vesicles in the decanoic acid solution were imaged by fluorescence microscopy without (A) and with (B) 10 mM serine. Panels A and B are cropped sections of Fig. 2A-B, with linear contrast enhancement. Arrows indicate paucilamellar vesicles; wedges indicate multilamellar vesicles. Scale bars are 10 µm. **C.** Amino acids were dissolved in the decanoic acid solution to yield 10 mM solutions. Turbidity was measured by absorbance 30 minutes later. pH was constant. The graph shows the change in turbidity relative to a control without amino acid. **D-E.** Vesicle structure in decanoic acid solutions without (D) and with (E) 10 mM serine was imaged by cryo TEM. Scale bars are 100 nm. Cryo TEM records images of vesicles that are two orders of magnitude smaller than fluorescence microscopy does because vesicles >300 nm are not retained on TEM grids. **F.** The fraction of vesicles with >3 lamellae is higher in decanoic acid solutions containing serine.

Additional evidence that serine increases lamellarity comes from cryo TEM, which interrogates submicron structures. Without amino acids, > 80% of submicron vesicles are paucilamellar, with ≤ 3 nested vesicles (Fig. 6.3D and 6.3F). Only ~10% of vesicles have ≥ 4 lamellae. When vesicle solutions include serine, which stabilizes vesicles against Mg^{2+}, the percentage of vesicles with ≥ 4 lamellae jumps to > 30% (Fig. 6.3E and 6.3F). The increase in lamellarity induced by serine persists following the addition of Mg^{2+} (SI Appendix, Fig. 6S6).

An increase in lamellarity is also beneficial in the context of protocell growth and division. As Joyce and Szostak have noted: "In contrast to the behavior of multilamellar vesicles, large unilamellar vesicles are fragile and tend to rupture with extensive loss of contents under shear stress. These features combine to make multilamellar vesicles … attractive as a means of simple, environmentally driven cycles of growth and division, requiring only episodic delivery of additional amphiphiles and a moderately turbulent environment" (286).

The amino acid leucine presents an interesting counterpoint. Leucine does not protect large, ~10 μm vesicles against Mg^{2+} (Fig. 6.2). However, leucine does protect against flocculation of vesicles in the presence of NaCl. Therefore, stabilization against flocculation by NaCl does not appear to rely upon an increase in the number of lamellae.

Serine, Glycine and the Other Relatively Hydrophilic Amino Acids Increase Turbidity

Above, we showed that an increase in the number of lamellae of decanoic acid vesicles correlates with an increase in vesicle brightness when solutions contain serine (Fig. 6.3). To establish a correlation that can be measured with a higher-throughput technique, we also evaluated solution turbidity, specifically, solution absorbance at 490 nm. As summarized in Table S1, vesicle brightness (which we measured for solutions containing serine, glycine, and leucine) correlates with turbidity: the highest turbidities are observed when the four most hydrophilic amino acids (serine, threonine, glycine, and alanine) are mixed with the decanoic acid solution (Fig. 6.3C).

In these turbidity experiments, the decanoic acid solution was added to solid amino acids. Mineral surfaces (305) and ionic strength (82) are known to affect vesicle formation. To test whether the high turbidity of solutions containing the more hydrophilic amino acids results from interactions of the decanoic acid with the surfaces of the solid amino acid or from altered conditions (pH or ionic strength) in the vicinity of the dissolving amino acid, we repeated our experiments by adding amino acids as concentrated solutions rather than solids. We found that amino acids added as solutions produce the same results as when amino acids are added as solids: turbidity increases and the most hydrophilic amino acid produces the highest increase (Fig. 6S7).

Increases in solution turbidity due to amino acids can be long-lived and can arise at low concentrations. For example, when decanoic acid solutions are prepared with 10 mM serine, elevated turbidity persists at least four days (SI Appendix, Fig. 6S8), and a significant increase occurs with serine concentrations as low as 1.25 mM (SI Appendix, Fig. 6S9). The cryo TEM images in Fig. 6.3D-E suggest that the serine-induced increase in turbidity is due to an increase in vesicle lamellarity. This interpretation is consistent with a recent theoretical analysis predicting a strong effect of lamellarity on turbidity (306). We rule out that the increased turbidity is due to oil drops forming (SI Appendix, Fig. 6S3) or a decrease in the minimum concentration at which decanoic acid forms vesicles (SI Appendix, Fig. 6S10). In addition, we do not observe a significant increase in the size of individual vesicles, either by fluorescence microscopy (Fig. 6.2 and SI

Appendix, Fig. 6S3), or by dynamic light scattering analysis of the apparent hydrodynamic diameter (which was 206 nm for decanoic acid vesicles without amino acid, 205 nm with 10 mM serine). We know that the mechanism by which serine (or any other amino acid that we tested) increases lamellarity and turbidity is not through a change in solution pH because the pH values were the same before and after the addition of amino acid.

Amino Acids Plausibly Increase Vesicle Lamellarity in Pools Undergoing Wet-Dry Cycles

Damer and Deamer propose that protocells arose in pools undergoing cycles of drying and wetting (307). Concentrations of amino acids and decanoic acid in these pools could have changed in at least two scenarios. In the first scenario, all solutes in a pool could have fully dried together and then have been rehydrated simultaneously. Fig. 6.4A shows that under these conditions, the three relatively hydrophilic amino acids increase turbidity (and, presumably, the number of lamellae in each vesicle), just as in solutions that are not subjected to drying (Fig. 6.3C). Therefore, the amino acids' beneficial effects on vesicles persist through periods of drying and wetting.

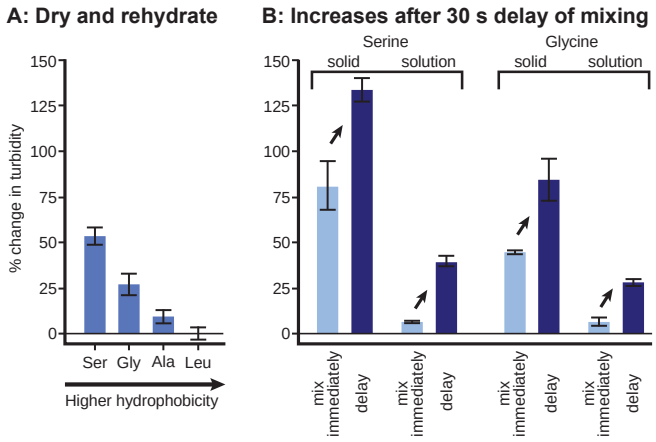

Figure 6.4. Amino acids increase turbidity of vesicle solutions in two scenarios that recapitulate pools undergoing cycles of drying and wetting. **A.** Drying and rehydration of the decanoic acid solution containing amino acids results in elevated turbidity (absorbance at 490 nm) relative to a solution without amino acids. Error bars show standard error of the mean for four experiments with glycine, alanine, and serine and show average error for two leucine experiments. **B.** Delayed mixing of decanoic acid solutions and amino acid results in higher turbidity, even when final concentrations are constant. The result holds equally well when the amino acid is a solid and when it is in solution. In "solid" samples, the decanoic acid solution was added to a test tube containing solid amino acid such that the final amino acid concentration was 10 mM. In "solution" samples, 10 µL of 1 M amino acid in 50 mM sodium phosphate at pH 6.83 (or the buffer alone) was placed on top of 990 µL of the decanoic acid solution. For both types of samples, mixing by vortexing occurred either immediately or after a delay of 30 seconds. Error bars show average error for duplicate samples.

In the second scenario, the concentration of amino acid relative to decanoic acid could have been transiently elevated. For example, a pool containing amino acids could have partially or completely dried and then fluid containing decanoic acid vesicles could have flowed in. Complete mixing would not have occurred immediately, so the concentration of amino acid would have been high within a boundary layer in contact with the dried or partially dehydrated material. The turbidity experiments in Fig. 6.3C and SI Appendix, Fig. 6S7 reproduce this scenario *in vitro* through the addition of vesicle solutions to solid amino acids or by the deposition of a concentrated amino acid solution on a vesicle solution, with a brief delay before mixing.

To determine whether the delay is required for the increased turbidity in the second scenario, we repeated the experiments in parallel with samples that were mixed immediately. The solutions mixed after a delay were indeed more turbid (and presumably contained more multilamellar vesicles) than solutions that were mixed immediately (Fig. 6.4B), whether the amino acid was serine or glycine. It is important to note that all final concentrations were equivalent, whether the solutions were mixed immediately or after a delay. These results imply that vesicle structures that form during a period of transiently high amino acid concentration, established either as the amino acid dissolves from a solid or as it diffuses from a concentrated solution, persist after dilution caused by mixing. In other words, systems of amino acids and fatty acid vesicles require a long time to reach equilibrium, even when the vesicles are composed of dynamic molecules like decanoic acid and even when solutions are mixed by vortexing.

Overall, the implication of the results in this section is that amino acids could plausibly have had large effects on protocell structure even if they were at low abundance; amino acids merely needed to be transiently held at higher concentrations, as could have occurred in pools undergoing dehydration and rehydration.

6.4 DISCUSSION AND CONCLUSIONS

We used multiple techniques to find that a set of unmodified, prebiotic amino acids binds to decanoic acid membranes and stabilizes large, ~10 μm vesicles in the presence of Mg^{2+} or NaCl. These results are important for two reasons: (1) they help explain how simple prebiotic vesicles could have survived in the presence of divalent cations and salt, and (2) they help explain how the building blocks of biological polymers co-localized with early membranes. In a prebiotic scenario,

several types of small molecules likely bound to fatty acid membranes, with varying affinities and different contributions toward stabilizing the large vesicles. Because we found dramatic differences in the consequences of binding (*e.g.* serine and glycine preserved ~10 μm vesicles in the presence of Mg^{2+} whereas leucine did not), large vesicles with a distinct repertoire of bound amino acids could have emerged even if most amino acids had equal binding affinities.

Our fluorescence microscopy, cryo TEM and turbidity data suggest that serine and glycine (amino acids that lack hydrophobic sidechains) stabilize individual large, ~10 μm fatty acid vesicles against Mg^{2+} by increasing the number of lamellae. In contrast, an amino acid that has a hydrophobic side chain (leucine) does not protect the membranes from Mg^{2+} and does not increase vesicle lamellarity (based on fluorescence microscopy and turbidity).

To our knowledge, no other researchers have previously addressed the question of whether prebiotic compounds that stabilize prebiotic fatty acid membranes also increase lamellarity. Monoacyl glycerols and long-chain alcohols probably increase membrane stability by hydrogen bonding with fatty acid headgroups (81, 282). Membrane stabilization by amino acids may also entail hydrogen bonding, particularly in the cases of serine and threonine since the sidechain of each bears a hydroxyl group. However, serine does not lower the critical vesicle concentration whereas monoacyl glycerols and long-chain alcohols do (80, 81, 282). Several other mechanisms of membrane stabilization have been proposed, but none explain our results in full. Citrate increases membrane stability by chelating Mg^{2+} (91); the structures of the amino acids we tested do not suggest chelation as a likely mechanism. Decylamine presumably stabilizes membranes via an electrostatic interaction with fatty acid headgroups (284). This mechanism may also be relevant to amino acids given that the amine group should be positively charged under conditions typically employed for formation of fatty acid vesicles. Since membranes that contain a mixture of amphiphiles are more stable than pure membranes (80, 81, 281–283), it will be interesting to determine whether amino acids stabilize large, ~10 μm vesicles of mixed composition in addition to vesicles of decanoic acid alone.

Our results (summarized in Table S1) are particularly compelling in the context of the hypothesis that protocells arose in pools undergoing cycles of drying and rehydration (307). Such cycles would have produced transiently high concentrations of amino acids. We find that transiently high serine and glycine concentrations cause increases in the turbidity of a decanoic

acid solution (a correlate of lamellarity) that persist following dilution. Our results open up exciting research questions about chemical reactions that would enable the next stage of protocell evolution – does self-assembly of vesicles and amino acids increase synthesis of peptides, and is the system sufficiently robust to support divalent cation-dependent ribozyme activity? Moreover, these discoveries reinforce our previous report that RNA bases bind to and stabilize fatty acid membranes (92). Taken together, those findings and the results reported here support a coherent scenario in which aggregates of fatty acids, which would have spontaneously self-assembled, bound the building blocks of RNA and proteins (nucleobases, ribose, and amino acids), generating the concentration and conformational constraints required for abiotic synthesis of RNA and protein.

6.5 ACKNOWLEDGEMENTS

The Keller and Drobny laboratories were supported by NASA grant NNX17AK86G (Exobiology). K.K.L. and J.A.W. were supported by NIH grant R01-GM099989. C.E.C. and A.M. were funded by the National Institutes of General Medical Sciences of the National Institutes of Health under award T32GM008268 (to C.E.C.) and T32-GM007750 (to A.M.). M.G. and A.R. were supported as undergraduate researchers by National Science Foundation grant MCB-1402059 to S.L.K. We thank our anonymous reviewers for their particularly careful reading of our manuscript and for their in-depth comments.

Figure 6S1. Structures of amino acids, the nucleobase uracil and its related base thiouracil, decanoic acid, a micelle, and a vesicle.

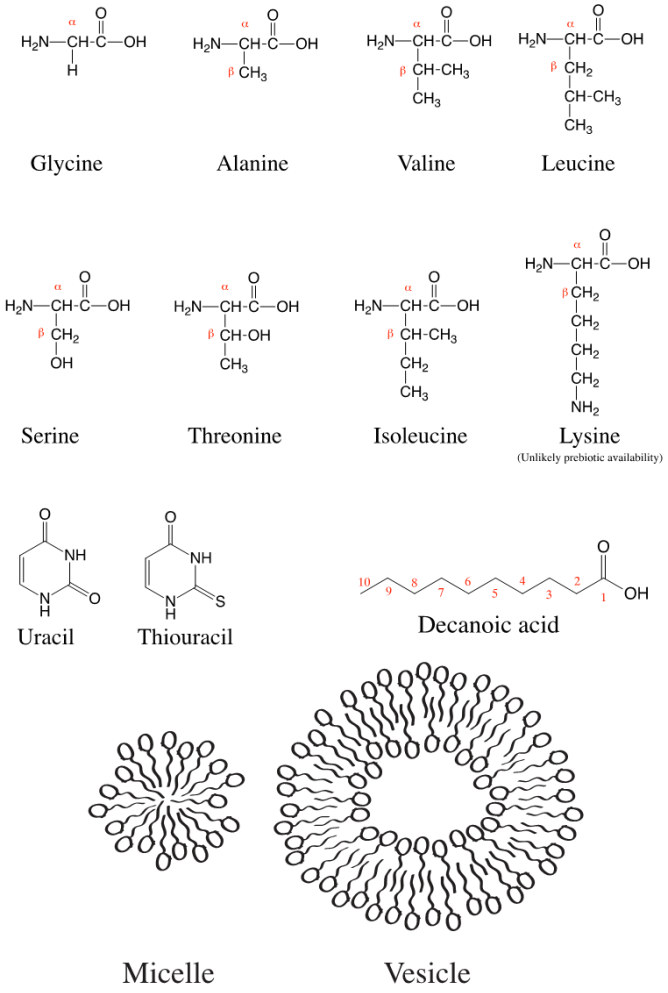

Figure 6S2. Dephasing as a function of time of leucine uniformly labeled with 13C. Dephasing is due to (A) decanoic acid 2H-labeled at the terminal methyl group of the carbon chain (decanoic-10,10,10-2H3 acid) and (B) decanoic acid 2H-labeled near the carbonyl group (decanoic-2,2-2H2 acid). The spectrum without dephasing (S0) is shown in black and the spectrum with dephasing (S1) is shown in red. ΔS is shown in blue, with a vertical offset for clarity. Note that the broad peak does not uniformly diphase. The two distinct peaks likely represent leucine molecules in two different environments: one at 177 ppm in which leucine interacts with the decanoic acid and one at 176 ppm in which it does not.

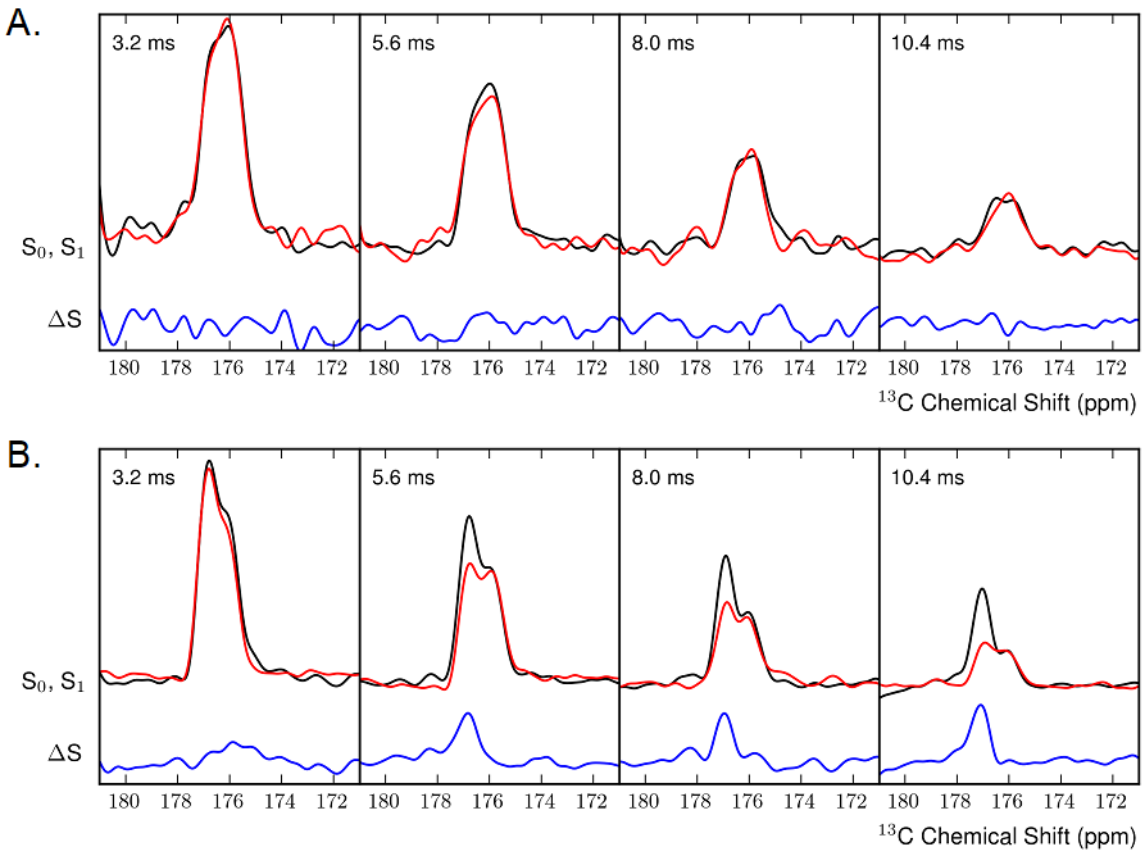

Figure 6S3. Solutions of decanoic acid (with or without serine or glycine) contain individual, ~10 μm vesicles with aqueous interiors that can be labeled with calcein. Top panels show structures labeled by rhodamine 6G, a probe that labels fatty acid membranes. Bottom panels show fluorescence from calcein, a negatively-charged hydrophilic probe that does not label membranes. Calcein that was not encapsulated in vesicles was removed by running solutions through size exclusion chromatography (SEC) column(s), as described in the Methods. All scale bars are 10 μm. A-B. In the absence of amino acid, the decanoic acid solution contains individual, ~10 μm vesicles with membranes labeled by rhodamine 6G. After only one purification step by SEC, calcein is seen both inside and outside the vesicles. C F. When 10 mM serine or glycine is included in the decanoic acid solution, bright structures are observed in both the rhodamine 6G and calcein channels, with little calcein fluorescence outside the vesicles, consistent with multilamellar vesicles that retain calcein in their interiors.

(Figure caption is continued on the next page.)

We carried out three controls to validate our SEC procedure:
1: We verified that the structures in Panels A-F are inconsistent with oil droplets.
2: We confirmed that the interiors of the vesicles in Panels A-B are aqueous.
3: We verified that our size-exclusion chromatography separates vesicles from calcein.
G-H. Control 1: We lowered the pH of the calcein-containing decanoic acid solution to 6.3 to induce the formation of oil droplets. Panel G shows that oil droplets are labeled by rhodamine 6G, and Panel H shows that calcein is excluded from oil droplets.

I J. Control 2: We ran a calcein-containing decanoic acid solution over a SEC column, merged fractions 3 and 4, ran 0.5 mL of this pool over a second SEC column to further remove excess free calcein, and then analyzed early-eluting fractions from the second run by fluorescence microscopy. As observed after only one run (Panels A-B), vesicle membranes were labeled by rhodamine 6G and the lumen was labeled by calcein. As expected, the second SEC run removed more unencapsulated calcein such that the calcein fluorescence inside the vesicles became clearly greater than outside the vesicles (unlike in panel B). The vesicles that emerged from the second SEC run were consistently smaller than after the first run.

K-L. Control 3: We measured the fluorescence intensity due to calcein (at 520 nm) for each fraction eluted from the first (Panel K) and second (Panel L) SEC runs described within Control 2. To eliminate any vesicles that might affect calcein fluorescence, the data in Panels K-L were collected after adding NaOH to each sample (to a final concentration of 1 M), which converts decanoic acid vesicles to decanoate micelles. After the first SEC run, total fluorescence from free calcein in solution appeared higher than the fluorescence associated with vesicles. After the second SEC run, the level of free calcein in solution was much lower than the level in vesicles.

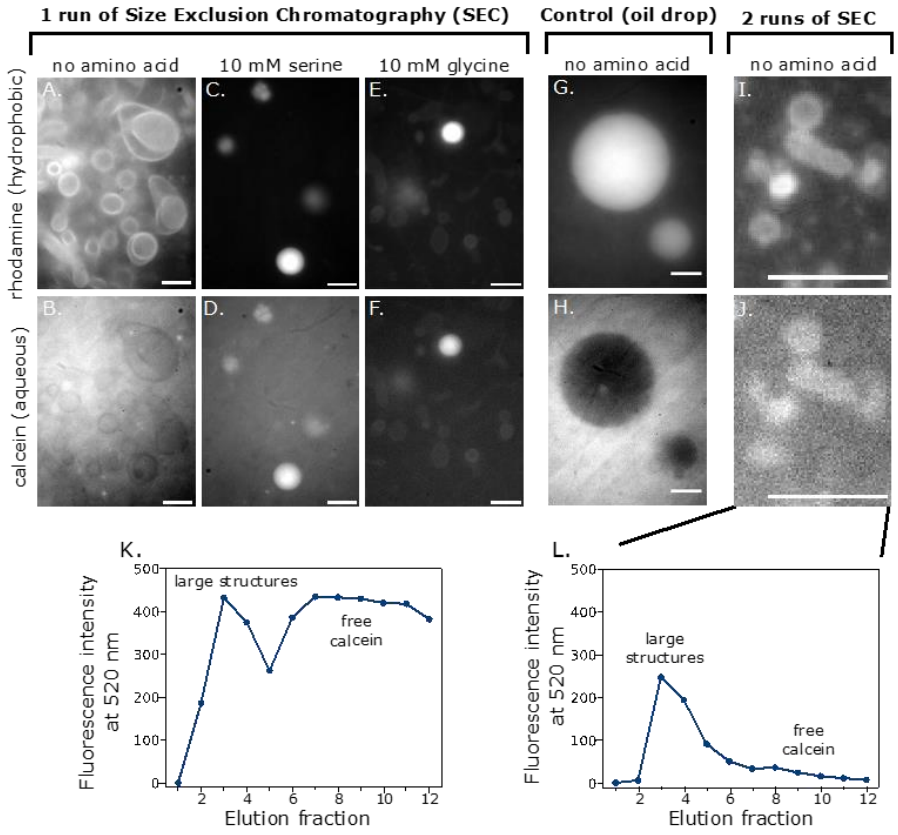

Figure 6S4. Individual, ~10 µm decanoic acid vesicles with serine are not disrupted by 10 mM Mg2+; they retain calcein in their lumens. Vesicle solutions were prepared as described in the Methods, except that 5 mM calcein was added before the decanoic acid. The pH of the solutions was then adjusted to 6.83 and serine was either added (to a final concentration of 10 mM) or not. Next, MgCl2 was added to a concentration of 10 mM, the solutions were briefly vortexed, and the pH was re-adjusted to 6.83.

Free calcein was separated from vesicles by size exclusion chromatography as described in the Methods, and early eluting fractions were used for fluorescence microscopy. Top panels show structures labeled by rhodamine 6G, a probe that labels decanoic acid membranes, and bottom panels show fluorescence due to calcein, a negatively charged, hydrophilic probe. A-B. In the absence of serine, only small structures are observed. In some cases, these structures are labeled by both rhodamine 6G and calcein, which suggests that at least some of the structures are vesicles. However, few of the vesicles approach 1 µm in size, and the poor correspondence between structures labeled with rhodamine 6G and calcein implies that the membranes allow significant leakage of vesicle contents. C-D. In the presence of both serine and Mg2+, ~10 µm structures are observed that are labeled by both rhodamine 6G and calcein. These structures are indistinguishable from those prepared in the absence of Mg2+ (compare to SI Appendix, Fig. 6S3 C-D). Scale bars are 10 µm.

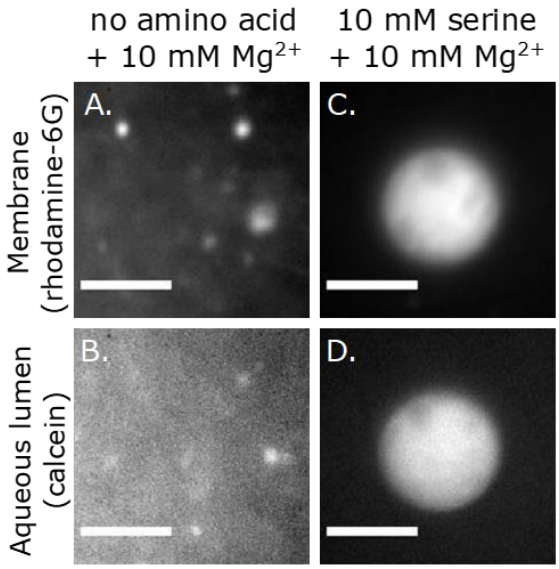

Figure 6S5. No millimeter-scale or micron-scale evidence of oil droplets appears in solutions of decanoic acid at pH 6.83, whether or not the solutions contain amino acids (serine, glycine, or leucine). All samples containing NaCl were prepared with 80 mM decanoic acid at pH 7.65, as in reference 2. NaCl was added at room temperature, and then the samples were brought to 32 ˚C, where they remained for the duration of the experiment. In the images, all test tubes are 13 mm wide and were photographed with an iPhone camera under ambient light.

(Figure caption is continued on the next page.)

Millimeter-scale Behavior: A. Decanoic acid solutions at pH 6.83 appear uniformly cloudy because they contain paucilamellar micron-scale vesicles. B. Shifting the pH to 6.1 causes oil droplets of decanoic acid to form. When solutions with oil droplets are allowed to sit for 24 h, the bottom half of the solutions becomes relatively clear because oil droplets have floated to the top of the test tube. C-F. The appearance of solutions containing 10 mM Mg2+ is inconsistent with the formation of oil droplets: the solution at the bottom of the test tubes is not more clear than at the top. Mg2+ destabilizes individual, ~10 µm vesicles (Fig. 2). Mg2+ also appears to cause some precipitate to form at the bottom of the test tubes. G-J. The appearance of solutions containing 300 mM NaCl is also inconsistent with the formation of oil droplets: the solution at the bottom of the test tubes is not more clear than at the top. In Panel G, millimeter-scale flocs are observed, and reduced flocculation is seen in Panel J.

Micrometer-scale Behavior: All samples contain rhodamine 6G, a fluorophore that labels decanoic acid membranes and oil droplets. All scale bars on fluorescence micrographs are 10 µm. K-N, Q-V. In solutions containing serine, glycine, or leucine, with Mg2+ or NaCl as indicated, micron-scale structures persist after 24 h without significantly increasing in size. The lumens of at least some of the structures are not labeled by rhodamine 6G, in contrast to oil droplets, which have interiors labeled by this dye (SI Appendix, Fig. S3, Panel G) and should coalesce over time. O-P. In solutions containing Mg2+ and leucine, vesicles with distinct lumens appear after 24 h.

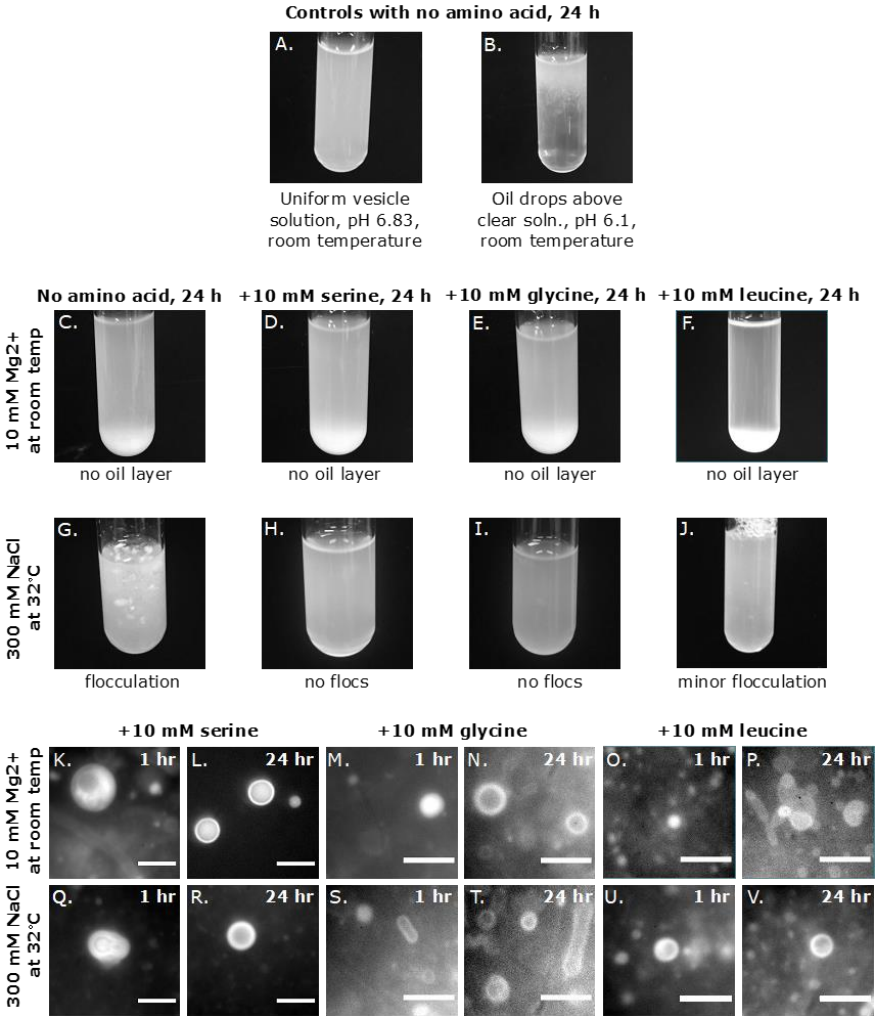

Figure 6S6. Cryo TEM shows that with serine present, multilamellar vesicles persist in the presence of 10 mM Mg2+. A. No amino acid added. B. 10 mM serine added. Cryo TEM records images of vesicles that are smaller than vesicles seen in fluorescence micrographs because vesicles larger than 300 nm are not retained on TEM grids. Vesicles less than 50 nm in diameter persist in the presence of 10 mM Mg2+ even without addition of any amino acid; these vesicles would be unresolvable by fluorescence microscopy. Scale bars are 100 nm.

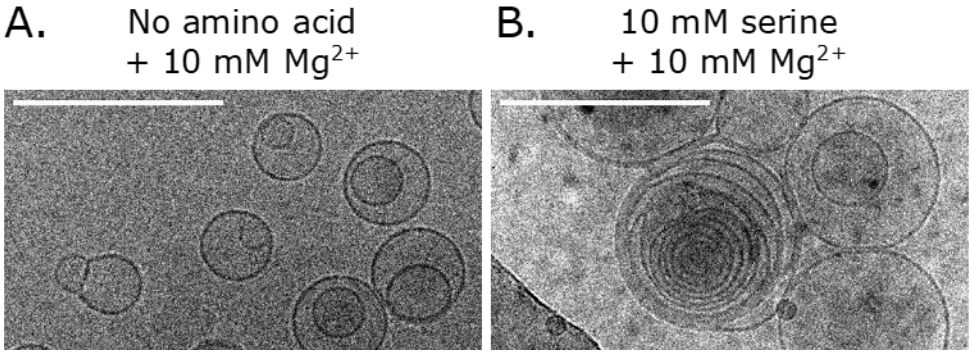

Figure 6S7. Amino acids increase the turbidity (the absorbance at 490 nm) of the decanoic acid solution when added as concentrated solutions. 10 µL of a 1 M solution of each amino acid in 50 mM sodium phosphate at pH 6.83 ± 0.03 was overlaid on 990 µL of a solution that contained 50 mM decanoic acid, 30 mM sodium phosphate, and 100 mM NaCl at pH 6.83. Twenty seconds later, the sample was vortexed for ~6 seconds. For a control, 10 µl of the same phosphate buffer (with no amino acid) was added. The relative effectiveness of the amino acids, with diminished turbidity for more hydrophobic amino acids, is similar to that seen when the amino acids are added as solids (c.f. Fig 6.3C in the main text).

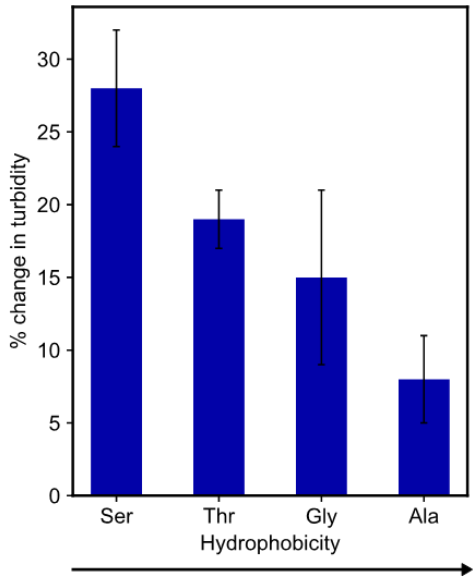

Figure 6S8. The increase in turbidity in decanoic acid solutions caused by the addition of serine and glycine decays over a period of days. The decanoic acid solution was added to solid amino acid such that the resulting solution contained 10 mM amino acid, or to an empty tube as a control. One minute later, samples were vortexed for ~6 seconds. Turbidity (absorbance at 490 nm) of the samples was determined 30 minutes later and then daily. The figure records the percentage change of the test with respect to the control. Three experiments were conducted: one extended through Day 2 and two extended through Day 4. Standard errors of the mean are shown for Days 0, 1, and 2, and average errors are shown for Days 3 and 4, unless the errors are smaller than the symbols.

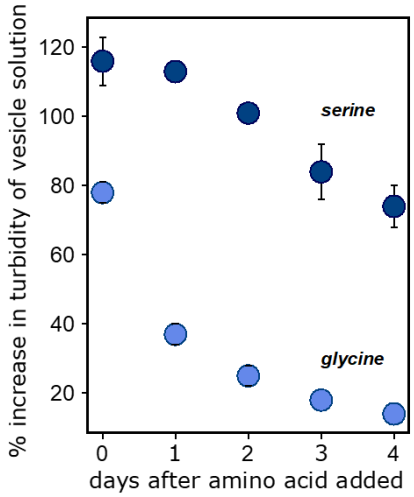

Figure 6S9. At concentrations of 1.25 mM and higher, amino acids serine and glycine significantly increase turbidity of solutions containing decanoic acid vesicles, and the effect increases with concentration of the amino acid. The decanoic acid solution was added to a test tube containing solid amino acid such that the final amino acid concentration was 0, 1.25, 2.5, 5 or 10 mM. One minute after each addition, samples were vortexed for ~6 seconds. Turbidity, measured by absorbance at 490 nm, was determined 30 minutes later. The graph shows the percent increase in turbidity relative to the control with no amino acid. Each point is the average of at least three experiments. Error bars denote standard deviations, including when the error is smaller than the symbol size.

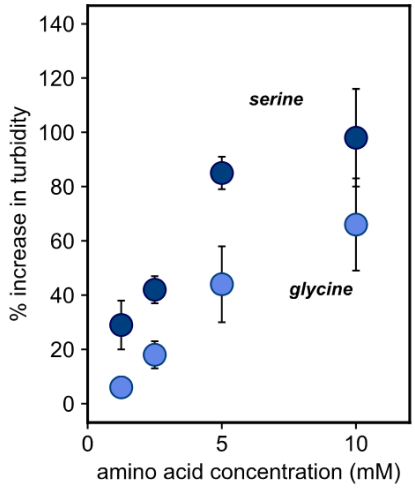

Figure 6S10. Serine does not affect the critical vesicle concentration of decanoic acid solutions, as determined by two methods. A. Solutions containing 25 mM decanoic acid, 30 mM sodium phosphate, and 100 mM NaCl at pH 6.83, with and without 10 mM serine, were diluted until the concentration of decanoic acid was as low as 10 mM. The diluting solution contained all of the same compounds except decanoic acid. The critical vesicle concentration was identified as a sharp change in the absorbance of the sample at 490 nm. B. The critical vesicle concentration was measured via an assay that employs merocyanine 540, a dye. The absorption spectrum of this dye shifts in hydrophobic environments, including surfactant aggregates (7). Solutions containing 10-25 mM decanoic acid with or without 10 mM serine were prepared as in the Methods. At least 30 min later, 8 µL of 1 mg/mL merocyanine 540 that had been dissolved in 1:1 water:ethanol was added to 2.5 mL of each decanoic acid solution. The critical aggregate concentration was measured as in (3). Briefly, each sample's absorbance was measured at 530, 564, and 630 nm (denoted A_{530}, A_{564}, and A_{630}). The critical aggregate concentration was identified by a sharp change in the quantity: $(A_{564} - A_{630})/(A_{530} - A_{630})$.

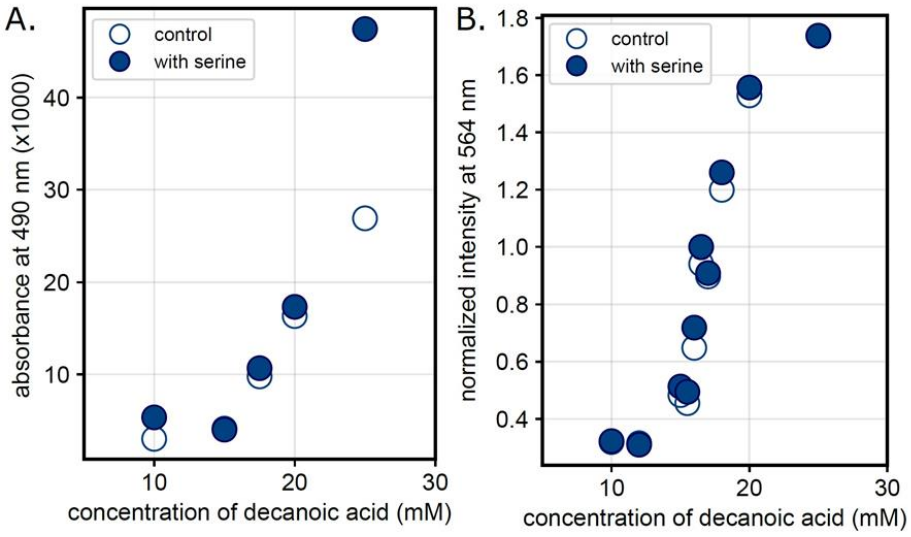

Table 6S1. Summary of Results.

Lys	Ser	Thr	Gly	Ala	Val	Leu	Ile
	(These seven amino acids are considered prebiotic.)						

Diffusion NMR	**Yes**	**Yes**	**–**	**Yes**	**–**	**–**	**Yes**	**–**
Strength of evidence	Strong	Strong	–	Strong	–	–	Strong	–
Retention w/ vesicles	**–**	**Maybe**	**Maybe**	**Maybe**	**Yes**	**Yes**	**Yes**	**Yes**
Strength of evidence	–	Error bars overlap control	Error bars overlap control	Error bars overlap control	Clearly exceeds control	Clearly exceeds control	Clearly exceeds control	Clearly exceeds control

Cryo TEM w/ more layers	**–**	**Yes**	**–**	**–**	**–**	**–**	**–**	**–**
Strength of evidence	–	Strong	–	–	–	–	–	–
Increase in brightness	**–**	**Yes**	**–**	**Yes**	**–**	**–**	**No**	**–**
Strength of evidence	–	Strong	–	Strong	–	–	Strong	–
Protects vs. 10mM Mg2+	**–**	**Yes**	**–**	**Yes**	**–**	**–**	**No**	**–**
Strength of evidence	–	Strong	–	Strong	–	–	Strong	–
Protects vs. 300 mM NaCl	**–**	**Yes**	**–**	**Yes**	**–**	**–**	**Some**	**–**
Strength of evidence	–	Strong	–	Strong	–	–	Strong	–
Increase in turbidity	**–**	**Yes**	**Yes**	**Yes**	**Yes**	**No**	**No**	**No**
Strength of evidence	–	Strong data. Indirect result likely due to more lamellae	Strong data. Indirect result likely due to more lamellae	Strong data. Indirect result likely due to more lamellae	Strong data. Indirect result likely due to more lamellae	Strong data. Indirect result likely due to more lamellae	Strong data. Indirect result likely due to more lamellae	Strong data. Indirect result likely due to more lamellae

Table 6S2. Diffusion coefficients of amino acids and water in solutions without and with decanoic acid.

		Diffusion Coefficient (m^2/s)		
		fast	**slow**	**water**
Samples *without* decanoic acid vesicles	Glycine	$7.6445\times10^{-10} \pm 1.6\times10^{-13}$	none	$1.69715\times10^{-9} \pm 3.7\times10^{-13}$
	Leucine Trial 1	$5.20932\times10^{-10} \pm 8.4\times10^{-14}$	none	$1.67917\times10^{-9} \pm 2.8\times10^{-13}$
	Leucine Trial 2	$5.21152\times10^{-10} \pm 7.4\times10^{-14}$	none	$1.68409\times10^{-9} \pm 3.1\times10^{-13}$
	Serine	$6.3733\times10^{-10} \pm 3.86\times10^{-13}$	none	$1.69553\times10^{-9} \pm 5.7\times10^{-13}$
	Lysine	$4.8876\times10^{-10} \pm 5.8\times10^{-13}$	none	$1.70501\times10^{-9} \pm 2.0\times10^{-13}$
Samples *with* decanoic acid vesicles	Glycine	$7.3974\times10^{-10} \pm 2.4\times10^{-13}$	$1.04\times10^{-12} \pm 3.1\times10^{-13}$	$1.59499\times10^{-9} \pm 3.3\times10^{-13}$
	Leucine Trial 1	$4.9420\times10^{-10} \pm 1.5\times10^{-13}$	$2.98\times10^{-12} \pm 1.9\times10^{-13}$	$1.52258\times10^{-9} \pm 2.8\times10^{-13}$
	Leucine Trial 2	$4.9601\times10^{-10} \pm 1.33\times10^{-13}$	$2.98\times10^{-12} \pm 1.8\times10^{-13}$	$1.53912\times10^{-9} \pm 1.9\times10^{-13}$
	Serine	$6.1322\times10^{-10} \pm 6.3\times10^{-13}$	$1.76\times10^{-12} \pm 1.07\times10^{-12}$	$1.5932\times10^{-9} \pm 5\times10^{-13}$
	Lysine	$4.580\times10^{-10} \pm 1.7\times10^{-12}$	$1.03\times10^{-11} \pm 2.1\times10^{-12}$	$1.56629\times10^{-9} \pm 2.0\times10^{-13}$

COMPLETE BIBLIOGRAPHY

1. Robertson, J.L. 2018. The lipid bilayer membrane and its protein constituents. J. Gen. Physiol. 150: 1472–1483.
2. Hooke, R. 1665. Micrographia, or, Some physiological descriptions of minute bodies made by magnifying glasses: With observations and inquiries thereupon. London: Jo. Martyn and Ja. Allestry.
3. Pfeffer, W. 1877. Osmotische Untersuchungen. Engelmann, Leipzig P.
4. Perouansky, M. 2015. The Overton in Meyer – Overton: a biographical sketch commemorating the 150th anniversary of Charles Ernest Overton's birth. Br. J. Anaesth. 114: 537–541.
5. Meyer, H. 1899. Zur Theorie der Alkoholnarkose Erste Mittheilung. Welche Eigenschaft der Anästhetica bedingt ihre narkotische Wirkung? Arch. für Exp. Pathol. und Pharmakologie. 42: 109–118.
6. Overton, C.E. 1901. Studien uber die narkose: zugleich ein beitrag zur allgemeinen pharmakologi. Jena: Gustav Fischer.
7. Rayleigh, L. 1890. Measurements of the amount of oil necessary in order to check the motions of camphor upon water. Proc. R. Soc. London. 47: 364–367.
8. Pockels, A. 1892. On the Relative Contamination of the Water-Surface by Equal Quantities of Different Substances. Nature. 46: 418–419.
9. Langmuir, I. 1917. The Constitution and Fundamental Properties of Solids and Liquids. II. Liquids. J. Am. Chem. Soc. 39: 1848–1906.
10. Gorter, E., and F. Grendel. 1924. On bimolecular layers of lipoids on the chromocytes of the blood. J. Exp. Med. 41: 439–443.
11. Robertson, J.D. 1959. The Ultrastructure of Cell Membranes and Their Derivatives. Biochem. Soc. Symp. 16: 3–43.
12. Levine, Y.K., and M.H.F. Wilkins. 1971. Structure of Oriented Lipid Bilayers. Nature. 230: 69–72.
13. Wilkins, M.H.F., A.E. Blaurock, and D.M. Engelman. 1971. Bilayer Structure in Membranes. Nature. 230: 72–76.
14. Singer, S.J., and G.L. Nicolson. 1972. The Fluid Mosaic Model of the Structure of Cell Membranes. Science. 175: 720–731.
15. Gobley, T.N. 1947. Recherches Chimiques sur le Jaune d'Oeuf (Deuxième Mémoire). J. Pharm. Chim. 11: 409–417.
16. van Meer, G., D.R. Voelker, and G.W. Feigenson. 2008. Membrane lipids: where they are and how they behave. Nat. Rev. Mol. Cell Biol. 9: 112–124.
17. Seddon, J.M., and R.H. Templer. 1995. Polymorphism of Lipid-Water Systems. Handb. Biol. Phys. 1: 97–160.
18. Seifert, U., K. Berndl, and R. Lipowsky. 1991. Shape transformations of vesicles : Phase diagram for spontaneous- curvature and bilayer-coupling models. Phys. Rev. A. 44: 1182–1202.
19. Nagle, J.F., and S. Tristram-Nagle. 2000. Structure of lipid bilayers. Biochim. Biophys. Acta. 1469: 159–195.
20. Marsh, D. 2009. Cholesterol-induced fluid membrane domains: A compendium of lipid-raft ternary phase diagrams. Biochim. Biophys. Acta - Biomembr. 1788: 2114–2123.
21. Ejsing, C.S., J.L. Sampaio, V. Surendranath, E. Duchoslav, K. Ekroos, R.W. Klemm, K. Simons, and A. Shevchenko. 2009. Global analysis of the yeast lipidome by quantitative

shotgun mass spectrometry. Proc. Natl. Acad. Sci. 106: 2136–2141.
22. Sampaio, J.L., M.J. Gerl, C. Klose, C.S. Ejsing, H. Beug, and K. Simons. 2011. Membrane lipidome of an epithelial cell line. Proc. Natl. Acad. Sci. 108: 1903–1907.
23. Hjort Ipsen, J., G. Karlström, O.G. Mourtisen, H. Wennerström, and M.J. Zuckermann. 1987. Phase equilibria in the phosphatidylcholine-cholesterol system. BBA - Biomembr. 905: 162–172.
24. Ferguson, F.D., and T.K. Jones. 1966. The Phase Rule. London: Butterworths & Co. (Publishers) Ltd.
25. Veatch, S.L., and S.L. Keller. 2005. Seeing spots: Complex phase behavior in simple membranes. Biochim. Biophys. Acta - Mol. Cell Res. 1746: 172–185.
26. Blosser, M.C., C.E. Cornell, S.P. Rayermann, and S.L. Keller. 2019. Phase diagrams and tie-lines in GUVs. In: Dimova R, C Marques, editors. The Giant Vesicle Book. Milton Park: Taylor & Francis.
27. Veatch, S.L., K. Gawrisch, and S.L. Keller. 2006. Closed-loop miscibility gap and quantitative tie-lines in ternary membranes containing diphytanoyl PC. Biophys. J. 90: 4428–4436.
28. Marsh, D. 2010. Liquid-ordered phases induced by cholesterol: A compendium of binary phase diagrams. Biochim. Biophys. Acta - Biomembr. 1798: 688–699.
29. Simons, K., and E. Ikonen. 1997. Functional rafts in cell membranes. Nature. 387: 569–572.
30. Simons, K., and W.L.C. Vaz. 2004. Model systems, lipid rafts, and cell membranes. Annu. Rev. Biophys. Biomol. Struct. 33: 269–295.
31. Dietrich, C., L.A. Bagatolli, Z.N. Volovyk, N.L. Thompson, M. Levi, K. Jacobson, and E. Gratton. 2001. Lipid rafts reconstituted in model membranes. Biophys. J. 80: 1417–1428.
32. Veatch, S.L., and S.L. Keller. 2005. Miscibility phase diagrams of giant vesicles containing sphingomyelin. Phys. Rev. Lett. 94: 3–6.
33. Veatch, S.L., and S.L. Keller. 2002. Organization in Lipid Membranes Containing Cholesterol. Phys. Rev. Lett. 89: 11–14.
34. Veatch, S.L., and S.L. Keller. 2003. Separation of liquid phases in giant vesicles of ternary mixtures of phospholipids and cholesterol. Biophys. J. 85: 3074–3083.
35. Vossenberg, J.L.C.M. Van De, A.J.M. Driessen, and W.N. Konings. 1998. The essence of being extremophilic : the role of the unique archaeal membrane lipids. Extremophiles. 2: 163–170.
36. Kara, S., S. Afonin, O. Babii, A.N. Tkachenko, I. V Komarov, and A.S. Ulrich. 2017. Diphytanoyl lipids as model systems for studying membrane-active peptides. Biochim. Biophys. Acta - Biomembr. 1859: 1828–1837.
37. Recktenwald, D.J., and H.M. McConnell. 1981. Phase Equilibria in Binary Mixtures of Phosphatidylcholine and Cholesterol. Biochemistry. 20: 4505–4510.
38. Heberle, F.A., J. Wu, S.L. Goh, R.S. Petruzielo, and G.W. Feigenson. 2010. Comparison of Three Ternary Lipid Bilayer Mixtures : FRET and ESR Reveal Nanodomains. Biophys. J. 99: 3309–3318.
39. Heberle, F.A., R.S. Petruzielo, J. Pan, P. Drazba, N. Kucerka, R.F. Standaert, G.W. Feigenson, and J. Katsaras. 2013. Bilayer thickness mismatch controls domain size in model membranes. J. Am. Chem. Soc. 135: 6853–6959.
40. Scott, H.L., A. Skinkle, E.G. Kelley, M.N. Waxham, I. Levental, and F.A. Heberle. 2019. On the mechanism of bilayer separation by extrusion, or why your LUVs are not really

unilamellar. Biophys. J. 117: 1381–1386.
41. Bangham, A.D., and R.W. Horne. 1964. Negative Staining of Phospholipids and their Structural Modification by Surface-active Agents as observed in. J. Mol. Biol. 8: 660–668.
42. Bagatolli, L.A. 2006. To see or not to see: Lateral organization of biological membranes and fluorescence microscopy. Biochim. Biophys. Acta - Biomembr. 1758: 1541–1556.
43. Sezgin, E., T. Sadowski, and K. Simons. 2014. Measuring Lipid Packing of Model and Cellular Membranes with Environment Sensitive Probes. Langmuir. 30: 8160–8166.
44. Klymchenko, A.S., and R. Kreder. 2014. Fluorescent Probes for Lipid Rafts : From Model Membranes to Living Cells. Chem. Biol. 21: 97–113.
45. Sezgin, E., I. Levental, M. Grzybek, G. Schwarzmann, V. Mueller, A. Honigmann, V.N. Belov, C. Eggeling, Ü. Coskun, K. Simons, and P. Schwille. 2012. Partitioning, diffusion, and ligand binding of raft lipid analogs in model and cellular plasma membranes. Biochim. Biophys. Acta - Biomembr. 1818: 1777–1784.
46. Cornell, C.E., N.L.C. McCarthy, K.R. Levental, I. Levental, N.J. Brooks, and S.L. Keller. 2017. n-Alcohol Length Governs Shift in Lo-Ld Mixing Temperatures in Synthetic and Cell-Derived Membranes. Biophys. J. 113: 1200–1211.
47. Angelova, M.I., S. Soleau, P. Méléard, J.F. Faucon, and P. Bothorel. 1992. Preparation of giant vesicles by external AC electric fields. Kinetics and applications. Prog. Colloid Polym. Sci. 89: 127–131.
48. Gray, E., J. Karslake, B.B. Machta, and S.L. Veatch. 2013. Liquid general anesthetics lower critical temperatures in plasma membrane vesicles. Biophys. J. 105: 2751–2759.
49. Belkin, M., and W.G. Hardy. 1961. Relation Between Water Permeability and Integrity of Sulfhydryl Groups in Malignant and Normal Cells. J. Biophys. Biochem. Cytol. 9: 733–745.
50. Scott, R.E. 1976. Plasma membrane vesiculation: a new technique for isolation of plasma membranes. Science. 12: 743–745.
51. Baumgart, T., A.T. Hammond, P. Sengupta, S.T. Hess, D.A. Holowka, B.A. Baird, and W.W. Webb. 2007. Large-scale fluid/fluid phase separation of proteins and lipids in giant plasma membrane vesicles. Proc. Natl. Acad. Sci. U.S.A. 104: 3165–3170.
52. Mitra, K., I. Ubarretxena-belandia, T. Taguchi, G. Warren, and D.M. Engelman. 2004. Modulation of the bilayer thickness of exocytic pathway membranes by membrane proteins rather than cholesterol. Proc. Natl. Acad. Sci. 101: 4083–4088.
53. Dupuy, A.D., and D.M. Engelman. 2008. Protein area occupancy at the center of the red blood cell membrane. Proc. Natl. Acad. Sci. 105: 2848–2852.
54. Mesmin, B., and F.R. Maxfield. 2009. Intracellular sterol dynamics. Biochim. Biophys. Acta. 1791: 636–645.
55. Swatsgood, M., and M. Schindler. 1989. Lateral Diffusion of Lectin Receptors in Fibroblast Membranes as a Function of Cell Shape. Exp. Cell Res. 180: 515–528.
56. Wier, M.L., and M. Edidin. 1986. Effects of Cell Density and Extracellular Matrix on the Lateral Diffusion of Major Histocompatibility Antigens in Cultured Fibroblasts. J. Cell Biol. 103: 215–222.
57. Sako, Y., and A. Kusumi. 1995. Barriers for Lateral Diffusion of Transferrin Receptor in the Plasma Membrane as Characterized by Receptor Dragging by Laser Tweezers : Fence versus Tether. J. Cell Biol. 129: 1559–1574.
58. Sheets, E.D., G.M. Lee, R. Simson, and K. Jacobson. 1997. Transient Confinement of a Glycosylphosphatidylinositol-Anchored Protein in the Plasma Membrane. Biochemistry.

36: 12449–12458.
59. Sperotto, M.M., and O.G. Mouritsen. 1991. Monte Carlo simulation studies of lipid order parameter profiles near integral membrane proteins. Biophys. J. 59: 261–270.
60. Simons, K., and D. Toomre. 2000. Lipid Rafts and Signal Transduction. Nat. Rev. Mol. Cell Biol. 1: 31–39.
61. Machta, B.B., S. Papanikolaou, J.P. Sethna, and S.L. Veatch. 2011. Minimal model of plasma membrane heterogeneity requires coupling cortical actin to criticality. Biophys. J. 100: 1668–1677.
62. Veatch, S.L., P. Cicuta, P. Sengupta, A.R. Honerkamp-Smith, D. Holowka, and B.A. Baird. 2008. Critical fluctuations in plasma membrane vesicles. ACS Chem. Biol. 3: 287–293.
63. Honerkamp-Smith, A.R., P. Cicuta, M.D. Collins, S.L. Veatch, M. den Nijs, M. Schick, and S.L. Keller. 2008. Line Tensions, Correlation Lengths, and Critical Exponents in Lipid Membranes Near Critical Points. Biophys. J. 95: 236–246.
64. Levental, K.R., and I. Levental. 2015. Giant Plasma Membrane Vesicles: Models for Understanding Membrane Organization. In: Kenworthy A, editor. Current Topics in Membranes. . pp. 25–57.
65. Kaiser, H.-J., D. Lingwood, I. Levental, J.L. Sampaio, L. Kalvodova, L. Rajendran, and K. Simons. 2009. Order of lipid phases in model and plasma membranes. Proc. Natl. Acad. Sci. U. S. A. 106: 16645–16650.
66. Levental, K.R., J.H. Lorent, X. Lin, A.D. Skinkle, M.A. Surma, E.A. Stockenbojer, A.A. Gorfe, and I. Levental. 2016. Polyunsaturated Lipids Regulate Membrane Domain Stability by Tuning Membrane Order. Biophys. J. 110: 1800–1810.
67. Sezgin, E., T. Gutmann, T. Buhl, R. Dirkx, M. Grzybek, Ü. Coskun, M. Solimena, K. Simons, I. Levental, and P. Schwille. 2015. Adaptive Lipid Packing and Bioactivity in Membrane Domains. PLoS One. 10: 1–14.
68. Lorent, J.H., B. Diaz-Rohrer, X. Lin, K. Spring, A.A. Gorfe, K.R. Levental, and I. Levental. 2016. Structural determinants and functional consequences of protein affinity for membrane rafts. Biophys. J. 110: 205a.
69. Moor, H., and K. Muhlethaler. 1963. Fine structure in frozen-etched yeast cells. J. Cell Biol. 17: 609–628.
70. Toulmay, A., and W.A. Prinz. 2013. Direct imaging reveals stable, micrometer-scale lipid domains that segregate proteins in live cells. J. Cell Biol. 202: 35–44.
71. Seo, A.Y., P. Lau, D. Feliciano, P. Sengupta, M.A. Le Gros, B. Cinquin, C.A. Larabell, and J. Lippincott-Schwartz. 2017. AMPK and vacuole-associated Atg14p orchestrate m - lipophagy for energy production and long-term survival under glucose starvation. Elife. 6: e21690.
72. Wang, C., Y. Miao, and Y. Chang. 2014. A sterol-enriched vacuolar microdomain mediates stationary phase lipophagy in budding yeast. J. Cell Biol. 206: 357–366.
73. Tsuji, T., and T. Fujimoto. 2018. Lipids and lipid domains of the yeast vacuole. Biochem. Soc. Trans. : 1–8.
74. Rayermann, S.P., G.E. Rayermann, C.E. Cornell, A.J. Merz, and S.L. Keller. 2017. Hallmarks of reversible separation of living, unperturbed cell membranes into two liquid phases. Biophys. J. 113: 2425–2432.
75. Numrich, J., M. Pe, H. Arlt, A. Sardu, J. Griffith, T. Levine, S. Engelbrecht-vandre, F. Reggiori, C. De Virgilio, and C. Ungermann. 2015. The I-BAR protein Ivy1 is an effector

of the Rab7 GTPase Ypt7 involved in vacuole membrane homeostasis. J. Cell Sci. 128: 2278–2292.
76. Murley, A., J. Yamada, B.J. Niles, A. Toulmay, W.A. Prinz, and T. Powers. 2017. Sterol transporters at membrane contact sites regulate TORC1 and TORC2 signaling. J. Cell Biol. 216: 2679–2689.
77. Murley, A., R.D. Sarsam, A. Toulmay, J. Yamada, W.A. Prinz, and J. Nunnari. 2015. Ltc1 is an ER-localized sterol transporter and a component of ER–mitochondria and ER–vacuole contacts. J. Cell Biol. 209: 539–548.
78. Morigaki, K., and P. Walde. 2007. Fatty Acid Vesicles. Curr. Opin. Colloid Interface Sci. 12: 75–80.
79. Deamer, D., J.P. Dworkin, S.A. Sandford, M.. . Bernstein, and L.J. Allamandola. 2002. The First Cell Membranes. Astrobiology. 2: 371–381.
80. Monnard, P.-A., C.L. Apel, A. Kanavarioti, and D.W. Deamer. 2002. Influence of ionic inorganic solutes on self-assembly and polymerization processes related to early forms of life: implications for a prebiotic aqueous medium. Astrobiology. 2: 139–152.
81. Apel, C.L., D.W. Deamer, and M.N. Mautner. 2002. Self-assembled vesicles of monocarboxylic acids and alcohols: conditions for stability and for the encapsulation of biopolymers. Biochim. Biophys. Acta. 1559: 1–9.
82. Maurer, S.E., and G. Nguyen. 2016. Prebiotic vesicle formation and the necessity of salts. Orig. Life Evol. Biosph. 46: 215–222.
83. Black, R.A., and M.C. Blosser. 2016. A Self-Assembled Aggregate Composed of a Fatty Acid Membrane and the Building Blocks of Biological Polymers Provides a First Step in the Emergence of Protocells. Life. 6.
84. Xue, M., R.A. Black, C.E. Cornell, G.P. Drobny, and S.L. Keller. 2020. A Step toward Molecular Evolution of RNA : Ribose Binds to Prebiotic Fatty Acid Membranes , and Nucleosides Bind Better than Individual Bases Do. ChemBioChem. 21: 1–5.
85. Dzieciol, A.J., and S. Mann. 2012. Designs for life : protocell models in the laboratory elected as a Fellow of the. Chem. Soc. Rev. 41: 79–85.
86. Zhu, T.F., and J.W. Szostak. 2009. Coupled Growth and Division of Model Protocell Membranes. JACS. 131: 5705–5713.
87. Chen, I.A., and J.W. Szostak. 2004. Membrane growth can generate a transmembrane pH gradient in fatty acid vesicles. Proc. Natl. Acad. Sci. 101: 7965–7970.
88. Lawless, J.G., M. Field, and G.U. Yuen. 1979. Quantification of monocarboxylic acids in the Murchison carbonaceous meteorite. Nature. 282: 396–398.
89. Proskurowski, G., M.D. Lilley, J.S. Seewald, G.L. Früh-, E.J. Olson, J.E. Lupton, S.P. Sylva, D.S. Kelley, G. Proskurowski, M.D. Lilley, S. Seewald, and G.L. Friih-green. 2008. Abiogenic hydrocarbon production at Lost City hydrothermal field. Science (80-.). 319: 604–607.
90. Monnard, P.-A., C.L. Apel, A. Kanavarioti, and D.W. Deamer. 2002. Influence of Ionic Inorganic Solutes on Self-Assembly and Polymerization Processes Related to Early Forms of Life : Implications for a Prebiotic Aqueous Medium. Astrobiology. 2: 139–152.
91. Adamala, K., and J.W. Szostak. 2013. Nonenzymatic template-directed RNA synthesis inside model protocells. Science. 342: 1098–1100.
92. Black, R.A., M.C. Blosser, B.L. Stottrup, R. Tavakley, D.W. Deamer, and S.L. Keller. 2013. Nucleobases bind to and stabilize aggregates of a prebiotic amphiphile , providing a viable mechanism for the emergence of protocells. Proc. Natl. Acad. Sci. 110: 13272–

13276.
93. Cornell, C.E., R.A. Black, M. Xue, H.E. Litz, A. Ramsay, M. Gordon, A. Mileant, Z.R. Cohen, J.A. Williams, K.K. Lee, G.P. Drobny, and S.L. Keller. 2019. Prebiotic amino acids bind to and stabilize prebiotic fatty acid membranes. Proc. Natl. Acad. Sci. 116: 17239–17244.
94. Barry, J.A., and K. Gawrisch. 1994. Direct NMR Evidence for Ethanol Binding to the Lipid-Water Interface of Phospholipid Bilayers. Biochemistry. 33: 8082–8088.
95. Chin, J.H., and D.B. Goldstein. 1981. Membrane-Disordering Action of Ethanol: Variation with Membrane Cholesterol Content and Depth of the Spin Label Probe. Mol. Pharmacol. 19: 425–431.
96. Pang, K.Y., M.L. Braswell, L. Chang, T.J. Sommer, and K.W. Miller. 1980. The Pertubation of Lipid Bilayers by General Anesthetics: A Quantative Test of the Disordered Lipid Hypothesis. Mol. Pharmacol. 18: 84–90.
97. Chen, S.-Y., B. Yang, K. Jacobson, and K.K. Sulik. 1996. The membrane disordering effect of ethanol on neural crest cells in vitro and the protective role of GM1 ganglioside. Alcohol. 13: 589–595.
98. Rifici, S., C. Corsaro, C. Crupi, V.C. Nibali, C. Branca, G. D'Angelo, and U. Wanderlingh. 2014. Lipid diffusion in alcoholic environment. J. Phys. Chem. B. 118: 9349–9355.
99. Dickey, A.N., and R. Faller. 2007. How alcohol chain-length and concentration modulate hydrogen bond formation in a lipid bilayer. Biophys. J. 92: 2366–2376.
100. Pang, K.Y., T.L. Chang, and K.W. Miller. 1979. On the coupling between anesthetic induced membrane fluidization and cation permeability in lipid vesicles. Mol. Pharmacol. 15: 729–738.
101. Ly, H. V, and M.L. Longo. 2004. The influence of short-chain alcohols on interfacial tension, mechanical properties, area/molecule, and permeability of fluid lipid bilayers. Biophys. J. 87: 1013–33.
102. Safinya, C.R., E.B. Sirota, D. Roux, and G.S. Smith. 1989. Universality in Interacting Membranes: The Effect of Cosurfactants on the Interfacial Rigidity. Phys. Rev. Lett. 62: 1134–1137.
103. Rowe, E.S. 1983. Lipid Chain Length and Temperature Dependence of Ethanol-Phosphatidylcholine Interactions. Biochemistry. 22: 3299–3305.
104. Hornby, A.P., and P.R. Cullis. 1981. Influence of local and neutral anaesthetics on the polymorphic phase preferences of egg yolk phosphatidylethanolamine. BBA - Biomembr. 647: 285–292.
105. Cantor, R.S. 2001. Breaking the Meyer-Overton rule: predicted effects of varying stiffness and interfacial activity on the intrinsic potency of anesthetics. Biophys. J. 80: 2284–2297.
106. Pringle, M.J., K.B. Brown, and K.W. Miller. 1981. Can the lipid theories of anesthesia account for the cutoff in anesthetic potency in homologous series of alcohols? Mol. Pharmacol. 19: 49–55.
107. Herskovits, T.T., B. Gadegbeku, and H. Jaillet. 1970. On the Structural Stability and Solvent Denaturation of Proteins. J. Biol. Chem. 245: 2588–2598.
108. Holowka, D., and B.A. Baird. 1983. Structural studies on the membrane-bound immunoglobulin E-receptor complex. 1. Characterization of large plasma membrane vesicles from rat basophilic leukemia cells and insertion of amphipathic fluorescent probes. Biochemistry. 22: 3466–3474.

109. Fridriksson, E.K., P.A. Shipkova, E.D. Sheets, D. Holowka, B.A. Baird, and F.W. McLafferty. 1999. Quantitative analysis of phospholipids in functionally important membrane domains from RBL-2H3 mast cells using tandem high-resolution mass spectrometry. Biochemistry. 38: 8056–8063.
110. Sezgin, E., H.-J. Kaiser, T. Baumgart, P. Schwille, K. Simons, and I. Levental. 2012. Elucidating membrane structure and protein behavior using giant plasma membrane vesicles. Nat. Protoc. 7: 1042–1051.
111. Blosser, M.C., J.B. Starr, C.W. Turtle, J. Ashcraft, and S.L. Keller. 2013. Minimal Effect of Lipid Charge on Membrane Miscibility Phase Behavior in Three Ternary Systems. Biophys. J. 104: 2629–2638.
112. Nishimura, S.Y., M. Vrljic, L.O. Klein, H.M. McConnell, and W.E. Moerner. 2006. Cholesterol depletion induces solid-like regions in the plasma membrane. Biophys. J. 90: 927–938.
113. Magee, A.I., J. Adler, and I. Parmryd. 2005. Cold-induced coalescence of T-cell plasma membrane microdomains activates signalling pathways. J. Cell Sci. 118: 3141–3151.
114. Bleecker, J.V., P.A. Cox, R.N. Foster, J.P. Litz, M.C. Blosser, D.A. Castner, and S.L. Keller. 2016. Thickness mismatch of coexisting liquid phases in noncanonical lipid bilayers. J. Phys. Chem. B. 120: 2761–2770.
115. Angelova, M.I., and D.S. Dimitrov. 1986. Liposome Electroformation. Faraday Discuss. Chem. Soc. 81: 303–311.
116. Vierl, U., L. Löbbecke, N. Nagel, and G. Cevc. 1994. Solute effects on the colloidal and phase behavior of lipid bilayer membranes: ethanol-dipalmitoylphosphatidylcholine mixtures. Biophys. J. 67: 1067–1079.
117. Baumgart, T., G. Hunt, E.R. Farkas, W.W. Webb, and G.W. Feigenson. 2007. Fluorescence probe partitioning between Lo/Ld phases in lipid membranes. Biochim. Biophys. Acta - Biomembr. 1768: 2182–2194.
118. Stanich, C.A., A.R. Honerkamp-Smith, G.G. Putzel, C.S. Warth, A.K. Lamprecht, P. Mandal, E. Mann, T.-A.D. Hua, and S.L. Keller. 2013. Coarsening Dynamics of Domains in Lipid Membranes. Biophys. J. 105: 444–454.
119. Alifimoff, J.K., L.L. Firestone, and K.W. Miller. 1989. Anaesthetic potencies of primary alkanols: implications for the molecular dimensions of the anaesthetic site. Br. J. Pharmacol. 96: 9–16.
120. Sezgin, E., D. Waithe, J. Bernardino de la Serna, and C. Eggeling. 2015. Spectral Imaging to Measure Heterogeneity in Membrane Lipid Packing. ChemPhysChem. 16: 1387–1394.
121. Stanich, C.A., A.R. Honerkamp-Smith, P. Cicuta, M.C. Blosser, and C.S. Warth. 2012. Track_Vesicle.
122. Veatch, S.L., O. Soubias, S.L. Keller, and K. Gawrisch. 2007. Critical fluctuations in domain-forming lipid mixtures. Proc. Natl. Acad. Sci. U.S.A. 104: 17650–17655.
123. Purushothaman, S., P. Cicuta, O. Ces, and N.J. Brooks. 2015. Influence of High Pressure on the Bending Rigidity of Model Membranes. J. Phys. Chem. B. 119: 9805–9810.
124. McCarthy, N.L.C., O. Ces, R.V. Law, J.M. Seddon, and N.J. Brooks. 2015. Separation of liquid domains in model membranes induced with high hydrostatic pressure. Chem. Commun. 51: 8675–8678.
125. Janoff, A.S., M.J. Pringle, and K.W. Miller. 1981. Correlation of general anesthetic potency with solubility in membranes. Biochim. Biophys. Acta - Biomembr. 649: 125–128.

126. Lange, Y., J. Ye, M.-E. Duban, and T.L. Steck. 2009. Activation of membrane cholesterol by 63 amphipaths. Biochemistry. 48: 8505–15.
127. Myher, J.J., A. Kuksis, and S. Pind. 1989. Molecular species of glycerophospholipids and sphingomyelins of human erythrocytes: improved method of analysis. Lipids. 24: 396–407.
128. Ionova, I.V., V.A. Livshits, and D. Marsh. 2012. Phase diagram of ternary cholesterol/palmitoylsphingomyelin/palmitoyloleoyl-phosphatidylcholine mixtures: Spin-label EPR study of lipid-raft formation. Biophys. J. 102: 1856–1865.
129. Meerschaert, R.L., and C. V Kelly. 2015. Trace membrane additives affect lipid phases with distinct mechanisms : a modified Ising model. Eur. Biophys. J. 44: 227–233.
130. Machta, B.B., E. Gray, M. Nouri, N.L.C. McCarthy, E.M. Gray, A.L. Miller, N.J. Brooks, and S.L. Veatch. 2016. Conditions that Stabilize Membrane Domains Also Antagonize n-Alcohol Anesthesia. Biophys. J. 111: 537–545.
131. Prigogine, I., and R. Defay. 1954. Chemical Thermodynamics. London: Longmans Greenand Co.
132. Widom, B. 1967. Plait Points in Two- and Three-Component Liquid Mixtures. J. Chem. Phys. 46: 3324–3333.
133. Schick, M., and D.W. Allender. 2017. The Effect of Solutes on the Temperature of Miscibility Transitions in Multi-component Membranes. Biophys. J. 113: 1814–1821.
134. Leung, S.S.W., and J. Thewalt. 2017. Link between Fluorescent Probe Partitioning and Molecular Order of Liquid Ordered-Liquid Disordered Membranes. J. Phys. Chem. B. 121: 1176–1185.
135. Bagatolli, L.A., S.A. Sanchez, T. Hazlett, and E. Gratton. 2003. Giant vesicles, Laurdan, and two-photon fluorescence microscopy: evidence of lipid lateral separation in bilayers. Methods Enzymol. 360: 481–500.
136. Veatch, S.L., S.S.W. Leung, R.E.W. Hancock, and J.L. Thewalt. 2007. Fluorescent Probes Alter Miscibility Phase Boundaries in Ternary Vesicles. J. Phys. Chem. B Lett. 111: 502–504.
137. Barry, J.. A., and K. Gawrisch. 1995. Effects of ethanol on lipid bilayers containing cholesterol, gangliosides, and sphingomyelin. Biochemistry. 34: 8852–60.
138. Westerman, P.W., J.M. Pope, N. Phonphok, J.W. Doane, and D.W. Dubro. 1988. The interaction of n-alkanols with lipid bilayer membranes : a 2H-NMR study. Biochim. Biophys. Acta. 939: 64–78.
139. Johnson, D.A., C.F. Valenzuela, and R. Zidovetzki. 1992. A deuterium NMR and steady-state fluorescence anisotropy study of the effects of cholesterol on the lipid membrane-disordering actions of ethanol. Biochem. Pharmacol. 44: 769–774.
140. Lyon, R.C., J.A. McComb, J. Schreurs, and D.B. Goldstein. 1981. A relationship between alcohol intoxication and the disordering of brain membranes by a series of short-chain alcohols. J. Pharmacol. Exp. Ther. 218: 669–675.
141. Chin, J.H., and D.B. Goldstein. 1984. Cholesterol blocks the disordering effects of ethanol in biomembranes. Lipids. 19: 929–935.
142. Rowe, E.S., F. Zhang, T.W. Leung, J.S. Parr, and P.T. Guy. 1998. Thermodynamics of membrane partitioning for a series of n-alcohols determined by titration calorimetry: Role of hydrophobic effects. Biochemistry. 37: 2430–2440.
143. Trandum, C., P. Westh, K. Jørgensen, and O.G. Mouritsen. 2000. A Thermodynamic Study of the Effects of Cholesterol on the Interaction between Liposomes and Ethanol.

Biophys. J. 78: 2486–2492.
144. Huster, D., K. Arnold, and K. Gawrisch. 1998. Influence of Docosahexaenoic Acid and Cholesterol on Lateral Lipid Organization in Phospholipid Mixtures. Biochemistry. 37: 17299–17308.
145. Litz, J.P., N. Thakkar, T. Portet, and S.L. Keller. 2016. Depletion with Cyclodextrin Reveals Two Populations of Cholesterol in Model Lipid Membranes. Biophys. J. 110: 635–645.
146. Kučerka, N., J. Pencer, M.P. Nieh, and J. Katsaras. 2007. Influence of cholesterol on the bilayer properties of monounsaturated phosphatidylcholine unilamellar vesicles. Eur. Phys. J. E. 23: 247–254.
147. Uline, M.J., G.S. Longo, M. Schick, and I. Szleifer. 2010. Calculating Partition Coefficients of Chain Anchors in Liquid-Ordered and Liquid-Disordered Phases. Biophys. J. 98: 1883–1892.
148. Meyer, H.K., and H. Hemmi. 1935. Beitrage zur theorie der narkose. III. Biochem Z. 277: 39–71.
149. Cantor, R.S. 2001. Bilayer Partition Coefficients of Alkanols: Predicted Effects of Varying Lipid Composition. J. Phys. Chem. B. 105: 7550–7553.
150. Shen, Y., A.K. Lindemeyer, C. Gonzalez, X.M. Shao, I. Spigelman, R.W. Olsen, and J. Liang. 2012. Dihydromyricetin as a novel anti-alcohol intoxication medication. J. Neurosci. 32: 390–401.
151. Wallner, M., H.J. Hanchar, and R.W. Olsen. 2006. Low-dose alcohol actions on a4B3y GABAA receptors are reversed by the behavioral alcohol antagonist Ro15-4513. Proc. Natl. Acad. Sci. 103: 8540–8545.
152. Krasowski, M.D., A. Jenkins, P. Flood, A.Y. Kung, A.J. Hopfinger, and N.L. Harrison. 2001. General anesthetic potencies of a series of propofol analogs correlate with potency for potentiation of gamma-aminobutyric acid (GABA) current at the GABA(A) receptor but not with lipid solubility. J. Pharmacol. Exp. Ther. 297: 338–51.
153. Kapoor, S., A. Werkmüller, C. Denter, Y. Zhai, J. Markgraf, K. Weise, N. Opitz, and R. Winter. 2011. Temperature–pressure phase diagram of a heterogeneous anionic model biomembrane system: Results from a combined calorimetry, spectroscopy and microscopy study. Biochim. Biophys. Acta - Biomembr. 1808: 1187–1195.
154. Fraser, D.M., L.C.M. Van Gorkom, and A. Watts. 1991. Partitioning behaviour of 1-hexanol into lipid membranes as studied by deuterium NMR spectroscopy. Biochim. Biophys. Acta. 1069: 53–60.
155. Gray, E.M., G. Díaz-Vázquez, and S.L. Veatch. 2015. Growth conditions and cell cycle phase modulate phase transition temperatures in RBL-2H3 derived plasma membrane vesicles. PLoS One. 10: 1–16.
156. Snyder, R.B., and C.A. Eckert. 1973. Effect of third component on liquid-liquid critical point. J. Chem. Eng. Data. 18: 282–285.
157. Schick, M. 2016. Shift in membrane miscibility transition temperature upon addition of short-chain alcohols. Phys. Rev. E. 94: 062114.
158. Landau, L.D., and E.M. Lifshitz. 1958. Statistical Physics. Reading, MA: Addison-Wesley.
159. 2016. Avanti Polar Lipids, Inc.
160. Yanagisawa, M., M. Imai, T. Masui, S. Komura, and T. Ohta. 2007. Growth dynamics of domains in ternary fluid vesicles. Biophys. J. 92: 115–125.

161. Schmid, F. 2017. Physical mechanisms of micro- and nanodomain formation in multicomponent lipid membranes. Biochim. Biophys. Acta - Biomembr. 1859: 509–528.
162. Honerkamp-Smith, A.R., B.B. Machta, and S.L. Keller. 2012. Experimental Observations of Dynamic Critical Phenomena in a Lipid Membrane. Phys. Rev. Lett. 108: 1–5.
163. Ehrig, J., E.P. Petrov, and P. Schwille. 2011. Near-critical fluctuations and cytoskeleton-assisted phase separation lead to subdiffusion in cell membranes. Biophys. J. 100: 80–89.
164. Toner, J., and D.R. Nelson. 1981. Smectic, cholesteric, and Rayleigh-Benard order in two dimensions. Phys. Rev. B. 23: 316–334.
165. Schick, M. 2018. Strongly correlated rafts in both leaves of an asymmetric bilayer. J. Phys. Chem. B. 122: 3251–3258.
166. Schick, M. 2012. Membrane heterogeneity: Manifestation of a curvature-induced microemulsion. Phys. Rev. E. 85: 031902.
167. Shlomovitz, R., L. Maibaum, and M. Schick. 2014. Macroscopic Phase Separation, Modulated Phases, and Microemulsions: A Unified Picture of Rafts. Biophys. J. 106: 1979–1985.
168. Angelova, M.I., S. Soleau, and P. Méléard. 1992. Preparation of giant vesicles by external AC electric fields. Kinetics and applications. Trends Colloid Interface Sci. IV. 89: 127–131.
169. Veatch, S.L., K. Gawrisch, and S.L. Keller. 2006. Closed-Loop Miscibility Gap and Quantitative Tie-Lines in Ternary Membranes Containing Diphytanoyl PC. Biophys. J. 90: 4428–4436.
170. Shimobayashi, S.F., M. Ichikawa, and T. Taniguchi. 2016. Direct observations of transition dynamics from macro- to micro-phase separation in asymmetric lipid bilayers induced by externally added glycolipids. Eur. Phys. Lett. 113: 560051–560056.
171. Burns, M., K. Wisser, J. Wu, I. Levental, and S.L. Veatch. 2017. Miscibility Transition Temperature Scales with Growth Temperature in a Zebrafish Cell Line. Biophys. J. 113: 1212–1222.
172. Baumgart, T., S.T. Hess, and W.W. Webb. 2003. Imaging coexisting fluid domains in biomembrane models coupling curvature and line tension. Nature. 425: 821–824.
173. He, S., and L. Maibaum. 2018. Identifying the Onset of Phase Separation in Quaternary Lipid Bilayer Systems from Coarse-Grained Simulations. J. Phys. Chem. B. 122: 3961–3973.
174. Alam Shibly, S.U., C. Ghatak, M.A. Sayem Karal, M. Moniruzzaman, and M. Yamazaki. 2016. Experimental Estimation of Membrane Tension Induced by Osmotic Pressure. Biophys. J. 111: 2190–2201.
175. Rozovsky, S., Y. Kaizuka, and J.T. Groves. 2005. Formation and Spatio-Temporal Evolution of Periodic Structures in Lipid Bilayers. JACS. 127: 36–37.
176. Amazon, J.J., and G.W. Feigenson. 2014. Lattice simulations of phase morphology on lipid bilayers : Renormalization, membrane shape, and electrostatic dipole interactions. Phys. Rev. E. 89: 0227021–02270211.
177. Goh, S.L., J.J. Amazon, and G.W. Feigenson. 2013. Toward a better raft model: Modulated phases in the four-component bilayer, DSPC/DOPC/POPC/CHOL. Biophys. J. 104: 853–862.
178. Amazon, J.J., S.L. Goh, and G.W. Feigenson. 2013. Competition between line tension and curvature stabilizes modulated phase patterns on the surface of giant unilamellar vesicles : A simulation study. Phys. Rev. E. 87: 0227081–02270810.

179. Konyakhina, T.M., S.L. Goh, J.J. Amazon, F.A. Heberle, J. Wu, and G.W. Feigenson. 2011. Control of a Nanoscopic-to-Macroscopic Transition : Modulated Phases in Four-Component DSPC / DOPC / POPC / Chol Giant Unilamellar Vesicles. Biophys. J. 101: L08-L10.
180. Usery, R.D., T.A. Enoki, S.P. Wickramasinghe, M.D. Weiner, W.C. Tsai, M.B. Kim, S. Wang, T.L. Torng, D.G. Ackerman, F.A. Heberle, J. Katsaras, and G.W. Feigenson. 2017. Line Tension Controls Liquid-Disordered + Liquid-Ordered Domain Size Transition in Lipid Bilayers. Biophys. J. 112: 1431–1443.
181. Shimokawa, N., R. Mukai, M. Nagata, and M. Takagi. 2017. Formation of modulated phases and domain rigidification in fatty acid-containing lipid membranes. Phys. Chem. Chem. Phys. 19: 13252–13263.
182. Hirose, Y., S. Komura, and D. Andelman. 2012. Concentration fluctuations and phase transitions in coupled modulated bilayers. Phys. Rev. E. 86: 0219161–02196113.
183. Palmieri, B., and S.A. Safran. 2013. Hybrid lipids increase the probability of fluctuating nanodomains in mixed membranes. Langmuir. 29: 5246–5261.
184. Turner, M.S., P. Sens, and N.D. Socci. 2005. Nonequilibrium raftlike membrane domains under continuous recycling. Phys. Rev. Lett. 95: 3–6.
185. Fan, J., M. Sammalkorpi, and M. Haataja. 2010. Formation and regulation of lipid microdomains in cell membranes: Theory, modeling, and speculation. FEBS Lett. 584: 1678–1684.
186. Fujiwara, T.K., K. Iwasawa, Z. Kalay, T.A. Tsunoyama, Y. Watanabe, Y.M. Umemura, H. Murakoshi, K.G.N. Suzuki, Y.L. Nemoto, N. Morone, and A. Kusumi. 2016. Confined diffusion of transmembrane proteins and lipids induced by the same actin meshwork lining the plasma membrane. Mol. Biol. Cell. 27: 1101–1119.
187. Lillemeier, B.F., J.R. Pfeiffer, Z. Surviladze, B.S. Wilson, and M.M. Davis. 2006. Plasma membrane-associated proteins are clustered into islands attached to the cytoskeleton. Proc. Natl. Acad. Sci. 103: 18992–18997.
188. Huang, K.C., R. Mukhopadhyay, and N.S. Wingreen. 2006. A curvature-mediated mechanism for localization of lipids to bacterial poles. PLoS Comput. Biol. 2: 1357–1364.
189. Ursell, T.S., W.S. Klug, and R. Phillips. 2009. Morphology and interaction between lipid domains. Proc. Natl. Acad. Sci. U. S. A. 106: 13301–13306.
190. Semrau, S., and T. Schmidt. 2009. Membrane heterogeneity – from lipid domains to curvature effects. Soft Matter. 5: 3174.
191. Komura, S., N. Shimokawa, and D. Andelman. 2006. Tension-Induced Morphological Transition in Mixed Lipid Bilayers. Langmuir. 22: 6771–6774.
192. Sapp, K., R. Shlomovitz, and L. Maibaum. 2014. Seeing the Forest in Lieu of the Trees: Continuum Simulations of Cell Membranes at Large Length Scales. Annu. Reports Comput. Chem. 10: 47–76.
193. Funkhouser, C.M., M. Mayer, F.J. Solis, and K. Thornton. 2013. Effects of interleaflet coupling on the morphologies of multicomponent lipid bilayer membranes. J. Chem. Phys. 024909: 0249091–02490912.
194. Wolff, J., S. Komura, and D. Andelman. 2015. Budding of domains in mixed bilayer membranes. Phys. Rev. E. 91: 1–10.
195. Sadeghi, S., M. Müller, and R.L.C.L.C. Vink. 2014. Raft Formation in Lipid Bilayers Coupled to Curvature. Biophys. J. 107: 1591–1600.
196. Harden, J.L., F.C. MacKintosh, and P.D. Olmstead. 2005. Budding and domain shape

transformations in mixed lipid films and bilayer membranes. Phys. Rev. E. 72: 0119031–01190313.
197. Leibler, S., and D. Andelman. 1987. Ordered and curved meso-structures in membranes and amphiphilic films. J. Phys. 48: 2013–2018.
198. Liu, J., S. Qi, J.T. Groves, and A.K. Chakraborty. 2005. Phase Segregation on Different Length Scales in a Model Cell Membrane System. J. Phys. Chem. B. 109: 199601–199609.
199. Liu, J., J.T. Groves, and A.K. Chakraborty. 2006. Kinetic pathways of phase ordering in lipid raft model systems. J. Phys. Chem. B. 110: 8416–8421.
200. Perlmutter, J.D., and J.N. Sachs. 2011. Interleaflet interaction and asymmetry in phase separated lipid bilayers: Molecular dynamics simulations. J. Am. Chem. Soc. 133: 6563–6577.
201. Kirk, G.L., and S.M. Gruner. 1985. Lyotropic effects of alkanes and headgroup composition on the Lα -HII lipid liquid crystal phase transition : hydrocarbon packing versus intrinsic curvature. J. Phys. Paris. 46: 761–769.
202. Gruner, S.M. 1985. Intrinsic curvature hypothesis for biomembrane lipid composition: a role for nonbilayer lipids. Proc. Natl. Acad. Sci. 82: 3665–3669.
203. Blosser, M.C., A.R. Honerkamp-Smith, T. Han, M. Haataja, and S.L. Keller. 2015. Transbilayer Colocalization of Lipid Domains Explained via Measurement of Strong Coupling Parameters. Biophys. J. 109: 2317–2327.
204. Rozovsky, S., J.T. Groves, Y. Kaizuka, and J.T. Groves. 2005. Formation and Spatio-Temporal Evolution of Periodic Structures in Lipid Bilayers. J. Am. Chem. Soc. 127: 36–37.
205. Kawakatsu, T., D. Andelman, K. Kawasaki, and T. Taniguchi. 1993. Phase transitions and shapes of two component membranes and vesicles I : strong segregation limit. J. Phys. II Fr. 3: 971–997.
206. Kawakatsu, T., D. Andelman, K. Kawasaki, and T. Taniguchi. 1994. Phase transitions and shapes of two component membranes and vesicles II : weak segregation limit. J. Phys. II Fr. 4: 1333–1362.
207. Shlomovitz, R., and M. Schick. 2013. Model of a Raft in Both Leaves of an Asymmetric Lipid Bilayer. Biophys. J. 105: 1406–1413.
208. Andelman, D., and R.E. Rosensweig. 2009. Modulated Phases : Review and Recent Results. J. Phys. Chem. B. 113: 3785–3798.
209. Lipowsky, R. 1992. Budding of Membranes Induced by Intramembrane Domains. J. Phys. Paris. 2: 1825–1840.
210. Moy, V.T., H.M. McConnell, and D.J. Keller. 1986. Theory of superstructures in lipid monolayer phase transitions. J. Phys. Chem. 90: 2311–2315.
211. McConnell, H.M. 1991. Structures and Transitions in Lipid Monolayers at the Air-Water Interface. Annu. Rev. Phys. Chem. 421: 171–195.
212. Keller, S.L., and H.M. McConnell. 1999. Stripe phases in lipid monolayers near a miscibility critical point. Phys. Rev. Lett. 82: 1602–1605.
213. Schneider, M.F., D. Andelman, and M. Tanaka. 2005. Stripes of partially fluorinated alkyl chains: Dipolar Langmuir monolayers. J. Chem. Phys. 122: 0947171–0947175.
214. Travesset, A. 2006. Effect of dipolar moments in domain sizes of lipid bilayers and monolayers. J. Chem. Phys. 125: 0849051–08490512.
215. Rim, J.E., T.S. Ursell, R. Phillips, and W.S. Klug. 2011. Morphological Phase Diagram

for Lipid Membrane Domains with Entropic Tension. Phys. Rev. Lett. 106: 11–14.
216. Hansen, J.P., and I.R. McDonald. 2013. Theory of Simple Liquids. 4th ed. Oxford: Academic Press.
217. Oliphant, T.E. 2007. Python for Scientific Computing. Comput. Sci. Eng. 9: 10–20.
218. Jones, E., T.E. Oliphant, and P. Peterson. 2001. SciPy: Open Source Scientific Tools for Python. http://www.scipy.org.
219. Grakoui, A., S.K. Bromley, M.M. Sumen, A.S. Shaw, P.M. Allen, and M.L. Dustin. 1999. The immunological synapse: A molecular machine controlling T cell activation. Science. 285: 221–227.
220. Cornell, C.E., A.D. Skinkle, S. He, I. Levental, K.R. Levental, and S.L. Keller. 2018. Tuning Length Scales of Small Domains in Cell-Derived Membranes and Synthetic Model Membranes. Biophys. J. 115: 690–701.
221. Grant, C.W., S.H. Wu, and H.M. McConnell. 1974. Lateral phase separations in binary lipid mixtures: correlation between spin label and freeze-fraction electron microscopic studies. Biochim. Biophys. Acta. 363: 151–158.
222. Luna, E.J., and H.M. McConnell. 1978. Multiple phase equilibria in binary mixtures of phospholipids. Biochim. Biophys. Acta. 509: 462–473.
223. Stewart, T.P., S.W. Hui, A.R. Portis Jr., and D. Papahadjopoulos. 1979. Complex phase missing of phosphatidylcholine and phosphatidylserine in multilamellar membrane vesicles. Biochim. Biophys. Acta. 556: 1–16.
224. Lentz, B.R., D.R. Alford, M. Hoechli, and F.A. Dombrose. 1982. Phase behavior of mixed phosphatidylglycerol/phosphatidylcholine multilamellar and unilamellar vesicles. Biochemistry. 21: 4212–4219.
225. Wilson, B.S., S.L. Steinberg, K. Liederman, J.R. Pfeiffer, Z. Surviladze, J. Zhang, L.E. Samelson, L.-H. Yang, P.G. Kotula, and J.M. Oliver. 2004. Markers for detergent-resistant lipid rafts occupy distinct and dynamic domains in native membranes. Mol. Biol. Cell. 15: 2580–2592.
226. LaRocca, T.J., P. Pathak, S. Chiantia, A. Toledo, J.R. Silvius, J.L. Benach, and E. London. 2013. Proving lipid rafts exist: Membrane domains in the prokaryote Borrelia burgdorferi have the same properties as eukaryotic lipid rafts. PLoS Pathog. 5: e1003353.
227. Veatch, S.L., B.B. Machta, S.A. Shelby, E.N. Chiang, D.A. Holowka, and B.A. Baird. 2012. Correlation functions quantify super-resolution images and estimate apparent clustering due to over-counting. PLoS One. 7: e31457.
228. Stottrup, B.L., S.L. Veatch, and S.L. Keller. 2004. Nonequilibrium behavior in supported lipid membranes containing cholesterol. Biophys. J. 86: 2942–2950.
229. Garcia-Saez, A.J., S. Chiantia, P. Schwille, A.J. Garcı, S. Chiantia, and P. Schwille. 2007. Effect of line tension on the lateral organization of lipid membranes. J. Biol. Chem. 282: 33537–33544.
230. Connell, S.D., G. Heath, P.D. Olmsted, and A. Kisil. 2013. Critical point fluctuations in supported lipid membranes. Faraday Discuss. 161: 91–111.
231. Bhatia, T., P. Husen, J.H. Ipsen, L.A. Bagatolli, and A.C. Simonsen. 2014. Fluid Domain Patterns in Free-Standing Membranes Captured on a Solid Support. Biochim. Biophys. Acta. 1838: 2503–2510.
232. Khadka, N.K., C.S. Ho, and J. Pan. 2015. Macroscopic and Nanoscopic Heterogeneous Structures in a Three-Component Lipid Bilayer Mixtures Determined by Atomic Force Microscopy. Langmuir. 31: 12417–12425.

233. Bleecker, J.V., P.A. Cox, and S.L. Keller. 2016. Mixing temperatures of bilayers not simply related to thickness differences between Lo and Ld phases. Biophys. J. 110: 2305–2308.
234. Sibold, J., V.E. Tewaag, T. Vagedes, and C. Steinem. 2020. Phase separation in pore-spanning membranes induced by differences in surface adhesion. Phys. Chem. Chem. Phys. 22: 9308–9315.
235. Sezgin, E. 2017. Super-resolution optical microscopy for studying membrane structure and dynamics. J. Phys. Condens. Matter. 29: 273001.
236. Chen, F., P.W. Tillberg, and E.S. Boyden. 2015. Expansion Microscopy. Science (80-.). 347: 543–548.
237. Schmid, E.M., M.H. Bakalar, K. Choudhuri, and J. Weichsel. 2016. Size-dependent protein segregation at membrane interfaces. Nat. Phys. 12: 704–711.
238. Scheve, C.S., P.A. Gonzales, N. Momin, and J.C. Stachowiak. 2013. Steric Pressure between Membrane-Bound Proteins Opposes Lipid Phase Separation. JACS. 135: 1185–1188.
239. Zheng, S.Q., E. Palovcak, J.P. Armache, K.A. Verba, Y. Cheng, and D.A. Agard. 2017. MotionCor2: anisotropic correction of beam-induced motion for improved cryo-electron microscopy. Nat. Methods. 14: 331–332.
240. Lander, G.C., S.M. Stagg, N.R. Voss, A. Cheng, D. Fellmann, J. Pulokas, C. Yoshioka, C. Irving, A. Mulder, P.W. Lau, D. Lyumkis, C.S. Potter, and B. Carragher. 2009. Appion: an integrated, database-driven pipeline to facilitate EM image processing. J. Struct. Biol. 166: 95–102.
241. Hagen, W.J.H., W. Wan, and J.A.G. Briggs. 2017. Implementation of a cryo-electron tomography tilt-scheme optimized for high resolution subtomogram averaging. J. Struct. Biol. 197: 191–198.
242. Mastronarde, D.N., and S.R. Held. 2017. Automated tilt series alignment and tomographic reconstruction in IMOD. J. Struct. Biol. 197: 102–113.
243. Kremer, J.R., D.N. Mastronade, and J.R. McIntosh. 1996. Computer Visualization of Three-Dimensional Image Data Using IMOD. J. Struct. Biol. 116: 71–76.
244. Rohou, A., and N. Grigorieff. 2015. CTFFIND4: Fast and accurate defocus estimation from electron micrographs. J. Struct. Biol. 192: 216–221.
245. Schneider, C.A., W.S. Rasband, and K.W. Eliceiri. 2012. NIH Image to ImageJ: 25 years of image analysis. Nat. Methods. 9: 671–675.
246. van der Walt, S., J.L. Schonberger, J. Nunez-Iglesias, F. Boulogne, J.D. Warner, N. Yager, E. Gouillart, and T. Yu. 2014. scikit-image: Image processing in Python. Peer J. 2: e453.
247. Angelova, M.I. 1998. Lipid swelling and liposome formation in electric fields. PhD Thesis. Bulgarian Academy of Sciences, Sofia, Bulgaria.
248. Blosser, M.C., B.G. Horst, and S.L. Keller. 2016. cDICE method produces giant lipid vesicles under physiological conditions of charged lipids and ionic solutions. Soft Matter. 12: 7364–7371.
249. Durre, K., and A.R. Bausch. 2019. Formation of phase separated vesicles by double layer cDICE. Soft Matter. 15: 9676–9681.
250. Hammond, A.T., F.A. Heberle, T. Baumgart, D. Holowka, B. Baird, and G.W. Feigenson. 2005. Crosslinking a lipid raft component triggers liquid ordered-liquid disordered phase separation in model plasma membranes. Proc. Natl. Acad. Sci. 102: 6320–6325.

251. Simunovic, M., C. Prevost, A. Callan-Jones, and P. Bassereau. 2016. Physical basis of some membrane shaping mechanisms. Philos. Trans. R. Soc. A. 374: 20160034.
252. Ayuyan, A.G., and F.S. Cohen. 2006. Lipid Peroxides Promote Large Rafts: Effects of Excitation of Probes in Fluorescence Microscopy and Electrochemical Reactions During Vesicle Formation. Biophys. J. 91: 2172–2183.
253. Wu, B., Y. Chen, and J.D. Muller. 2009. Fluorescence Fluctuation Spectroscopy of mCherry in Living Cells. Biophys. J. 96: 2391–2404.
254. Veatch, S.L., I.V. Polozov, K. Gawrisch, and S.L. Keller. 2004. Liquid domains in Vesicles Investigated by NMR and Fluorescence Microscopy. Biophys. J. 86: 2910–2922.
255. Zhao, J., J. Wu, F.A. Heberle, T.T. Mills, P. Klawitter, G. Huang, G. Costanza, and G.W. Feigenson. 2007. Phase studies of model biomembranes: Complex behavior of DSPC/DOPC/Cholesterol. Biochim. Biophys. Acta. 1768: 2764–2776.
256. Heftberger, P., B. Kollmitzer, A.A. Rieder, H. Amenitsch, and G. Pabst. 2015. In situ determination of structure and fluctuations of coexisting fluid membrane domains. Biophys. J. 108: 854–862.
257. Heerklotz, H. 2002. Triton Promotes Domain Formation in Lipid Raft Mixtures. Biophys. J. 83: 2693–2701.
258. Williamson, J.J., and P.D. Olmsted. 2015. Nucleation of symmetric domains in the coupled leaflets of a bilayer. Soft Matter. 11: 8948–8959.
259. Fowler, P.W., J.J. Williamson, M.S.P. Sansom, and P.D. Olmsted. 2016. Roles of interleaflet coupling and hydrophobic mismatch in lipid membrane phase-separation kinetics. J. Am. Chem. Soc. 138: 11633–11642.
260. Hung, W.C., M.T. Lee, F.Y. Chen, and H.W. Huang. 2007. The Condensing Effect of Cholesterol in Lipid Bilayers. Biophys. J. 92: 3960–3967.
261. Kucerka, N., J. Gallova, D. Uhrikova, P. Balgavy, M. Bulacu, S.J. Marrink, and J. Katsaras. 2009. Areas of monounsaturated diacylphosphatidylcholines. Biophys. J. 97: 1926–1932.
262. Pan, J., S. Tristram-Nagle, and J.F. Nagle. 2009. Effect of cholesterol on structural and mechanical properties of membranes depends on lipid chain saturation. Phys. Rev. E. 80: 021931.
263. Gallova, J., D. Uhrikova, N. Kucerka, J. Teixeira, and P. Balgavy. 2010. Partial area of cholesterol in monounsaturated diacylphosphatidylcholine bilayers. Chem. Phys. Lipids. 163: 765–770.
264. Kucerka, N., M.P. Nieh, and J. Katsaras. 2011. Fluid phase lipid areas and bilayer thickness of commonly used phosphatidylcholines as a function of temperature. Biochim. Biophys. Acta (BBA)- Biomembr. 1808: 2761–2771.
265. Heftberger, P., B. Kollmitzer, F.A. Heberle, J. Pan, M. Rappolt, H. Amenistch, N. Kucerka, J. Katsaras, and G. Pabst. 2014. Global small-angle X-ray scattering data analysis for multilamellar vesicles: the evolution of the scattering density profile model. J. Appl. Crystallogr. 47: 173–180.
266. Palmer, C.P., and J. Lowe. 2013. A cylindrical specimen holder for electron cryo-tomography. Ultramicroscopy. 137: 20–29.
267. Phillips, R., and R. Milo. 2016. What is the power consumption of the cell? In: Cell Biology by the Numbers. .
268. Weber, S.C., and C.P. Brangwynne. 2012. Getting RNA and Protein in Phase. Cell. 149: 1188–1191.

269. Alberti, S. 2017. Phase separation in biology. Curr. Biol. 27: R1097–R1102.
270. Shin, Y., and C.P. Brangwynne. 2017. Liquid phase condensation in cell physiology and disease. Science. 357: eaaf4.
271. Moeller, C.H., and W.W. Thomson. 1979. An Ultrastructural Study of the Yeast Tonoplast during the Shift from Exponential to Stationary Phase. J. Ultrastruct. Res. 68: 28–37.
272. Kane, P.M. 2006. The Where , When , and How of Organelle Acidification by the Yeast Vacuolar H+-ATPase. Microbiol. Mol. Biol. Rev. 70: 177–191.
273. Hunter, K., and A.H. Rose. 1972. Lipid composition of Saccharomyces Cerevisiae as Influenced by Growth Temperature. Biochim. Biophys. Acta. 260: 639–653.
274. Jackowski, S. 1996. Cell Cycle Regulation of Membrane Phospholipid Metabolism. J. Biol. Chem. 271: 20219–20222.
275. Ernst, R., C.S. Ejsing, and B. Antonny. 2016. Homeoviscous Adaptation and the Regulation of Membrane Lipids. J. Mol. Biol. 428: 4776–4791.
276. Kates, M., and R.M. Baxter. 1962. Lipid Composition of Mesophilic and Psychrophilic Yeasts (Candida Species) as Influenced by Environmental Temperature. Can. J. Biochem. Physiol. 40: 1213–1227.
277. Deamer, D., J.P. Dworkin, S.A. Sandford, M.P. Bernstein, and L.J. Allamandola. 2002. The first cell membranes. Astrobiology. 2: 371–381.
278. Knauth, L.P. 2005. Temperature and salinity history of the Precambrian ocean: implications for the course of microbial evolution. Palaeogeogr. Palaeoclimatol. Palaeoecol. 219: 53–69.
279. Szostak, J.W. 2012. The eightfold path to non-enzymatic RNA replication. J. Syst. Chem. 3: 2–14.
280. Jin, L., A.E. Engelhart, W. Zhang, K. Adamala, and J.W. Szostak. 2018. Catalysis of template-directed nonenzymatic RNA copying by Iron(II). J. Am. Chem. Soc. 140: 15016–15021.
281. Chen, I.A., K. Salehi-Ashtiani, and J.W. Szostak. 2005. RNA catalysis in model protocell vesicles. J. Am. Chem. Soc. 127: 13351–13355.
282. Maurer, S.E., D. Deamer, J. Boncella, and P.-A. Monnard. 2009. Chemical evolution of amphiphiles: Glycerol monoacyl derivatives stablize plausible prebiotic membranes. Astrobiology. 9: 979–987.
283. Mansy, S.S., and J.W. Szostak. 2008. Thermostability of model protocell membranes. Proc. Natl. Acad. Sci. 105: 13351–13355.
284. Namani, T., and D. Deamer. 2008. Stability of model membranes in extreme environments. Orig. Life Evol. Biosph. 38: 329–341.
285. Maurer, S.E., K.T. Sorensen, Z. Iqbal, J. Nicholas, K. Quirion, M. Gioia, P.-A. Monnard, and M.M. Hanczyc. 2018. Vesicle self-assembly of monoalkyl amphiphiles under the effects of high ionic strengh, extreme pH, and high temperature environments. Langmuir. 34: 15560–15568.
286. Joyce, G.F., and J.W. Szostak. 2018. Protocells and RNA self-replication. Cold Spring Harb. Perspect. Biol. 10: a034801.
287. Longo, M.L., and M. Blaber. 2012. Protein design at the interface of the pre-biotic and biotic worlds. Arch Biochem Biophys. 526: 16–21.
288. Doi, N., K. Kakukawa, Y. Oishi, and H. Yanagawa. 2005. High solubility of random-sequence proteins consisting of five kinds of primitive amino acids. Protein Eng Des Sel.

18: 279–284.
289. McDonald, G.D., and M.C. Storrie-Lombardi. 2010. Biochemical constraints in a protobiotic earth devoid of basic amino acids: The “BAA(-) world.” Astrobiology. 10: 989–1000.
290. Cleaves, H.J. 2010. The origin of biologically coded amino acids. J. Theor. Biol. 263: 490–498.
291. Adamala, K., and J.W. Szostak. 2013. Competition between model protocells driven by an encapsulated catalyst. Nat. Chem. 5: 495–501.
292. Murillo-Sanchez, S., D. Beaufils, J.M. Gonzalez Manas, R. Pascal, and K. Ruiz-Mirazo. 2016. Fatty acids’ double role in the prebiotic formation of a hydrophobic dipeptide. Chem. Sci. 7: 3406–3413.
293. Kamat, N.P., S. Tobe, I.T. Hill, and J.W. Szostak. 2015. Electrostatic localization of RNA to protocell membranes by cationic hydrophobic peptides. Angew. Chemie - Int. Ed. 127: 11901–11905.
294. Blocher, M., D. Liu, P. Walde, and P.L. Luisi. 1999. Liposome-assisted selective polycondensation of alpha-amino acids and peptides. Macromolecules. 32: 7331–7334.
295. Mayer, C., U. Schreiber, M.J. Davila, O.J. Schmitz, A. Bronja, M. Meyer, J. Klein, and S.W. Meckelmann. 2018. Molecular Evolution in a Peptide-Vesicle System. Life. 8: 16.
296. McDowell, L.M., S.M. Holl, S. Qian, E. Li, and J. Schaefer. 1993. Inter-tryptophan distances in rat cellular retinol binding protein II by solid-state NMR. Biochemistry. 32: 4560–4563.
297. Valeri, D., and A.J.A. Meirelles. 1997. Viscosities of fatty acids, triglycerides and their binary mixtures. J. Am. Oil Chem. Soc. 74: 1221–1226.
298. Zhang, W., K.J. Haman, J.M. Metzger, B.J. Hackel, F.S. Bates, and T.P. Lodge. 2017. Quantifying binding of ethylene oxide-propylene oxide block copolymers with lipid bilayers. Langmuir. 33: 12624–12634.
299. Lindblom, G., G. Oradd, and A. Filippov. 2006. Lipid lateral diffusion in bilayers with phosphatidylcholine, sphingomyelin, and cholesterol: an NMR study of dynamics and lateral phase separation. Chem. Phys. Lipids. 141: 179–184.
300. Jia, L., S. Liang, K. Sackett, U. Ghosh, and D.P. Weliky. 2015. REDOR solid-state NMR as a probe of the membrane location of membrane-associated peptides and proteins. J. Magn. Reson. 253: 154–165.
301. Xie, L., U. Ghosh, S.D. Schmick, and D.P. Weliky. 2013. Residue-specific membrane location of peptides and proteins using specifically and extensively deuterated lipids and 13C-2H rotational-echo double-resonance solid-state NMR. J. Biomol. NMR. 55: 11–17.
302. Gullion, T., R. Kishore, and T. Asakura. 2012. Determining dihedral angles and local structure in silk peptide by 13C-2H REDOR. J. Am. Chem. Soc. 101: 283–290.
303. Luthra, S.A., M. Utz, E.M. Gorman, M.J. Pikal, E.J. Munson, and J.W. Lubach. 2012. Carbon-deuterium rotational-echo double-resonance NMR spectroscopy of lyophilized aspartame formulations. Sci. J. Pharm. 101: 283–290.
304. Monnard, P.-A., and D. Deamer. 2003. Preparation of Vesicles from Nonphospholipid Amphiphiles. Methods Enzymol. 37.
305. Hanczyc, M.M., S.S. Mansy, and J.W. Szostak. 2007. Mineral surface directed membrane assembly. Orig. Life Evol. Biosph. 37: 67–82.
306. Wang, A., C.C. Miller, and J.W. Szostak. 2019. Core-shell modeling of light scattering by vesicles: effect of size, contents, and lamellarity. Biophys. J. 116: 659–669.

307. Damer, B., and D. Deamer. 2015. Coupled phases and combinatorial selection in fluctuating hydrothermal pools: A scenario to guide experimental approaches to the origin of cellular life. Life. 5: 872–887.

APPENDIX A: EXTENDED METHODS

A.A.1 Preparation of Giant Unilamellar Vesicles (GUVs) via Electroformation

1. All lipid stocks are stored at -20°C in glass scintillation vials, stopped with a Teflon coated septum. Lipid stocks are typically 10 mg/mL dissolved in chloroform ($CHCl_3$) or a solvent mix with $CHCl_3$, methanol, and/or DMSO. Dye is typically 1 mg/mL.

2. For every set of samples grab two small test tubes: one for the sample mix and one for waste.

3. Rinse a glass Hamilton 10 µL syringe with $CHCl_3$, first by using a glass pipet to rinse the outside of the needle. Then, clean the interior by filling the syringe with 10 µL $CHCl_3$ and transferring it to the waste tube 10x.

4. Rinse the sample test tube by adding a small amount (about 3 cm of the vial should be sufficient) of $CHCl_3$, spinning the solvent in the tube using a vortexer, followed by discarding the solvent.

5. Measure out lipid solution components using the Hamilton syringe into the rinsed test tube. Be sure to rinse the syringe, as described in step 3, between different lipid components to prevent contamination of the stock solutions.

6. Add a small amount (one tip-full of a Pasteur pipet) to rinse down the sides of the sample test tube.

7. Place the sample test tube into a pre-heated heat block set to 60°C (at least 10°C above the highest T_m of the lipids in the sample).

8. While lipid solutions heat, re-seal stock solutions with 1) Teflon tape, and 2) parafilm. Lipid stocks should be returned to the -20°C freezer.

9. For each sample, slice an indium-tin-oxide (ITO) slide in half using a glasscutter. Use a multimeter to locate the coated (resistive) side of each slide. Label the non-resistive side with a permanent marker.

10. Clean the resistive side of each ITO slide with ethanol and a lint-free wipe to remove all dirt and dust. Anything left on the slide can hinder the formation of a smooth lipid film.

11. Heat the ITO slides on the 60°C heat block with the resistive sides face-up.

12. Rinse one Pasteur pipet per sample 1-3x with $CHCl_3$. After rinsing the pipettes, place them on the 60°C heating block.

13. Clean Teflon strips (~3 mm thick and ~1.25 inches long) with ethanol. There should be two Teflon strips per sample.

14. To spread a lipid film on the ITO slides, use a pre-heated Pasteur pipet (1 per sample) and suck up ~half of the lipid solution and deposit drops on the conductive side of the ITO slide. Evenly move the tip of the pipet across the slide surface until all of the solvent has evaporated and a film remains that has a rainbow sheen. The thinner and smoother the lipid film, the higher quality the GUVs produced by electroformation.

15. Using a Pasteur pipet, run a thin line of vacuum grease along the longer edges of the ITO slides (~the length of a Teflon strip).

16. Place Teflon strips down on top of the vacuum grease on the ITO slide, specifically on the side with the lipid film.

17. Complete each electroformation chamber by placing the slide without the Teflon strips grease-side down on the strips of the other slide so that the edges are offset (Fig. A.A.1).

18. Secure the chamber with binder clips.

19. Place the chambers in a vacuum desiccation chamber and keep chambers under vacuum for at least 30 min. The chamber should be impenetrable to light to keep lipids from photo oxidizing.

20. After solvent is sufficiently evaporated from chambers, seal one open edge of the chamber with vacuum grease.

21. Fill the chamber with MilliQ water, buffer, or a sucrose solution. Add solution slowly to avoid air bubbles. If air bubbles form, gently tap the chamber.

22. Seal the open edge of the chamber with more vacuum grease. Remove any air bubbles.

23. Clean excess vacuum grease with ethanol.

24. Clip chambers to two conductive metal rails with strong binder clips. One side will be above the metal rail, the other below. See Fig. A.A.1 for details.

Figure Appendix A 1: Diagram of electroformation procedure. Figure from Joan Bleecker.

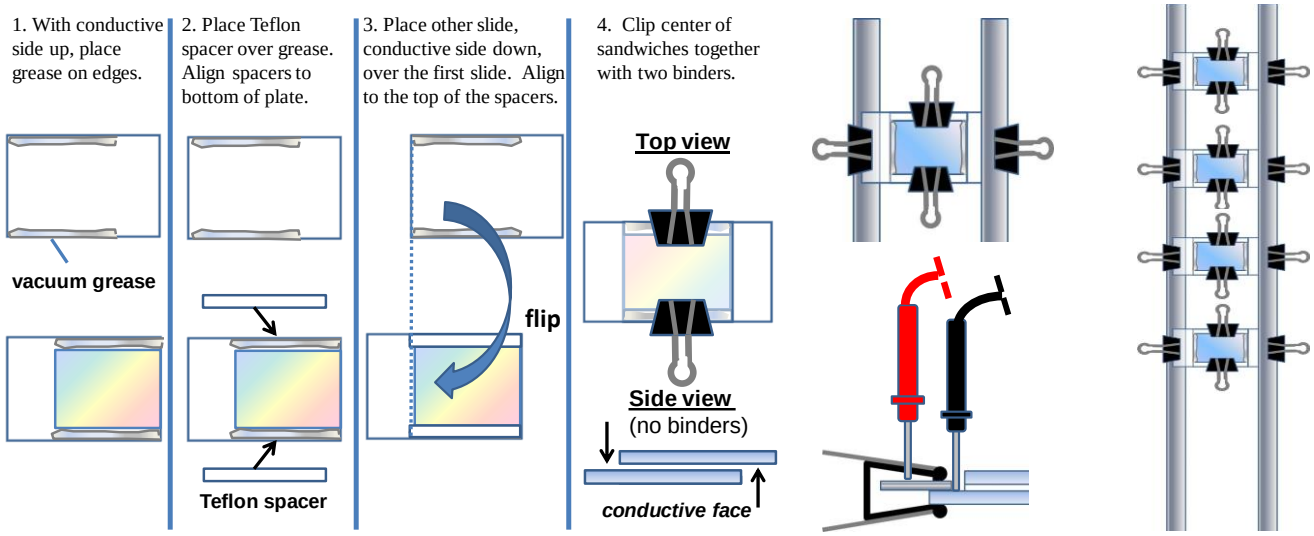

25. Test the electrical connections with a multimeter. The meter should read 100-200 Ω when one lead is in contact with the ITO slide and the other with the rail connected to the opposite side of the chamber. Test both sides of the chamber.

26. Place the rails and chambers in a 60°C oven (again, at least 10°C above the highest T_m of the lipids in the sample) and attach to a function generator. The sample should have an AC current continuously run through it at 10 Hz and 1.5 V for 1 hour.

27. After an hour, turn off the function generator and detach the leads from the rails. Detach the chambers from the rails. Gently crack open the chambers (or use a syringe to suck up the materials) and deposit the solution into an Eppendorf tube.

28. Dilute the vesicles with an appropriate amount of either MilliQ water, buffer, or glucose solution. This amount will depend on the experimental context. If vesicles are to be used for T_{mix} quantification via fluorescence microscopy, dilute the vesicles ~10fold with glucose solution that is osmotically matched with the internal sucrose solution of the vesicles. Allow vesicles to settle to the bottom of the Eppendorf tube for at least 2-3 min.

A.A.2. Fluorescence Microscopy of GUVs to Determine T_{mix}.

1. Electroformed and diluted vesicles should be kept in Eppendorf tubes in a 60°C oven throughout the duration of the experiment. Vesicles should be kept at high temperature until they are at the microscope.

2. For microscopy experiments, it is ideal to make vesicles in a 200-300 mM sucrose solution and subsequently dilute them in a 200-300 mM glucose solution (the inner and outer sugar solutions must be osmotically matched to ensure that vesicles are taut). To ensure that vesicles are completely taut, an internal sucrose solution of ~10 mM higher than the outer glucose solution may be used.

3. Allow vesicles to sediment to the bottom of the Eppendorf tube for at least 2-3 min.

4. Prepare imaging chambers by adding a thin layer of vacuum grease to all four edges of a square 25 x 25 mm coverslip. Place greased coverslips in the 60°C.

5. While working in the oven, pipette 10 µL of sedimented vesicles onto a pre-heated coverslip. Add 90 µL of the dilution solution and seal the imaging chamber with another square coverslip.

6. Transfer the sample over to a pre-heated (~60°C) microscope stage. The coverslip should be in thermal contact with the stage and the best way to achieve this is to coat the microscope stage in thermal grease.

7. For an initial temperature sweep to locate the approximate T_{mix}, decrease the temperature of the stage from 60°C in 2°C increments, turning on the light source and the camera at each increment (but not for long, keep the time light is on the sample to a minimum to prevent photo oxidation). Record the temperature that vesicles begin to phase separate and the temperature at which all vesicles are phase separated.

8. For the quantitative temperature sweep, lower the temperature of the stage to 1-2°C above the temperature at which phase separated vesicles began to appear in the initial sweep.

9. Decrease the temperature of the stage in 0.5°C increments, imaging vesicles at each temperature and counting the number of phase-separated vesicles and fully mixed vesicles. Try to minimize the time spent with the light source on the sample. At each temperature increment, at least 20 vesicles should be counted (and ideally, far more than 20) to ensure decent counting statistics.

10. Keep decreasing the temperature until at least 90% of vesicles in the field of view are phase separated.

11. To compute the T_{mix}, fit the following equation to the percent of phase separated vesicles at each temperature:

$$\%\ Phase\ Separated = 100 * 1 - \frac{1}{1 + e^{-\frac{(x-c)}{d}}}$$

Where x is the value of T_{mix} and represents the temperature at which 50% of the vacuoles are phase separated.

12. Confidence intervals come from bootstrap resampling of the fit. Scripts to count vesicles, fit the data, and compute confidence intervals can be found in Appendix B.

A.A.3 Preparation of Large Unilamellar Vesicles (LUVs) via Extrusion

1. Create GUVs via electroformation as described in A.A.1. Multilamellar LUVs can be created via simple hydration (see https://avantilipids.com/tech-support/liposome-preparation/lmv for detailed instructions).

2. Unscrew the extrusion apparatus, exposing the Teflon internal components. Clean all the Teflon and o-ring components in ethanol, followed by MilliQ water.

3. Pre-wet the surface inside the O-ring of the Teflon cylinder with a drop of MilliQ water or the buffer that vesicles are suspended within.

4. Place one or two filter supports in the middle of each of the two o-rings on the pre-wet surface. Using more than one filter support allows for faster extrusion.

5. Place a filter membrane on top of one of the filter supports on one of the Teflon cylinders. Make sure that the filer membrane has been wet by the filter support and lies flat on the surface. Two filters can be placed inside if it is very important to have uniform vesicles. Membranes and spacers are made by Whatman Nucleopore and can be purchased from Avanti Polar Lipids.

6. Place the Teflon cylinder with the filter membrane on it into the larger metal sheath.

7. Place the other Teflon cylinder into the larger metal sheath so that the spacers maintain their position in the center of the O-ring, and that the O-ring makes contact with the filter membrane.

8. Assemble the remaining elements of the stainless-steel apparatus. Tighten the apparatus until the threads are snug, but do not crank down on it as the Teflon is soft and will flow under plastic deformation. The hexagonal outer grips on both pieces should be aligned.

9. Place the stainless-steel apparatus in the extruder holder. If using a ternary composition of lipids, make sure that the entire apparatus has been pre-heated in an oven at a temperature at least 10°C above the T_{mix}.

10. Clean the two vacuum syringes by flushing them with $CHCl_3$ and then plenty of MilliQ to ensure that the $CHCl_3$ is completely flushed from the syringes.

11. Wet everything inside the extruder by drawing ~500 µL of sample buffer in one syringe and pushing it through the extruder into the other syringe. Push the solution back and forth through the extruder ~11x. Expel this solution and draw up the sample, which will likely be a cloudy solution. Keep solution and extruder in the oven for temperature-sensitive samples.

12. Secure the syringes into the apparatus with the securing latches on the sides of the apparatus.

13. Gently push in the plunger of the syringe containing the lipid mixture and the syringe on the opposite side of the apparatus should draw up the liquid without any assistance. The first pass of

the vesicles through the filter is always the most difficult. The smaller the membrane pores, the more difficult the sample will be to extrude.

14. Push the sample back from the second syringe into the first syringe. Repeat this 19-29x. A higher number of passes through the extruder correlates with a narrower distribution of vesicle sizes.

15. Put the extruded vesicles into a plastic or glass vial for immediate use.

A.A.5 Cryogenic Freezing of LUVs via a Vitrobot

* This protocol is written for use with a Vitrobot™ Mark IV (FEI; Hillsboro, OR)

1. Apply Vitrobot™ 50 mm filter paper to the two pads of the Vitrobot™.

2. Attach the humidifier to the Vitrobot™ and fill it with 60 mL of MilliQ water

3. Turn on the Vitrobot™ and set the internal temperature to 25°C with 100% humidity.

4. Set the blotting parameters:

- For liposomes on 2x2 QUANTIFOIL® holey-carbon grids (Electron Microscopy Sciences; Hatfield, PA), use a single blot for 2.5 or 3 s.

- For liposomes on 2x2x2 C-flat™ holey-carbon grids (Electron Microscopy Sciences; Hatfield, PA), use a single blot for 7 or 8 s.

- For fatty acid vesicles on 2x2x2 C-flat™ holey-carbon grids (Electron Microscopy Sciences; Hatfield, PA), use a 4s/4s double blot.

5. Cool down the Vitrobot™ dewar with liquid N_2. The heat transfer topper should be placed in the dewar so that the copper cup (later filled with liquid ethane) is cooled to liquid N_2 temperature. Cover the entire apparatus with a plastic beaker to ensure that no liquid water gets in.

6. While the dewar is cooling, prepare the grids.

7. Grids are stored in a desiccator. Remove the necessary grids and place them carbon-side-up on a petri dish. Place the petri dish into a glow discharger and plasma treat them for 15 s. at 25 mA.

8. Fill the copper cup in the Vitrobot™ dewar with liquid ethane. Briefly, deposit gaseous ethane into the cooled copper cup and it should transition to a liquid.

9. Keep the heat transfer topper on the copper cup until a thin film of ice begins to form on the surface of the liquid ethane. Remove the heat transfer topper and place the dewar into the Vitrobot™.

10. Pick up a glow-discharged grid with the Vitrobot™ tweezers and insert the tweezers into the vitrobot such that the carbon-side of the grid faces the side portal of the Vitrobot™.

11. Deposit 3.5 µL of liposome sample (or 3 µL fatty acid sample) onto the grid. Allow the liposome solution to deposit on the grid for at least 30 s. Do not allow the fatty acid solution to sit long on the grid.

12. Blot the sample.

13. Transfer the plunge-frozen grid into a storage box. Seal the storage box and store in liquid N_2 until it is ready to be imaged.

A.A.6 Preparation of In-Cell Yeast Vacuoles for Fluorescence Imaging

* The yeast strain contains the following genetic mutations: *MATa, his3D1, lys2D0, leu2D0, VPH1-GFP::HIS3M*.

1. The day before, start pre-cultures with 1-2 colonies scraped from an agar plate submerged in 10-20 mL of synthetic complete media with 0.4% glucose. Grow cultures at 30°C and 225 rpm for 10-12 hrs.

2. After 10-12 hrs, inoculate 1 L (log stage) or 200 mL (stationary stage) with enough pre-culture to have an OD_{600} of 0.001.

3. Allow culture to grow at 30°C and 225 rpm until the culture has an OD_{600} = 0.85-1.3 for log stage (~17 hrs) or OD_{600} = 6-8 for stationary stage (~3 days).

4. To dilute cells for imaging, make an isosmotic solution of conditioned media and 20% OptiPrep. This solution is prepared by centrifuging 1 mL of culture at 1100 rpm for 2 min, collecting the supernatant, and spinning again at 1100 rpm for 2 min to remove all cells. This solution is contained with OptiPrep to a final concentration of 20% v/v OptiPrep.

5. For temperature experiments, Concavilin-A (ConA) coated coverslips should be prepared. Coat clean coverslips with 3 µL of 1 mg/mL ConA in coat buffer (50 nM HEPES, 20 mM calcium acetate, 1 mM $MnSO_4$ pH 7.5). Immediately prior to use, rinse all of the residual salt off of coverslips using MilliQ water and dry under a stream of N_2.

6. Add 5 µL of cells to a coated coverslip and dilute with an additional 5 µL of conditioned media containing 20% OptiPrep. Place another coverslip on top and allow the cells to settle onto the coated surface for at least 10 min.

7. For T_{mix} experiments, place the sample on a pre-heated temperature stage set to a temperature 5°C below the growth temperature of the sample.

8. Heat the sample in 2°C increments, taking images at every temperature increment from 3-5 fields of view. Continuing heating the sample until all vacuoles appear mixed.

9. Repeat this for several samples from the same preparation.

10. Images can be post-processed using the scripts MiscibilityTemp.py and CombinedPlotter_V2.py found in Appendix B.

A.A.7 Preparation of Isolated Vacuoles for Fluorescence Imaging

* The yeast strain contains the following genetic mutations: *MATa, his3D1, lys2D0, leu2D0, VPH1-GFP::HIS3M*.

1. The day before, start pre-cultures with 1-2 colonies scraped from an agar plate submerged in 10-20 mL of synthetic complete media with 0.4% glucose. Grow cultures at 30°C and 225 rpm for 10-12 hrs.

2. After 10-12 hrs, inoculate 1 L (log stage) or 200 mL (stationary stage) with enough pre-culture to have an OD_{600} of 0.001.

3. Allow culture to grow at 30°C and 225 rpm until the culture has an OD_{600} = 0.85-1.3 for log stage (~17 hrs) or OD_{600} = 6-8 for stationary stage (~3 days). If the OD_{600} for log stage vacuoles is too high (> 1.3), back dilute to 0.4-0.7 and grow to 0.85.

4. Transfer the sample to either 1 L Nalgene bottles (log stage) or 250 mL Nalgene bottles (stationary stage).

5. Centrifuge the sample at 4000 rpm for 10 min at room temperature.

6. Discard the supernatant and make the wash buffer (45 mL H_2O, 5 mL 1 M Tris-HCl pH 9.4, 0.077 g DTT; 50 mL per L of culture).

7. Wash the cells by resuspending each pellet in 50 mL of wash buffer.

8. Transfer to Falcon tubes and incubate in a 30°C water bath for 10 min, swirling occasionally.

9. Centrifuge for 5 min at 4000 rpm at room temperature. Save the pellet.

10. Re-suspend the pellet in spheroplasting buffer (1 mL 1M KPi pH 7.5, 1.6 mL media, 3 mL 4M sorbitol, 14.4 mL H_2O; 15 mL per L of culture).

11. Swirl by hand with rests on ice until fully re-suspended.

12. Add lyticase. For log stage experiments, at 444 μL/0.73*OD*L for Δpro8 yeast). For stationary stage experiments, add 2 mL of lyticase.

13. For log stage experiments, incubate at 30°C for 25 minutes. For stationary stage experiments, incubate at 30°C for 1 hour. Swirl every few minutes.

14. Centrifuge the sample for 2 min at 3000 rpm and 4°C.

15. Place tubes on ice and remove supernatant gently using vacuum. The pellet should be gelatinous, not rigid.

16. Add 2 mL of 15% Ficoll to each pellet.

17. Add DEAE-dextran solution (~20 μL for Δpro8 yeast; Float 10 mg DEAE-Dextran on 1 mL of 15% Ficoll and vortex after a couple of minutes).

18. Incubate for 2 min on ice, then 3 minutes at 30°C with occasional swirling, and then place on ice.

19. Load 3-4 mL of yeast lysate to the bottom of a pre-chilled SW-41 tube.

20. Overlay with ~3 mL of 8% Ficoll, followed by ~3 mL of 4% Ficoll. Be extremely careful to not disrupt the barrier between the two densities.

21. Fill to within 5 mm of the top of the tube with PS buffer. The layer between 0% Ficoll (PS buffer) and 4% Ficoll is where yeast vacuoles will sediment. Be extremely careful to not disrupt this layer.

22. Ultracentrifuge samples in a swinging-bucket SW-41 rotor at 30,000 rpm for 90 min at 4°C.

23. Trim the tip of a p200 pipette tip and withdraw the white material from the 4% Ficoll/PS buffer interface in 200 µL batches

24. Vacuole suspensions should be stored on wet ice until use.

25. To immobilize vacuoles for microscopy, mix 5 µL of vacuoles with ~5 µL of 2% agarose and allow to solidify between sandwiched coverslips.

A.A.8 Preparation of Fatty Acid Vesicles for Fluorescence Imaging

1. Prepare solutions of fatty acid vesicles: Mix 180 mM decanoic acid, 190 mM NaOH, 0.5 M NaH_2PO_4, and 4 M NaCl. Titer the pH to 6.83 ± 0.2.

2. If desired, add this solution to solid amino acid, to a concentration of 10 mM amino acid.

3. Once the decanoic acid solution is added to the solid amino acid, allow amino acid to dissolve for 60 s. Then, vortex the mix for 3 s 2x and vortex a final time for 1 s.

4. Let the sample sit for ~30 min, with brief vortexing at 15 min.

5. For fluorescence imaging, pipette 100 µL of sample into a separate test tube. Add 0.5 µL of 2 mM Rhodamine-6G and swirl.

6. Pipette this solution onto a greased coverslip (the 4 sides of the coverslip should have a smaller layer of vacuum grease).

7. Place another coverslip on top and sandwich the sample.

8. Place the sample on the microscope stage. There will be a lot of background fluorescence from the Rhodamine-6G, so it is easier to view the sample if the microscope aperture is closed as much as possible.

9. There is a very narrow depth-of-field in which vesicles are visible. In all other depths-of-field, the solution flows rapidly. This depth-of-field is near the top of the sample, as vesicles float to the top of the solution.

APPENDIX B: CODE

A.B.1 Code for "Tuning Length Scales of Small Domains in Cell-Derived and Synthetic Model Membranes

Name: 1DPairCorrelation_truncate.py

```
""" This script will take an 8-bit image and compute a pair correlation function, G(r),
of the pixels in the image. First, a pair correlation is calculated along the x-direction. This generates a 2D pair correlation with correlations between particles in X and Y. The code then plots one slice of the G(r) in the x-direction against the radius.

The pair correlation function will be normalized around 0 and this code can also calculate an envelope function of the G(r). The code fits either an exponential or a power law function to the G(r) or envelope and gives error bounds.This version truncates the envelope function after the first several peaks of the G(r). This script is adapted from code written by Shushan He."""

import matplotlib.pyplot as plt
import numpy as np
from scipy.misc import imread
from scipy.optimize import curve_fit

 def calcrdf(phi):
        ''' This function calculates the radial distribution function of an image composed of an array of pixels. It returns a 2D G(r) integrated over the average contrast intensity '''

        ## Set up the size of the array
        Lx = phi.shape[0]
        Ly = phi.shape[1]

        ## Define field as contrast from average
        ## pixel intensity (can be negative)
        dphi = phi - np.average(phi)

        ## Calculate the average contrast intensity
        diphiavg2 = np.average(dphi**2)

        ## Define the array for a 2D G(r)
        rho2 = np.zeros((Lx+1, Ly+1))

        ## Calculate the 2D G(r)
        for dx in np.arange(Lx):
                for dy in np.arange(Ly):
                        phi2 = dphi
                        rho2[dx,dy] = np.average(phi2[0:Lx-dx,0:Ly-dy] * phi2[dx:Lx,dy:Ly])

        return rho2/diphiavg2

```

```
38.  def exponential(x, a, b, c):
39.          return a * np.exp(-b * x) + c
40.
41.  def power(x, a, b, c):
42.          return a * (x**(-b)) + c
43.
44.  def power2(x, a, b):
45.          return a * (x**(-b))
46.
47.  if __name__ == "__main__":
48.
49.          ## Load in the image
50.          im = imread("14_croprotate.tif")
51.          phi = im
52.
53.          ## Calculate the 2D G(r) using the RDF function
54.          dgr_2d = calcrdf(phi)
55.
56.          ## Slice the 2D G(r) in the x-direction, where
57.          ## dy=0 to obtain a 1D G(r)
58.          dgr_1d = dgr_2d[0]
59.          print (len(dgr_1d))
60.
61.          ## Calculate the numerical derivative of G(r)
62.          ## to find the maxima to fit to an exponential
63.          ## or power law curve
64.          gr_deriv = np.diff(dgr_1d)
65.
66.          ## Roll the derivative over one to see where
67.          ## it changes sign
68.          gr_derivposition = np.array(gr_deriv > 0, dtype=int)
69.          gr_derivposition2 = np.roll(gr_derivposition, 1)
70.          np.array(gr_derivposition - gr_derivposition2 == -1,
   dtype=int)
71.          maxX = np.array(gr_derivposition-gr_derivposition2 == -1,
   dtype=int)
72.
73.          ## Define the array in units of pixels
74.          ## (will need the max number of pixels)
75.          r = np.arange(59)
76.
77.          ## Define the array in units of microns
78.          ## (will need the resolution of the image)
79.          r = r*0.16
80.
81.          ## Redefine r to shift by half a pixel length.
82.          ## This is due to an error in fitting a power law
83.          ## when there are 0's present in r. The
84.          ## uncertainty of the self correlation is on the
85.          ## order of the size of the pixel (0.17 µm)
86.          r = r+0.16/2
87.
88.          ## Redefine the bounds of the 1D G(r)
89.          g_r = dgr_1d[:59]
90.
91.          ## For plotting, set the maxX at 0 equal to 1
92.          ## and find the x values where maxX is 1
```

```
        ## and the y values where x is 1 multiplied
        ## by the 1D G(r)
        maxX[0] = 1
        envelopeX = r[maxX==1]
        envelopeY = maxX[maxX==1]*g_r[maxX==1]

        ## Truncate the envelope at ~6 µm
        ## and delete erroneous point at 1 pixel noise
        envelopeX = envelopeX[:3]
        envelopeY = envelopeY[:3]
        print(envelopeX)
        #envelopeX = np.delete(envelopeX,2)
        #envelopeY = np.delete(envelopeY,2)

        ## Fit the data to an exponential curve or power law
        poptE, pcovE = curve_fit(exponential, envelopeX, envelopeY)#,
   p0=[1,1],maxfev=10000)
        fitE = exponential(envelopeX, *poptE)
        poptP, pcovP = curve_fit(power2, envelopeX, envelopeY, p0
   =[1,1])
        fitP = power2(envelopeX, *poptP)
        #print(popt)
        #print(pcov)

        # Calculate the error based on a taylor expansion
        # and the most weighted parameters (a and c)
        perrE = np.sqrt(np.diag(pcovE))
        upperE = fitE + (perrE[0]+perrE[2])
        lowerE = fitE - (perrE[0]+perrE[2])

        perrP = np.sqrt(np.diag(pcovP))
        upperP = fitP + (perrP[0])
        lowerP = fitP - (perrP[0])

        # Calculate the residual and the variance to obtain
        # the R-squared value for both fits

        residualE = np.sum((envelopeY - fitE)**2)
        varianceE = np.sum((envelopeY- envelopeY.mean())**2)
        r_squaredE = 1 - (residualE/varianceE)
        print(r_squaredE)

        residualP = np.sum((envelopeY - fitP)**2)
        varianceP = np.sum((envelopeY - envelopeY.mean())**2)
        r_squaredP = 1 - (residualP/varianceP)
        print(r_squaredP)

        ### Plot the G(r)

        # Make a plot with space for subplots
        fig, axes = plt.subplots(1,1,sharex=True, sharey=True,
   figsize=(6,6))

        # Plot the G(r) and the fit with error bounds
        x = np.linspace(envelopeX.min(),envelopeX.max(),200)
        axes.axhline(0, color = "black", linestyle ='--', alpha=0.2 )
```

```
146.        #axes.axvline(5.695, color = "black", linestyle='--',
   alpha=0.2)
147.        axes.plot(r, g_r, color = "black", alpha = 0.7, label =
   'data')
148.        axes.plot(x, exponential(x,*poptE), color = "blue", alpha =
   0.7, linestyle = '-.', label = 'exponential fit')
149.        axes.plot(x, power2(x,*poptP), color = "green", alpha = 0.4,
   label = 'power law fit')
150.        axes.plot(envelopeX,envelopeY, marker = "o", linestyle =
   "None", markersize = 5, markeredgecolor = "grey", markerfacecolor =
   "None")
151.        axes.set_ylabel("G(r)", fontname="Arial", fontsize=15)
152.        axes.set_xlabel("Radius (μm)", fontname="Arial", fontsize=15)
153.        axes.text(3.5, 0.85, '$R^2$ exponential = 1.00 \n$R^2$ power =
   0.906', style='normal',
154.         bbox={'facecolor':'None', 'alpha':0.5, 'pad':3})
155.        #axes.legend()
156.
157.        # Save the figure as a PDF
158.
159.        plt.savefig("GPMV_14deg_combinedtruncate.pdf")
160.        plt.show()
```

Name: 1DStructureFactor.py

```
1.  """ This script will take an 8-bit image and compute a pair
   correlation function, G(r), of the pixels in the image. First, a pair
   correlation is calculated along the x-direction. This generates a 2D
   pair correlation with correlations between particles in X and Y. The
   code then plots one slice of the G(r) in the x-direction against the
   radius.
2.
3. The code will then calculate a fourier transform of the 1D G(r) to
   obtain an S(k). This script is adapted from code written by Shushan
   He."""
4.
5. import matplotlib.pyplot as plt
6. import numpy as np
7. from scipy.misc import imread
8. from scipy.optimize import curve_fit
9.
10.  def calcrdf(phi):
11.         ''' This function calculates the radial distribution function
12.         of an image composed of an array of pixels. It returns a 2D
13.         G(r) integrated over the average contrast intensity '''
14.
15.         ## Set up the size of the array
16.         Lx = phi.shape[0]
17.         Ly = phi.shape[1]
18.
19.         ## Define field as contrast from average
20.         ## pixel intensity (can be negative)
21.         dphi = phi - np.average(phi)
22.
23.         ## Calculate the average contrast intensity
```

```
24.         diphiavg2 = np.average(dphi**2)
25.
26.         ## Define the array for a 2D G(r)
27.         rho2 = np.zeros((Lx+1, Ly+1))
28.
29.         ## Calculate the 2D G(r)
30.         for dx in np.arange(Lx):
31.                 for dy in np.arange(Ly):
32.                         phi2 = dphi
33.                         rho2[dx,dy] = np.average(phi2[0:Lx-dx,0:Ly-dy]
    * phi2[dx:Lx,dy:Ly])
34.
35.         return rho2/diphiavg2
36.
37.  def exponential(x, a, b, c):
38.         return a * np.exp(-b * x) + c
39.
40.  def power(x, a, b, c):
41.         return a * (x**(-b)) + c
42.
43.  def power2(x, a, b):
44.         return a * (x**(-b))
45.
46.  if __name__ == "__main__":
47.
48.         ## Load in the image
49.         im = imread("GMPV_16deg_rotate.tif")
50.         phi = im
51.         print(len(phi))
52.
53.         ## Calculate the 2D G(r) using the RDF function
54.         dgr_2d = calcrdf(phi)
55.
56.         ## Slice the 2D G(r) in the x-direction, where
57.         ## dy=0 to obtain a 1D G(r)
58.         dgr_1d = dgr_2d[0]
59.
60.         ## Define the array in units of pixels
61.         ## (will need the max number of pixels)
62.         r = np.arange(38)
63.
64.         ## Define the array in units of microns
65.         ## (will need the resolution of the image)
66.         r = r*0.16
67.
68.
69.         ## Truncate the radius to cut off the
70.         ## mirrored part of the plot
71.         #r = r[:24]
72.         print(r)
73.
74.         ## Calculate the S(k) by taking a Fourier
75.         ## Transform of the magnitude squared of the
76.         ## 1D G(r)
77.         rho_k = np.fft.fft(dgr_1d)
78.         s_k = np.real(rho_k)**2 + np.imag(rho_k)**2
79.
```

```
80.
81.         ## Truncate the s_k to cut off the
82.         ## mirrored part of the plot
83.         s_k = s_k[0:18]
84.
85.         ## Define the q-space array in units of
86.         ## inverse microns
87.         q = np.fft.fftfreq(len(r))
88.         q = q/0.16
89.         q = q[0:18]
90.         print(q)
91.         #wavelength = 1/q
92.         #print(wavelength)
93.
94.         ## Redefine the bounds of the 1D G(r)
95.         ## The bound depends on the number of pixels in the x
96.         g_r = dgr_1d[:34]
97.
98.         ### Plot the S(k)
99.
100.        # Make a plot with space for subplots
101.        fig, axes = plt.subplots(1,1,sharex=True, sharey=True,
   figsize=(6,6))
102.
103.        # Plot the S(k) and the fit with error bounds
104.        #axes.axhline(0, color = "black", linestyle ='--', alpha=0.2 )
105.        axes.axvline(1.151, color = "black", linestyle ='--',
   alpha=0.2)
106.        axes.plot(q, s_k, color = "blue", alpha = 0.6, label = 'data')
107.        axes.set_ylabel("S(k)", fontname="Arial", fontsize=14)
108.        axes.set_xlabel("Wavenumber ($μm^{-1}$)", fontname="Arial",
   fontsize=14)
109.        axes.text(1.5, 17, '$\lambda_c$ = 0.86 ± 0.08 μm',
   style='normal',fontname="Arial", fontsize=14)
110.        #axes.legend()
111.
112.        # Save the figure as a PDF
113.
114.        #plt.savefig("GPMV_14deg_S(k).pdf")
115.        plt.show()
```

A.B.2 Code for "Direct Imaging of Liquid Domains in Membranes by Cryo Electron Tomography"

Name: BilayerHeightMeasurements.py

```
1. """ This script imports 0 angle images from Tomograms of lipid
   bilayers. A Canny edge detection algorithm is applied to the image to
   find the edges of the bilayer. The process of determining sigma for the
   gaussian filter in the Canny algorithm is semi-iterative. The edge
   image is a boolean array that is then converted to a binary array. The
   binary array is converted to XY. These XY coordinates are converted to
   polar coordinates and the origin is shifted to the center of the image.
```

```
2. The radii and theta values for each point along an edge are stored in a
   pandas dataframe. The program differentiates between the two edges by
   taking an average between the two and setting a boundary for above and
   below the average value. The theta values are binned so that radii are
   an average value within each bin. Once the inner and outer leaflet are
   determined, the script calculates the difference between a pixel on the
   inner leaflet with every pixel on the outer leaflet and chooses the
   minimum distance. The final height measurements are averaged by taking
   a rolling average over two pixel values. This information is stored in
   a dataframe."""
3.
4. import os
5. import matplotlib.pyplot as plt
6. import numpy as np
7. import pandas as pd
8. import cv2
9.
10.  # Canny filter
11.  from skimage.feature import canny
12.  # Denoise
13.  from skimage.restoration import denoise_nl_means, estimate_sigma
14.  # Equalize histogram
15.  from skimage.exposure import equalize_hist
16.
17.
18.  ## Set global matplotlib parameters
19.  plt.rcParams["font.family"] = "Serif"
20.  plt.rcParams["font.size"] = 12
21.  plt.rcParams["figure.figsize"] = (20,18)
22.  plt.rcParams["image.cmap"] = "bone"
23.
24.  def MrSifter(root_dir):
25.
26.  '''This function returns the file path of all the tif files within
   root_dir.'''
27.
28.          fnames = []
29.          for root, dirs, files in os.walk(root_dir):
30.
31.                  ## Loop through the files
32.                  ## Check for .tif extension
33.                  ## save if it has one
34.
35.                  for file in files:
36.                          if file.endswith(".tif"):
37.                                  fnames.append(os.path.join(root, file))
38.
39.          return fnames
40.
41.
42.  def InteractiveCanny(Image):
43.  ''' This function allows the user to interactively change the values
   of sigma in the gaussian filter portion of the Canny edge detection
   algorithm. '''
44.
45.          Filtered = canny(Image, sigma=4) # 4 for tomos and 6 for
   projections
```

```
46.          plt.imshow(Filtered)
47.          plt.show()
48.
49.          ## Inquire if the sigma value is correct
50.          Question = int(input('Input 1 if the filter i good, 0 if it is
   bad: '))
51.
52.          ## Decide whether to move on or test different values of sigma
53.          if Question !=0:
54.                  New_sigma = float(input('Enter the original value of
   sigma: '))
55.          else:
56.                  New_sigma = float(input('Enter new value of sigma: '))
57.
58.          ## Generate a new filtered image
59.          Filtered = canny(Image, sigma=New_sigma)
60.
61.          ## Show the new image
62.          plt.imshow(Filtered)
63.          plt.show()
64.          plt.close()
65.
66.          return Filtered
67.
68.  def TemplateArray(Image):
69.
70.  """ This function takes an array of binary filtered images and returns
71.  a mapped template array in polar coordinates."""
72.
73.          ## Input the image resolution in nm per pixel
74.          res = 0.191 # on TF20, 0.254
75.
76.          ## Create an XY array of the same shape as the image
77.          x,y = np.arange(Image.shape[1]), np.arange(Image.shape[0])
78.          X,Y = np.meshgrid(x, y)
79.
80.          ## Reposition the origin of the template array to be in the
   center of the filtered image
81.          X = Image * X #-Image.shape[1] # X for right, its Image*X-
   Image.shape[1] for left
82.          Y = Image *(Y-(0.5*Image.shape[0])) # This gives 1/2 the yaxis
   length
83.
84.          ## Convert the XY coordinates to polar coordinates (theta, r)
85.          ## Invert the theta coordinate so thtat it goes from 0 to pi
86.          fr = (np.sqrt(X**2 + Y**2)*Image)*res
87.          ft = abs(Image*np.arctan2(X,Y)) # normally, arctan2 takes Y,X
   but this is inverted
88.
89.          ## Isolate the radii and theta values for the edges and store
   them
90.          ## in an array outside the loop
91.          fr_edge = fr[fr !=0]
92.          ft_edge = ft[fr !=0] # us fr so that both are flattened in the
   same way
93.
94.          ## Create a pandas dataframe to store the values
```

```
95.         df = pd.DataFrame({"fr":fr_edge, "theta":ft_edge})
96.
97.         ## Create an array of values for bins in theta
98.         theta_bins = np.linspace(0, np.pi, 30)
99.
100.        ## Apply bins to the values of theta and add to the dataframe
101.        df["theta_cut"] = pd.cut(df.theta, theta_bins)
102.
103.        ## Make labels for the bins that are the middle value in the
    bin range
104.        theta_labels = 0.5*(theta_bins[:-1]+theta_bins[1:])
105.        df["theta_labels"] = pd.cut(df.theta, theta_bins,
    labels=theta_labels)
106.
107.        ## Convert the theta labels to float values instead of
    categories
108.        df.theta_labels = df.theta_labels.astype(float)
109.
110.        ## Find the average between the two edges so that we
111.        ## can distinguish between the two by seeing their position
112.        ## with respect to the average value
113.        fr_avg = df.groupby("theta_labels")["fr"].mean()
114.
115.        ## Define the top edge of the two edges by putting an addition
    to the data frame
116.        ## that checks the radius values against the average radius
    values in the bins
117.        ## and if they are above those values, places it in the top
118.        df["top_edge"] = df["fr"] >
    fr_avg.loc[df["theta_labels"]].values
119.
120.        ## Create a new data frame with only the values for the top
    edge
121.        top_df = df.loc[df["top_edge"] == True]
122.
123.        ## Define the bottom edge and create a new dataframe with only
    those values
124.        bottom_df = df.loc[df["top_edge"] == False]
125.
126.        return top_df, bottom_df
127.
128.
129.
130. if __name__ == '__main__':
131.
132.
133.        ## Set the root directory
134.        root_dir =
    "C:\\Users\\caitl\\Documents\\Tomograms\\HalfSample\\50Lo_Height\\Right
    \\"
135.
136.        ## Return a list of file names
137.        fnames = MrSifter(root_dir)
138.
139.        ## Loop through the images
140.        for name in fnames:
```

```
141.                 Image = cv2.imread(name, 0) # 0 is a key to import the
   image as greyscale
142.
143.                 ## Parse the file name to get the image name
144.                 sample =
   name[name.rfind("Right\\")+6:name.rfind(".tif")] # change depending on
   names (left is 5, right is 6)
145.                 print(f"File name = {sample}")
146.
147.                 ## Select an ROI on the image
148.                 roi = cv2.selectROI(Image)
149.
150.                 ## Close the selection window
151.                 cv2.destroyWindow('roi')
152.
153.                 ## Crop the image
154.                 imCrop = Image[int(roi[1]):int(roi[1]+roi[3]),
   int(roi[0]):int(roi[0]+roi[2])]
155.
156.                 ## Display the cropped image
157.                 cv2.imshow("Cropped Image", imCrop)
158.                 cv2.waitKey(0)
159.
160.                 ## Perform a Canny Filter algorithm
161.                 Filtered = InteractiveCanny(imCrop)
162.
163.                 ## Create a dataframe containing r and theta
   information about the edge
164.                 ## detected in the Canny filter
165.                 top_df, bottom_df = TemplateArray(Filtered)
166.
167.                 ## Compute the thicknesses by finding the minimum
   distance from a point
168.                 ## on the bottom to any point on the top
169.                 optim_thickness = []
170.                 for bx in zip(bottom_df["fr"], bottom_df["theta"]):
171.                         delta = np.sqrt(top_df["fr"].values**2 +
   bx[0]**2-2.*top_df["fr"].values * bx[0]*np.cos(top_df["theta"].values -
   bx[1]))
172.                         optim_thickness.append(delta.min())
173.                 optim_thickness = pd.Series(optim_thickness,
   index=bottom_df["theta"], name="thickness")
174.
175.                 ## Compute a rolling average of the optim_thickness
   values to smooth out
176.                 ## pixel to pixel variations
177.                 optim_thickness = optim_thickness.rolling(window=2,
   center=False).mean()
178.
179.                 ## Calculate the averages for the top and bottom edges
   and store
180.                 top_avg = top_df.groupby("theta_labels")["fr"].mean()
181.                 bottom_avg =
   bottom_df.groupby("theta_labels")["fr"].mean()
182.
183.                 ## Calculate the thickness of the bilayer
184.                 thickness = top_avg - bottom_avg
```

```
185.
186.                 # Rename the vector to the correct name and store
187.                 thickness.rename("thickness", inplace=True)
188.
189.                 ## Plot the two different thickness measurements
190.                 fig, axes = plt.subplots(figsize=(10,8))
191.                 axes.plot(thickness.index,thickness.values,lw=2,c="k",
    label="binned theta method")
192.
     axes.plot(optim_thickness,color="C3",marker="o",markersize=13,
    label="optimization method")
193.                 axes.set_xlabel("Theta")
194.                 axes.set_ylabel("Bilayer Thickness (nm)")
195.                 axes.legend()
196.                 plt.tight_layout()
197.                 plot_file = name[:name.rfind(".tif")]
198.                 #plt.savefig(plot_file + "_optim.pdf")
199.                 plt.show()
200.                 plt.close()
201.
202.                 ## Plot the radii vs theta figure
203.                 figs, axes = plt.subplots(1,1, figsize = (10,8))
204.                 axes.plot(top_df.theta, top_df.fr, marker="o",
    Linestyle="None", markersize=15, alpha=0.3, color= '#004445')
205.                 axes.plot(bottom_df.theta, bottom_df.fr, marker="o",
    Linestyle="None", markersize=15, alpha=0.3, color = '#6FB98F' )
206.                 axes.plot(top_df.theta_labels, top_df.fr, marker="s",
    Linestyle="None", markersize=12, alpha=0.5, color='#2C7873')
207.                 axes.plot(bottom_df.theta_labels, bottom_df.fr,
    marker="s", Linestyle="None", markersize=15, alpha=0.5, color =
    '#6FB98F' )
208.                 axes.set_xlabel("Theta (rad)")
209.                 axes.set_ylabel("Radii (nm)")
210.                 plt.tight_layout()
211.
212.                 ## Save the figure with the image title
213.                 plt.savefig(plot_file + ".pdf")
214.                 plt.show()
215.                 plt.close()
216.
217.                 ## Save the optimum thickness to a .csv file
218.                 df_opti =
    pd.DataFrame({"optim_thickness":optim_thickness})
219.                 df_opti.to_csv(name[:name.rfind(".tif")] +
    "_NewResults.csv")
```

Name: CombinedPlotter.py

```
1.    """ This script combines .csv files from BilayerHeightMeasurements.py
    into one .csv file that is fed into MixtureModel.py"""
2.
3. import os
4. import pandas as pd
5.
6. def MrSifter(root_dir):
```

```
7.
8.   """This function returns the file path of all the tif files within
   root_dir."""
9.
10.         fnames = []
11.         for root, dirs, files in os.walk(root_dir):
12.
13.                 ## Loop through the files
14.                 ## Check for .tiff extension
15.                 ## save if it has one
16.
17.                 for file in files:
18.                         if file.endswith("_thickresults.csv"): #
   "_NewResults.csv" for 5050sample, "_optiresults.csv" for 8020
19.                                 fnames.append(os.path.join(root, file))
20.
21.                 ## YOU HAVE BEEN SIFTED
22.
23.         return fnames
24.
25.  if __name__ == '__main__':
26.
27.         root_dir =
   "C:\\Users\\caitl\\Documents\\Tomograms\\ThickTomo\\80Sample\\"
28.
29.         files = MrSifter(root_dir)
30.
31.         dfs = []
32.         for file in files:
33.
34.                 df = pd.read_csv(file)
35.                 dfs.append(df)
36.
37.         master = pd.concat(dfs)
38.
39.         master.to_csv(root_dir + '80Sample.csv')
```

Name: MixtureModel.py

```
1.  """ This script uses Lo and Ld thickness measurements to approximate
   the probability of observing certain bilayer thicknesses in each phase.
2.
3. Those approximations form a 2 component mixture model that we fit to
   mixed samples, infering the fraction of each sample in each phase.
4.
5. Data comes from processed imagery. Script adapted from code written by
   Niket Thakkar. """
6.
7. ## For file paths, etc.
8. import sys
9. import os
10.
11.  ## For data manipulation, I/O, and
12.  ## visualization.
13.  import numpy as np
```

```
14.  import pandas as pd
15.  import matplotlib.pyplot as plt
16.
17.  ## Set up the plotting environment
18.  plt.rcParams["font.family"] = "Arial"
19.  plt.rcParams["font.size"] = 14
20.  plt.rcParams["savefig.dpi"] = 600
21.  plt.rcParams["axes.linewidth"] = 1.5
22.  plt.rcParams["xtick.major.width"] = 1.0
23.  plt.rcParams["ytick.major.width"] = 1.0
24.  plt.rcParams["lines.linewidth"] = 2.0
25.
26.  ## Set some colors as well, used in the plots
27.  ## throughout.
28.  light_blue = "#90AFC5"
29.  blue = "#336B87"
30.  dark_blue = "#2A3132"
31.  red = "#763626"
32.  lightest_green = "#C4E2CC"
33.  light_green = '#92C7AC'
34.  dark_green = '#3C6571'
35.
36.  ## For model fitting and KDE construction
37.  from scipy.stats import gaussian_kde
38.  from scipy.optimize import minimize
39.
40.  def LogPosterior(alpha,p_t_Lo,p_t_Ld,
41.                                    a=1,b=1):
42.
43.  """ This is the log of the posterior probability distribution, p(alpha
     | {t in sample}, p_Lo(t), p_Ld(t)) with a beta distribution, Beta(a,b),
     as the prior. This can be numerically integrated to give an exact
     posterior or it can be optimized via scipy.minimize to compute a
     gaussian approximation to alpha.
44.
45.  Note: p_t_Lo and p_t_Ld should be numpy arrays computed by evaluating
     the respective KDEs at each of the sample heights. """
46.
47.          ## Start by computing the contribution of the prior. This
     comes
48.          ## from the probability density of the beta distribution. See
49.          ## https://en.wikipedia.org/wiki/Beta_distribution for more
50.          ## details.
51.          log_prior = (a-1)*np.log(alpha) + (b-1)*np.log(1-alpha)
52.
53.          ## Now compute the likelihood.
54.          log_like = np.log(alpha*p_t_Lo + (1-alpha)*p_t_Ld).sum()
55.
56.          return log_prior + log_like
57.
58.  def SamplePosterior(alpha,posterior,num_samples=5000):
59.
60.  """ This is wrapper on np.random.choice which uses the alpha values
     and their associated posterior probabilities to draw samples. This
     technically treats alpha as a discrete parameter, so the spacing
     between alphas has to be very small, i.e. alpha should be a long numpy
     array. """
```

```
61.
62.         return
    np.random.choice(alpha,replace=True,size=(num_samples,),p=posterior)
63.
64.  if __name__ == "__main__":
65.
66.         ## Get the data from CSV
67.         print("\nGetting the data...")
68.         data_dir =
    os.path.join("C:\\Users\\caitl\\Documents\\PythonScripts\\TEM","mixture
    2")
69.         Lo_samples = pd.read_csv(os.path.join(data_dir,"Lo.csv"),
70.                                                         header=None,
71.                                                         usecols=[1],
72.
    dtype={1:np.float64},
73.
    names=["thickness"])["thickness"]
74.         Ld_samples = pd.read_csv(os.path.join(data_dir,"Ld.csv"),
75.                                                         header=None,
76.                                                         usecols=[1],
77.
    dtype={1:np.float64},
78.
    names=["thickness"])["thickness"]
79.         mixed_samples =
    pd.read_csv(os.path.join(data_dir,"Height.csv"),
80.
     header=None,
81.
     usecols=[1],
82.
     dtype={1:np.float64},
83.
     names=["thickness"])["thickness"]
84.
85.         ## Get rid of un-physical values
86.         Lo_samples = Lo_samples[(Lo_samples >= 2) & (Lo_samples <= 6)]
87.         Ld_samples = Ld_samples[(Ld_samples >= 2) & (Ld_samples <= 6)]
88.         mixed_samples = mixed_samples[(mixed_samples >= 2) &
    (mixed_samples <= 6)]
89.
90.
91.         ## Construct KDE approximations. We use the Lo and
92.         ## Ld approximation for fitting. The mixed_sample KDE
93.         ## is just for visualizing the results.
94.         print("Computing KDEs...")
95.         p_Lo = gaussian_kde(Lo_samples.values )
96.         p_Ld = gaussian_kde(Ld_samples.values)
97.         p_mixed = gaussian_kde(mixed_samples.values)
98.
99.         ## Evaluate the Lo and Ld distributions at each of
100.        ## the mixed points.
101.        p_t_Lo = p_Lo(mixed_samples.values)
102.        p_t_Ld = p_Ld(mixed_samples.values)
103.
104.        ## Compute the log poserior accross alpha points. This is done
```

```
105.         ## by evaluating the function above and then exponentiating
   with
106.         ## a scale factor to keep everything numerically stable.
   Finally,
107.         ## the posterior is normalized by dividing by the total (i.e.
   a
108.         ## right-hand rule numerical integration).
109.         print("Calculating posterior distribution...")
110.         alpha = np.linspace(0.01,0.99,1000)
111.         posterior = np.zeros(alpha.shape)
112.         normalization = 0
113.         stability_constant = LogPosterior(0.01,p_t_Lo,p_t_Ld)
114.         for i, a in enumerate(alpha):
115.                 posterior[i] = np.exp(LogPosterior(a,p_t_Lo,p_t_Ld)\
116.                                                                 -
   stability_constant)
117.                 normalization += posterior[i]
118.         posterior = posterior/normalization
119.
120.         ## Compute the mean and standard deviation by integrating
121.         ## the posterior times alpha and the posterior time (alpha-
   E[alpha])**2
122.         mean_alpha = (alpha*posterior).sum()
123.         var_alpha = (posterior*(alpha-mean_alpha)**2).sum()
124.         std_alpha = np.sqrt(var_alpha)
125.         print("Alpha estimate = {} +/-
   {}".format(mean_alpha,2.*std_alpha))
126.
127.         ## Plot the results
128.         fig, axes = plt.subplots(1,2, figsize=(9,5))
129.
130.         ## Set up an x axis that covers a wide range
131.         ## of thicknesses
132.         x_low = min([Lo_samples.min(),
133.                                 Ld_samples.min(),
134.                                 mixed_samples.min()])
135.         x_high = max([Lo_samples.max(),
136.                                  Ld_samples.max(),
137.                                  mixed_samples.max()])
138.         x = np.linspace(0.9*x_low,1.1*x_high,500)
139.
140.         ## Plot the KDE approximations
141.         axes[0].plot(x,p_Ld(x), color=lightest_green)
142.         axes[0].fill_between(x,0,p_Ld(x),
143.
   color=lightest_green,alpha=0.5)
144.         axes[0].plot(x,p_mixed(x), color=light_green)
145.         axes[0].fill_between(x,0,p_mixed(x),
146.                                                 color=light_green,alpha=0.5)
147.         axes[0].plot(x,p_Lo(x), color=dark_green)
148.         axes[0].fill_between(x,0,p_Lo(x),
149.                                                 color=dark_green,alpha=0.5)
150.
151.         ## Finish up the details, axes limits, etc.
152.         axes[0].set(ylim=(0,2.25),xlabel="Measured thickness",
153.                                 ylabel=r"$p(t\,|\,$sample type$)$")
154.         axes[0].set_xlim(1,5)
```

```
        axes[0].set_yticks([])
        fig.tight_layout()

        # ## Plot the posterior distribution
        # axes[1].fill_between(alpha,0,posterior,
        #                                 color=red,alpha=0.8)
        #
   axes[1].errorbar(mean_alpha,1.025*posterior.max(),xerr=2.*std_alpha,
        #                           color="k",lw=1,marker="o",ls="None")
        # axes[1].set(xlim=(0,1),ylim=(0,None),
        #               xlabel=r"$\alpha$",
        #               ylabel=r"$p(\alpha\,|\,$dataset$)$")
        # axes[1].set_yticks([])
        # fig.tight_layout()

        ## Make a plot of the KDE fit
        print("Computing fit and uncertainty...")
        alpha_samples = SamplePosterior(alpha,posterior,

    num_samples=10000)
        p_Lo_x = p_Lo(x)
        p_Ld_x = p_Ld(x)
        fit_samples = np.zeros((len(alpha_samples),len(x)))
        for i, a in enumerate(alpha_samples):
                fit_samples[i] = a*p_Lo_x + (1-a)*p_Ld_x

        ## Compute the CI's via np.percentile (just some summary)
        ## statistics of the sample
        mean = mean_alpha*p_Lo_x + (1-mean_alpha)*p_Ld_x
        low = np.percentile(fit_samples,2.5,axis=0)
        high = np.percentile(fit_samples,97.5,axis=0)

        ## Plot the fit
        axes[1].fill_between(x,low,high,color=dark_blue,alpha=0.5)
        axes[1].plot(x,mean,color=dark_blue,alpha=1)
        axes[1].plot(x,p_mixed(x),color=light_green,alpha=1)
        axes[1].fill_between(x, 0, p_mixed(x), color=light_green,
   alpha=0.5)
        axes[1].set(ylim=(0,2.25),
                        xlabel="Measured thickness",
                        ylabel=r"$p(t\,|\,$sample type$)$")
        axes[1].text(3.25, 2, "alpha = 27 +/- 8%")
        axes[1].set_xlim(1,5)
        axes[1].set_yticks([])
        fig.tight_layout()
        #fig.savefig(os.path.join("C:\\Users\\caitl\\Documents\\Python
   Scripts\\TEM","FigureThickTomo_May19.pdf"))

        ## Finish up
        plt.show()
```

Name: ColorMapMask_V2.py

```
""" This script performs the same function as ColorMapMask.py version
   1, with some operational changes. The script loads a .csv file that
```

```
   contains all of the measurement data from the
   BilayerHeightMeasurement.py script. KDE's are computed from the data
   for Lo, Ld, and mixed samples. A color map is plotted on the original
   image by taking the bilayer thickness value from the sample and
   computing a 'likelihood ratio' that the measurement falls in either the
   Lo or the Ld distributions."""
2.
3. ## For file paths, etc.
4. import os
5.
6. ## For data manipulation, I/O, and
7. ## visualization.
8. import cv2
9. import numpy as np
10.  import pandas as pd
11.  import matplotlib
12.  import matplotlib.pyplot as plt
13.
14.  ## For image manipulation
15.  from skimage.feature import canny
16.
17.  ## For custom color map
18.  from matplotlib.colors import ListedColormap
19.  from matplotlib.colors import LinearSegmentedColormap
20.
21.  ## For KDE construction
22.  from scipy.stats import gaussian_kde
23.
24.  ## Set up the plotting environment
25.  plt.rcParams["font.family"] = "Arial"
26.  plt.rcParams["font.size"] = 12
27.  plt.rcParams["savefig.dpi"] = 600
28.  plt.rcParams["axes.linewidth"] = 1.5
29.  plt.rcParams["xtick.major.width"] = 1.0
30.  plt.rcParams["ytick.major.width"] = 1.0
31.  plt.rcParams["lines.linewidth"] = 2.0
32.  plt.rcParams["image.cmap"] = "gray"
33.
34.  ## Set some colors as well, used in the plots
35.  ## throughout.
36.  red = '#cc0000'
37.  blue = '#0039e6'
38.  white = '#ffffff'
39.
40.  def MrSifter(root_dir):
41.
42.  """This function returns the file path of all the tif files within
   root_dir."""
43.
44.          fnames = []
45.          for root, dirs, files in os.walk(root_dir):
46.
47.                  ## Loop through the files
48.                  ## Check for .tiff extension
49.                  ## save if it has one
50.
51.                  for file in files:
```

```
52.                         if file.endswith("_NewResults.csv"): #
   "_NewResults.csv" for 5050sample, "_optiresults.csv" for 8020
53.                             fnames.append(os.path.join(root, file))
54.
55.                 ## YOU HAVE BEEN SIFTED
56.
57.         return fnames
58.
59.  def InteractiveCanny(image):
60.
61.  """ This function allows the user to interactively change the values
   of sigma in the gaussian filter portion of the Canny edge detection
   algorithm. The Canny filtered binary image is returned."""
62.
63.         ## Compute the Canny Filter
64.         Filtered = canny(image, sigma=4)
65.         plt.imshow(Filtered)
66.         plt.show()
67.
68.         ## Inquire if the sigma value is correct
69.         Question = int(input('Input 1 if the filter is good, 0 if it
   is bad: '))
70.
71.         ## Decide whether to move on or test different values of sigma
72.         if Question !=0:
73.                 New_sigma = float(input('Enter the original value of
   sigma: '))
74.         else:
75.                 New_sigma = float(input('Enter the new value of sigma:
   '))
76.
77.         ## Generate a new filtered image
78.         Filtered = canny(image, sigma=New_sigma)
79.
80.         return Filtered
81.
82.  def TemplateArray(image):
83.
84.  """ This function takes an array of binary filtered images and their
   cut-off values and returns a mapped template array in polar
   coordinates."""
85.
86.         ## Create the cut-off version of the image
87.         plt.imshow(image)
88.         plt.show()
89.         cut_off_x = int(input('Enter the cut_off_x number: '))
90.         cut_off_y = int(input('Enter the cut_off_y number: '))
91.         cut_filter = image[:cut_off_y, :cut_off_x]
92.         plt.imshow(cut_filter)
93.         plt.show()
94.
95.         ## Input the image resolution in nm per pixel
96.         res = 0.254 # 0.191 for Glacios and 0.254 for TF20
97.
98.         ## Create the XY array of the same shape as the image
99.         x, y = np.arange(cut_off_x), np.arange(cut_off_y)
100.        X,Y = np.meshgrid(x,y)
```

```
101.
102.         ## Store the pixel locations in image space
103.         pixel_x = X*cut_filter
104.         pixel_y = Y*cut_filter
105.         pixel_x = pixel_x[pixel_x != 0]
106.         pixel_y = pixel_y[pixel_y != 0]
107.
108.         ## Re-position the origin of the template array to be in the
     center
109.         ## of the filter image
110.         X = cut_filter*X # Change for right side image, # *X for right
     side, * X-cut_off_x for left
111.         Y = cut_filter*(Y-(0.5*cut_off_y))
112.
113.         ## Convert the XY coordinates to polar coordinates (theta, r)
114.         ## Invert the theta coordinate so that it goes from 0 to pi
115.         fr = (np.sqrt(X**2 + Y**2)*cut_filter)*res
116.         ft = abs(cut_filter*np.arctan2(X,Y))
117.
118.         ## Isolate the radii and theta values for the edges and store
     them
119.         ## in an array outside the loop
120.         fr_edge = fr[fr !=0]
121.         ft_edge = ft[fr !=0] # use fr so that both are flattened the
     same way
122.
123.         ## Create a pandas dataframe to store the values
124.         df = pd.DataFrame({"fr":fr_edge, "theta":ft_edge,
125.                                          "pixel_x":pixel_x,
     "pixel_y":pixel_y})
126.
127.         ## Create an array of values for bins in theta
128.         theta_bins = np.linspace(0, np.pi, 30)
129.
130.         ## Apply bins to the values of theta and add to the dataframe
131.         df["theta_cut"] = pd.cut(df.theta, theta_bins)
132.
133.         ## Make labels for the bins that are the middle value in the
     bin range
134.         theta_labels = 0.5*(theta_bins[:-1]+theta_bins[1:])
135.         df["theta_labels"] = pd.cut(df.theta,theta_bins,
     labels=theta_labels)
136.
137.         ## Convert the theta labels to float values instead of
     categories
138.         df.theta_labels = df.theta_labels.astype(float)
139.
140.         ## Find the average between the two edges so that we
141.         ## can distinguish between the two by seeing their position
142.         ## with respect to the average value
143.         fr_avg = df.groupby("theta_labels")["fr"].mean()
144.
145.         ## Define the top edge of the two edges by putting an
146.         ## addition to the data frame that checks the radius
147.         ## values against the average radius values in the bings
148.         ## and if they are above those values, places it in the top
```

```
149.         df["top_edge"] = df["fr"] >
   fr_avg.loc[df["theta_labels"]].values
150.
151.         # Create a new data frame with only the values for the top
   edge
152.         top_df = df.loc[df["top_edge"] == True]
153.
154.         ## Define the bottom edge and create a new dataframe with only
   those values
155.         bottom_df = df.loc[df["top_edge"] == False]
156.
157.         return top_df, bottom_df, cut_filter
158.
159. def GetKDEs():
160.
161.         ## Define the root directory
162.         root_dir =
   "C:\\Users\\caitl\\Documents\\Tomograms\\HalfSample\\"
163.         ## For 80/20 sample,
   "C:\\Users\\caitl\\Documents\\Tomograms\\"
164.         ## For 50/50 sample,
   "C:\\Users\\caitl\\Documents\\Tomograms\\HalfSample\\"
165.
166.         ## Return a list of filenames
167.         fnames = MrSifter(root_dir)
168.
169.         ## Store the filenames in a list
170.         Lo = []
171.         Ld = []
172.
173.         ## Loop through the files and sort the .csv files into
   dataframes for each sample category
174.         for name in fnames:
175.
176.                 ## Parse the file name to get the parent folder
177.                 sample =
   name[name.rfind("HalfSample\\")+11:name.rfind("_Height")+7]
178.                 ## For 80/20 sample, sample =
   name[name.rfind("Tomograms\\")+10:name.rfind("_Height")+7]
179.                 ## For 50/50 sample, sample =
   name[name.rfind("HalfSample\\")+11:name.rfind("_Height")+7]
180.
181.                 if sample == "50Lo_Height":
182.                         ## For 80/20 sample, sample == "Lo_Height"
183.                         ## For 50/50 sample, sample == "50Lo_Height"
184.                         Lo.append(name)
185.                 if sample == "50Ld_Height":
186.                         ## For 80/20 sample, sample == "Ld_Height"
187.                         ## For 50/50 sample, sample == "50Ld_Height"
188.                         Ld.append(name)
189.
190.         ## Loop through the files in each category and import the data
191.
192.         # Set up the empty lists
193.         Lo_df = []
194.         Ld_df = []
195.         for name in Lo:
```

```
196.                ## Import the data
197.                Lo_df.append(pd.read_csv(name, header=0,
   index_col=None))
198.        for name in Ld:
199.                ## Import the data
200.                Ld_df.append(pd.read_csv(name, header=0,
   index_col=None))
201.
202.        ## Concatenate each of the category dataframes
203.        Lo_df = pd.concat(Lo_df, axis=0)
204.        Lo_thickness = Lo_df["optim_thickness"]
205.        Lo_thickness = Lo_thickness[(Lo_thickness >= 2) &
   (Lo_thickness <= 5)]
206.
207.        Ld_df = pd.concat(Ld_df, axis=0)
208.        Ld_thickness = Ld_df["optim_thickness"]
209.        Ld_thickness = Ld_thickness[(Ld_thickness >= 2) &
   (Ld_thickness <= 5)]
210.
211.
212.        ## Compute KDEs for Height, Lo, and Ld
213.        Lo_kernel = gaussian_kde(Lo_thickness, bw_method='scott')
214.        Ld_kernel = gaussian_kde(Ld_thickness, bw_method='scott')
215.
216.        return Lo_kernel, Ld_kernel
217.
218. if __name__ == '__main__':
219.
220.        ## Load in an image to analyze
221.        Image =
   cv2.imread("C:\\Users\\caitl\\Documents\\Tomograms\\HalfSample\\50Both_
   Height\\Right\\Sample_046_8.tif", 0)
222.
223.        ## Perform a Canny Filter on the image
224.        Filtered = InteractiveCanny(Image)
225.
226.        ## Create a dataframe containing r and theta information about
   the
227.        ## edge detected in the Canny Filter
228.        top_df, bottom_df, cut_filter = TemplateArray(Filtered)
229.
230.        ## Compute the thickness by finding the minimum distance from
   a point
231.        ## on the bottom to any point on the top
232.        thickness = []
233.        pairs = []
234.        centers = []
235.        for i, row in bottom_df.iterrows():
236.                bx = (row["fr"], row["theta"])
237.                delta = np.sqrt(top_df["fr"].values**2 +bx[0]**2-
   2.*top_df["fr"].values
238.
    *bx[0]*np.cos(top_df["theta"].values-bx[1]))
239.                min_index = np.argmin(delta)
240.                tx =
   (top_df["pixel_x"].values[min_index],top_df["pixel_y"].values[min_index
   ])
```

```
241.                 thickness.append(delta[min_index])
242.                 pairs.append([(row["pixel_x"],row["pixel_y"]),tx])
243.                 centers.append((0.5*(tx[0]+row["pixel_x"]),
   0.5*(tx[1]+row["pixel_y"])))
244.         thickness = pd.Series(thickness,index=bottom_df["theta"],
   name="thickness")
245.         #thickness_avg = thickness.rolling(window=2,
   center=True).mean()
246.         centers = np.array(centers)
247.
248.         ################### Construct KDEs ########################
249.
250.         ## Get the KDEs
251.         Lo_kde, Ld_kde = GetKDEs()
252.
253.         ## Probability density of being Lo phase or Ld phase
254.         Lo_density = Lo_kde(thickness.values)
255.         Ld_density = Ld_kde(thickness.values)
256.
257.         ## Percentage of probability density ratio
258.         #  percentage = Lo_density/(Lo_density + Ld_density)
259.
260.         ## Probability of Lo phase given distance
261.         ## From MixtureModel.py, the mixing ratio (alpha) is 0.43 for
   Ratio 2 and 0.20 for Ratio 5
262.         prob_Lo = (Lo_density * 0.20) / ((0.20 * Lo_density) + (1-
   0.20) * Ld_density)
263.         percentage = prob_Lo * 100
264.
265.         plt.imshow(cut_filter)
266.         for p in pairs:
267.                 bx, by = p[0]
268.                 tx, ty = p[1]
269.                 plt.plot([bx,tx],[by,ty],c=blue)
270.
271.
272.         fig, axes = plt.subplots(1,3, figsize=(12,5))
273.
274.         ################### Continuous color map
   ########################
275.
276.         # Create a customized cmap
277.         basic_cols=[blue, white,  red]
278.         newcmp=LinearSegmentedColormap.from_list('mycmap', basic_cols)
279.         # RdBuBig = matplotlib.cm.get_cmap('RdBu', 512)
280.         # newcmp =
   matplotlib.colors.ListedColormap(RdBuBig(np.linspace(0.2, 0.9, 256)))
281.
282.         #Normalize the colors based on the likelihood ratio
283.         norm =
   matplotlib.colors.Normalize(vmin=percentage.min(),vmax=percentage.max()
   ,clip=True)
284.         #Map the colormap colors to the normalized values
285.         mapper = matplotlib.cm.ScalarMappable(norm=norm,cmap=newcmp)
286.         #Create an array of RGBA values for the colors
287.         colors = [mapper.to_rgba(prd) for prd in percentage]
288.
```

```
        # Use contourf to provide colorbar info, then clear figure
        Z = [[0,0],[0,0]]
        steps = 0.1
        levels = np.arange(percentage.min(), percentage.max(),steps)
        CS3 = plt.contourf(Z, levels, cmap=newcmp)

        ################### Plot ########################

        # Plot the thickness values with the likelihood ratio
        axes[0].plot(centers[:,1],thickness.values,lw=2,color="grey",
   alpha=0.5)
        axes[0].scatter(centers[:,1],thickness.values,
   marker="o",color=colors, s=10**2, edgecolor="#000000")
        axes[0].set_ylim(1.0,4.0,1)
        axes[0].set(xlabel="Pixel position",ylabel="Thickness (nm)")
        axes[0].set_title("Filtered Thickness Values")

        # Plot the original image (cropped)
        Image = Image[:125, :57]
        axes[1].imshow(Image, cmap='bone')
        axes[1].set_title("Original Image")

        # Plot the filtered image with the likelihood_ratio
   superimposed on top
        axes[2].imshow(cut_filter)
        #plt.scatter(bottom_df["pixel_x"].values,bottom_df["pixel_y"].
   values,color=colors,marker="s",s=10**2)
        axes[2].scatter(centers[:,0],centers[:,1],color=colors,marker=
   "s",s=10**2, linestyle='None')
        axes[2].set_title("Filtered Image")
        plt.colorbar(CS3)


        plot_file =
   "C:\\Users\\caitl\\Documents\\Tomograms\\HalfSample\\50Both_Height\\Rig
   ht\\"
        plt.savefig(plot_file + "Sample_046_8.pdf")
        plt.show()
```

A.B.3 Code for "Yeast Alter Vacuole Phase Behavior to Adapt to Their Growth Environment"

Name: MiscibilityTemp.py

```
""" This script will loop through a folder of TIFF files, open each
   image, and allow the user to click on objects in the image. It will
   store the coordinates of these objects. It will then compute the length
   of the array of coordinates to give a count of the objects. The user
   will also input an array of temperatures. The script will take the
   counted objects and calculate the percentage of each object relative to
   the whole. The second part of the script will fit the percentages vs
   temperature to a sigmoid curve. The user can extract the 50% mark and
```

```
   95% confidence bounds. The 50% value and the 95% confidence intervals
   will be stored in a .csv file.
2. This file will be indexed by the date, which is input by the user. """
3.
4. import os
5. import numpy as np
6. import pandas as pd
7. import matplotlib.pyplot as plt
8. import scipy.optimize as optimize
9. from skimage import io
10.  from pylab import ginput
11.  from collections import defaultdict
12.
13.
14.  ## Set global matplotlib parameter
15.  plt.rcParams["font.family"] = "Sans"
16.  plt.rcParams["font.size"] = 32
17.  plt.rcParams["figure.figsize"] = (30,20)
18.  plt.rcParams["image.cmap"] = "bone"
19.
20.  def MrSifter(root_dir):
21.
22.  """This function returns the file path of all the tiff files within
   root_dir."""
23.
24.          fnames = []
25.          for root, dirs, files in os.walk(root_dir):
26.
27.                  ## Loop through the files
28.                  ## Check for .tiff extension
29.                  ## save if it has one
30.
31.                  for file in files:
32.                          if file.endswith(".tif"):
33.                                  fnames.append(os.path.join(root, file))
34.
35.                  ## YOU HAVE BEEN SIFTED
36.
37.                  return fnames
38.
39.  def VesicleCounter(fnames):
40.
41.  """This function opens up tif files and allows the user to click and
42.  collect coordinates for phase separated and mixed yeast vacuoles. It
43.  stores the coordinates in a dictionary with key:value =
   temperature:coordinates."""
44.
45.          ## Set up a dictionary of temperatures with corresponding
   coordinates
46.          PS_coords = {} # Phase separated vesicle coordinates
47.          MIX_coords = {} # Mixed vesicle coordinates
48.
49.          ## Loop through the files and open the tifs:
50.          for name in fnames:
51.
52.                  ## Print the file name to obtain the temperature
53.                  print("filename = ", name)
```

```
54.
55.                 ## Open up the tiff stack and save as an array
56.                 ## the array has dimensions (z, x, y) where z
57.                 ## represents the number of slices in the stack
58.                 ImageStack = io.imread(name)
59.                 print("ImageStack Dimensions = ", ImageStack.shape)
60.                 Position1 = int(input("Transpose? Then input -1,
   otherwise 0,: "))
61.                 ImageStack = np.moveaxis(ImageStack, Position1 ,0) #
   Transpose the stack so that the z axis is the number of tiffs
62.                 ImageStack = ImageStack[1:,:,:] # the first image is
   black, so skip
63.
64.                 ## Store the variables
65.                 ps_coords = []
66.                 mix_coords = []
67.
68.                 ## Loop through the images in the image stack:
69.                 for image in ImageStack:
70.
71.                         ## Display the image and count phase separated
72.                         plt.imshow(image)
73.                         print("Click on phase separated vacuoles")
74.                         ps_coords.append((ginput(show_clicks=True, n=-
   1, timeout=0)))
75.                         plt.close()
76.
77.                         ## Display the image and count mixed
78.                         plt.imshow(image)
79.                         print("Click on mixed vacuoles")
80.                         mix_coords.append((ginput(show_clicks=True, n=-
   1, timeout=0)))
81.                         plt.close()
82.
83.                         ## User inputs the temperature
84.                         temp = input("Input the temperature")
85.
86.                 ## Populate the dictionary with coordinates and
   temperature
87.                 PS_coords[temp] = ps_coords
88.                 MIX_coords[temp] = mix_coords
89.
90.         return PS_coords, MIX_coords
91.
92.  def ExtractDictValues(PS_coords, MIX_coords):
93.
94.         """Loop through the temperatures and replace the coordinates
95.         with the number of phase separated and the number of mixed
96.         vacuoles at each temperature."""
97.
98.         ## Set up a new dictionary of temperatures and counted
   coordinates
99.         PS_num = {}
100.        MIX_num = {}
101.
102.        ## Loop through the temperatures in PS_coords
103.        for temp in PS_coords:
```

```
104.                # Extract the values for each temperature
105.                values = PS_coords[temp]
106.
107.                # Concatenate the sublists within the "values" list
108.                new_values = [j for i in values for j in i]
109.                #new_values = sum(values) ## this should be faster
110.
111.                # Replace the coordinates of the clicks with the number
    of clicks in
112.                # the new dictionary
113.                PS_num[temp] = len(new_values)
114.
115.        ## Loop through the temperatures in MIX_coords
116.        for temp in MIX_coords:
117.                # Extract the values for each temperature
118.                values = MIX_coords[temp]
119.
120.                # Concatenate the sublists within the "values" list
121.                new_values = [j for i in values for j in i]
122.
123.                # Replace the coordinates of the clicks with the number
    of clicks in
124.                # the new dictionary
125.                MIX_num[temp] = len(new_values)
126.
127.        return PS_num, MIX_num
128.
129.
130. if __name__ == "__main__":
131.
132.        ## Define the root directory
133.        root_dir =
    "C:\\Users\\caitl\\Documents\\YeastProject\\20190418_30c\\Exp3"
134.
135.        ## Get the file names
136.        fnames = MrSifter(root_dir)
137.
138.        ## Load the images and count the vacuoles
139.        PS_coords, MIX_coords = VesicleCounter(fnames)
140.
141.
142.        ## Extract the vacuole numbers from coordinates
143.        PS_num, MIX_num = ExtractDictValues(PS_coords, MIX_coords)
144.
145.        ## Calculate the total number of vacuoles counted
146.        #VacuoleNum = PS_num + MIX_num
147.
148.        ## Combine the two dictionaries under the same key
149.        CombinedDict = defaultdict(list)
150.        # Loop through the two dictionaries and combine them under one
    key
151.        for dictionary in (PS_num, MIX_num): # these are the input
    dictionaries
152.                for key, value in dictionary.items():
153.                        CombinedDict[key].append(value)
154.
155.        # Create an empty list of phase separation values
```

```
156.        PercentPS = []
157.
158.        # Loop through the temperatures and calculate the percent PS
    at each
159.        for temp in CombinedDict:
160.                Pair = CombinedDict[temp]
161.                PS = (Pair[0] / (Pair[0] + Pair[1])) * 100
162.                PercentPS.append(PS)
163.
164.        ## Extract a list of temperatures as integers in list
165.        Temperatures = list(map(int, CombinedDict.keys()))
166.
167.        ## Get the name of the first file in the stack
168.        name = fnames[0]
169.
170.        ## Save the data as a dataframe of Temperatures and Percent PS
171.        ## Save the arrays to the location where
172.        ## fname lives.
173.        df =
    pd.DataFrame({"Temperatures":pd.Series(Temperatures,name="Temperatures"
    ),
174.
    "PercentPS":pd.Series(PercentPS,name="PercentPS")})
175.        df.to_csv(name[:name.rfind(".tif")]+"_results.csv")
```

Name: CombinedPlotter_V2.py

```
1.    ''' This script takes temperature vs phase separation data from
    multiple experiments and plots them on top of eachother. The user loads
    in .csv files from one folder and each file is assigned to its own
    experiment. '''
2.
3. import os
4. import matplotlib.pyplot as plt
5. import pandas as pd
6. import numpy as np
7.
8. ## For least-squares fit of data
9. from scipy.optimize import minimize
10.
11.  ## Set global matplotlib parameters
12.  plt.rcParams["font.family"] = "Arial"
13.  plt.rcParams["font.size"] = 22
14.  plt.rcParams["savefig.dpi"] = 600
15.  plt.rcParams["axes.linewidth"] = 2.0
16.  plt.rcParams["xtick.major.width"] = 1.5
17.  plt.rcParams["ytick.major.width"] = 1.5
18.  plt.rcParams["errorbar.capsize"] = 1.0
19.
20.  ## Set some colors as well, used in the plots
21.  ## throughout.
22.  sage = "#B6CDB1"
23.  yellow = "#EBBC4E"
24.  red = "#D24C2B"
25.  blue = "#273253"
```

```
26.  green = '#92C7AC'
27.  dark_green = '#3C6571'
28.
29.
30.  def Sigmoid(x, theta):
31.
32.          """This function computes a sigmoid from percentage data and
33.          temperature data"""
34.
35.          ## a = asymptote
36.          ## c = Tmix value (inflection point of the curve)
37.          ## d = rate of the sigmoid decay
38.
39.          a,c,d = theta
40.
41.          return a * (1 - 1 / (1 + np.exp(-(x - c) / d)))
42.
43.  def L2_cost_function(dataset, theta):
44.          '''This function computes a weighted least squares loss (or
    cost) function
45.          for a fit to data. The loss function has the form L2 =
    sum((y_true - y_pred)**2)'''
46.
47.          y_pred = Sigmoid(dataset[:,0], theta)
48.          return (((dataset[:,1] - y_pred)**2).sum())
49.
50.  def Fit(dataset, theta0):
51.          '''This function fits the data to a model and minimizes the
    cost function to
52.          give the best fit parameters for the model to the data.'''
53.
54.          f = lambda x: L2_cost_function(dataset, x)
55.          result = minimize(f, x0=theta0)
56.          return result
57.
58.  def BootStrap(ModelResults, dataset):
59.          ''' Compute the confidence intervals for a particular model of
    the dataset
60.          using bootstrap resampling. Here, random samples are drawn
    from the results
61.          of the "Fit" function. Each of these samples is taken from the
    parameters and
62.          covariance matrix of the fit. Each of these samples is then
    fit to a line.
63.          The percentiles for the sample lines are computed to give
    confidence intervals.'''
64.
65.          ## Draw random samples of parameters from the fit.
66.          #  ModelResults.x  = parameters
67.          #  ModelResults.hess_inv = covariance matrix
68.          p_samples = np.random.multivariate_normal(mean=ModelResults.x,
    cov=ModelResults.hess_inv, size=(5000,))
69.
70.          ## Make a series of x values that cover 0.8 of the minimum
    value of X in the dataset
71.          ## and 1.15 of the maximum value of x in the dataset
```

```
72.         x = np.linspace(0.8*dataset[:,0].min(),
   1.15*dataset[:,0].max(), 100)
73.
74.         ## Fit lines to the random samples
75.         samples = np.zeros((5000,100))
76.         for i, p_i in enumerate(p_samples):
77.                 samples[i] = Sigmoid(x, p_i)
78.
79.         ## Compute the percentiles
80.         low = np.percentile(samples, 2.5, axis=0)
81.         high = np.percentile(samples, 97.5, axis=0)
82.         mid = Sigmoid(x, np.array([ModelResults.x[0],
   ModelResults.x[1], ModelResults.x[2]]))
83.
84.         return low, high, mid, x
85.
86.  def MrSifter(root_dir):
87.
88.         """This function returns the file path of all the tif files
   within root_dir."""
89.
90.         fnames = []
91.         for root, dirs, files in os.walk(root_dir):
92.
93.                 ## Loop through the files
94.                 ## Check for .tiff extension
95.                 ## save if it has one
96.
97.                 for file in files:
98.                         if file.endswith(".csv"):
99.                                 fnames.append(os.path.join(root, file))
100.
101.                ## YOU HAVE BEEN SIFTED
102.
103.        return fnames
104.
105. if __name__ == "__main__":
106.
107.        ## Define the root directory
108.        root_dir =
   "C:\\Users\\caitl\\Documents\\YeastProject\\InCell_dat\\30C_Growth"
109.
110.        ## Get the filenames
111.        fnames = MrSifter(root_dir)
112.
113.        ## Loop through the filenames
114.        ##### 1. Sort the data into a dataframe
115.        ##### 2. Fit a sigmoid function to the data and compute
   confidence intervals
116.        ##### 3. Add fit and confidence intervals to the dataframe
117.        ##### 4. Concatenate all the data frames, organized by the
   sample name
118.
119.        sample_dfs = []
120.        model_dfs = []
121.        Tmix = []
122.
```

```
123.        for name in fnames:
124.
125.                df = pd.read_csv(name, usecols= ['Temperatures',
   'PercentPS']).sort_values('Temperatures')
126.
127.
128.                ## Parse the file name to get the date and experiment
   number
129.                sample =
   (name[name.rfind("\\2019")+5:name.rfind("_results")])
130.
131.                df['Name'] = sample
132.
133.                ## Fit a sigmoid
134.                x_vector = np.linspace(df['Temperatures'].values.min(),
   df['Temperatures'].values.max(), 1000)
135.                dataset = df[['Temperatures', 'PercentPS']].values
136.                Result = Fit(dataset, np.array([46,20,100])) # The
   theta values may need to be adjusted
137.                low, high, mid, x_array = BootStrap(Result, dataset)
138.
139.                ## Grab the Tmix value
140.                Tmix.append(Result.x[1])
141.
142.                ## Create a dataframe for the model and bootstrap
   results
143.                model_df = pd.DataFrame({'Name': sample, 'Low': low,
   'High': high, 'Mid': mid, 'Temp': x_array})
144.
145.
146.                sample_dfs.append(df)
147.                model_dfs.append(model_df)
148.
149.        ## Combine all of the dataframes and organize them by the
   sample name
150.        sample_df =
   pd.concat(sample_dfs).set_index('Name').sort_index()
151.        model_df = pd.concat(model_dfs).set_index('Name').sort_index()
152.
153.        ## Plot it all!
154.
155.        figs, axes = plt.subplots(figsize=(8,10))
156.
157.        #names = ['0208_Exp2', '0208_Exp3', '0405_Exp1', '0405_Exp2',
   '0405_Exp3', '0405_Exp4', '0412_Exp1', '0412_Exp2'] # Room Temp
158.        names = ['0418_Exp3', '0418_Exp4', '0419_Exp1', '0419_Exp2',
   '0419_Exp3', '0419_Exp4', '0201_Exp3', '0201_Exp4', '0205_Exp1',
   '0205_Exp2'] # 30 C
159.
160.
161.        for i in np.arange(len(names)):
162.
163.
164.                model = model_df.loc[names[i]]
165.                sample = sample_df.loc[names[i]]
166.
```

```
167.                axes.plot(model['Temp'].values, model['Mid'].values,
   linestyle='-', linewidth= 4, alpha=0.7, color = yellow)
168.                axes.plot(sample['Temperatures'].values,
   sample['PercentPS'].values, linestyle='None', marker='o',
   markersize=10, alpha=0.8, color = yellow)
169.                axes.fill_between(model['Temp'].values,
   model['Low'].values, model['High'].values, alpha=0.5, color = yellow)
170.                axes.set_ylim(-5, 85)
171.                axes.set_xlabel('Temperature')
172.                axes.set_ylabel('% Phase Separation')
173.
174.        ## Add the average Tmix with standard deviation
175.        avg_tmix = np.array(Tmix).mean()
176.        std_tmix = np.array(Tmix).std()
177.        fifty_per = sample_df['PercentPS'].values.max() / 2
178.
179.        axes.errorbar(avg_tmix, fifty_per, xerr = std_tmix,
   linestyle='None', marker='o', markersize=10, alpha=0.6, color='k',
   capsize=3, linewidth=3, zorder=11)
180.
181.        #plt.savefig('RoomT_Growth.pdf')
182.        plt.show()
```